

NASA CR-166,185



# JOINT INSTITUTE FOR AERONAUTICS AND ACOUSTICS



National Aeronautics and  
Space Administration  
Ames Research Center

NASA-CR-166185  
19810012485



Stanford University

## JIAA TR-26

# KINEMATICS AND DYNAMICS OF VORTEX RINGS IN A TUBE

JAMES G. BRASSEUR

STANFORD UNIVERSITY  
Department of Aeronautics and Astronautics  
Stanford, California 94305



MAY 1 1981

AUGUST 1979



JIAA TR - 26

# KINEMATICS AND DYNAMICS OF VORTEX RINGS IN A TUBE

JAMES G. BRASSEUR

AUGUST 1979

The work here presented has been supported by the National Science Foundation under Grant No. ENG 74-22615, by the Department of Aeronautics and Astronautics, and by the Joint Institute for Aeronautics and Acoustics.

*N81-21014#*

(The natural) laws are not forces external to things,  
but represent the harmony of movement immanent in them.

-from the I Ching.



# Abstract

Although vortex rings have been studied mathematically and experimentally for over a century, the transition in characteristics from viscous to turbulent vortex rings, and the effects of boundaries on their evolution is not well understood. In this study kinematic theory and flow visualization experiments are combined to examine the dynamic processes which control the evolution of vortex rings from very low to very high Reynolds numbers, and to assess the effects of the wall as a vortex ring travels up a tube.

**THEORY.** We model the vortex ring as a circular vortex filament axisymmetrically placed in an infinitely long tube. Using the Biot-Savart law, a kinematic expression which linearly relates a given distribution of vorticity to its velocity field, the closed form solutions to the non-steady potential and streamline fields are obtained. Transferring to a frame moving with the ring, the outermost closed streamline outlines the spheroidal volume of fluid carried along with the vortex core. We find that the effect of the tube on the vortex ring is to increase its volume and decrease its speed as compared with an identical ring in an unbounded flow. By superposition of vortex filaments, we conclude that the size and shape of typical vortex rings are accurately predicted by concentrating their strength along a circle, and by neglecting vorticity in a wake.

**EXPERIMENT.** Vortex rings are produced by ejecting a single pulse of water through orifices mounted in a plexiglass tube of diameter 11.88 cm. Seven orifices with orifice-to-tube diameters between 0.10 and 0.64 are used. The piston speed is adjusted so as to produce tube Reynolds numbers of roughly 5000, 4000, and 3000, resulting in the production of vortex rings with Reynolds numbers between 690 and 50'00. To visualize the flow, dye and hydrogen

bubbles are used, high speed 16mm movies recording all combinations of tube Reynolds number and orifice size. From the movies detailed measurements are made of the distance, size, and shape as a function of time for 26 rings at different Reynolds numbers. A careful examination of the data reveals:

1. The time dependent form of the ring velocity can be identified within regimes for all vortex rings, two regimes being separated by a rapid change in velocity.
2. From the form of time dependence in velocity, three classes of vortex rings can be identified and grouped by Reynolds number.

Qualitative observations are combined with the measurements to study the character of vortex rings in each of these three groups and the periods of rapid change between regimes.

COMBINATION OF THEORY WITH EXPERIMENT. The kinematic relationships among the size, shape, speed, and strength of vortex rings in a tube are computed from the theory. Previous methods for computation of the total circulation required a measurement of the velocity field within the vortex ring. Together with these kinematic relationships, however, relatively simple flow visualization measurements can be used to calculate the total circulation of a vortex ring at a given time. Using this method we have computed and plotted the strength as a function of time for our experimentally produced vortex rings. Reynolds number relationships are established and quantitative differences among the three Reynolds number groups are discussed. The accuracy of the method, assessed by comparing with the measurements of Sullivan *et al.*, is felt to be excellent.

# Acknowledgements

It is very difficult in the course of one's work to express one's true feelings of gratitude and appreciation to all those who have helped along the way. Instead, we are left at the end with the page called "acknowledgements." I only hope that those who have been so good to me over the past five years realize that my thanks go much deeper than I can possibly express here.

I feel very fortunate to have had as my adviser Dr. I-Dee Chang. Both a fine scientist and a wonderful person, he has taught me, among many other things, that the point of research is to learn.

For the help and support given me by Dr. K. Karamcheti and the Joint Institute for Aeronautics and Acoustics, I am truly grateful. The Institute's activities have been a constant source of stimulation and knowledge.

I thank those who have given me their technical expertise and help. Dr. Sotiris Koutsoyannis played a major role in the design of the experimental apparatus and in the execution of the experiment; the apparatus was built by Vadim Matte and Jerry DeWerk. Bill Janeway designed and built the timer used to calibrate our movies as well as other circuitry, and Jack MacGowen helped with the design of the hydrogen bubble visualization.

Much of this work would not have been possible without the generous help and computer support given me by Dr. John Wilcox and his solar physics group in the Institute for Plasma Research. A warm thanks to Dr. Philip Scherrer for the many hours he has spent teaching me about computers, and to Eileen Gandolfini for her help, and her smile.

So many others have been so helpful, and so kind. Theresa Storm, Susan Triefenbach, Minnie Pasin, Ella Zvigna, Joyce Parker, Maribel Quesada, Carolyn Edwards, Cherry Bobier, Dick Rimmel, Susan Richardson, Jill Izzarelli, ... thank you all!

The first three years of this research were supported by the National Science Foundation under Grant No. ENG 74-22615. Additional support has come from the Department of Aeronautics and Astronautics in the form of a Departmental Research Assistantship, and from the Joint Institute for Aeronautics and Acoustics.

# Contents

Abstract	iii
Acknowledgements	v
List of Illustrations	ix
List of Symbols	xii
1 INTRODUCTION	1
1-1 Historical Outline	1
1-2 Objectives and Organization	4
2 BACKGROUND	6
2-1 Kinematics of Vorticity	6
2-2 Dynamics of Vorticity	10
2-3 Vortex Rings in an Ideal Fluid	12
2-3.1 The Classical Vortex Ring	12
2-3.2 Thick Core Vortex Rings	18
2-4 Vortex Rings in a Real Fluid	19
2-4.1 Vortex Ring Formation	19
2-4.2 Vortex Ring Evolution	20
2-5 Concepts Behind the Present Study	25
3 THEORY	32
3-1 Solution for a Circular Vortex Filament in a Tube	32
3-1.1 Harmonic Expansion for the Unbounded Ring	32
3-1.2 Monopole Solution: The Green Function	36
3-1.3 The Potential and Stream Functions in Non-Steady Coordinates	37
3-2 The Potential and Streamline Fields in the Fixed Frame	39
3-2.1 Inner and Outer Expansions for the Unbounded Ring	39
3-2.2 Expansions for the Induced Field	40
3-2.3 The Potential and Streamline Fields	42
3-3 The Velocity of the Vortex Ring in a Tube	48
3-4 The Potential and Streamline Fields in the Moving Frame	54
3-4.1 The Kinematic Relationships Among Vortex Ring Parameters	54
3-4.2 The Effect of a Finite Core on Ring Shape	66

4	EXPERIMENT	70
	4-1 Apparatus and Experiment	70
	4-2 Qualitative Observations	76
	4-3 Quantitative Results	81
	4-3.1 Data Acquisition	81
	4-3.2 Vortex Ring Velocity	85
	4-3.3 Vortex Ring Radius and Thickness	90
	4-4 Discussion	92
	4-4.1 Reynolds Number Dependence	92
	4-4.2 Periods of Rapid Change: Instabilities	95
	4-4.3 Additional Observations	97
5	COMBINATION OF THEORY WITH EXPERIMENT	102
	5-1 Total Circulation as a Function of Time	102
	5-2 Accuracy of the Computation Method	109
	5-2.1 The Effect of Wake Vorticity on Ring Shape	109
	5-2.2 Comparisons with Measured and Estimated Values	110
	5-3 Vortex Rings and the Reynolds Number	115
	5-4 Arterial Stenoses and the Wall Pressure	121
6	SUMMARY	130
	APPENDICES	
	A Vortex Ring Trajectory, Size, and Shape Plots	135
	B Vortex Ring Strength and Velocity Plots	187
	BIBLIOGRAPHY	206

# List of Illustrations

FIGURES	page	
2-1	Definitions for a vortical flowfield	8
2-2	Definitions for a vortex tube or filament	8
2-3	The cylindrical coordinate system	14
2-4	A vortex filament-loop	14
2-5	The classical vortex ring in steady and non-steady coordinates	17
2-6	The velocity and vorticity distributions in a real vortex ring	21
2-7	Laminar and turbulent vortex rings	23
2-8	Ring Reynolds numbers previously covered in experimental studies of vortex rings	26
3-1	Definitions for a circular vortex filament axisymmetrically placed in a tube	33
3-2	Representing a circular vortex filament as a disk of dipoles of uniform strength	33
3-3	The streamlines and constant potential lines in the fixed frame for an unbounded vortex ring with $\epsilon = 0.40$	45
3-4	The streamlines and constant potential lines in the fixed frame for a bounded vortex ring with $\epsilon = 0.40$	46
3-5	The wall-induced streamline and constant potential lines in the fixed frame for a bounded vortex ring with $\epsilon = 0.40$	47
3-6	The Domb-Sykes plot for $\hat{U}_i$	51
3-7	The wall-induced velocity of a vortex ring in a tube	52
3-8	The analog of a vortex pair in a channel	53
3-9	The streamlines and constant potential lines in the moving frame for a bounded and unbounded vortex ring with $\epsilon = 0.40$	58
3-10	The streamlines and constant potential lines in the moving frame for a bounded and unbounded vortex ring with $\epsilon = 0.70$	61
3-11	The variation of $T/R$ with $\hat{U}_0$ for different values of $\epsilon$	64
3-12	The variation of $R'/R$ with $\hat{U}_0$ for different values of $\epsilon$	65
3-13	Constant potential lines for a vortex ring with a finite core compared with a circular vortex filament	68

FIGURES (continued)		page
4-1	The basic experimental apparatus	71
4-2	The main components of the experiment	73
4-3	Piston trajectory characteristics	75
4-4	Photograph of a vortex ring at the highest Reynolds numbers	78
4-5	Refraction corrections: apparent vs. real radius	84
4-6	The velocity distribution for Run 9	86
4-7	The least squares fit slopes and residuals vs. point number for Run 9	88
4-8	Repeatability: comparison in trajectory between Runs 9 and 10	91
4-9	Correlation of sudden velocity changes with instabilities	96
4-10	The rocking oscillation observed in Run 5	98
4-11	Rocking oscillation: velocity plot for Run 5	99
5-1	The variation of $T/R'$ with $R'/\rho_0$ for different values of $\hat{U}_0$	104
5-2	Comparison of mean velocity and strength with point by point calculations for Run 1	107
5-3	The streamlines for a vortex ring with a wake compared with a wakeless vortex ring	111
5-4	Comparison of vortex ring strengths computed using the kinematic theory with estimates and one measurement	114
5-5	Relationship between $Re_R$ and $Re_T$ for newly formed vortex rings	117
5-6	Relationships between $Re_R$ or $Re_T$ and $Re_j$ for newly formed vortex rings	118
5-7	The drag coefficient of vortex rings plotted against Reynolds number	122
5-8	Speed and Reynolds number of blood ejected from a human heart into the aorta	124
5-9	The non-dimensional wall velocity as a function of $z/\rho_0$ for different values of $\epsilon$	126
5-10	The pressure at the tube wall 1.5 diameters from the orifice for Run 1	128
5-11	The pressure at the tube wall 1.5 diameters from the orifice for Run 3	129

FIGURES IN THE APPENDICES		page
A-1 through A-26	Vortex ring trajectory, size, and shape plots for Runs 1 - 26	135
B-1 through B-17	Vortex ring strength and velocity plots	187
TABLES		
3-1	Numerically computed values for $M_n$	43
3-2	Coefficients for the wall-induced velocity of a vortex ring in a tube	50
4-1	General identification for experimental vortex ring runs	82
TABLES IN THE APPENDICES		
A-1	Summary of experimental values for each run	136
A-2	Summary of regime slopes for each run	137
B-1	Initial vortex ring parameters for each run	188

# List of Symbols

## LATIN SYMBOLS

a	radius of the core cross-sectional area (Fig. 2-3)
d	diameter of the orifice
D	inner diameter of the tube
$I_0, I_1$	modified Bessel functions of the first kind
$J_0, J_1$	Bessel functions of the first kind
$K_0, K_1$	modified Bessel functions of the second kind
n	normal to a surface
$\vec{P}, P$	total fluid impulse, or the impulse of a vortex ring
p	static pressure, usually along the tube wall
$\vec{r}$	position vector: $\vec{x} - \vec{\zeta}$
R	radius of a vortex ring to the core centerline (Fig. 2-5)
R'	radius of a vortex ring to the outermost closed streamline (Fig. 2-5)
t	time
T	the thickness of a vortex ring (Fig. 2-5)
$\vec{u}$	Eulerian flowfield velocity
u, $u_z$	z component of $\vec{u}$
$u_p$	average piston speed
$u_j$	average jet or slug-flow velocity through the orifice
U	velocity of a vortex ring
$\hat{U}$	non-dimensional ring velocity (Eq. (3-31))
V	volume of the vortex ring
$V_{ej}$	volume of fluid ejected from the orifice
$\vec{x}$	position vector from the origin
$x_p(t)$	piston trajectory
$X_p$	piston stroke length
$x_r$	distance of the vortex ring from the orifice
z	axial coordinate (Fig. 2-3)

### GREEK SYMBOLS

$\Gamma$	total circulation of a fluid element, vortex filament, or vortex ring
$\epsilon$	$R/\rho_0$
$\vec{\zeta}$	position vector, designating a vortical fluid element or the dipole field (Fig. 2-1 or 2-4)
$\nu$	kinematic viscosity
$\rho, \theta, z$	cylindrical coordinates where $z$ corresponds to the axis of the vortex ring
$\tilde{\rho}, \tilde{z}$	outer variables $\rho/\rho_0, z/\rho_0$
$\bar{\rho}, \bar{z}$	inner variables $\rho/R, z/R$
$\rho_0$	tube radius
$\rho_m$	mass density
$\tau_p$	piston stroke time (sec.)
$\Phi$	velocity potential
$\Psi$	axisymmetric stream function
$\hat{\Phi}, \hat{\Psi}$	non-dimensional potential and stream functions (Eq. (3-19))
$\vec{\omega}$	vorticity vector

### REPEATED SUBSCRIPTS

$i$	a quantity induced by the presence of boundaries
$o$	a quantity related to a vortex ring in an unbounded flow

### DIMENSIONLESS GROUPS

$C_D$	coefficient of drag
$Re$	Reynolds number
$Re_j, Re_T$	jet and tube Reynolds numbers (Eqs. (4-2) and (4-3))
$Re_R, Re_\Gamma$	ring Reynolds numbers based on $R$ and $\Gamma$ (Eqs. (2-23))

# Introduction

*After noticing Helmholtz's admirable discovery of the law of vortex motion in a perfect liquid--that is, in a fluid perfectly destitute of viscosity (or fluid friction)-- . . . this discovery inevitably suggests the idea that Helmholtz's rings are the only true atoms.*

*-Lord Kelvin, "On Vortex Atoms"*

## 1-1 HISTORICAL OUTLINE

Vortex rings have fascinated people for over a century. After Helmholtz published his celebrated paper in 1867 describing the basic laws of the flow of frictionless, incompressible fluids, a great deal of excitement and activity developed around the observation that a thin core vortex ring in such a fluid would never change in character. The permanence of the "Helmholtz ring" led Kelvin [64, article 1] to propose the vortex ring as a model for the atom. Differences among elements would be accounted for by different degrees of "knottedness" of the vortex core, and the radiation of heat and light by core vibrations. Extensive mathematical analyses of "classical" vortex rings continued through the turn of the century [10, 21-24, 62-64].

Serious experimental study of vortex rings in a real fluid began with the impressive flow visualization work of Kruttsch in 1939. Further studies of vortex rings were precluded by the onset of World War II, until G.I. Taylor rekindled interest with a letter to the editor of the Journal of Applied Physics in 1953. Soon thereafter J.S. Turner published his excellent paper on buoyant vortex rings with the suggestion that such rings might prove useful in seeding clouds to induce the production of rain. Several other papers appeared in the fifties and sixties concerning buoyant vortex rings [13, 41, 69, 70],

along with the suggestion that even if vortex rings would not prove useful in seeding clouds, perhaps they could be used to transport industrial wastes high into the atmosphere. Fortunately for all of us this scheme never bore fruit.

Interest in vortex rings exploded in the seventies. What was before a trickle of papers soon became a steady stream and is now showing signs of becoming a flood. Detailed experimental studies of neutrally buoyant vortex rings resumed once again with publications by Maxworthy in the West, and Oshima in the East. Mathematicians such as Norbury, Fraenkel, and Saffman extended the theory of vortex rings to include larger cores and viscous effects. Extensive mathematical treatments of vortex ring stability have come from Widnall and her group at M.I.T.

The rapid increase in interest in vortex rings is perhaps a result of their increasing application to a wide range of physical problems. Vortices are commonly found in nature at all scales, from the flowfield produced by insects, to large atmospheric low pressure systems covering thousands of square kilometers. Vortex rings provide an ideal experimental and mathematical model for studying general aspects of vortex evolution. The rollup of shear layers into vortices, the diffusion of vorticity from regions where vorticity is concentrated, the convection of vorticity and vortex filaments, the instability and breakdown of vortices and vortex lines, the development of turbulence from such breakdowns, vortex stretching, ... all of these topics relate to the study of vortex rings.

Vortex rings themselves have more direct applications to many problems of practical and academic interest. Current studies of the larger scale structures in turbulent flows have led to interest in the vortex ring as a possible model for the large eddies observed especially in turbulent shear flows [9, 53]. In the development of turbulent jets, for example, vortex rings can be observed to form at

the lip of the jet and to go through complicated pairing processes to form larger, less coherent rings farther downstream.\* These vortex rings are found to play an important role as well in the structure of the sound field around turbulent jets [39]. Atmospheric thermals can be visualized as large, buoyant vortex rings [41, 59]. Birds such as hawks and eagles soar around the center of these large vortices, using the vertical winds and upward movement of the buoyant air to gain altitude with little expenditure of their own energy [8]. Propulsive flight of insects and birds also involves the production of vortex rings. In two recent articles [52], Rayner has modeled the wake of birds and insects as chains of vortex rings which carry away the reaction momentum to the lift and thrust produced by the motion of the wings. Plasma physicists have been interested in the evolution of vortex rings as they travel through fluids such as liquid helium II [11, 12, 18, 72, 73], principally to study the quantized nature of the total circulation. Vortex rings were even used by Bjerknes in 1926 to model the occurrence of sunspots!

Initially, our interest in vortex rings developed from the study of the transient flowfield behind arterial stenoses, or blockages in the human arterial system, caused by the buildup of cholesterol on the arterial wall or from diseased heart valves which will not open completely. The pulsatile nature of the blood as it is ejected through these constrictions results in the production of rather incoherent, turbulent vortex rings which travel up the artery and eventually collide with the arterial wall. This has led, therefore, to our interest in the effect of boundaries such as a tube on vortex ring evolution.

---

\*E. Bouchard and W.C. Reynolds in the Department of Mechanical Engineering here at Stanford have produced beautiful movies of this process.

## 1-2 OBJECTIVES AND ORGANIZATION

In the past, experimental studies have concentrated on vortex rings in unbounded flows, and over a limited range of Reynolds numbers. Our emphasis in this study is two-fold:

We would like to examine the dynamic processes and differences in characteristics from very low Reynolds number viscous vortex rings to very high Reynolds number turbulent vortex rings, and we would like to assess the effects of the wall as vortex rings travel up a tube.

The dynamic processes in which we are interested involve the loss of vorticity from vortex rings as they propagate. We would like to predict the change in strength, or total circulation as a function of time for vortex rings at different Reynolds numbers. To accomplish this dynamic calculation we develop a method based on a purely kinematic theory which allows us to relate the strength of a vortex ring to quantities which can be measured from flow visualization experiments.

In the next chapter the background to this work is established, and in Section 2-5 the concepts behind our method for calculating the strength of a vortex ring is discussed. In order to better understand the theoretical and experimental analyses which follow in succeeding chapters, it is suggested that Section 2-5 not be skipped.

In Chapter 3 we develop the kinematic theory for a vortex ring in a tube. We find the potential and streamline fields for vortex rings of different size, and learn what the effect of the tube is on the shape and speed of a vortex ring as compared with the same ring in an unbounded flow.

Flow visualization experiments in which vortex rings were produced and observed as they travel up a tube are discussed in Chapter 4. Qualitative observations and quantitative measurements of vortex ring velocity, size, and shape are combined to study

differences in vortex rings as they relate to Reynolds number.

In Chapter 5 the flow visualization measurements are combined with the kinematic theory to calculate the total circulation as a function of time for our experimentally produced vortex rings. Relationships with Reynolds number are established, and quantitative differences discussed, again with emphasis on changes relating primarily to the Reynolds number of the vortex ring.

# 2

## Background

*The maelstrom!*  
We knew that at the tide the pent-up waters  
between the islands of Ferros and Loffoden  
rush with irresistible violence, forming a  
whirlpool from which no vessel ever escapes ...  
It was describing a spiral, the circumference  
of which was lessening by degrees, and the  
boat...was carried along with giddy speed ...  
we heard a crashing noise, the bolts gave way,  
and the boat, torn from its groove, was  
hurled like a stone from a sling into the  
midst of the whirlpool . .

-Jules Verne, 20,000 Leagues Under the Sea

### 2-1 KINEMATICS OF VORTICITY

Vorticity is a measure of the angular velocity, or spin of fluid particles. In a fluid of constant density, as we consider here, spin is imparted by frictional forces in the fluid, for example along a boundary or surface within the flow. Although vorticity is a dynamic quantity a great deal can be learned by considering the kinematic relationships between the vorticity field and the velocity field, that is, by considering only the conservation of mass and the definition for vorticity.

BIOT-SAVART LAW. Consider an incompressible and, for the moment, an unbounded flow at rest at infinity. At the time  $t$  the velocity at the point  $\vec{x}$  is given by  $\vec{u}(\vec{x})$  and the vorticity at the point  $\vec{\zeta}$  by  $\vec{\omega}(\vec{\zeta})$ . Thus we have

$$\text{Conservation of Mass: } \operatorname{div} \vec{u} = 0 \quad (2-1)$$

$$\text{Definition of Vorticity: } \operatorname{curl} \vec{u} = \vec{\omega} \quad (2-2)$$

We can satisfy Eq. (2-1) identically by letting  $\vec{u} = \operatorname{curl} \vec{B}$ .  $\vec{B}$  is chosen such that  $\operatorname{div} \vec{B} = 0$ , so that application of Eq. (2-2) results in the Poisson equation:

$$\nabla^2 \vec{B} = -\vec{\omega}$$

with the solution:

$$\vec{B}(\vec{x}) = \frac{1}{4\pi} \iiint_{-\infty}^{\infty} \frac{\vec{\omega}(\vec{\zeta})}{r} d\zeta^3 \quad (2-3)$$

As shown in Fig. 2-1,  $\vec{r} = \vec{x} - \vec{\zeta}$  and  $r = |\vec{r}|$ . Taking the curl of Eq. (2-3) results in the well known law of Biot and Savart:

$$\vec{u}(\vec{x}) = -\frac{1}{4\pi} \iiint_{-\infty}^{\infty} \frac{\vec{r} \times \vec{\omega}(\vec{\zeta})}{r^3} d\zeta^3 \quad (2-4)$$

At any time  $t$  the velocity at the point  $\vec{x}$  is given by an integral of the vorticity field over the whole flowfield. Two important features of Eq. (2-4) should be given special note:

1. This is a kinematic expression; only conservation of mass has been used in its derivation. Thus, even for a time-dependent flow, laminar or turbulent, where vorticity is diffused and convected, if at any time the vorticity field is known or can be well approximated, the velocity field can in principle be computed from Eq. (2-4).
2. The velocity field is related linearly to the vorticity field. The vorticity field can therefore be divided into elements, the velocity field found for each element separately, and summed to find the total velocity at any point in space and time.

BOUNDARIES. Although Eq. (2-4) was derived for an unbounded flow, it can be extended to a flow with boundaries by adding a potential velocity (i.e., irrotational and divergenceless)  $\vec{u}_1(\vec{x})$  to Eq. (2-4), chosen to satisfy the boundary conditions.

VORTEX FILAMENTS. In vortical flows it is common to find vorticity concentrated along curved lines, so that it is natural to idealize the concentrated region of vortical flow as a vortex tube, or in the limit of zero tube radius, a vortex filament. The vorticity

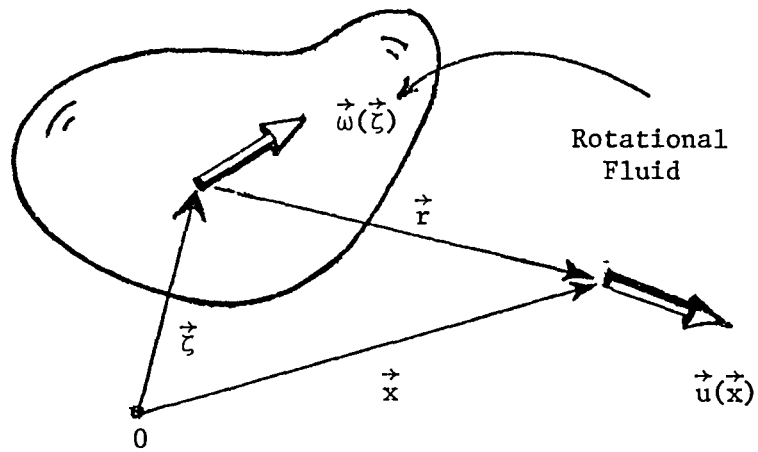


FIGURE 2-1

Definitions for a vortical flowfield

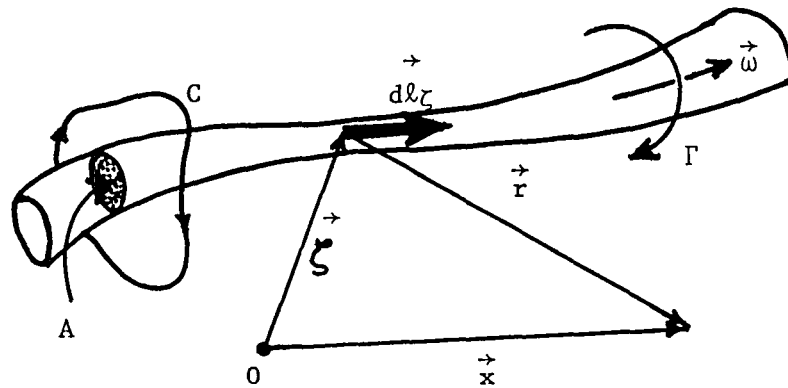


FIGURE 2-2

Definitions for a vortex tube or filament

content of a vortex tube (or a fluid element) is characterized by the circulation, or strength  $\Gamma$  where

$$\Gamma = \oint_C \vec{u} \cdot d\vec{\ell} \equiv \iint_A \vec{\omega} \cdot d\vec{A} \quad (2-5)$$

$C$  is a closed material curve around the vortex tube (or fluid element) and  $A$  is the cross-sectional area, as shown in Fig. 2-2. Mathematically a vortex tube is often idealized as a filament, or line where the strength is given in the limit  $A \rightarrow 0$ . The accuracy of such an idealization depends on the degree to which vorticity is concentrated, and the region of the flow in which we are interested. It is often the case that "far" from the region of concentrated vorticity the velocity field is accurately described by vortex filaments, whereas the flow "near" the vortical region must take into account the details of the vorticity distribution.

Using the divergence theorem and the divergenceless nature of  $\vec{\omega}$  it is easy to show that the circulation  $\Gamma$  must be constant along a vortex tube. This kinematic result has the consequence that a vortex tube cannot end in the fluid. The filaments must either form loops (e.g., vortex rings) or extend to the boundary (e.g., the horseshoe vortex observed in turbulent boundary layers).

For a vortex filament of strength  $\Gamma$  the Biot-Savart Law, Eq. (2-4), reduces to the more familiar form:

$$\vec{u}(\vec{x}) = - \frac{\Gamma}{4\pi} \oint_{\text{filament}} \frac{\vec{r} \times d\vec{\ell}_\zeta}{r^3} \quad (2-6)$$

where  $\vec{\ell}_\zeta$  is along the filament in the direction of  $\vec{\omega}$ .

**IMPULSE.** One additional kinematic expression of interest is that for the fluid impulse, the total impulsive force which would be required to set the vortical flowfield into motion. The total impulse  $\vec{P}$ , derived by Batchelor [2, p. 518] and Lamb [29, p. 214] has the

units of momentum and is given by:

$$\vec{P} = \frac{1}{2} \rho_m \iiint \vec{\zeta} \times \vec{\omega}(\vec{\zeta}) d\zeta^3 \quad (2-7)$$

where  $\rho_m$  is the mass density of the fluid.

## 2-2 DYNAMICS OF VORTICITY

Like momentum, vorticity can diffuse down a gradient slope through the action of viscosity, or in the case of turbulent flows, through the action of small scale turbulent motions. The dynamics of viscous diffusion in an incompressible fluid is described by the vorticity equation:

$$\frac{\partial \vec{\omega}}{\partial t} + \vec{u} \cdot \nabla \vec{\omega} = \vec{\omega} \cdot \nabla \vec{u} + \nu \nabla^2 \vec{\omega} \quad (2-8)$$

The left hand side is, of course, the total derivative accounting for vorticity changes in fluid elements as they are convected with the flow. The term involving  $\nu$ , the kinematic viscosity, describes viscous diffusion of vorticity, and  $\vec{\omega} \cdot \nabla \vec{u}$  gives the change in  $\vec{\omega}$  due to vortex stretching. If a flow is of sufficiently high Reynolds number to disregard viscous diffusion over the time period of interest, yet low enough to disregard turbulent diffusion, the vortical content of a fluid element convected with the flow would only change via vortex stretching.

**KELVIN/HELMHOLTZ THEOREM.** Applying the total derivative to the definition of  $\Gamma$  in Eq. (2-5) and inserting the incompressible momentum equation for  $\frac{D\vec{u}}{Dt}$  one arrives at the following expression for the circulation of a fluid element as it is convected with the flow:

$$\frac{D\Gamma}{Dt} = -\nu \oint_C \text{curl} \vec{\omega} \cdot d\vec{\ell} = \nu \iint_A \nabla^2 \vec{\omega} \cdot d\vec{A} \quad (2-9)$$

where  $C$  and  $A$  are defined as in Eq. (2-5). The circulation can change only by the diffusion of vorticity from the element. If we again have a flow in which we can neglect the effects of friction we arrive at the Kelvin/Helmholtz theorem:

$$\frac{D\Gamma}{Dt} = 0 \quad (\text{inviscid}) \quad (2-10)$$

which states that the circulation of every fluid element remains constant in time. This has the important consequences that vortex tubes are convected with flow at the local fluid velocity, and that a vortex tube is always composed of the same fluid particles. The previous considerations of the vorticity equation show that as a vortex tube is stretched by the local velocity field the magnitude of the vorticity within the tube increases. Since  $\Gamma$  must remain constant, the area of the tube must therefore decrease.

In such flows where diffusion of vorticity can be neglected, the Biot-Savart law can be used to describe both the dynamic as well as the kinematic behavior of the flow. The velocity field is "induced" by the vorticity field. Since each vortex element moves with the local fluid velocity, the self-induced velocity field found from Eq. (2-6) can be integrated in time to find the subsequent location of the vortex elements. Again using Eq. (2-6) the velocity field at that later time can then be calculated and the process repeated.

In general, of course, diffusion of vorticity due to viscosity or turbulent motions is always present, but in many flows containing concentrated regions of vorticity, the rate of diffusion is slow as compared with the convection of vorticity, and important features of the flow can be understood from the inviscid considerations above. An example is the instability and rollup of a shear layer leading to the formation of linear vortices, which then proceed to pair [78].

**INVARIANCE OF IMPULSE.** Applying the total derivative to Eq. (2-7) and using the vorticity equation, one can eventually arrive at

an expression for the variance in the total fluid impulse in a bounded flow. If the vorticity and its normal derivative are zero along the boundary the result is:

$$\frac{d\vec{P}}{dt} = \frac{1}{2} \rho_m \oint_S u^2 d\vec{S} \quad (2-11a)$$

where  $S$  is the boundary surface. For an unbounded flow ( $S \rightarrow \infty$ ) at rest at infinity we see that

$$\frac{d\vec{P}}{dt} = 0 \quad (\text{unbounded}) \quad (2-11b)$$

Thus the total fluid impulse of an unbounded fluid is invariant for both viscous and inviscid flows.

## 2-3 VORTEX RINGS IN AN IDEAL FLUID

### 2-3.1 The Classical Vortex Ring

A vortex ring can be defined as a vortical region of fluid where the mean vorticity field has an azimuthal sense and is concentrated (peaks) along a circle.\* It is natural, therefore, to model the vortex ring as a circular vortex tube, where vorticity is confined to a torus of small cross-section. Helmholtz [20] proposed such a model for a vortex ring in an ideal (incompressible, inviscid), unbounded fluid about 100 years ago, and its properties were extensively studied around the turn of the century [10, 21-23, 62-64].

NON-STEADY COORDINATE SYSTEM. Consider an axisymmetric flow without swirl. We define a cylindrical coordinate system  $(\rho, \theta, z)$

---

\*We are concerned here with circular vortex rings, although more general shapes such as elliptical vortex rings can be found in nature and have been studied as well (1, 14, 26).

fixed in space\* such that at the time  $t$  a torus of vorticity of radius  $R$  is located in the  $z = 0$  plane axisymmetrically placed about the  $z$ -axis (see Fig. 2-3). The torus, called the vortex core, has a circular cross section with radius  $a$  and a total circulation, or strength  $\Gamma$ . Outside the core the flow is taken to be irrotational. Due to its self-induced velocity field the vortex ring is moving with speed  $U$  in the  $+z$  direction, so we are depicting the vortex ring in a non-steady frame of reference.

**CIRCULAR VORTEX FILAMENTS.** The classical vortex ring is a thin torus of vorticity embedded in a potential flow, as shown in Fig. 2-3. By "thin" we mean in the limit  $a/R \rightarrow 0$ . In this limit the flowfield outside of the core is that for a circular vortex filament of strength  $\Gamma$  (the flowfield within the core, of course, depends on the distribution of vorticity). In this region the flow is irrotational, so we can define a velocity potential,  $\Phi$ :

$$\vec{u} = \nabla \Phi \quad (2-12)$$

Applying Stokes Theorem to the Biot-Savart law, Eq. (2-6), one can obtain the following representation for the potential field due to a closed vortex filament:

$$\Phi(\vec{x}) = \iint_A \frac{\partial}{\partial n} \left( \frac{\Gamma}{4\pi r} \right) dA(\vec{\zeta}) \quad (2-13)$$

As indicated in Fig. 2-4,  $A$  is the surface bounded by the vortex filament-loop,  $\vec{\zeta}$  is a position vector to a point on that surface,  $n$  is the outward normal to the surface (defined by the direction of  $\Gamma$ ), and  $\vec{r} = \vec{x} - \vec{\zeta}$ . Eq. (2-13) shows that mathematically a vortex

\*By "fixed in space" we mean fixed with respect to the stagnant flow at infinity or, in the case of the vortex ring in a tube, fixed with respect to the boundaries.

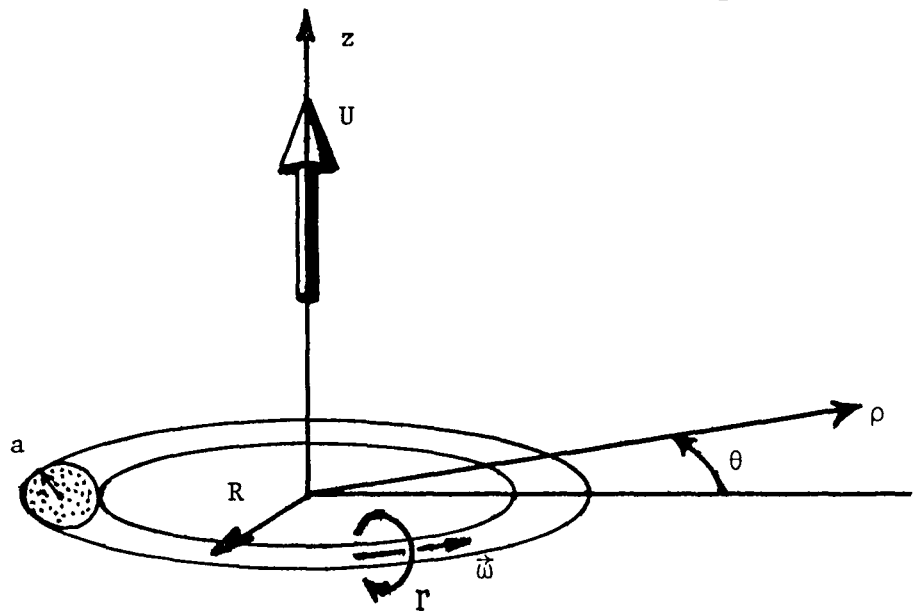


FIGURE 2-3

The cylindrical coordinate system

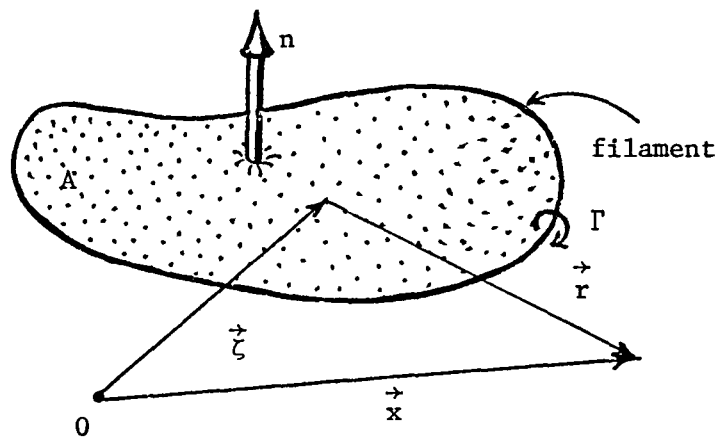


FIGURE 2-4

A vortex filament-loop

filament-loop of strength  $\Gamma$  can be replaced by a uniform distribution of dipoles of strength  $\Gamma$  over the surface bounded by the loop. This result applies to any arbitrarily shaped vortex filament-loop. In particular, a circular vortex filament can be replaced by a disk of dipoles of uniform strength; the potential at any point is just the integral of these dipoles over the disk. This suggests, as we show explicitly in Section 3-1.1, that a vortex ring in the non-steady frame of reference produces an outer flowfield with a basically dipole character. From Eq. (2-7) the fluid impulse for a circular vortex filament of strength  $\Gamma$  and radius  $R$  is found to be

$$P = \pi \rho_m \Gamma R^2 \quad (2-14)$$

where  $\vec{P} = P\hat{z}$ .

VELOCITY. As discussed in the previous section, in an ideal fluid a circular vortex tube will move due to its self-induced velocity field. Kelvin [64] and Lamb [29], using the Biot-Savart law, found the velocity of the classical vortex ring with a constant vorticity distribution in the core (i.e., the core rotates as a solid body) to be:

$$U = \frac{\Gamma}{4\pi R} \left[ \ln \frac{8R}{a} - \frac{1}{2} + O\left(\frac{a}{R}\right) \right] \quad (2-15)$$

This formula has been extended by Saffman [54], Fraenkel [15], and Widnall [74] to an arbitrary distribution of vorticity in the core:

$$U = \frac{\Gamma}{4\pi R} \left[ \ln \frac{8R}{a} - \frac{1}{2} + A \right] + O\left(\frac{\Gamma a}{R^2} \ln \frac{a}{R}\right) \quad (2-16)$$

where  $A$  is a constant which depends on the vorticity distribution. Saffman presents  $A$  in the following form:

$$A = \int_0^a \left( \frac{2\pi}{\Gamma} \int_0^s s' \omega_0(s') ds' \right)^2 \frac{ds}{s}$$

$s$  is a radial coordinate from the core's center and  $\omega_0(s)$  is the first

order vorticity distribution. For a uniform distribution  $A$  is  $1/4$ . For the continuous distribution  $\omega_0(s) = (s^2 - a^2)^2$  which has been used by Widnall in her studies of the stability of vortex rings, and is more realistic with respect to real vortex rings [36],  $A = 5/6$  so that:

$$U = \frac{\Gamma}{4\pi R} \left( \ln \frac{8R}{a} - \frac{1}{3} \right) \quad (2-17)$$

Note the presence of a logarithmic singularity as  $a/R \rightarrow 0$ . A result of locally induced velocities which in the limit of a vortex filament become infinite, a logarithmic singularity in velocity is a general feature of a curved vortex filament.

In an ideal fluid  $\Gamma$  is constant, and since vorticity cannot diffuse from the core,  $a$  cannot change. For an unbounded flow the impulse is invariant as well, so from Eq. (2-14) the radius of the vortex ring must remain constant. Thus, a thin core vortex ring in an unbounded, incompressible, completely frictionless flow would travel to infinity with all properties invariant.

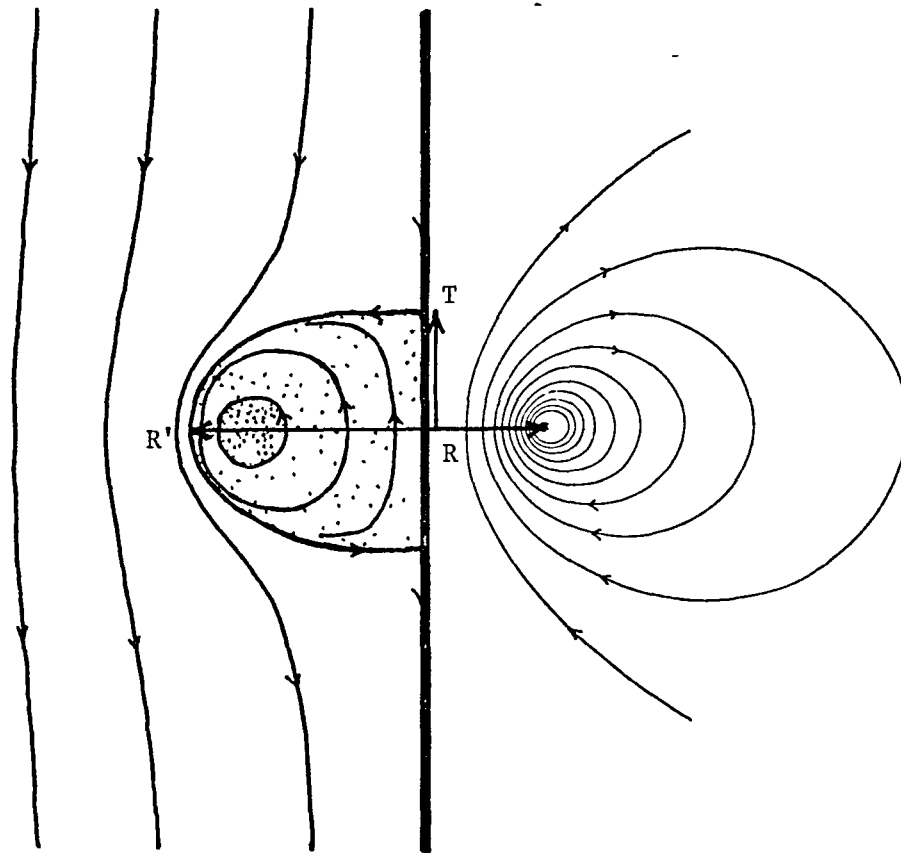
MOVING FRAME OF REFERENCE. In a coordinate system fixed in space, the instantaneous streamline field resembles that of a point dipole. If we allow the coordinate system as defined in Fig. 2-3 to move with the vortex ring,\* however, three regions are defined:

1. The toroidal core region in which the rotational fluid is confined.
2. A spheroidal region surrounding the core defined by an outermost closed streamline with a front and rear stagnation point.
3. The outermost region with streamlines which extend to infinity.

A classical vortex ring in steady and non-steady coordinates is

---

\*Such a frame of reference need not in general be steady (i.e., moving with constant speed), but for a vortex ring in an ideal fluid it is.



moving with the vortex  
ring (steady)

fixed in space  
(non-steady)

FIGURE 2-5

The classical vortex ring in steady and non-steady coordinates.

compared in Fig. 2-5. The fluid within the spheroidal region is confined to this region and is transported along with the core. When using the term, "vortex ring," we refer to the whole spheroidal region of fluid, including the region in which the vorticity is concentrated-- the vortex core.

### 2-3.2 Thick Core Vortex Rings

The classical vortex ring is a torus of vorticity in the limit of vanishing core thickness. We consider now vortex rings with thick cores. For such rings the cross-sectional area of the core is not circular and the distribution of vorticity within the core must be considered.

For an ideal fluid the vorticity equation, Eq. (2-8), can be written for axisymmetric flow without swirl as

$$\frac{D}{Dt} \left( \frac{\omega}{\rho} \right) = 0 \quad (2-18)$$

where  $\vec{\omega} = \omega \hat{\theta}$ . That is, for a flow where viscous diffusion can be neglected,  $\frac{\omega}{\rho}$  must be constant along a fluid streamline. Thus

$$\frac{\omega}{\rho} = f(\Psi) \quad (2-19)$$

where  $\Psi$  is the stream function in cylindrical coordinates:

$$u_{\rho} = \frac{1}{\rho} \frac{\partial \Psi}{\partial z} \quad u_z = -\frac{1}{\rho} \frac{\partial \Psi}{\partial \rho} \quad (2-20)$$

The stream function is defined so as to satisfy continuity; applying the definition for vorticity, then, results in a kinematic equation which can be solved for a given vorticity distribution to find  $\Psi$ . When combined with the dynamical result in (2-19) the stream function for a thick core vortex ring must satisfy:

$$\frac{\partial^2 \Psi}{\partial \rho^2} - \frac{1}{\rho} \frac{\partial \Psi}{\partial \rho} + \frac{\partial^2 \Psi}{\partial z^2} = \begin{cases} \rho^2 f(\Psi) & \text{in the core} \\ 0 & \text{elsewhere} \end{cases} \quad (2-21)$$

Several mathematicians have sought solutions to (2-21) for the case where  $f(\Psi)$  is a constant. At the extreme of thick core vortex rings is the solution found by Hill [24] for a spherical vortex in which vorticity occupies a sphere such that  $f(\Psi) = C$ , or equivalently,  $\omega = C \rho$ . An exact solution to Eq. (2-21) can be found for this case. The stream function and velocity for Hill's spherical vortex are given by:

$$\Psi = \frac{3}{2} \frac{\Gamma}{5\pi R'} \left[ 1 - \left( \frac{x}{R'} \right)^2 \right] \quad (2-22)$$

$$U = 2 \frac{\Gamma}{5\pi R'}, \quad \Gamma = \frac{\pi}{3} R'^3 C$$

where  $R'$  is the sphere radius and  $x^2 = \rho^2 + z^2$ . We note that even in the extreme case of a spherical vortex the same basic relations among the velocity, strength, and radius persist. That is, for both thin and thick core vortex rings the ring speed is directly proportional to the total circulation and inversely proportional to the radius. Norbury [42] has numerically computed solutions to Eq. (2-21) for  $f(\Psi)$  constant, and has shown that the classical vortex ring and Hill's spherical vortex are two extremes of a family of vortex rings based on the single parameter  $\alpha = a_{\text{eff}}/R$  where  $a_{\text{eff}}$  is the radius of the core as if it were circular with the same area.  $\alpha = \sqrt{2}$  represents Hill's spherical vortex and  $\alpha \rightarrow 0$  is the classical vortex ring of Kelvin and Lamb. The computed solutions indicate that for  $\alpha \leq 0.2$  the streamlines within the core and the core cross-section are very nearly circular.

## 2-4 VORTEX RINGS IN A REAL FLUID

### 2-4.1 Vortex Ring Formation

Vortex rings are typically formed by ejecting a fluid through an orifice or from a tube. As the fluid is ejected, a cylindrical sheet

of vorticity emerges, and due to its self-induced velocity field (Section 2-2) begins to spiral, concentrating vorticity in a toroidal region.\* As the rollup of the cylindrical vortex sheet continues, the vorticity in this region increases, until the vortex ring breaks from the orifice and begins moving into the ambient fluid with impulse and strength determined by the magnitude and amount of vorticity entrained.

When the ejected fluid is dyed the process of formation and the extent of the vortex ring can be visualized. A well-formed vortex ring is generally observed to consist of a darkly dyed torus surrounded by a more lightly dyed spheroid of fluid. The more darkly dyed region marks the core of the vortex ring. Measurements by Sullivan et al. [60] and Maxworthy [36] show that even for relatively "thick" vortex rings the vorticity distribution is highly peaked in the core with smaller amounts of vorticity residing in the outer region. In Fig. 2-6 are sketched the velocity and vorticity distributions measured by Sullivan et al. for a "thin" core and "thick" core vortex ring ( $a/R = 0.075$  and  $0.27$  respectively). The core diameter,  $2a$ , is defined as the distance between the maximum and minimum in velocity.

#### 2-4.2 Vortex Ring Evolution

The characteristics of vortex rings as they evolve are dependent to some extent on the initial state of the vortex ring, which depends on the conditions at formation. The ring strength, for example, initially depends on the magnitude and amount of vorticity ejected, which in turn is related to the velocity at ejection and volume of ejected fluid which forms the vortex ring (see Section 5-2.2). The

---

\*For beautiful pictures of vortex ring formation see Batchelor (2, plate 20) and Magarvey, MacLachy (32).

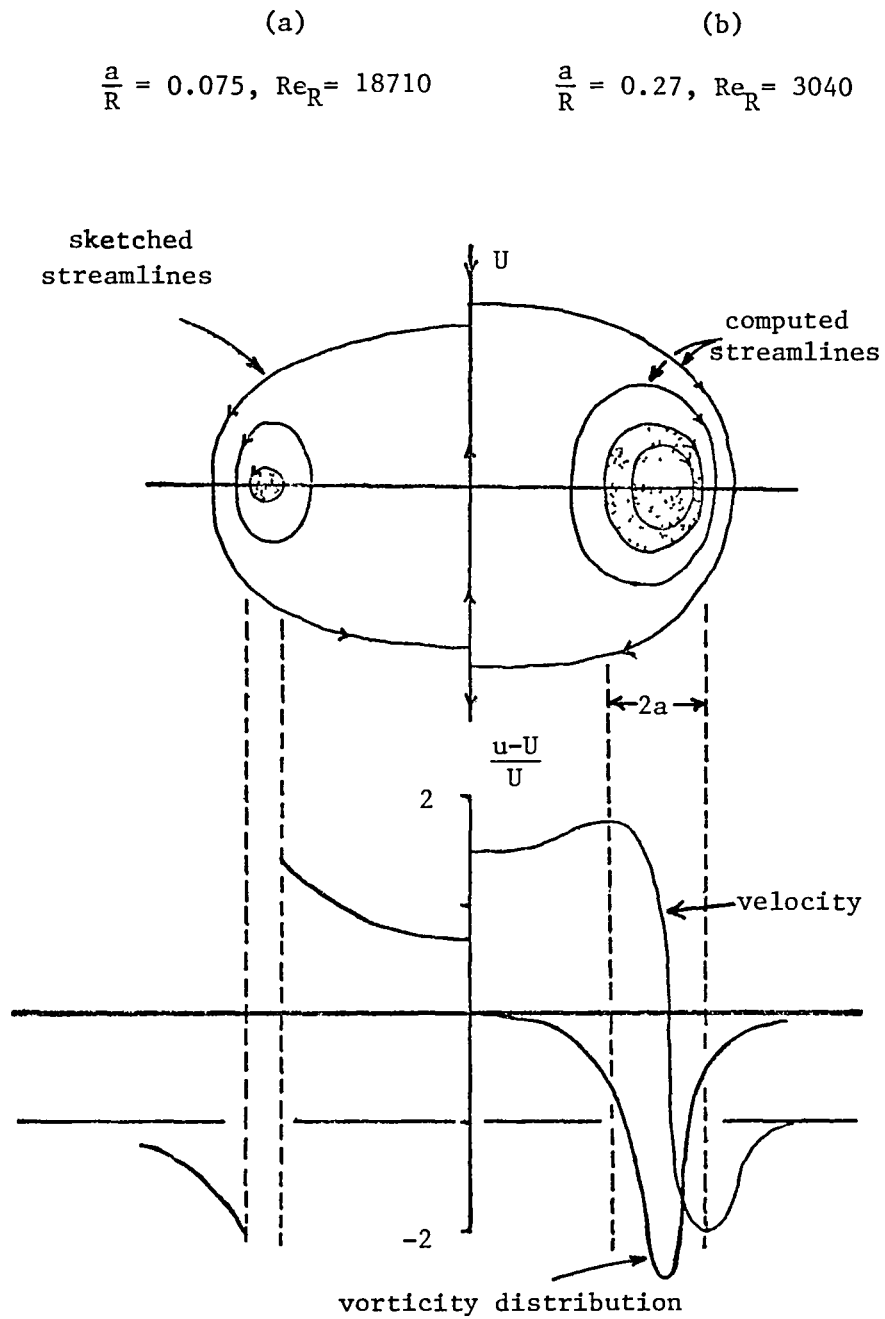


FIGURE 2-6

The velocity and vorticity distributions in a real vortex ring.

From Sullivan, Widnall, and Ezekiel (1973).

size of the vortex ring is expected to be related in some way to the diameter of the orifice through which the fluid is ejected [28], and the development of turbulence to the roughness and irregularities in the orifice geometry.

In general, as the vortex ring propagates through the ambient flowfield, vorticity diffuses from the core region and small amounts of ambient fluid are entrained into the rear of the vortex ring, mixing with the fluid exterior to the core [32]. Vorticity is subsequently convected into a wake region along with some dye, resulting in a more lightly colored outer region in comparison with the core. The loss of vorticity from the vortex ring results in a decrease in ring strength and impulse\* and, since  $U$  and  $\Gamma$  are directly related, a decrease in velocity.

RING REYNOLDS NUMBER. The relative importance of inertial to viscous forces in the evolution of the vortex ring is characterized by the Reynolds number. Two common definitions for the ring Reynolds number are based on the ring radius and velocity ( $Re_R$ ) and on the total circulation ( $Re_\Gamma$ ):

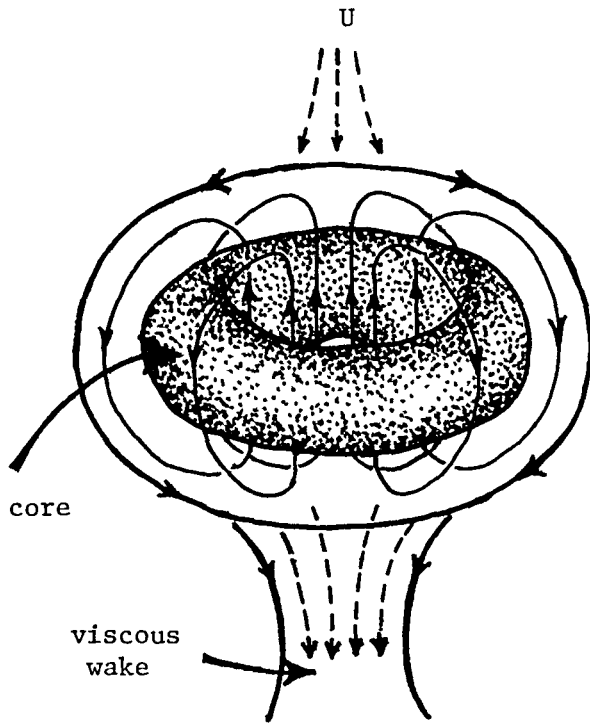
$$Re_R = \frac{2RU}{\nu} \quad Re_\Gamma = \frac{\Gamma}{\nu} \quad (2-23)$$

Since  $\Gamma \sim RU$ ,  $Re_R$  and  $Re_\Gamma$  are expected to be closely related (see Section 5-3).

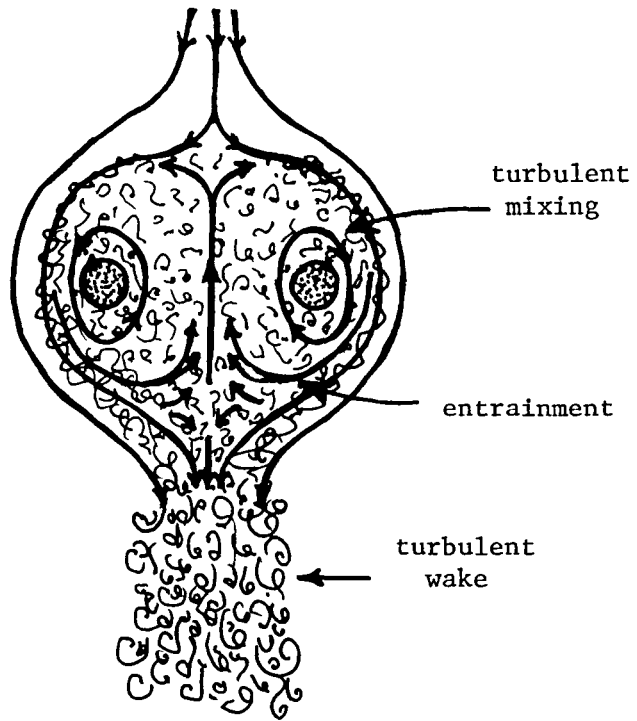
VISCOUS VORTEX RINGS. At low Reynolds numbers ( $Re_R \lesssim 600-1000$ ) vortex ring evolution is governed by viscous diffusion of vorticity from the core and its subsequent convection into a laminar wake. As illustrated in Fig. 2-7a streamline surfaces of viscous rings remain smooth and the core tends to be thick and visually not well defined.

---

\*The impulse of the ring plus wake is conserved by Eq. (2-11b).



(a) Viscous Vortex Ring



(b) Turbulent Vortex Ring

FIGURE 2-7

Laminar and turbulent vortex rings.

Tung and Ting [66] and Saffman [54] have derived an expression for the velocity of a thin core of viscous, rotational fluid embedded in a potential flow:

$$U = \frac{\Gamma}{4\pi R} \left[ \ln \frac{8R}{\sqrt{4\nu t}} - 0.558 + O\left(\frac{\sqrt{\nu t}}{R^2} \ln \frac{\nu t}{R^2}\right) \right] \quad (2-24)$$

Apparently, for thin core rings (i.e., in the limit  $a/R \rightarrow 0$ ) the core radius grows due to viscous diffusion like  $\sqrt{\nu t}$  and the velocity decreases as  $-\ln(\nu t)$ . Accompanying the growth of the core there is an exponentially slow decrease in ring strength [54], and since the impulse must remain constant, from Eq. (2-14) there is a slight increase in  $R$ .

For asymptotically large times, when  $t \sim R$  (i.e.,  $a/R \sim 1$ ), one finds a much more rapid decrease in  $U$  and increase in  $R$  [25, 52]:

$$U \sim (\nu t)^{-3/2} \quad \Gamma \sim (\nu t)^{-1/2} \quad R \sim \sqrt{\nu t} \quad (2-25)$$

Viscous vortex rings in a real fluid generally have thick cores, and measurements show a rate of decrease in velocity and increase in radius somewhere between that predicted by the extreme thin and thick core models just mentioned (see Section 4-4), although measurements made for large times [27] do suggest that the velocity approaches the asymptotic limit given in (2-25).

INSTABILITIES. Many researchers [28, 30, 34, 48, 73] have found that as the Reynolds number increases, although the flow is still laminar, azimuthal waves begin to appear along the core of the vortex ring. Five waves are typically observed to develop at ring Reynolds numbers on the order of 600 to 1000; as the Reynolds number increases the number of waves increases. At the lower Reynolds numbers unstable waves are observed to grow until the vortex ring collapses, but for higher Reynolds numbers the growth of unstable waves leads to a "breaking" process and the emergence of what is generally described as a more stable vortex ring.

The instability of vortex rings has been studied mathematically by Widnall et al. [74-77, 66] and Saffman [56]. Perturbations are found to become unstable when the locally induced rotation of waves around a circular vortex filament is forced to zero by the velocity field induced by the rest of the vortex ring.

TURBULENT VORTEX RINGS. As the Reynolds number increases further, the wave number of the unstable waves increases and small scale turbulence begins to develop. The Reynolds number at which turbulent motions begin to dominate the dynamics depends to a large extent on irregularities and roughness in the orifice geometry, the method of ejection [57], the state of the ambient fluid, etc., but transitional Reynolds numbers on the order of 20000 to 30000 are typical for carefully produced vortex rings. Because of turbulent mixing, the outer region of dyed fluid becomes lighter in color, revealing a fairly well-defined core. The core to ring radius of vortex rings tends to decrease as the Reynolds number increases [60, 57, 36], and the small scale motions in the turbulent core are relatively impervious to the larger scale motions in the outer mixing region [35, 68]. As indicated by Fig. 2-7b, turbulent diffusion and convection of vorticity into a turbulent wake results in a rapid decrease in ring strength and velocity.

## 2-5 PRELIMINARY CONCEPTS BEHIND THE PRESENT STUDY

Fig. 2-8 outlines the range of ring Reynolds numbers which have been covered in experimental studies of vortex rings, including the present study. In general, researchers have concentrated on a limited range of Reynolds numbers. The transition in characteristics from low Reynolds number, viscous vortex rings to high Reynolds number, turbulent vortex rings has not been adequately studied. This is an important aspect of the present work:

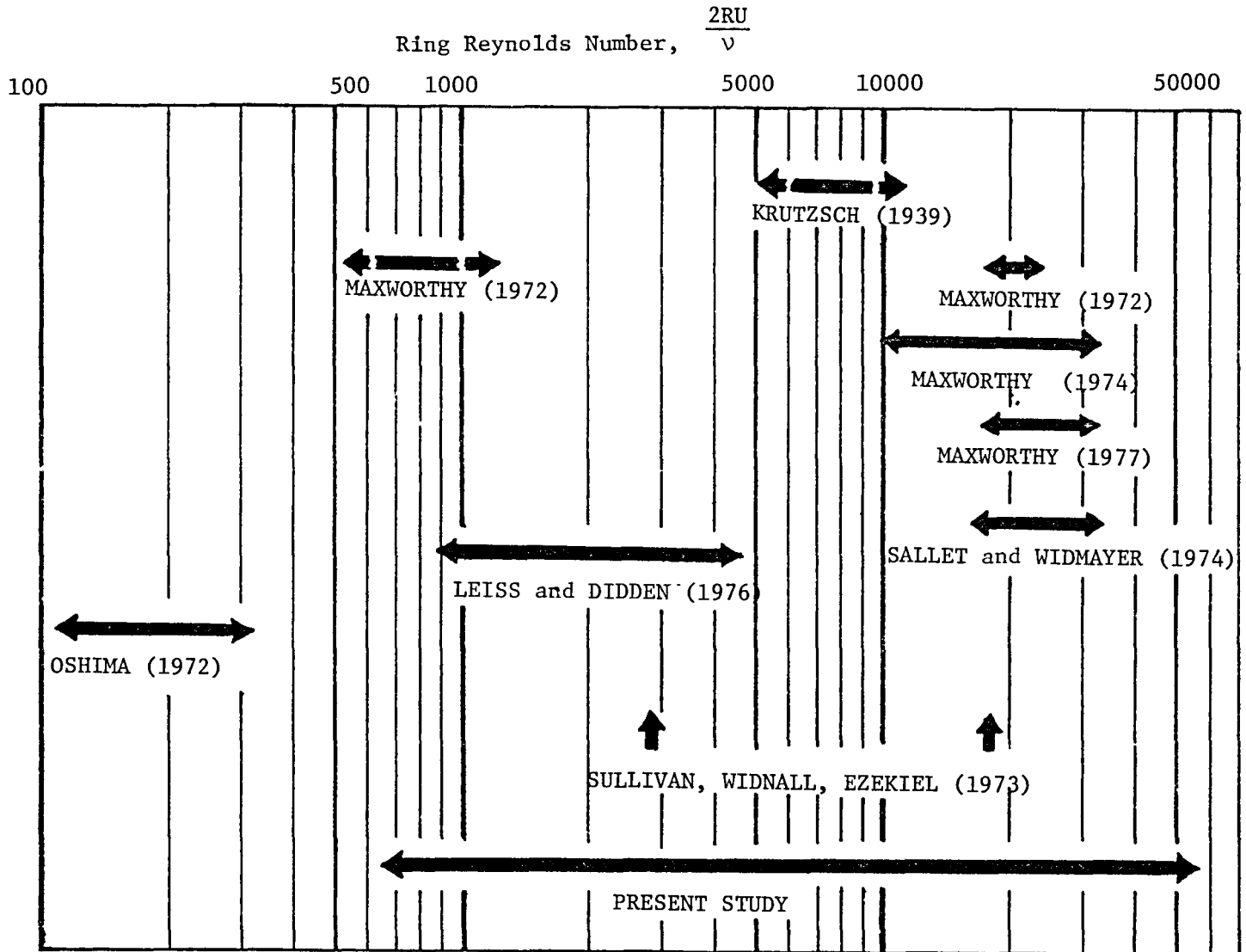


FIGURE 2-8 Comparison of Reynolds number range with previous studies.

To study the changes in the structure of vortex rings and the dynamic processes which control their evolution, from very low Reynolds numbers where viscosity dominates, to very high Reynolds numbers where turbulent diffusion dominates.

The dynamic processes in which we are interested involve the loss of strength and impulse from vortex rings as they evolve, processes which relate to the diffusion and convection of vorticity out of the vortex ring into a wake. A measurement of the strength (or total circulation) of a vortex ring at even one point in space, however, is difficult to obtain. In the past researchers have used laser doppler velocimeters [50, 36] and hot wire anemometers [57] to measure the velocity around the core of a vortex ring in order to compute the total circulation. Such measurements rely on a repeatable production of the vortex rings, and the use of hot wires raises questions as to interference with the inner flowfield. Furthermore, time constraints have allowed only a very limited number of such measurements.

**BASIC APPROACH.** We propose as part of the present study a method for computing the total circulation of a vortex ring from relatively simple flow visualization measurements of the size, shape, and velocity of the vortex ring. The basic idea is as follows:

Using the Biot-Savart law we find the stream function in non-steady coordinates for a vortex ring of strength  $\Gamma$  and radius  $R$  axisymmetrically placed in tube of radius  $\rho_0$  (results for an unbounded ring are obtained in the limit  $R/\rho_0 \rightarrow 0$ ). Transferring to a coordinate system moving with the vortex ring at the speed  $U$ , the outermost closed streamline outlines the volume of the vortex ring. Defining the thickness,  $T$ , and outer radius,  $R'$  of the vortex ring (see Fig. 2-5), we compute the kinematic relationships among the parameters  $R/\rho_0$ ,  $\Gamma$ ,  $U$ , and  $T/R'$ . A measurement of any three of these quantities will therefore yield the fourth. In particular, from

flow visualization measurements of  $R/\rho_0$ ,  $U$ , and  $T/R'$  at the time,  $t$ , we can compute  $\Gamma(t)$ , the total circulation of the vortex ring at that time.

Let us consider this approach in more detail.

**KINEMATICS.** Consider again the kinematic nature of the Biot-Savart law, Eq. (2-4). As discussed in Section 2-1, at any given time, whether the flow is laminar, turbulent, viscous, or inviscid, if we know the vorticity field we can in principle compute the velocity field from Eq. (2-4). In general we do not know the vorticity field exactly, or the integration of Eq. (2-4) is exceedingly difficult. However, in many cases the flowfield can be well approximated and the integration simplified by dividing it into vortex elements and modeling each element as a filament. In this way the simpler integration of Eq. (2-6) can be used. Because the Biot-Savart law is linear in vorticity, the individual flowfields of the vortex elements can then be summed to find the total flowfield. This is the case with vortex rings. We divide the vorticity field into two parts: the vortex ring itself, and the wake.

**APPROXIMATIONS.** Furthermore, we make the following approximations:

1. Since vorticity is highly concentrated in the core (see Fig. 2-6) we anticipate an inner and outer region to the flowfield.\* The inner region (in and "near" the core) will depend on the distribution and extent of vorticity within the core. The flowfield in the outer region ("far" from the core), however, should depend only on the total circulation of the vortex ring,

---

\*Such observations have led to the use of Matched Inner and Outer Expansions by Tung and Ting (67) to study a thin core viscous vortex ring.

and not the details of the distribution of that vorticity. The extent of the inner and outer regions will, of course, depend on the degree to which vorticity is concentrated in the core, however we assume that for typical vortex rings the vorticity is sufficiently concentrated that the shape of the vortex ring can be accurately predicted by concentrating the total circulation of the vortex ring along a circular vortex filament.

2. The amount of circulation lost to the wake is expected to be small in comparison with the total circulation of a vortex ring. We assume, therefore, that the circulation per unit length behind typical vortex rings is such a small fraction of the total circulation within the ring that the vorticity in the wake can be neglected in computations of the shape of the vortex ring.

MODEL. The accuracy of these two approximations will, of course, have to be tested (see Sections 3-3.2 and 5-2.1), but for the purposes of relating the total circulation to the ring size, shape, and velocity, we can now model the vortex ring as a circular vortex filament axisymmetrically placed in an infinitely long tube. Using the known solution for the potential function of a circular vortex filament in an unbounded flow, we derive the induced potential which must be added to Eq. (2-13) to account for the tube walls. From this solution the stream function is deduced and the streamlines in non-steady coordinates calculated. Transferring to a coordinate system moving with the vortex ring, we assess the effect of the tube on the size, shape and velocity of the vortex ring, and compute the relationships among the non-dimensional parameters

$$\frac{T}{R}, \quad \frac{R}{\rho_0}, \quad \text{and} \quad \frac{U}{\Gamma/4\pi R} \quad (2-26a)$$

and among

$$\frac{R'}{R}, \quad \frac{R}{\rho_0}, \quad \text{and} \quad \frac{U}{\Gamma/4\pi R} \quad (2-26b)$$

Because the details of the core are often washed out, flow visualization measurements of  $R'$  are generally more accurate than of  $R$ . By combining the computed relationships among the parameters in (2-26a) and (2-26b) we find that either  $R$  or  $R'$  can be used to compute the ring strength. Thus, from flow visualization measurements of  $R'(t)$ ,  $T(t)$  and  $U(t)$  we can compute both  $\Gamma$  and  $R$  as a function of time.

It should be pointed out that the approximation of concentrating the strength of the vortex ring along a circular vortex filament in order to compute  $T$  and  $R'$  is not the same as that made by Kelvin and Lamb to compute the velocity of a thin core vortex ring, Eqs. (2-15) and (2-16). In calculating the velocity, dynamics enters through the use of the Kelvin/Helmholtz theorem for an inviscid fluid, Eq. (2-10). Under this approximation the vortex core moves with the local fluid velocity, which in the limit  $a/R \rightarrow 0$  becomes infinite. The approximation used in our calculations assumes that the shape of the vortex ring is not much affected by the finite size of the core, so that for such a calculation the strength of the vortex ring can be concentrated along a circle. The calculation is totally kinematic, and singularities do not appear. Furthermore, kinematic relationships are very general in that they apply at any instant in time where the model is sufficiently accurate, and for both laminar and turbulent flows. Of course, dynamics must be included in some way to predict any one of these quantities; however, by combining the kinematic theory with relatively simple experiments, important dynamic information can be deduced.

In the next chapter we develop the theory and calculate the relationships among the parameters in (2-26). From the theory we assess the effect of the tube on the size, shape, and velocity of the vortex ring. In Chapter 4 flow visualization experiments are described, and measurements for vortex rings propagating up a tube are discussed. Finally, in Chapter 5 the flow visualization measurements are combined with theory to compute the total circulation as a

function of time for 17 vortex rings with initial Reynolds numbers ranging from 690 to 50100.

# 3

## Theory

*This primary matter, forced into a certain quantity of motion divinely bestowed, falls into a series of whirlpools or vortices, in which the visible bodies such as planets and terrestrial objects are carried around or impelled toward certain central points by the laws of vortical motion.*

-E.A. Burt on Descartes

### 3-1 INTEGRAL SOLUTION FOR A CIRCULAR VORTEX FILAMENT IN A TUBE

#### 3-1.1 Harmonic Expansion for the Unbounded Ring

Consider the problem illustrated in Fig. 3-1. We seek the solution for a circular vortex filament with strength  $\Gamma$  and radius  $R$  axisymmetrically placed in an infinite, rigid tube of radius  $\rho_0$ . The flow is incompressible, but not necessarily inviscid. Because the flow is axisymmetric (and without swirl), we introduce the cylindrical coordinate system  $(\rho, \theta, z)$  fixed with respect to the tube such that at the time  $t$  the vortex filament is located in the  $z = 0$  plane. The vortex ring is moving in the  $+z$  direction with the speed,  $U$ ; we seek the solution for the flowfield at an instant in time in a non-steady frame of reference.

Outside of the vortex filament the flow is irrotational, so we define the velocity potential:

$$\vec{u}(\vec{x}) = \nabla\Phi(\vec{x}) \quad (3-1)$$

where  $\vec{x}$  is a position vector to the point  $(\rho, z)$ .  $\Phi$  is further divided into two parts:

$$\Phi = \Phi_0 + \Phi_1 \quad (3-2)$$

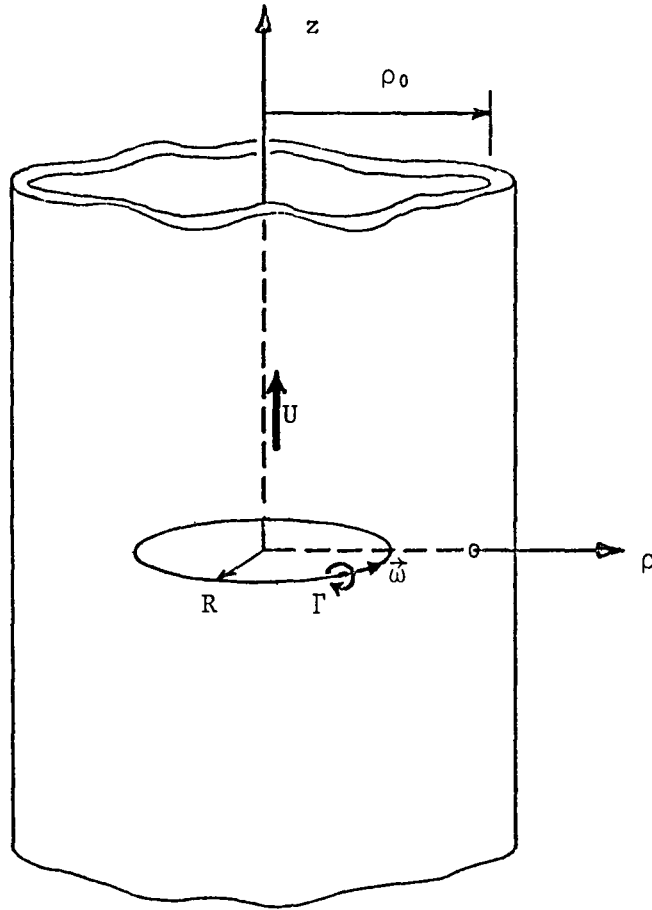


FIGURE 3-1

Definitions for a circular vortex filament axisymmetrically placed in a tube.

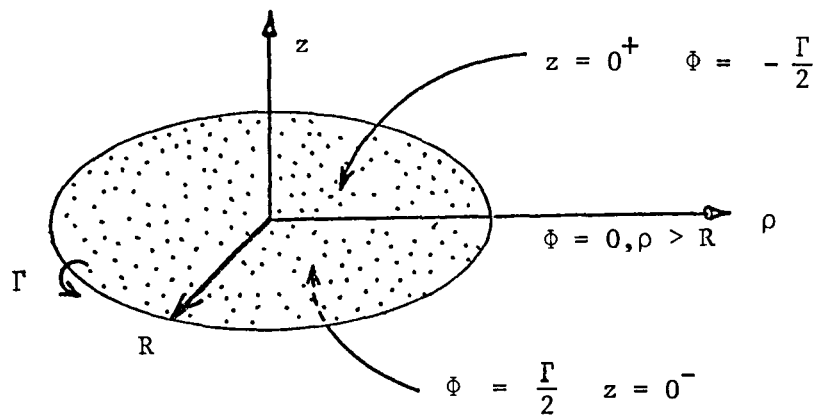


FIGURE 3-2

Representing a circular vortex filament as a disk of dipoles of uniform strength.

$\Phi_0(\vec{x})$  is the potential for a circular vortex filament in an unbounded flow and  $\Phi_1(\vec{x})$  represents the potential field induced by the presence of the tube.  $\Phi_1$  must satisfy Laplace's equation and, together with  $\Phi_0$ , the boundary condition of no flow through the tube wall:

$$\nabla^2 \Phi_1 = 0 \quad (3-3a)$$

$$\frac{\partial}{\partial \rho} (\Phi_0 + \Phi_1) \quad \text{at } \rho = \rho_0 \quad (3-3b)$$

$\Phi_0$  is given by Eq. (2-13) as:

$$\Phi_0(\vec{x}) = \iint_A \frac{\partial}{\partial z} \left( \frac{\Gamma}{4\pi r} \right) dA(\vec{\zeta}) \quad (3-4a)$$

where  $A$  is the area of the disk bounded by the filament,  $\vec{\zeta}$  is a position vector to a point on the disk and  $\vec{r} = \vec{x} - \vec{\zeta}$ . (see Fig. 2-4). This expression shows that the circular vortex filament can be represented mathematically as a disk of dipoles with uniform strength  $\Gamma$ . At the disk surface there is a discontinuity in potential of magnitude  $\Gamma$  as illustrated in Fig. 3-2. Lamb [29, p. 239] presents the potential for such a disk of dipoles in terms of Bessel functions of the first kind:

$$\Phi_0(\rho, z) = -\frac{\Gamma R}{2} \int_0^{\infty} e^{-kz} J_0(k\rho) J_1(kR) dk \quad (3-4b)$$

Eqs. (3-4a) and (3-4b) are equivalent expressions for the non-steady potential field due to a circular vortex filament in an unbounded flow.

In order to obtain the solution of the potential  $\Phi_1$  which must be added to Eq. (3-4) to satisfy the boundary condition at  $\rho_0$ , we expand into an harmonic series valid in the region  $\rho > R$  and find the induced potential for each term separately. Consider the outer

variables defined as

$$\tilde{\rho} = \frac{\rho}{\rho_0} \quad \tilde{z} = \frac{z}{\rho_0} \quad \tilde{x} = \frac{x}{\rho_0} \quad (3-5a)$$

and the inner variables:

$$\bar{\rho} = \frac{\rho}{R} \quad \bar{z} = \frac{z}{R} \quad \bar{x} = \frac{x}{R} \quad (3-5b)$$

where  $x = \sqrt{\rho^2 + z^2}$ . Rewriting (3-4b) in outer variables we obtain

$$\Phi_0(\tilde{\rho}, \tilde{z}) = -\frac{\epsilon \Gamma}{2} \int_0^\infty e^{-k\tilde{z}} J_0(k\tilde{\rho}) J_1(k\epsilon) dk \quad (3-6)$$

where  $\epsilon = R/\rho_0 < 1$ . The inner variable,  $\bar{\rho} = \tilde{\rho}/\epsilon$  indicates that to obtain an expansion valid in the far field we should expand in the limit  $\epsilon \rightarrow 0$ . Therefore we expand  $J_1(k\epsilon)$ :

$$J_1(k\epsilon) = \frac{(k\epsilon)}{2} - \frac{(k\epsilon)^3}{2^2 \cdot 4} + \frac{(k\epsilon)^5}{2^2 \cdot 4^2 \cdot 6} - \dots \quad (3-7)$$

Substituting Eq. (3-7) into (3-6) and noting that

$$\frac{\partial^n}{\partial z^n} e^{-kz} = (-k)^n e^{-kz} \quad (3-8)$$

results in

$$\Phi_0(\tilde{\rho}, \tilde{z}) = \frac{\epsilon \Gamma}{2} \left( \frac{\epsilon}{2} \frac{\partial}{\partial \tilde{z}} - \frac{\epsilon^3}{2^2 \cdot 4} \frac{\partial^3}{\partial \tilde{z}^3} + \frac{\epsilon^5}{2^2 \cdot 4^2 \cdot 6} \frac{\partial^5}{\partial \tilde{z}^5} - \dots \right) \int_0^\infty e^{-k\tilde{z}} J_0(k\tilde{\rho}) dk \quad (3-9)$$

The integral is the Laplace transform of  $J_0$  and has the value  $1/x$ . Thus in the region  $\rho > R$  we have reduced the integral in Eq. (3-6) to a series of harmonic poles at the origin:

$$\Phi_0(\tilde{\rho}, \tilde{z}) = \frac{\epsilon \Gamma}{2} \left( \frac{\epsilon}{2} \frac{\partial}{\partial \tilde{z}} \frac{1}{\tilde{x}} - \frac{\epsilon^3}{2^2 \cdot 4} \frac{\partial^3}{\partial \tilde{z}^3} \frac{1}{\tilde{x}} + \frac{\epsilon^5}{2^2 \cdot 4^2 \cdot 6} \frac{\partial^5}{\partial \tilde{z}^5} \frac{1}{\tilde{x}} - \dots \right) \quad (3-10)$$

The first harmonic, which is dominant in the far field, represents a dipole field, showing that at infinity a vortex ring looks like a point dipole. The higher order poles account for the variation from

that of a purely dipolar field due to the finite size of the vortex ring.

We note that the expansion given in Eq. (3-9) could have been obtained as well from the representation for  $\Phi_0$  given by Eq. (3-4a) by expanding  $1/r$  in a Taylor series about  $1/x$  and carrying out the integrations term by term.

### 3-1.2 Monopole Solution: The Green Function

Consider an expansion in a form similar to Eq. (3-10) for the total potential,  $\Phi = \Phi_0 + \Phi_1$  :

$$\Phi(\tilde{\rho}, \tilde{z}) = \frac{\epsilon\Gamma}{2} \left( \frac{\epsilon}{2} \frac{\partial}{\partial \tilde{z}} \phi_m - \frac{\epsilon^3}{2^2 \cdot 4} \frac{\partial^3}{\partial \tilde{z}^3} \phi_m + \frac{\epsilon^5}{2^2 \cdot 4^2 \cdot 6} \frac{\partial^5}{\partial \tilde{z}^5} \phi_m - \dots \right) \quad (3-11)$$

Examination of Eqs. (3-3) and (3-10) shows that  $\phi_m$  is the potential function for a monopole at the origin in a tube. That is,  $\phi_m$  is the Green function to Laplace's equation with the Neumann boundary condition and must satisfy:

$$\nabla^2 \phi_m = -4\pi \delta(\vec{x}) \quad (3-12a)$$

$$\frac{\partial \phi_m}{\partial \rho} = 0 \quad \text{at } \rho = 1 \quad (3-12b)$$

In a form which satisfies Eq. (3-12a) we write  $\phi_m$  as:

$$\phi_m(\rho, z) = \frac{1}{x} + \int_0^{\infty} f(k) I_0(k\rho) \cos(kz) dk \quad (3-13)$$

where  $f(k)$  is chosen to satisfy (3-12b).  $1/x$  has the integral representation [6]:

$$\frac{1}{x} = \frac{2}{\pi} \int_0^{\infty} K_0(k\rho) \cos(kz) dk$$

I and K are modified Bessel functions of the first and second kind

respectively. So Eq. (3-13) can be written:

$$\phi_m = \int_0^{\infty} \left[ \frac{2}{\pi} K_0(k\rho) + f(k) I_0(k\rho) \right] \cos(kz) dk$$

Applying the boundary condition, (3-12b) requires that

$$f(k) = \frac{2 K_1(k)}{\pi I_1(k)}$$

Inserting this expression into (3-13), the Green function becomes:

$$\phi_m(\rho, z) = \frac{1}{x} + \frac{2}{\pi} \int_0^{\infty} \frac{K_1(k)}{I_1(k)} I_0(k\rho) \cos(kz) dk \quad (3-14)$$

### 3-1.3 The Potential and Stream Functions in Non-Steady Coordinates

Substituting Eq. (3-14) into (3-11) for  $\phi_m(\tilde{\rho}, \tilde{z})$ , and subtracting  $\tilde{\phi}_0$  as given by Eq. (3-10) results in the following representation for the induced potential:

$$\phi_i(\tilde{\rho}, \tilde{z}) = \frac{\Gamma\varepsilon}{\pi} \left( \frac{\varepsilon}{2} \frac{\partial}{\partial \tilde{z}} - \frac{\varepsilon^3}{2^2 \cdot 4} \frac{\partial^3}{\partial \tilde{z}^3} + \frac{\varepsilon^5}{2^2 \cdot 4^2 \cdot 6} \frac{\partial^5}{\partial \tilde{z}^5} - \dots \right) \int_0^{\infty} \frac{K_1(k)}{I_1(k)} I_0(k\rho) \cos(k\tilde{z}) dk$$

Performing the differentiations results in

$$\phi_i(\tilde{\rho}, \tilde{z}) = - \frac{\Gamma\varepsilon}{\pi} \int_0^{\infty} \left[ \frac{\varepsilon k}{2} + \frac{(\varepsilon k)^3}{2^2 \cdot 4} + \frac{(\varepsilon k)^5}{2^2 \cdot 4^2 \cdot 6} + \dots \right] \frac{K_1(k)}{I_1(k)} I_0(k\tilde{\rho}) \sin(k\tilde{z}) dk$$

The series in the brackets is recognized as that for  $I_1(\varepsilon k)$ . Thus the potential field induced by the presence of the tube on a vortex ring is given in outer variables by

$$\boxed{\phi_i(\tilde{\rho}, \tilde{z}) = - \frac{\Gamma\varepsilon}{\pi} \int_0^{\infty} \frac{K_1(k)}{I_1(k)} I_1(\varepsilon k) I_0(k\tilde{\rho}) \sin(k\tilde{z}) dk} \quad (3-15a)$$

and in regular variables by

$$\Phi_i(\rho, z) = -\frac{\Gamma R}{\pi} \int_0^{\infty} \frac{K_1(\rho_0 k)}{I_1(\rho_0 k)} I_1(kR) I_0(k\rho) \sin(kz) dk \quad (3-15b)$$

The total potential for a circular vortex filament in a tube is, of course, given by  $\Phi = \Phi_0 + \Phi_1$  where  $\Phi_0$  is given by Eqs. (3-4b) and (3-6). The solution is valid at an instant in time in a frame fixed with respect to the tube.

**STREAM FUNCTION.** We define a stream function  $\Psi$  as in Eq. (2-20). Again we write the stream function as the sum of that for a circular vortex filament in an unbounded flow, plus the stream function induced by the presence of the tube:

$$\Psi = \Psi_0 + \Psi_1 \quad (3-16)$$

from the relations

$$\frac{1}{\rho} \frac{\partial \Psi_i}{\partial z} = \frac{\partial \Phi_i}{\partial \rho} \quad \text{and} \quad -\frac{1}{\rho} \frac{\partial \Psi_i}{\partial \rho} = \frac{\partial \Phi_i}{\partial z}$$

and Eq. (3-15b) one can deduce the induced stream function:

$$\Psi_1(\rho, z) = \frac{\Gamma R}{\pi} \rho \int_0^{\infty} \frac{K_1(k\rho_0)}{I_1(k\rho_0)} I_1(kR) I_1(k\rho) \cos(kz) dk \quad (3-17)$$

In a similar manner the stream function for an unbounded vortex ring can be deduced from Eq. (3-4b):

$$\Psi_0(\rho, z) = -\frac{\Gamma R}{2} \rho \int_0^{\infty} e^{-kz} J_1(k\rho) J_1(kR) dk \quad (3-18)$$

## 3-2 THE POTENTIAL AND STREAMLINE FIELDS IN THE FIXED FRAME

## 3-2.1 Inner and Outer Expansions for the Unbounded Ring

In order to compute the constant potential lines and streamlines for the bounded vortex ring we expand  $\Phi_0(\rho, z)$  and  $\Psi_0(\rho, z)$  into two series, one valid in the inner region  $\rho < R$ , and one in the outer region  $\rho > R$ . We will likewise expand the integral representations for and  $\Phi_1(\rho, z)$  into series, however only one series is required since there are no discontinuities in  $\Phi_1$  in the region  $\rho < \rho_0$ .

NON-DIMENSIONALIZATION. Computations are carried out in outer variables for the region  $\tilde{\rho} < 1$  and  $\tilde{z} < 1$ . Consider the following non-dimensional forms for the potential and stream function, designated with a hat:

$$\Phi(\tilde{\rho}, \tilde{z}) = \frac{\Gamma}{4\pi} \hat{\Phi}(\tilde{\rho}, \tilde{z}) = \frac{\Gamma}{4\pi} \left[ \hat{\Phi}_0(\tilde{\rho}, \tilde{z}) + \hat{\Phi}_1(\tilde{\rho}, \tilde{z}) \right] \quad (3-19a)$$

$$\Psi(\tilde{\rho}, \tilde{z}) = \frac{\Gamma R}{4\pi} \hat{\Psi}(\tilde{\rho}, \tilde{z}) = \frac{\Gamma R}{4\pi} \left[ \hat{\Psi}_0(\tilde{\rho}, \tilde{z}) + \hat{\Psi}_1(\tilde{\rho}, \tilde{z}) \right] \quad (3-19b)$$

OUTER EXPANSIONS. We are interested in expansions with which to compute  $\hat{\Phi}_0$  and  $\hat{\Psi}_0$  in the region  $\tilde{\rho} > \epsilon$ . Such an expansion is given for  $\hat{\Phi}_0$  by Eq. (3-10), resulting in the following expression for  $\hat{\Phi}_0$ :

Outer ( $\tilde{\rho} > \epsilon$ ):

$$\hat{\Phi}_0(\tilde{\rho}, \tilde{z}) = 2\pi \left( \epsilon^2 \frac{1}{2} \frac{\partial}{\partial \tilde{z}} - \epsilon^4 \frac{1}{2^2 \cdot 4} \frac{\partial^3}{\partial \tilde{z}^3} + \epsilon^6 \frac{1}{2^2 \cdot 4^2 \cdot 6} \frac{\partial^5}{\partial \tilde{z}^5} - \dots \right) \frac{1}{\tilde{x}} \quad (3-20)$$

where  $\tilde{x}^2 = \tilde{\rho}^2 + \tilde{z}^2$ . Note that as  $\tilde{z} \rightarrow 0$ ,  $\hat{\Phi}_0 \rightarrow 0$ . To derive the outer expansion for  $\hat{\Psi}_0(\tilde{\rho}, \tilde{z})$  we write Eq. (3-17) in outer variables and expand  $J_1(k\epsilon)$  for small  $\epsilon$ . Again using the relation given by Eq. (3-8) we end up with an expression similar to (3-9), except that the Laplace transform is of  $J_1(k\tilde{\rho})$  rather than  $J_0(k\tilde{\rho})$ . The resulting outer

expansion for  $\hat{\Psi}_0$  is:

Outer ( $\tilde{\rho} > \epsilon$ ):

$$\hat{\Psi}_0(\tilde{\rho}, \tilde{z}) = -2\pi \left( \epsilon \frac{1}{2} \frac{\partial}{\partial \tilde{z}} - \epsilon^3 \frac{1}{2^2 \cdot 4} \frac{\partial^3}{\partial \tilde{z}^3} + \epsilon^5 \frac{1}{2^2 \cdot 4^2 \cdot 6} \frac{\partial^5}{\partial \tilde{z}^5} - \dots \right) \frac{\tilde{z}}{x} \quad (3-21)$$

INNER EXPANSIONS. To derive an expansion for  $\hat{\Phi}_0$  valid in the region  $\tilde{\rho} < \epsilon$  we expand  $J_0(k\tilde{\rho})$  in Eq. (3-6) in the limit  $\tilde{\rho} \rightarrow 0$ . Again making use of Eq. (3-8) results in:

$$\hat{\Phi}_0(\tilde{\rho}, \tilde{z}) = -\frac{\Gamma}{2} \epsilon (1 - \tilde{\rho}^2) \frac{1}{2^2} \frac{\partial^2}{\partial \tilde{z}^2} + \tilde{\rho}^4 \frac{1}{2^2 \cdot 4^2} \frac{\partial^4}{\partial \tilde{z}^4} - \dots \int_0^\infty e^{-k\tilde{z}} J_1(k\epsilon) dk \quad (3-22)$$

The integral can be found in tables for Laplace transforms resulting in the inner expansion

Inner ( $\tilde{\rho} < \epsilon$ ):

$$\hat{\Phi}_0(\tilde{\rho}, \tilde{z}) = -2\pi + 2\pi (1 - \tilde{\rho}^2) \frac{1}{2^2} \frac{\partial^2}{\partial \tilde{z}^2} + \tilde{\rho}^4 \frac{1}{2^2 \cdot 4^2} \frac{\partial^4}{\partial \tilde{z}^4} - \dots \frac{\tilde{z}}{\sqrt{\tilde{z}^2 + \epsilon^2}} \quad (3-23)$$

Note that in the inner region as  $\tilde{z} \rightarrow 0^+$ ,  $\hat{\Phi}_0 \rightarrow -2\pi$  and  $\hat{\Psi}_0 \rightarrow -\frac{\Gamma}{2}$  as illustrated in Fig. 3-2. The inner expansion for  $\hat{\Psi}_0$  is derived from Eq. (3-18) in a similar manner, first converting to outer variables, then expanding  $J_1(k\tilde{\rho})$  for small  $\tilde{\rho}$ . The resulting series is:

Inner ( $\tilde{\rho} < \epsilon$ ):

$$\hat{\Psi}_0(\tilde{\rho}, \tilde{z}) = \frac{2\pi}{\epsilon} \left( -\tilde{\rho}^2 \frac{1}{2} \frac{\partial}{\partial \tilde{z}} + \tilde{\rho}^4 \frac{1}{2^2 \cdot 4} \frac{\partial^3}{\partial \tilde{z}^3} - \tilde{\rho}^6 \frac{1}{2^2 \cdot 4^2 \cdot 6} \frac{\partial^5}{\partial \tilde{z}^5} + \dots \right) \frac{\tilde{z}}{\sqrt{\tilde{z}^2 + \epsilon^2}} \quad (3-24)$$

### 3-2.2 Expansions for the Induced Field

The wall-induced fields can be thought of as resulting from an "image" vorticity distribution outside the tube. The flow within the tube is therefore potential and expansions of  $\Psi_1$  and  $\Phi_1$  are uniformly valid throughout.

Consider the integral solution for  $\hat{\Psi}_1$  written in inner variables. From Eq. (3-17):

$$\hat{\Psi}_1(\bar{\rho}, \bar{z}) = 2\bar{\rho}\epsilon \int_0^{\infty} \frac{K_1(k)}{I_1(k)} I_1(k\epsilon) I_1(k\epsilon\bar{\rho}) \cos(k\epsilon\bar{z}) dk \quad (3-25)$$

We expand  $I_1(k\epsilon)$ ,  $I_1(k\epsilon\bar{\rho})$  and  $\cos k\epsilon\bar{z}$  in the limit of small  $\epsilon$ . The result is a series in  $\epsilon$  which we write in the form:

$$\hat{\Psi}_1(\bar{\rho}, \bar{z}) = \hat{\Psi}_3(\bar{\rho}, \bar{z}) \epsilon^3 + \hat{\Psi}_5(\bar{\rho}, \bar{z}) \epsilon^5 + \dots \quad (3-26a)$$

where

$$\begin{aligned} \hat{\Psi}_3(\bar{\rho}, \bar{z}) &= b_2 \gamma_2 \\ \hat{\Psi}_5(\bar{\rho}, \bar{z}) &= (b_4 + \frac{1}{2 \cdot 4} b_2) \gamma_4 \\ \hat{\Psi}_7(\bar{\rho}, \bar{z}) &= (b_6 + \frac{1}{2 \cdot 4} b_4 + \frac{1}{2 \cdot 4^2 \cdot 6} b_2) \gamma_6 \\ &\text{etc.} \end{aligned} \quad (3-26b)$$

The coefficients,  $b_n$  and  $\gamma_n$  are given by:

$$b_2 = \left(\frac{\bar{\rho}^2}{z}\right), \quad b_4 = \left(\frac{\bar{\rho}^4}{2^2 \cdot 4} - \frac{\bar{\rho}\bar{z}^2}{2 \cdot 2!}\right), \quad b_6 = \left(\frac{\bar{\rho}^6}{2^2 \cdot 4^2 \cdot 6} - \frac{\bar{\rho}^4}{2^2 \cdot 4^2 \cdot 2!} + \frac{\bar{\rho}^2 \bar{z}^4}{2 \cdot 4!}\right), \dots \quad (3-26c)$$

$$\gamma_n = 2 \int_0^{\infty} \frac{K_1(k)}{I_1(k)} k^n dk \quad (3-26d)$$

The same procedure is following in expanding  $\hat{\Phi}_1(\bar{\rho}, \bar{z})$ . We write Eq. (3-15) in inner variables and expand the integrand for small  $\epsilon$ , resulting in the following series:

$$\hat{\Phi}_1(\bar{\rho}, \bar{z}) = \hat{\Phi}_3(\bar{\rho}, \bar{z}) \epsilon^3 + \hat{\Phi}_5(\bar{\rho}, \bar{z}) \epsilon^5 + \hat{\Phi}_7(\bar{\rho}, \bar{z}) \epsilon^7 + \dots \quad (3-27a)$$

where

$$\begin{aligned} \hat{\Phi}_3 &= C_2 \gamma_2 \\ \hat{\Phi}_5 &= (C_4 + \frac{1}{2 \cdot 4} C_2) \gamma_4 \\ \hat{\Phi}_7 &= (C_6 + \frac{1}{2 \cdot 4} C_4 + \frac{1}{2 \cdot 4^2 \cdot 6} C_2) \gamma_6 \\ &\text{etc.} \end{aligned} \quad (3-27b)$$

and

$$C_2 = -\bar{z}, \quad C_4 = -\frac{\bar{\rho}^2 \bar{z}}{2^2} + \frac{\bar{z}^3}{3!}, \quad C_6 = -\frac{\bar{\rho}^4 \bar{z}}{2^2 \cdot 4^2} + \frac{\bar{\rho}^2 \bar{z}^3}{2^2 \cdot 3!} - \frac{\bar{z}^5}{5!}, \dots \quad (3-27c)$$

The integrals  $\gamma_n$  defined in (3-26d) must be evaluated numerically. Because  $\gamma_n$  gets large as  $n$  increases we compute instead

$$M_n = \frac{2^n}{n!} \int_0^\infty \frac{K_1(k)}{I_1(k)} k^n dk = \frac{2^{n-1}}{n!} \gamma_n \quad (3-28)$$

$M_n$  remains bounded, and has the following asymptotic form for large  $n$  [18]:

$$M_n = \pi \left( \frac{1}{2} + \frac{3}{4} \frac{1}{n} + \frac{9}{16} \frac{1}{n(n-1)} + \dots \right)$$

Values of  $M_n$  for  $n = 2, 4, 6, \dots, 100$  were numerically evaluated at the National Center for Atmospheric Research on their CDC-7600 computer and are given in Table 3-1.

We might note at this point that before the closed form solution for the potential function was found, we derived its expansion using the method of matched asymptotic expansions with  $\epsilon$  as the small parameter. The inner expansion is that for the unbounded vortex ring. The boundary condition is satisfied in the outer expansion which in the limit  $\epsilon \rightarrow 0$  represents a point dipole at the origin. Matching the two expansions at their appropriate limits produces the series given by Eq. (3-27).

### 3-2.3 The Potential and Streamline Fields

The streamline and potential fields were computed and plotted in the fixed frame. All computations were done using a PDP-11/45\*

---

\*The PDP-11/45 was actually emulating a Danish computer called the RC-4000. I was very kindly given free use of the computer by Dr. John Wilcox and his Solar Physics group in the Institute for Plasma Research, here at Stanford University.

$n$	$M_n$	$n$	$M_n$
2	5.0065950	52	1.6168130
4	2.5142592	54	1.6150816
6	2.0827486	56	1.6134759
8	1.9192741	58	1.6119827
10	1.8358962	60	1.6105904
12	1.7855132	62	1.6092893
14	1.7516317	64	1.6080706
16	1.7271765	66	1.6069268
18	1.7086378	68	1.6058511
20	1.6940734	70	1.6048377
22	1.6823163	72	1.6038812
24	1.6726200	74	1.6029771
26	1.6644831	76	1.6021210
28	1.6575556	78	1.6013094
30	1.6515855	80	1.6005387
32	1.6463865	82	1.5998061
34	1.6418178	84	1.5991086
36	1.6377712	86	1.5984440
38	1.6341616	88	1.5978098
40	1.6309220	90	1.5972041
42	1.6279980	92	1.5966250
44	1.6253456	94	1.5960707
46	1.6229285	96	1.5955397
48	1.6207169	98	1.5950306
50	1.6186854	100	1.5945420

TABLE 3-1

Numerically computed values for  $M_n$ .

computer and an HP-7221A plotter. Developing algol procedures to calculate the cylindrical harmonics, Eqs. (3-20) and (3-21) were used to compute the potential and streamlines in the outer region ( $\tilde{\rho} > \epsilon$ ), and Eqs. (3-23) and (3-24) in the inner region ( $\tilde{\rho} < \epsilon$ ) of the unbounded circular vortex filament.

To compute the induced field, the expanded forms of  $\hat{\Psi}_1$  and  $\hat{\Phi}_1$  as given by Eqs. (3-26) and (3-27) were used along with the numerically calculated values for  $M_n$  given in Table 3-1. The total potential and streamline fields are the sums of the unbounded and induced fields which were calculated separately. All computations were performed in outer variables over a 51x51 point grid in the region  $0 \leq (\tilde{\rho}, \tilde{z}) \leq 1$ , and extended to the region  $-1 \leq \tilde{z} \leq 0$  by symmetry. Plots were made in the region  $0 \leq \tilde{\rho} \leq 1$ ,  $-1 \leq \tilde{z} \leq 1$ ; half of the tube is shown in the figures.

The streamlines for an unbounded vortex ring in non-steady coordinates were previously sketched in Fig. 2-5. For comparison with figures to follow we show in Fig. 3-3 the streamlines (solid lines) and constant potential lines (dashed) for an unbounded vortex ring of size  $\epsilon = R/\rho_0 = 0.4$ . As demonstrated by Eq. (3-10), in a fixed frame of reference the non-steady outer field is dipolar in character with higher order harmonics becoming less and less important as  $\tilde{\rho} \rightarrow \infty$  (i.e., as  $\epsilon \rightarrow 0$ ).

Compare this with the potential and streamline fields for the same size vortex ring, but now bounded by the tube walls as shown in Fig. 3-4. Although the flowfield still has a dipole character, the flow is forced to turn parallel to the tube wall. The effect is a generally more axial flow. As the core is approached the streamlines approach those of the unbounded ring shown in Fig. 3-3. The constant potential lines must be perpendicular to both the boundary and the z axis for a bounded ring, resulting in two streamlines which extend to infinity in opposite directions.

The induced fields, the solid lines representing constant  $\hat{\Psi}_1$  and the dashed lines constant  $\hat{\Phi}_1$ , are shown in Fig. 3-5, again for

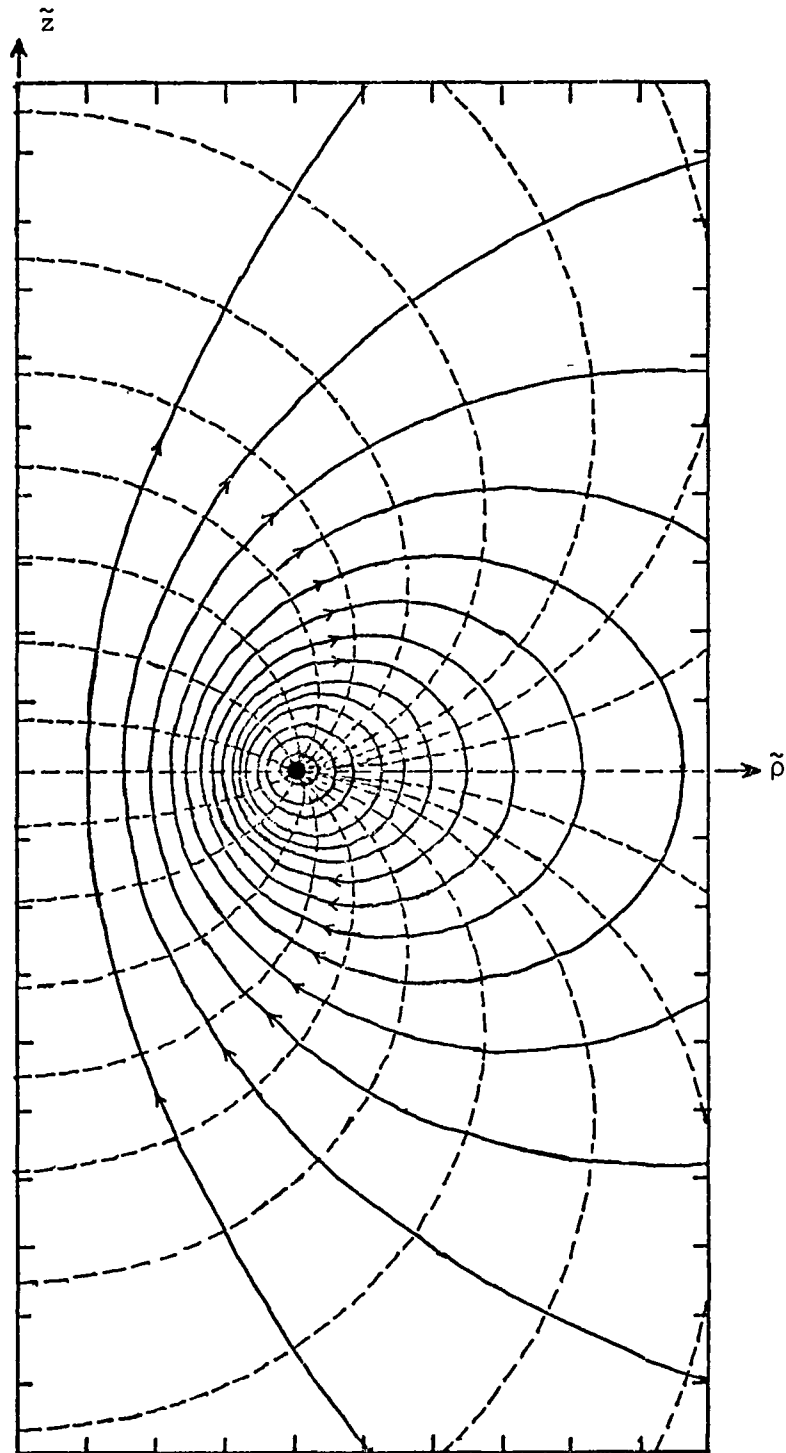


FIGURE 3-3

The streamlines and constant potential lines in the fixed frame for an unbounded vortex ring with  $\varepsilon = 0.40$ .

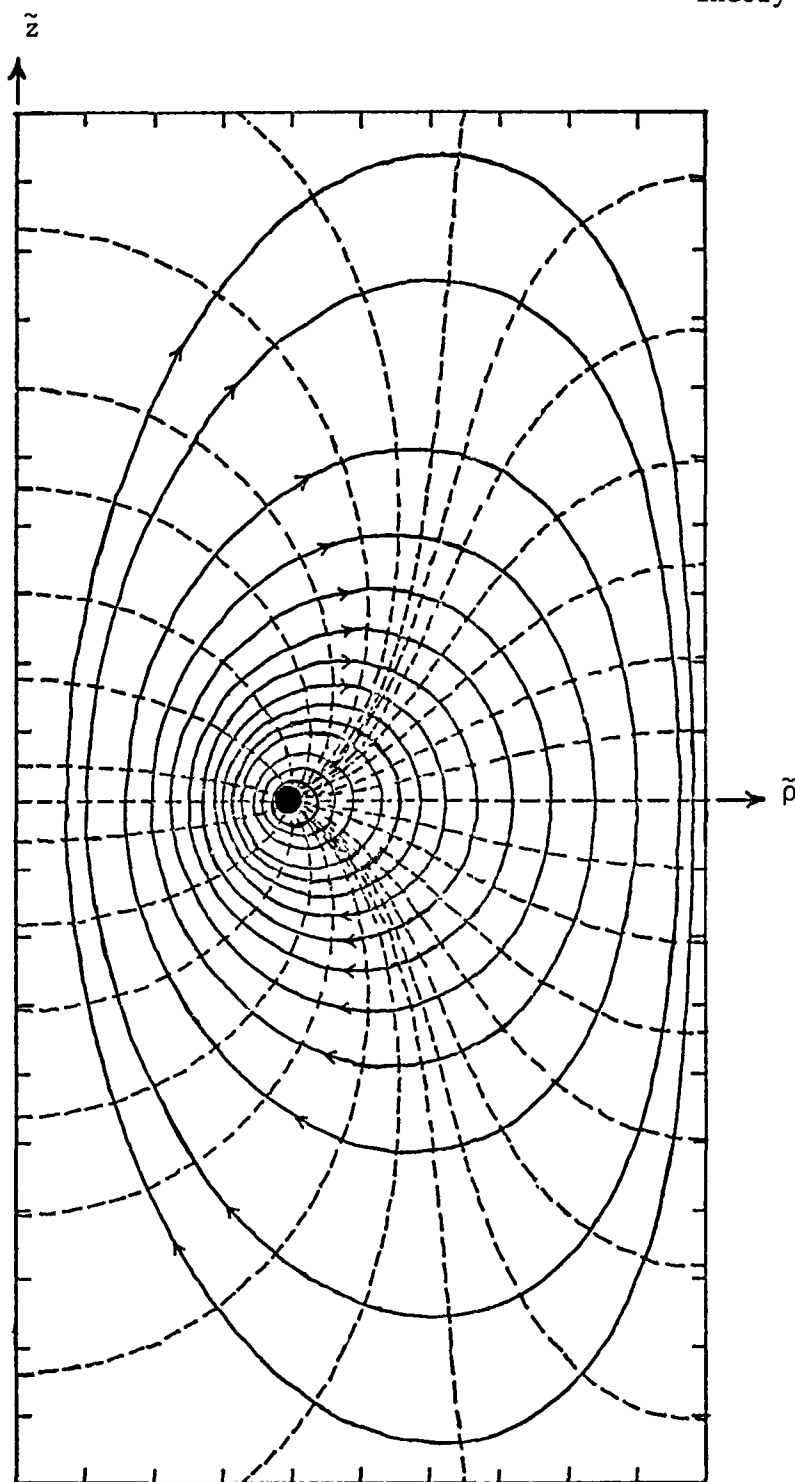


FIGURE 3-4

The streamlines and constant potential lines in the fixed frame for a bounded vortex ring with  $\varepsilon = 0.40$ .

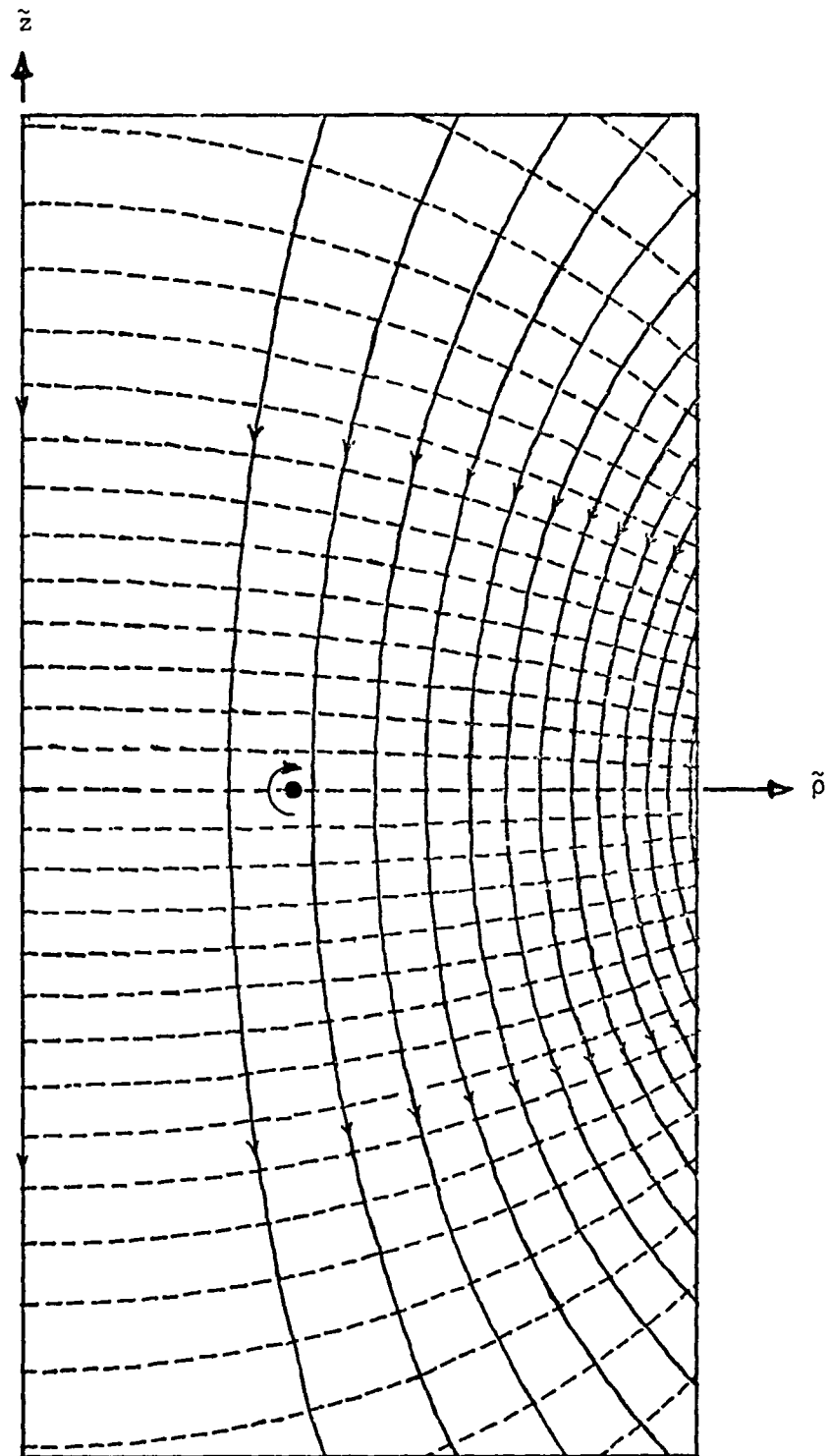


FIGURE 3-5

The wall-induced streamline and constant potential lines in the fixed frame for a bounded vortex ring with  $\varepsilon = 0.40$ .

$\epsilon=0.40$ . This field added to the unbounded field of Fig. 3-3 produces the pattern which was given in Fig. 3-4. Note that the induced velocity field acts in the opposite direction to the direction in which the vortex ring moves. Thus the tube acts to slow the vortex ring as compared with the same ring in an unbounded flow.

### 3-3 THE VELOCITY OF THE VORTEX RING IN A TUBE

As shown by the induced streamlines in Fig. 3-5 the velocity of a vortex ring in a tube is that which it would have were it in an unbounded flow, less the velocity induced by the presence of the tube:

$$U = U_0 - U_1 \quad (3-29)$$

where  $U_0$  is the velocity of the unbounded vortex ring and  $U_1$  the wall-induced velocity given by:

$$U_1 = \left[ -\frac{1}{R} \frac{\partial \Phi_1}{\partial \bar{z}}(\bar{\rho}, \bar{z}) \right]_{\bar{z} = 0, \bar{\rho} = 1}$$

Applying the derivative to Eq. (3-27) and using the numerically calculated values for  $M_n$  results in the following power series in  $\epsilon^2$ :

$$U_1 = \frac{\Gamma}{4\pi R} (5.006595 \epsilon^3 + 2.828542 \epsilon^5 + 2.440721 \epsilon^7 + \dots) \quad (3-30)$$

Note that  $U_1$  depends only on  $\Gamma$  and not on the details of the vorticity distribution in the core. This is because the induced velocity is in the far field of the image vortex system residing outside of the tube. We non-dimensionalize the velocity as follows:

$$U = \frac{\Gamma}{4\pi R} \hat{U} = \frac{\Gamma}{4\pi R} (\hat{U}_0 - \hat{U}_1) \quad (3-31)$$

and write  $\hat{U}_1$  in the form:

$$\hat{U}_1 = \hat{U}_3 \varepsilon^3 + \hat{U}_5 \varepsilon^5 + \hat{U}_7 \varepsilon^7 + \hat{U}_9 \varepsilon^9 \dots \quad (3-32)$$

The calculated values for the coefficients up to  $O(\varepsilon^{10})$  are given in Table 3-2.

**RADIUS OF CONVERGENCE.** Consider the power series  $P = \sum a_n \varepsilon^n$ . By the d'Alembert ratio test the radius of convergence  $\varepsilon_0$  is given by

$$\varepsilon_0 = \lim_{n \rightarrow \infty} \left| \frac{a_{n-1}}{a_n} \right| \quad (3-33)$$

Examining the coefficients in Table 3-2 for large  $n$  suggests a radius of convergence of 1. We show this graphically with a Domb-Sykes plot [71]. Assuming that near a singularity the power series can be represented as

$$P = \sum a_n \varepsilon^n \sim (\varepsilon_0 - \varepsilon)^\alpha \quad (3-34)$$

we expand using the binomial theorem in powers of  $1/n$  to produce:

$$\left| \frac{a_{n+1}}{a_n} \right| = \frac{1}{\varepsilon_0} \left[ 1 - \frac{\alpha+1}{n} + O\left(\frac{1}{n^2}\right) \right] \quad (3-35)$$

As  $n$  gets large this ratio approaches  $1/\varepsilon_0$  linearly with  $1/n$ . At  $1/n$  approaching zero, therefore, the intercept yields the radius of convergence, while the slope indicates the type of singularity.

The Domb-Sykes plot for  $U_1$  is given in Fig. 3-6. There is little doubt that the resulting curve approaches the ordinate at  $a_{n+1}/a_n = 1$  with a slope of 1. We conclude, therefore, that the power series for  $U_1$  converges for values of  $\varepsilon$  up to 1 (i.e., for any size vortex ring), with a simple pole at  $\varepsilon = 1$ .

The decrease in ring speed due to the presence of the tube is of order  $\varepsilon^3$ . Small vortex rings would not be much affected while larger rings might be substantially affected by the boundaries. In Fig. 3-7  $U_1/U_0$  is plotted as a function of  $\varepsilon$  for different values of  $\hat{U}_0$ . We express  $\hat{U}_0$  in terms of  $a/R$  as defined by the Kelvin/Lamb

$n$	$\hat{U}_n$	$n$	$\hat{U}_n$
3	5.006595	53	2.038892
5	2.828542	55	2.037434
7	2.440721	57	2.036082
9	2.296007	59	2.034824
11	2.223716	61	2.033650
13	2.180712	63	2.032554
15	2.152066	65	2.031526
17	2.131493	67	2.030562
19	2.115936	69	2.029655
21	2.103728	71	2.028800
23	2.093875	73	2.027993
25	2.085750	75	2.027230
27	2.078929	77	2.026508
29	2.073121	79	2.025823
31	2.068113	81	2.025172
33	2.063750	83	2.024554
35	2.059915	85	2.023965
37	2.056517	87	2.023404
39	2.053484	89	2.022869
41	2.050762	91	2.022357
43	2.048303	93	2.021868
45	2.046073	95	2.021400
47	2.044039	97	2.020951
49	2.042178	99	2.020521
51	2.040469	101	2.020108

TABLE 3-2

Coefficients for the wall-induced velocity  
of a vortex ring in a tube.

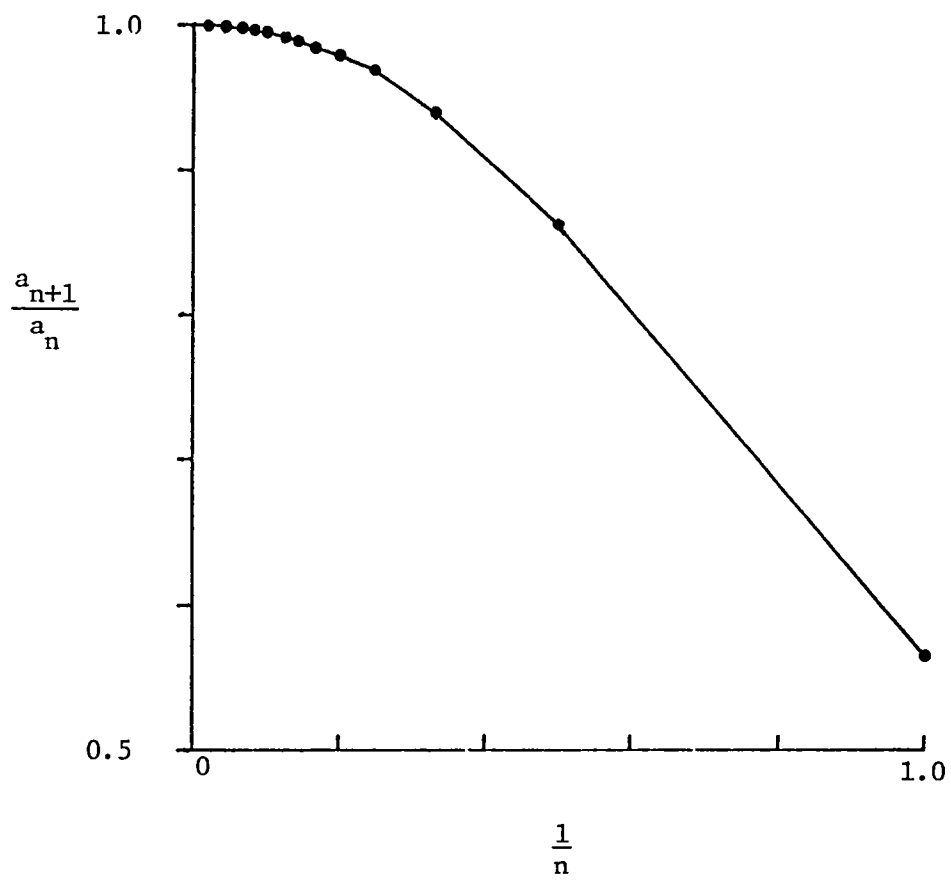


FIGURE 3-6

The Domb-Sykes plot for  $\hat{U}_i$ .

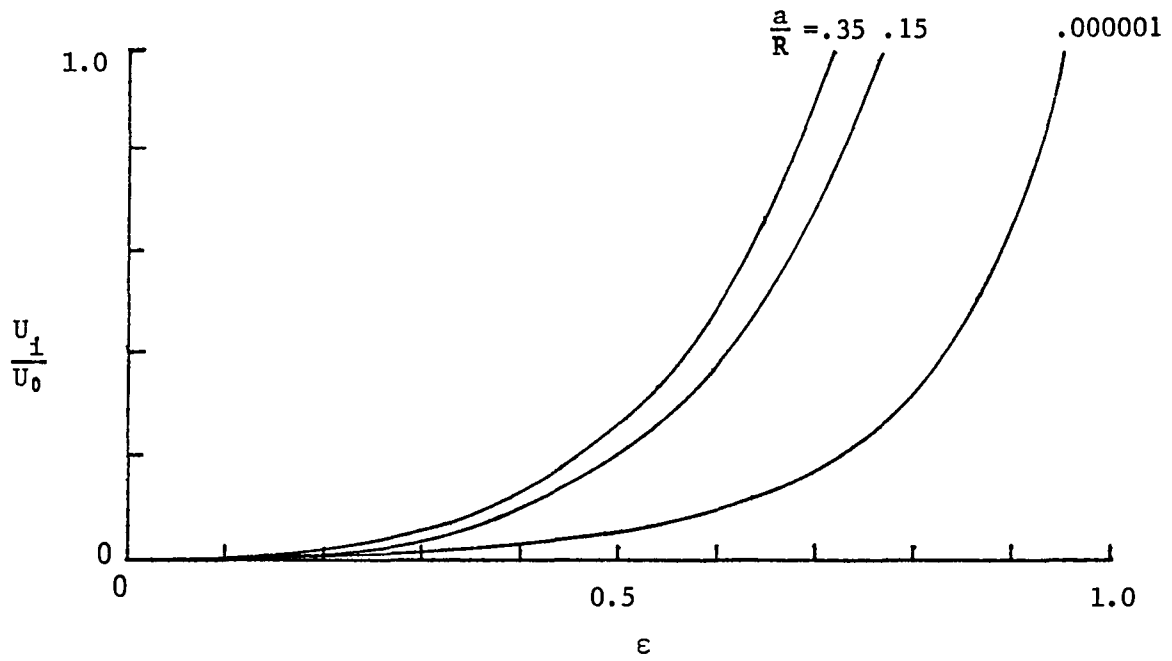


FIGURE 3-7

The wall-induced velocity of a vortex ring in a tube.

$U_0$  is given by the Kelvin/Lamb formula.

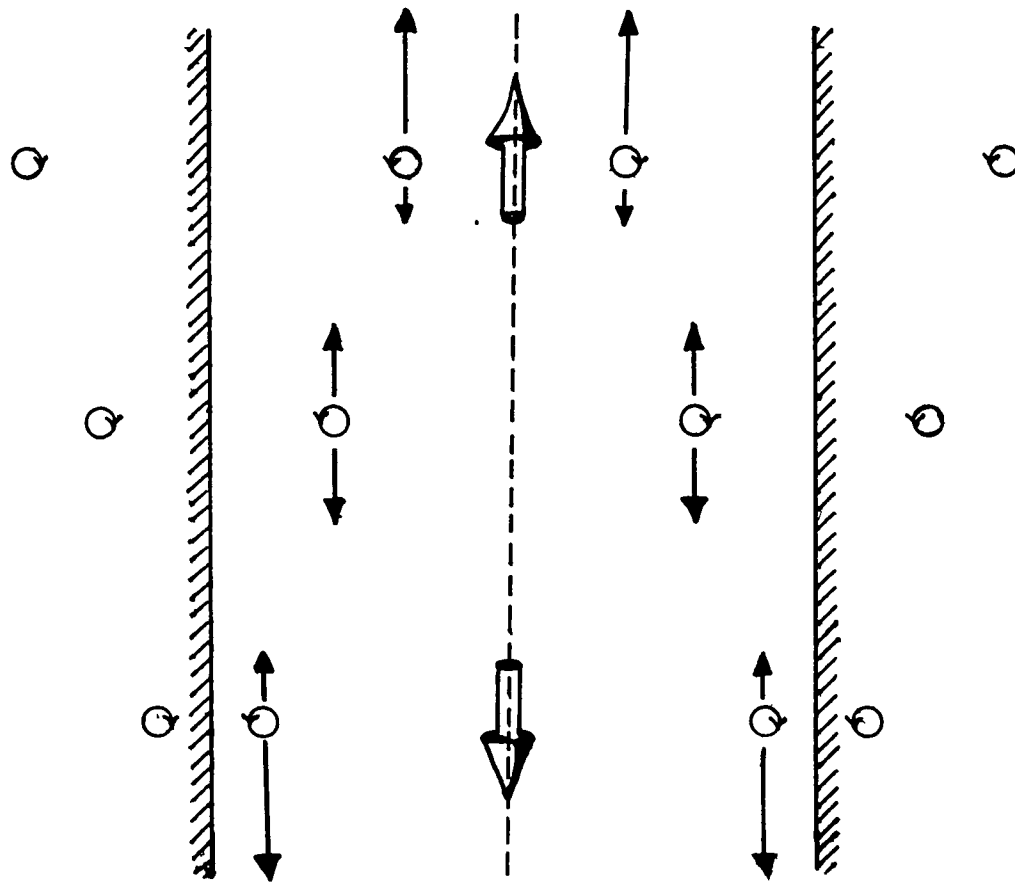


FIGURE 3-8

The analog of a vortex pair in a channel.

- i) only the first images are shown.
- ii) the upper arrows indicate the induced velocity from the opposite vortex, while the lower arrow is that for the image vortex.
- iii) the large arrows indicate the direction of motion of the vortex pair.

formula for the velocity of a thin core vortex ring with constant vorticity in the core [see Section 2-3.1, Eq. (2-15)]:

$$U_0 = \frac{\Gamma}{4\pi R} \left( \ln \frac{8R}{a} - \frac{1}{4} \right)$$

Note from Fig. 3-7 that for a given  $U_0$  (or  $a/R$ ), as the vortex ring increases in size, the wall induced velocity increases until it reaches a value equal to  $U_0$ . At this point the vortex ring does not move relative to the tube, and larger rings actually move backwards! This can be understood by considering the two-dimensional analog to the vortex ring in a tube: a vortex pair in a channel. As shown in Fig. 3-8 as the distance between the vortex pair increases (i.e., as  $\epsilon$  increases) the image vortices move closer to the wall, until a point is reached at which the velocity induced on one line vortex by its image is the same as that induced by the other line vortex. As  $\epsilon$  increases further the image system induces an even greater velocity on the vortex pair causing it to move backwards. We note also from Fig. 3-7 that in comparing two vortex rings of the same size the faster moving, and therefore more energetic vortex ring is affected less by the presence of the tube.

### 3-4 THE POTENTIAL AND STREAMLINE FIELDS IN THE MOVING FRAME

#### 3-4.1 The Kinematic Relationships Among Vortex Ring Parameters

Consider for a moment the dipole representation for a sphere in a uniform flow. It is well known that a point dipole of strength  $\Gamma$  embedded in a uniform flow with velocity  $U$  has a streamline pattern which represents an inviscid, potential flow around a sphere which is moving with constant velocity through a stagnant fluid. The size of the sphere can be adjusted by varying the dipole strength  $\Gamma$  or the free stream velocity  $U$ . For a given  $U$  the sphere radius  $R'$  increases

as  $\Gamma$  increases, however for a given dipole strength, the sphere size decreases as  $U$  increases. In other words, there is a kinematic relationship among  $R'$ ,  $\Gamma$ , and  $U$ .

Analagous to, but more complicated than the dipole in a uniform flow is the flowfield produced by a vortex ring. In a frame fixed in space the flow has a basically dipole character, with higher order poles accounting for the finite size of the vortex ring. However, when one takes into account the vortex ring velocity by transferring to a coordinate system moving with the ring, a spheroidal volume of fluid accompanying the vortex core is identified. Just as with the moving point dipole, the extent of this spheroidal volume is related kinematically to the strength  $\Gamma$  and speed  $U$  of the vortex ring, and as with the dipole, an increase in  $\Gamma$  or a decrease in  $U$  results in an increase in the volume of fluid within the spheroid. Unlike the point dipole, however, the vortex ring has a finite radius  $R$ , resulting in a spheroidal rather than a spherical region of fluid within the vortex ring.\* We might also expect that the finite extent of the core, and the vorticity distribution within the core would have an effect on the volume of the vortex ring. However, as shown in the next section, this effect is very slight.

For a vortex ring in a tube a purely kinematic relationship also exists among the vortex ring parameters, but with additional effects due to the boundaries. In the last section we analysed the effect of the tube on the velocity of the vortex ring. We will assess here changes in vortex ring size and shape resulting from the presence of the boundary. In addition, we compute and plot the kinematic relationship among non-dimensional parameters describing the vortex ring strength, velocity, size, and shape so that flow visualization measurements can be used to compute the total circulation of typical

---

\*We refer to the whole spheroidal volume as the "vortex ring" and the toroidal region in which vorticity is concentrated as the vortex core.

vortex rings in a tube or in an unbounded flow, as a function of time.\*

Let  $\Phi$  and  $\Psi$  be the potential and stream functions in a frame fixed to the tube. These functions can be further divided into unbounded and induced fields as given by Eqs. (3-2) and (3-16), and non-dimensionalized as in Eq. (3-19). The potential and stream functions in a frame moving with the vortex ring we give the subscript  $s$ , and can likewise be divided into the unbounded and induced fields. They are given by:

$$\Phi_s = \Phi - Uz \quad (3-36a)$$

$$\Psi_s = \Psi + \frac{1}{2} U \rho^2 \quad (3-36b)$$

In non-dimensionalized form they become:

$$\hat{\Phi}_s = \hat{\Phi} - \frac{1}{\epsilon} \hat{U} \tilde{z} \quad (3-37a)$$

$$\hat{\Psi}_s = \hat{\Psi} + \frac{1}{2\epsilon^2} \hat{U} \tilde{\rho}^2 \quad (3-37b)$$

where  $\hat{U}$  is the non-dimensionalized ring velocity as given by Eq. (3-31).

CHARACTERIZATION OF RING VELOCITY. Ultimately the velocity of the vortex ring must be specified either by a calculation which takes the dynamics of the flow (including the vorticity distribution) into consideration or, as we propose to do here, by an experimental measurement. For the purposes of determining its relationships with other parameters, however, we must vary  $U$  in a convenient way. We

---

\*For a discussion of the motivation and concepts behind this calculation please read Section 2-5.

begin by dividing it into an unbounded and induced velocity as given by Eq. (3-31):

$$\hat{U} = \hat{U}_0 - \hat{U}_1$$

- i)  $\hat{U}_1$  is determined from Eq. (3-32) and depends only on the size of the vortex ring relative to the tube.
- ii)  $\hat{U}_0$  is expressed more conveniently using the core parameter  $a/R$  as defined by the Kelvin/Lamb formula extended to a continuous vorticity distribution [see Section 2-3.1 and Eq. (2-17)]:

$$\hat{U}_0 = \lambda n \frac{8R}{a} - \frac{1}{3} \quad (3-38)$$

With this expression we use  $a/R$  to specify  $\hat{U}_0$ .

We should be careful to note that for the purposes of determining the kinematic relationships in which we are interested, Eq. (3-38) is only a convenient definition, and  $a/R$  is used only as a parameter to characterize  $\hat{U}_0$ . Of course, to the extent that the Kelvin/Lamb formula is accurate (see Section 5-2.2)  $a/R$  does have physical significance as a measure of an effective core radius to the radius of the vortex ring, but its use here should not necessarily imply its acceptance as an accurate representation of the velocity of a real vortex ring.

POTENTIAL AND STREAMLINES. In Figs. 3-3 and 3-4 we compared the non-steady streamlines for an unbounded and bounded vortex ring with  $\epsilon = 0.40$ . Streamlines and constant potential lines in a frame of reference attached to the vortex ring are shown in Fig. 3-9 for a vortex ring with  $\epsilon = 0.40$  and  $a/R = 0.20$  ( $\hat{U}_0 = 3.356$ ). Fig. 3-9a depicts the vortex ring in an unbounded flow, and 3-9b the same ring\* in a tube. Streamlines are shown as solid lines and constant

---

\*By the "same ring" we mean a vortex ring with the same radius (i.e.,  $\epsilon$  or  $R$ ), the same strength,  $\Gamma$ , and moving with the same unbounded velocity,  $U_0$  (i.e., having the same value of  $a/R$ ).

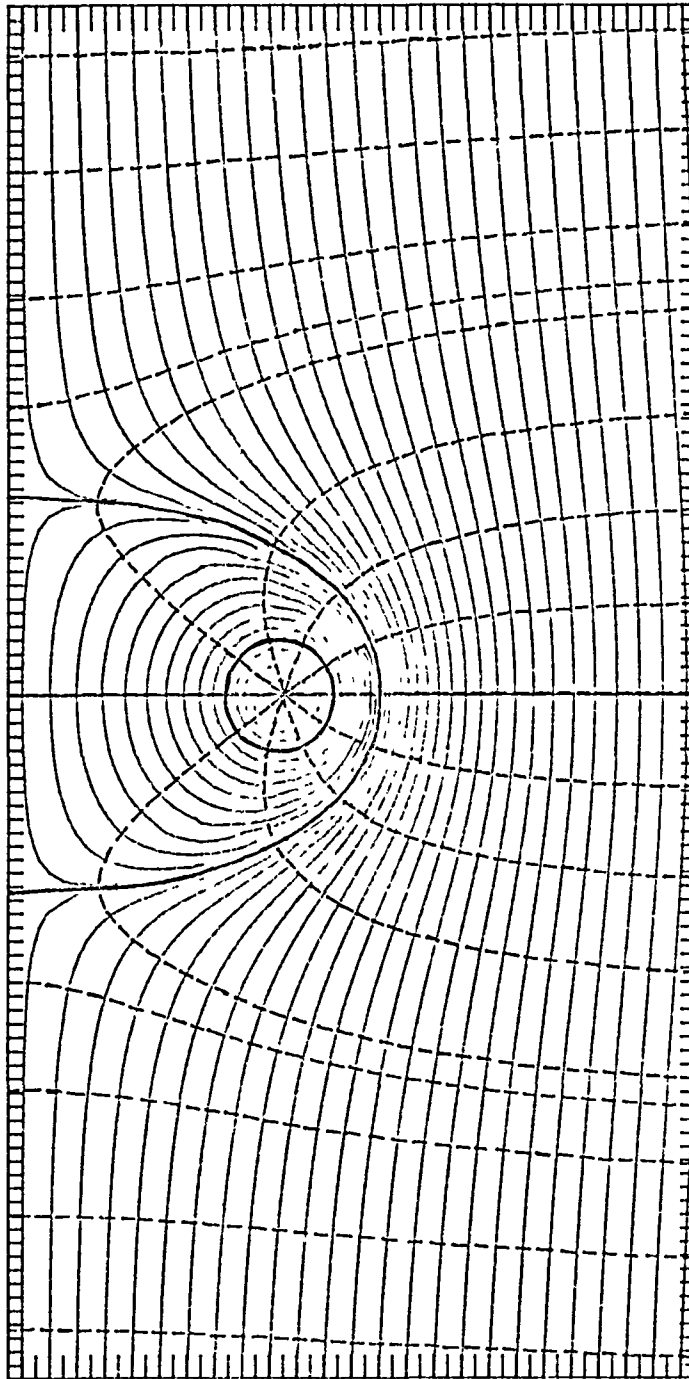


FIGURE 3-9

The streamlines and constant potential lines in the moving frame for a bounded and unbounded vortex ring with  $\epsilon = 0.40$ .

(a) unbounded vortex ring  $a/R = 0.20$

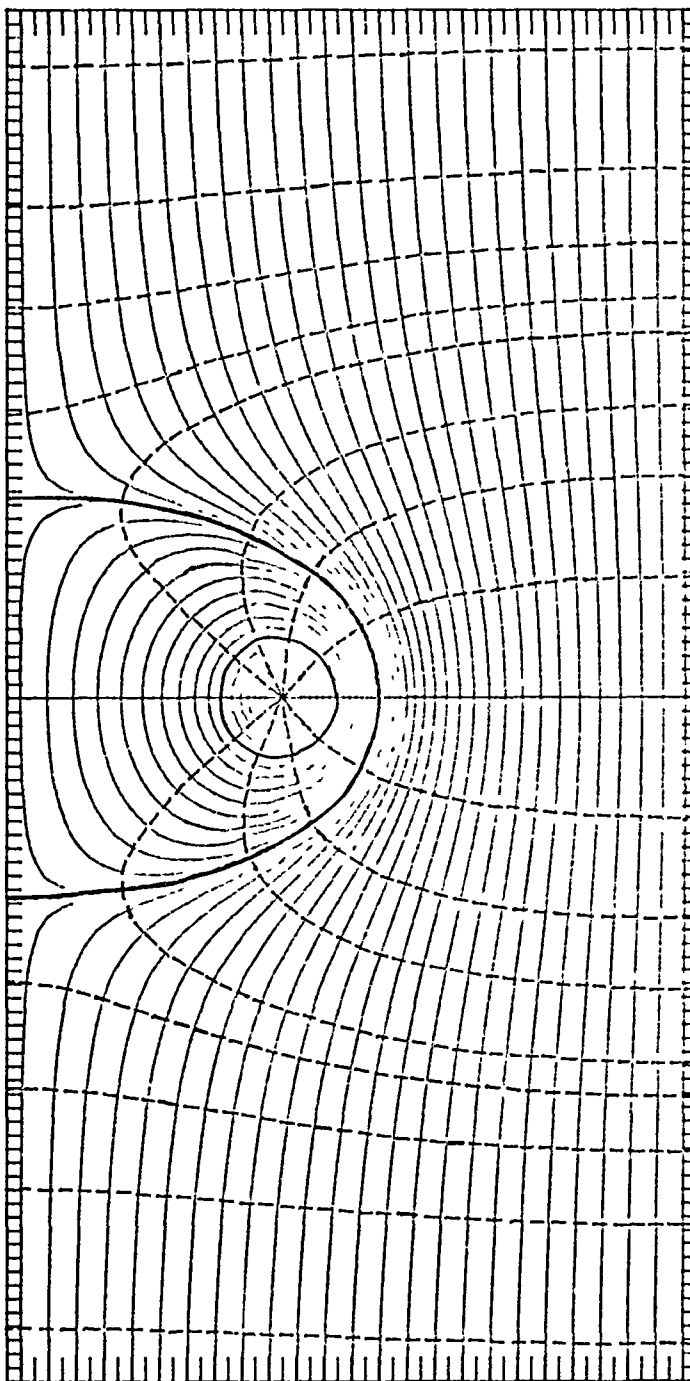


FIGURE 3-9

The streamlines and constant potential lines in the moving frame for a bounded and unbounded vortex ring with  $\varepsilon = 0.40$ .

(b) bounded vortex ring      $a/R = 0.20$

potential lines are shown dashed. For reference to the Kelvin/Lamb formula, the streamline corresponding to the designated value of  $a/R$  is darkened.

We note first the three regions commonly observed when a vortex ring is visualized with dye.

1. The core region, which in these calculations is concentrated along a circle. If you use the Kelvin/Lamb formula as an indication of core size the core would be roughly within the darker streamline corresponding to  $a/R = 0.20$ .
2. The spheroidal volume of fluid which accompanies the core. The extent of this region is delineated by the outermost closed streamline.
3. The outer ambient fluid through which the vortex ring propagates.

The streamlines in this region extend to infinity.

Second we note that the streamlines for the bounded vortex ring become parallel and the constant potential lines perpendicular to the tube wall as  $\tilde{\rho} \rightarrow 1$ , whereas this is not the case for the unbounded vortex ring. As to the size and shape of the vortex ring, the bounded vortex ring is slightly thicker than the unbounded ring, giving it a slightly greater volume, although for a vortex ring of this size the difference is not great.

In order to see more dramatically the effect of the tube on the size and shape of the vortex ring consider the extreme case of a very large vortex ring. In Figs. 3-10 are shown the streamlines for bounded and unbounded vortex rings with  $\varepsilon = 0.70$  and  $a/R = 0.25$ . Due to viscous effects at the tube wall, such a large vortex ring (relative to the tube) is not physically realistic, but it shows dramatically the change in size resulting from the presence of boundaries. The thickness of the vortex ring is increased, resulting in a larger volume of fluid carried along with the vortex core; however, this volume of fluid moves at a slower speed. The outer radius  $R'$  of this extremely large vortex ring is slightly less as a result of the tube.

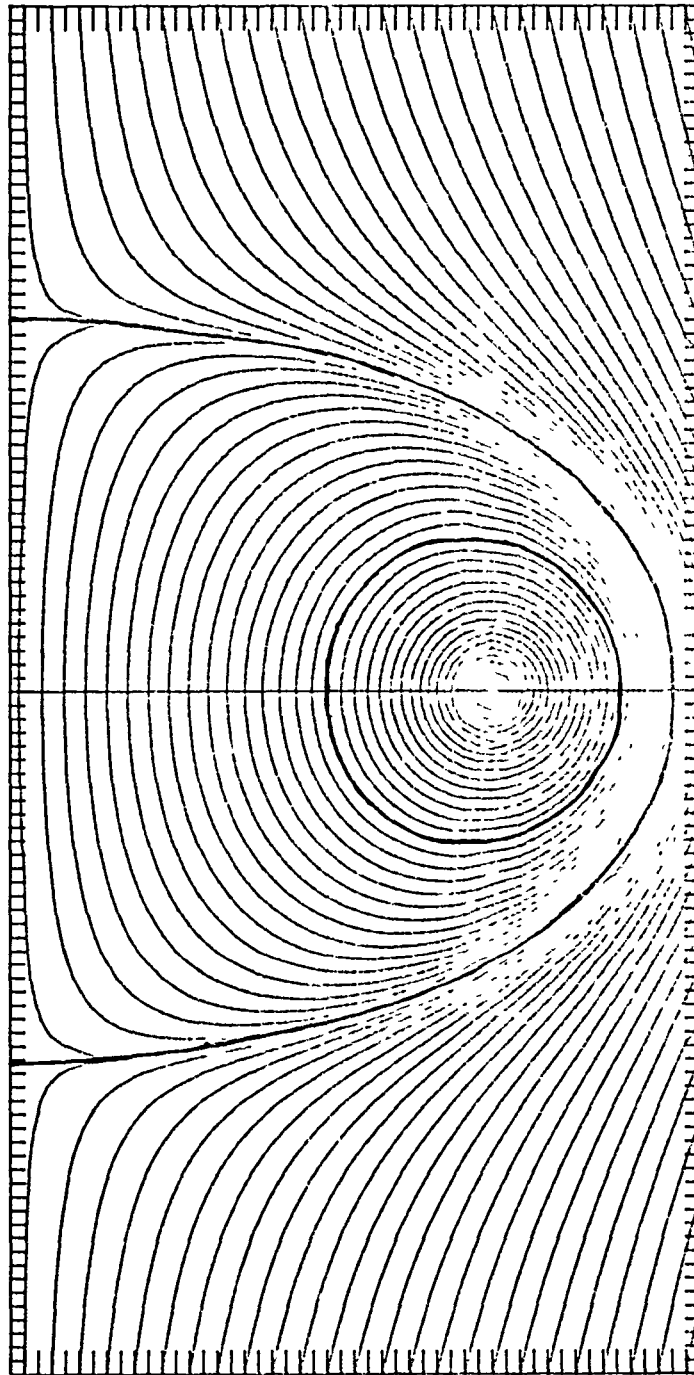


FIGURE 3-10

The streamlines and constant potential lines in the moving frame for a bounded and unbounded vortex ring with  $\varepsilon = 0.70$ .

(a) unbounded vortex ring

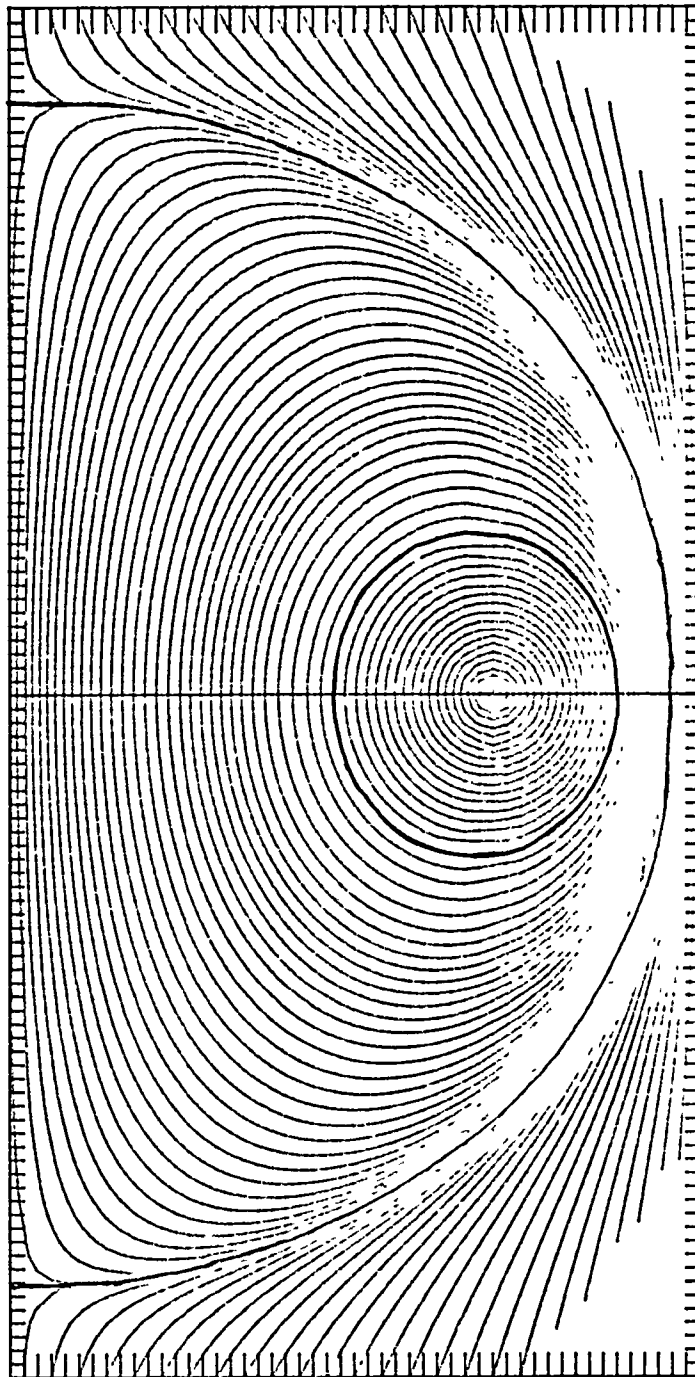


FIGURE 3-10

The streamlines and constant potential lines in the moving frame for a bounded and unbounded vortex ring with  $\epsilon = 0.70$ .

(b) bounded vortex ring

THE KINEMATIC RELATIONSHIPS. A more detailed description of the effects of the tube on the shape of the vortex ring will result from calculations of the kinematic relationships among the parameters which characterize the size, shape, strength and velocity of the vortex ring. These parameters, in non-dimensional form are:

$$i) \quad \hat{U} = \frac{U}{\Gamma/4\pi R} = \hat{U}_0 - \hat{U}_i \quad \text{where} \quad \hat{U}_i = \hat{U}_i(\epsilon) \quad \text{and} \quad \hat{U}_0 = \hat{U}_0(a/R)$$

$$ii) \quad \epsilon = R/\rho_0 \quad iii) \quad T/R \quad iv) \quad R'/R$$

Again we point out that  $a/R$  is used here only as a parameter to characterize  $\hat{U}_0$ , so that an unbounded vortex ring which is subsequently placed in a tube will have the same value of  $\hat{U}_0$ , and therefore the same value of  $a/R$ .

For a vortex ring with given  $\hat{U}_0$  and  $\epsilon$  (and therefore  $\hat{U}_i$ ), we have calculated the stream function  $\hat{\Psi}_s$  and potential function  $\hat{\Phi}_s$  from Eqs. (3-37a and b). The thickness  $T/R$  was then determined from  $\hat{\Phi}_s$  evaluated at  $\tilde{\rho}=0$ , and  $R'/R$  from  $\hat{\Psi}_s$  evaluated at  $\tilde{z}=0^*$ .

In Fig. 3-11 is shown the variation of  $T/R$  with  $U_0$  (or  $a/R$ ) for  $\epsilon = 0, 0.1, 0.2, \dots, 0.7$ . Note that  $\hat{U}_0$  decreases with increasing  $a/R$ . The solid curve corresponds to  $\epsilon = 0$ , the unbounded vortex ring, and the dashed curves to increasing values of  $\epsilon$ . We observe an upward trend in  $T/R$  as  $a/R$  increases, that is as  $\hat{U}_0$  decreases. Analogous to the dipole in a uniform flow (as discussed at the beginning of this section), this shows that for a vortex ring of given radius, the thickness (and volume) increases with either decreasing ring velocity or increasing ring strength. Related to this, we note also that the tube has a greater influence on vortex rings with smaller values of  $\hat{U}_0$ . That is, deviations from the solid curve are

---

\*T corresponds to the maximum in  $\hat{\Phi}_s$  along the  $z$  axis and  $R'$  corresponds to the zero along the  $\rho$  axis (away from  $\rho = 0$ ).

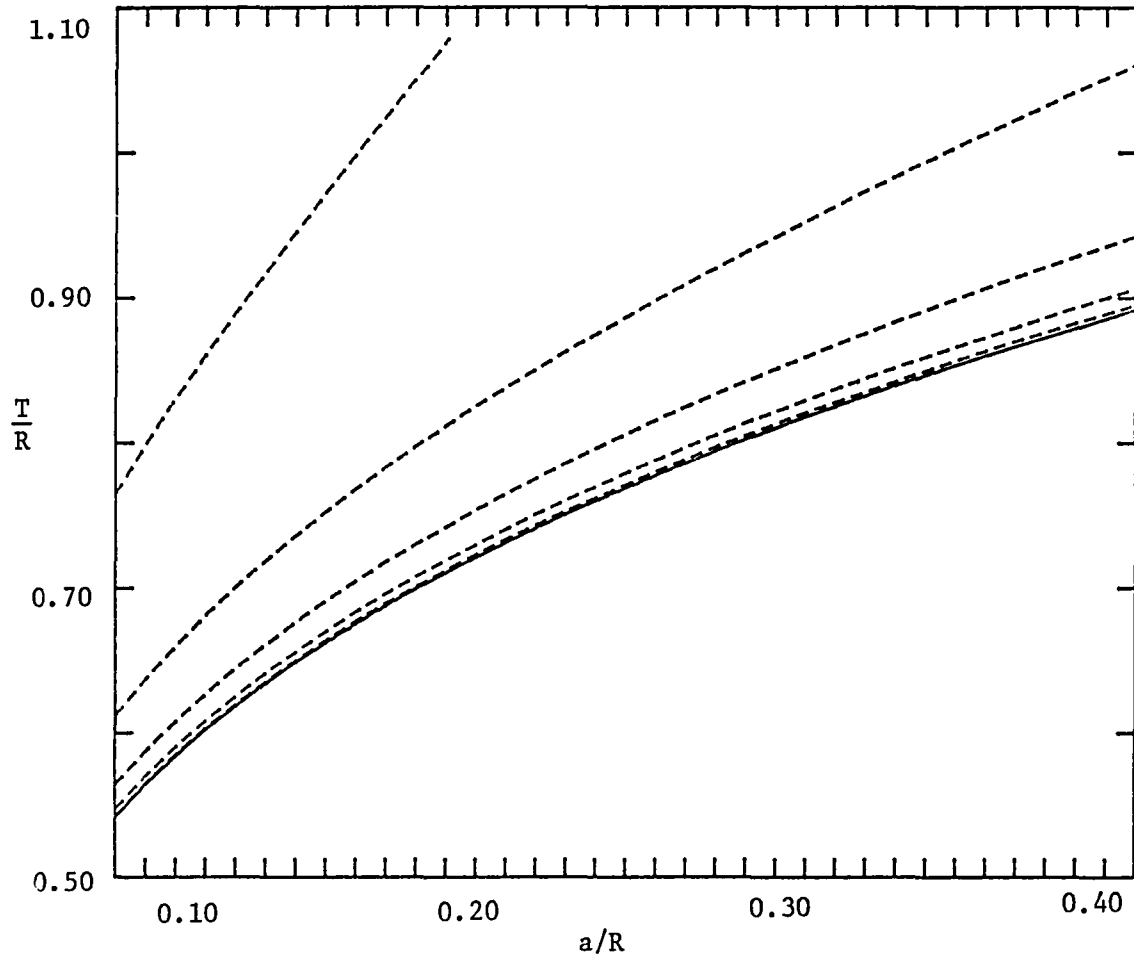


FIGURE 3-11

The variation of  $T/R$  with  $\hat{U}_0$  for different values of  $\epsilon$ .

Solid curve: unbounded vortex

Dashed curves:

1st:  $\epsilon = 0.30$

2nd:  $\epsilon = 0.40$

3rd:  $\epsilon = 0.50$

4th:  $\epsilon = 0.60$

5th:  $\epsilon = 0.70$

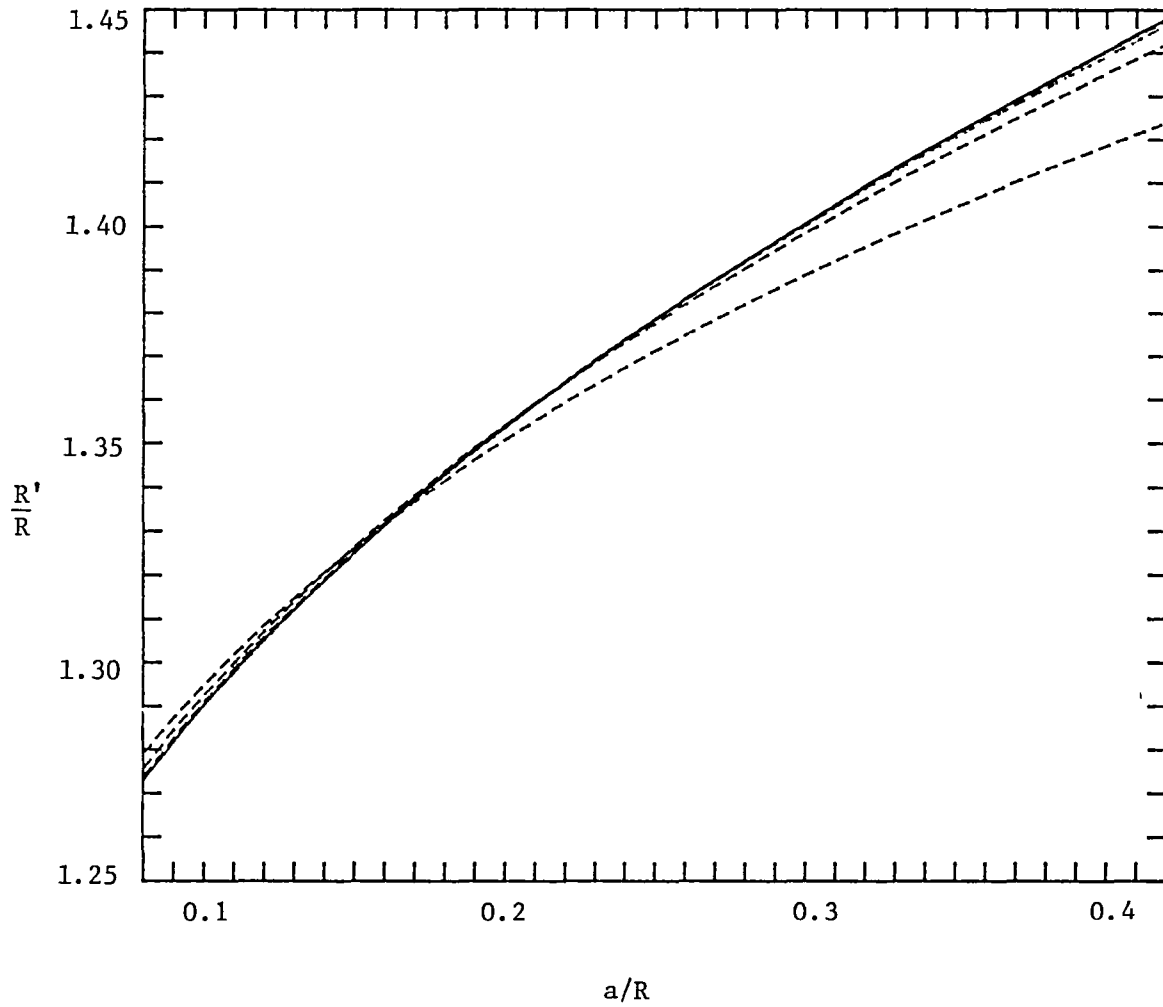


FIGURE 3-12

The variation of  $R'/R$  with  $\hat{U}_0$  for different values of  $\epsilon$ .

Solid curve: unbounded vortex ring

Dashed curves

1st:  $\epsilon = 0.50$

2nd:  $\epsilon = 0.60$

3rd:  $\epsilon = 0.70$

greater for slower and for stronger vortex rings. For  $\epsilon \leq 0.3$  there is little influence of the boundary on the thickness of the vortex ring. As  $\epsilon$  increases, however, the effect of the tube becomes more and more apparent as an increase in the thickness and volume of the vortex ring over the same ring in an unbounded flow.

The variation of  $R'/R$  with  $\hat{U}_0$  as a function of  $\epsilon$  is shown in Fig. 3-12 where again the solid curve corresponds to the unbounded vortex ring and the dashed curves to increasing values of  $\epsilon$ . For values of  $\epsilon$  up to about 0.4 the effect of the tube on  $R'/R$  is negligible and for values up to 0.50 slight. It is interesting that the effect of the tube is to increase  $R'$  for large values of  $\hat{U}_0$  but decrease  $R'$  for small values of  $\hat{U}_0$ . As  $\epsilon$  increases, the point at which the dashed curves cross the curve for an unbounded ring moves to the left. That is, for very large vortex rings, as in Fig. 3-10, the effect of the wall is to decrease  $R'$  over an identical, but unbounded vortex ring.

We point out once again that the relationships plotted in Figs. 3-11 and 3-12 are purely kinematic. Thus, measurements can be used in conjunction with these results to calculate quantities of interest. In Chapter 5 we discuss the use of flow visualization measurements together with these kinematic relationships to calculate the total circulation of vortex rings.

### 3-4.2 The Effect of a Finite Core on Ring Shape

As was discussed in detail in Section 2-5 we have made the assumption that in calculating the relationships between the shape and other parameters of the vortex ring we can neglect the finite extent of the core and concentrate the strength of the vortex ring along a circle. In this section we perform a calculation to test this hypothesis.

A vortex ring with  $\epsilon = 0.40$  and  $a/R = 0.25$  was chosen for the test.\* Thirty-seven vortex filaments were distributed in a roughly circular area with radius  $b$  such that  $b/R = 0.30$ . The vortex filaments were weighted according to the vorticity distribution in a real vortex ring as measured by Maxworthy [36, Fig. 6]. The sum of strengths of the individual filaments is the total circulation of the vortex ring. Using the linearity of the Biot-Savart law (see Section 2-1) the potential field was computed by adding the fields of the individual vortex filaments.

The constant potential lines for a bounded vortex ring with the total circulation concentrated along a single vortex filament are compared with the vortex ring having a finite core in Fig. 3-13. The 37 vortex filaments over which the circulation of the vortex ring is distributed are indicated with dots.

A careful comparison of the constant potential lines (e.g., using a light table) shows that differences in vortex ring shape between the finite core vortex ring and circular vortex filament are extremely small. There appears to be a very slight bulge in the vortex ring with the finite core, but  $T$  and  $R'$  are virtually unchanged. Even near the core where one might expect greater differences they are slight. This would suggest that for the purposes of computing the streamline and potential fields outside of the core of a vortex ring, a vortex filament model is quite accurate. In computations of the velocity of a vortex, of course, the size of the core remains a critical factor (Section 2-3). A comparison was also made between unbounded vortex rings, but with the same result as the bounded case.

---

\*These values were chosen because most of our experimentally produced vortex rings had values of  $\epsilon$  below 0.4 and calculations based on the Kelvin/Lamb formula suggest that for these rings,  $a/R \sim 0.25$  (Section 5-3).

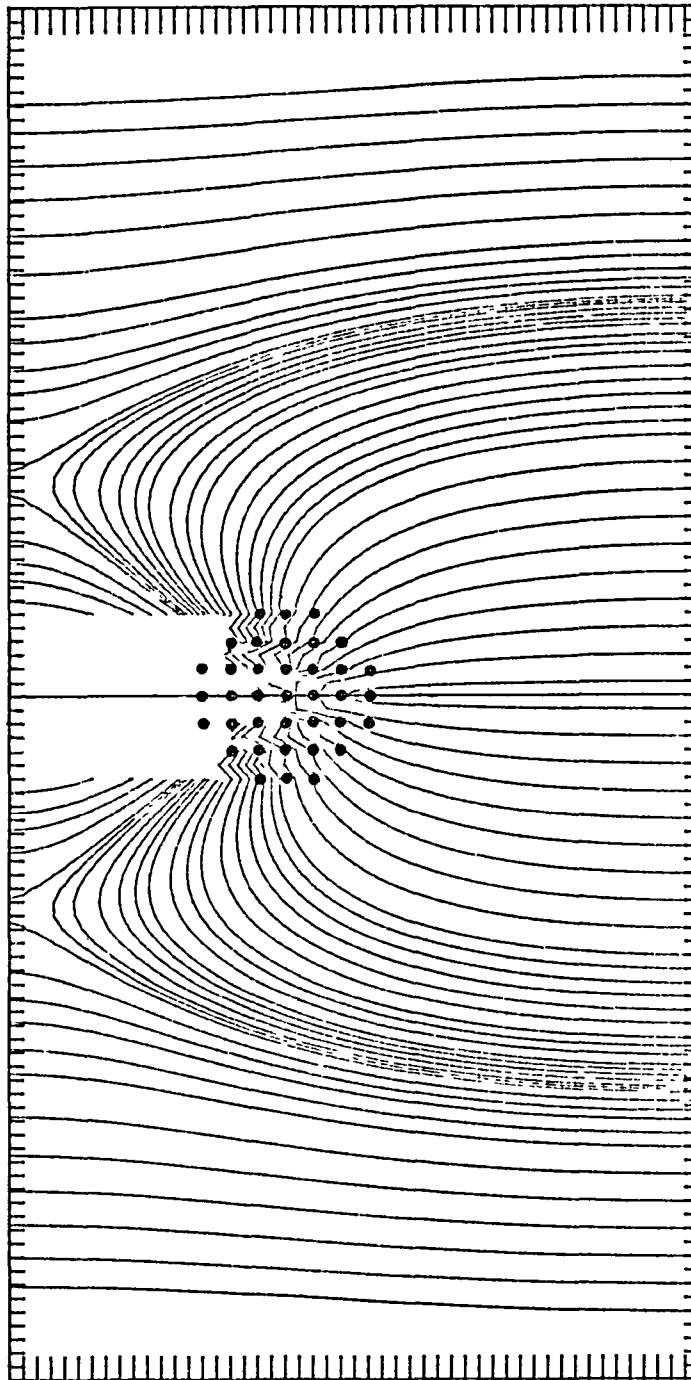


FIGURE 3-13

Constant potential lines for a vortex ring with a finite core compared with a circular vortex filament.

(a) finite core

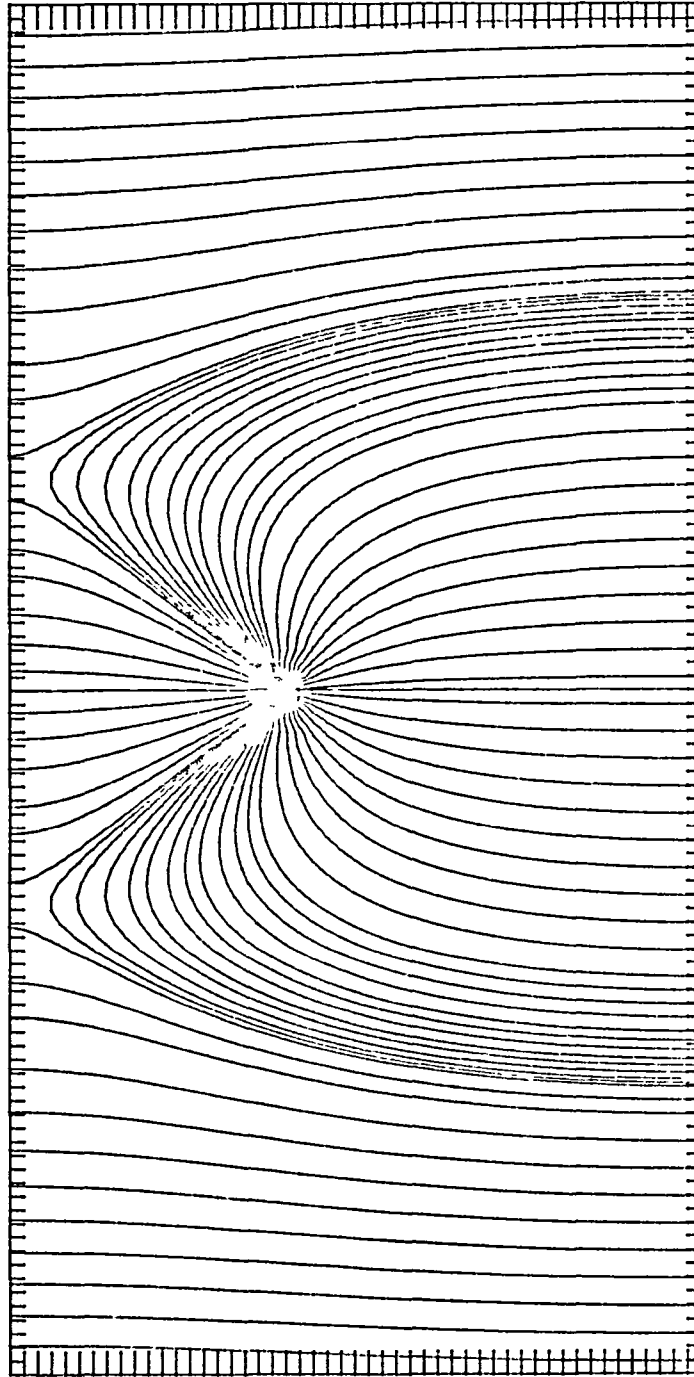


FIGURE 3-13

Constant potential lines for a vortex ring with a finite core compared with a circular vortex filament.

(b) circular vortex filament

# 4

## Experiment

*Big whirls have little whirls which feed on their velocity;  
little whirls have smaller whirls and so on to viscosity.*

-L. F. Richardson

Complementing the theoretical calculations, an experiment was performed to observe real vortex rings as they propagate up a tube. We combine qualitative observations with flow visualization measurements to study the characteristics and development of vortex rings from very low to very high Reynolds numbers. In Chapter 5 these measurements are combined with the kinematic relationships described in the last chapter to calculate the total circulation of our experimentally produced vortex rings as a function of time.

### 4-1 APPARATUS

BASIC APPARATUS. The basic apparatus is shown schematically in Fig. 4-1. A plexiglass tube with an internal diameter of 11.88 cm., a wall thickness of 1 cm., and a total height of 55 cm. is secured vertically on a heavy, cast iron mount. Seven circular orifices of different size, 2.5 cm. thick and tapered at an angle of  $60^{\circ}$  are mounted in the tube. Defining  $d$  as the orifice diameter and  $D$  as the tube diameter, the orifice sizes used in the experiment are:

$$d/D = 0.10, 0.15, 0.25, 0.32, 0.42, 0.48, 0.64.$$

By mounting two Endevco accelerometers on either side of the tube it was discovered that when filled with water the tube exhibited a



cantilever mode of vibration with a natural frequency of roughly 35 Hz. To dampen out these unwanted oscillations a heavy metal support was added to the top of the tube.

A single pulse of water is ejected through an orifice by an hydraulically activated piston. The piston speed and stroke length are adjustable. A linear potentiometer is attached to the piston to monitor its  $x_p$ - $t$  characteristics, and a travel dial is used to measure the stroke length  $X_p$ . From these measurements the average piston speed  $u_p$  is calculated, and from

$$u_j = \frac{u_p}{(d/D)^2} \quad (4-1)$$

the slug flow, or "jet" velocity determined. Defining the jet Reynolds number as

$$Re_j = \frac{u_j d}{\nu} \quad (4-2)$$

and combining with Eq. (4-1) we see that there is a general increase in  $Re_j$  with decreasing orifice size.

EXPERIMENT. The piston speed is adjusted to produce tube Reynolds numbers of roughly 5000, 4000, and 3000 where

$$Re_T = \frac{Du_p}{\nu} \quad (4-3)$$

The piston travel time is held roughly constant at about 0.170 sec; thus more fluid is ejected at the higher Reynolds numbers.

In Fig. 4-2 the main components of the experiment are sketched. The potentiometer output, a direct indication of  $x_p(t)$ , is displayed on a Tektronix oscilloscope and recorded photographically. Either an accelerometer attached to the piston or a pressure transducer mounted flush with the tube wall is used to trip the oscilloscope. It is found that, except at the lowest values of  $Re_T$ , the  $x_p$ - $t$  slope is

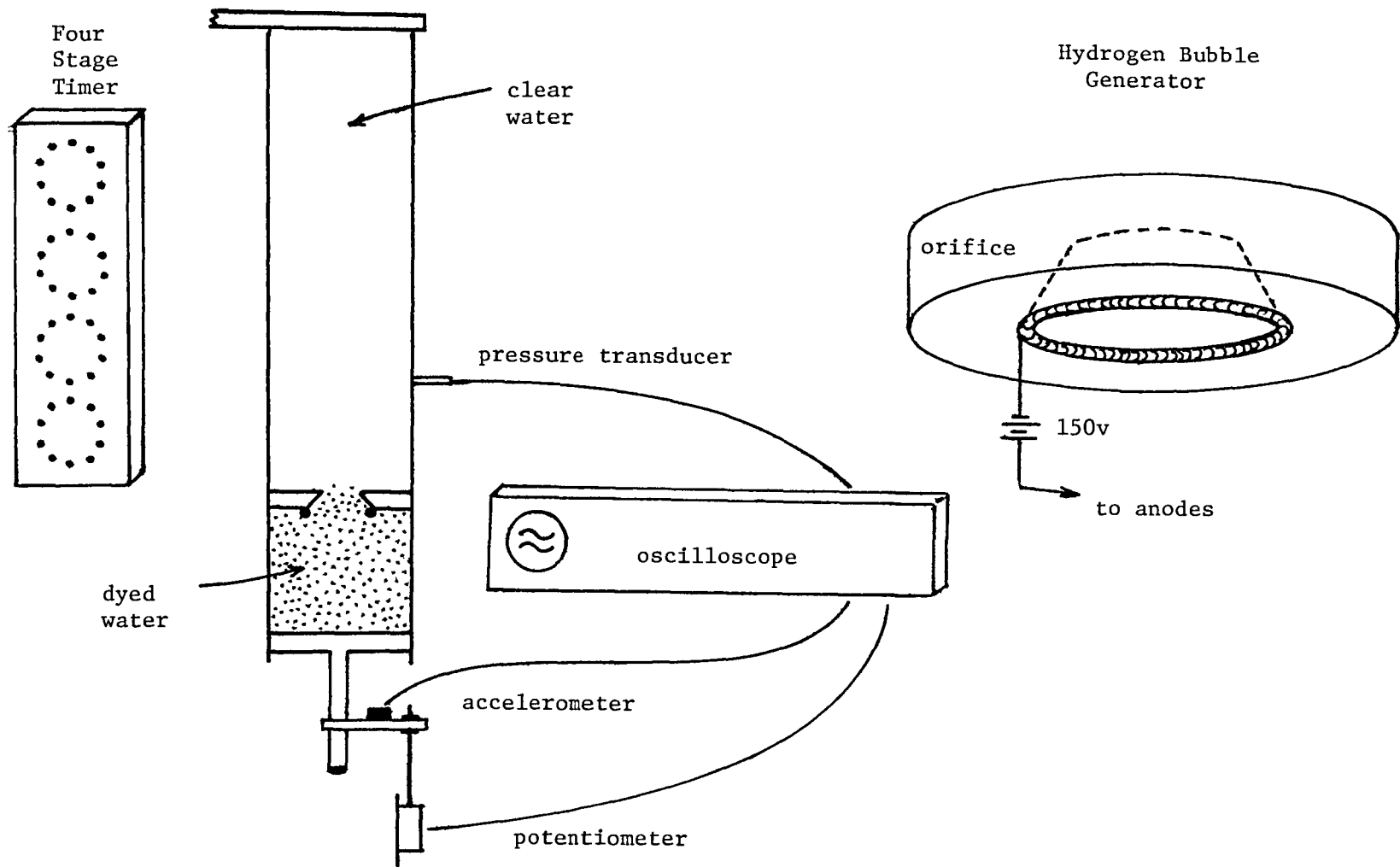


FIGURE 4-2

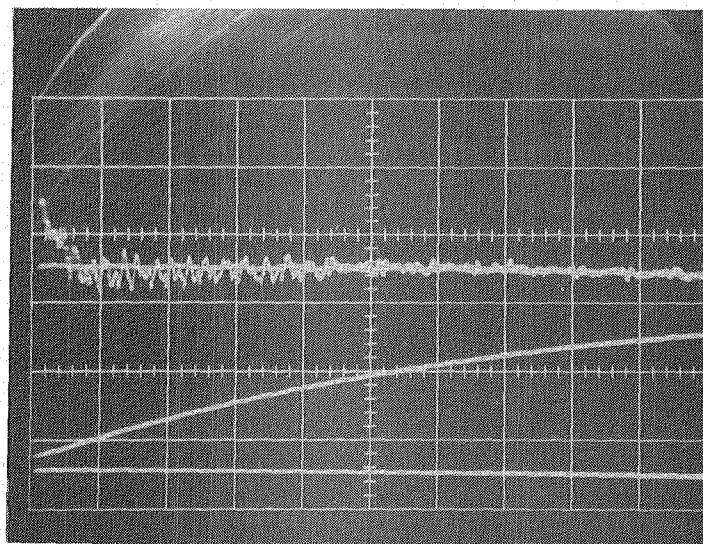
The main components of the experiment.

nearly linear, indicating constant piston speed. An example is shown in Fig. 4-3a. The upper curve is output from an accelerometer attached to the piston showing piston acceleration and deceleration periods of about 15 msec. For the lowest values of  $Re_T$ , the  $x_p-t$  characteristics are as shown in Fig. 4-3b. We approximate this piston trajectory as  $1/4$  of a sine wave.

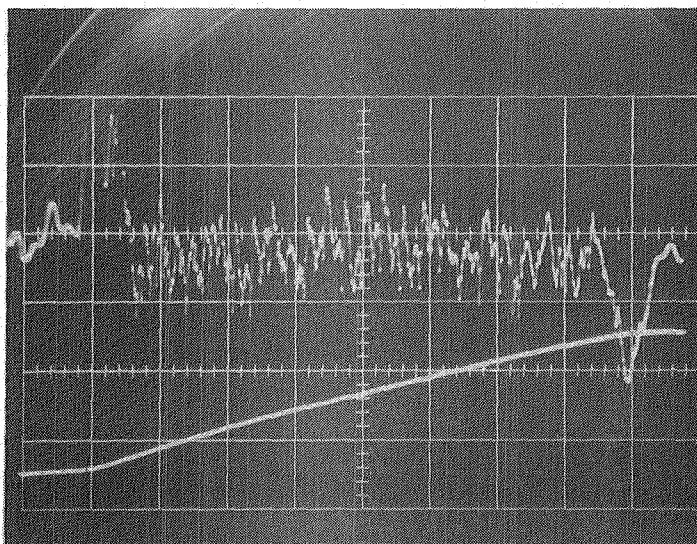
In order to visualize the flow, either dye is inserted into the chamber below the orifice or hydrogen bubbles are produced from thin rings,  $1/16$  inch in diameter, which just fit on the underside of the orifice (see Fig. 4-2). The rings are insulated and wrapped in a spiral fashion with 2 mil platinum wire to serve as the cathode in the electrolysis process. Two thin strips of 5 mil platinum sheet are glued vertically to opposite sides of the tube for the anodes. About 25 cc. of sodium sulfate was dissolved in the water as an electrolyte and 150 volts applied between the anode and cathode. Tiny hydrogen bubbles are swept into the vortex ring as it forms, all redissolving except for those trapped in the center of the core, a relatively stagnant region. In this way bubbles can be used to measure  $R$ , the radius of the vortex ring to the core centerline.

The use of dye, of course, allows visualization of the total extent of the vortex ring. Red food coloring was injected into the chamber below the orifice to a concentration of about 2% by volume. Dye gives the best description of the formation process as well as qualitative features such as the heaviness of the wake behind the vortex ring. Quantitative measurements of the shape of the vortex ring (i.e.,  $T$  and  $R'$ ) are made using the dye visualization. Unfortunately, although the core region is usually darker than the outer region of the vortex ring, it usually does not contain enough detail to determine with precision the location of the core centerline.

MOVIES. High speed 16 mm. color movies were taken for all combinations of orifice size and tube Reynolds number. Over 190



(b)



(a)

FIGURE 4-3

Piston trajectory characteristics.  
20 msec/div.

sequences, or "runs," were filmed of vortex rings ranging in Reynolds number from about 690 to 50100. These movies were subsequently analysed to obtain both qualitative and quantitative data.

With the hydrogen bubble technique lighting is a major problem. The intensity of the reflected light from the tiny bubbles is very sensitive to the lighting angle, and the round tube added unwanted reflections. By adjusting the lights so as to come from above the movie camera at an angle of roughly  $10^\circ$  from the vertical, we were able to obtain hydrogen bubble movies for all but the slowest vortex rings. When using the dye the lighting was from behind the tube and reflections were not a problem.

In order to accurately determine the film speed, a four stage timer was constructed\* (see Fig. 4-2) consisting of four divide-by-ten integrated circuits connected to light-emitting diodes so as to be visible in the movies. The diodes, which have a rise time of about 5 microseconds, are arranged in four circles of ten each, each circle representing a decimal place. A sine wave generator provides the power and calibration for the timer. With the timer visible in the movies, very accurate calibration of film speed was obtained. For most runs the film speed was about 100 frames per second.

#### 4-2 QUALITATIVE OBSERVATIONS

As dyed water is ejected through the orifice we observe the rollup of the emerging cylindrical vortex sheet into a vortex ring (see Section 2-4), its detachment from the orifice, and its propagation up the tube. In some cases the vortex ring can be

---

\*By William Janeway to whom we are indebted for a great deal of help with the electronics and experiment.

observed to veer from the tube axis and interact with the tube wall as well.

SMALLEST ORIFICES. The smallest orifices ( $d/D = 0.10, 0.15$ ) produce the smallest and most energetic vortex rings. Associated with the high jet Reynolds numbers, the vortex rings have very high values of ring Reynolds number and are turbulent in character. For these small orifices the formation of a vortex ring is followed by the production of a turbulent jet.\* The vortex ring initially occupies the tip of the jet, but due to the concentrated nature of the vorticity within the ring, soon breaks away and travels independently up the tube. After the piston has stopped, the jet quickly diffuses and spreads. The vortex ring, on the other hand, travels rapidly up the tube followed by a fairly heavy, turbulent wake.

A photograph and drawing of turbulent vortex rings are shown in Figs. 4-4 and 2-7b respectively. Within the vortex ring we observe a somewhat discernible core region surrounded by a lighter region of turbulent fluid. With the hydrogen bubble visualization, short wavelength fairly small amplitude waves can be observed along the core. In addition, a bending mode of oscillation is sometimes observed; as the vortex ring travels up the tube, the ring of bubbles defining its core is observed to bend back and forth symmetrically about the ring axis.

INTERMEDIATE ORIFICES. The intermediate sized orifices ( $d/D = 0.25, 0.32, 0.42$ ) are associated with intermediate values of jet Reynolds number, intermediate ring Reynolds numbers, and intermediate size vortex rings. For an example of an "intermediate" vortex ring, see the photograph at the beginning of this report (just

---

\*During the piston motion, a jet of dyed water is indeed observed, but after the piston has stopped this turbulent region continues to move and develop. In what follows we call this turbulent region a "jet," although it may not at all times correspond to an actual jet.

Experiment 78

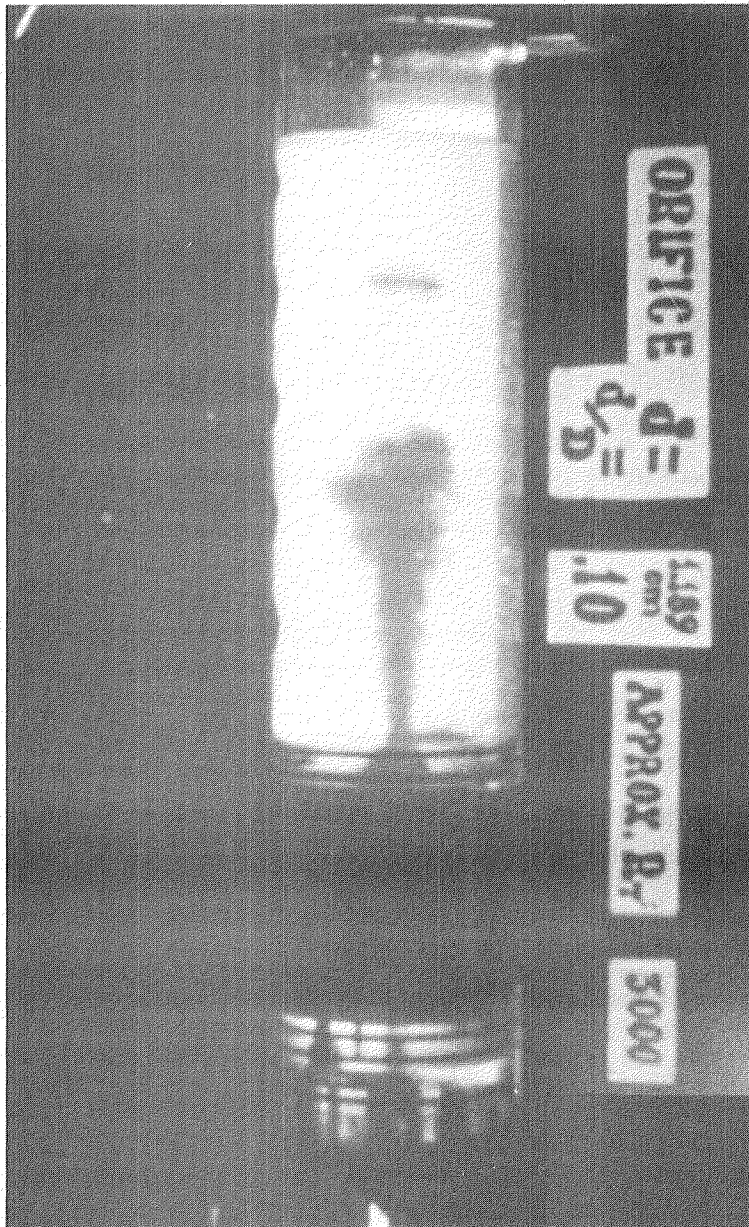


FIGURE 4-4  
Example of a vortex ring at the highest Reynolds numbers.  
Note the formation of a turbulent jet behind the vortex ring.

before the abstract). As can be observed from this photograph, these vortex rings tend to be well formed, laminar, and in general appear to be quite stable. The core region is typically well defined, and the vortex rings propagate with little or no observable wake.

LARGEST ORIFICES. The largest orifices ( $d/D = 0.48, 0.64$ ) produce the slowest vortex rings with the lowest Reynolds numbers. A result of viscous diffusion and convection of vorticity, dye is observed in a laminar wake region behind the vortex ring (see Fig. 2-7a). An interesting phenomenon is observed with the vortex ring filmed at the lowest Reynolds number. Apparently a result of interaction with the free surface in combination with the tube wall, the extremely slow, clearly viscous vortex ring is observed to bend back as it approaches the top of the tube. That is, the symmetry plane (the  $z=0$  plane of Fig. 2-3) takes the shape of a spherical cap, nose forward. As the vortex ring encounters the free surface the cap flattens out again, and the ring breaks down.

In general, when the vortex rings encounter the free surface the radius quickly increases, followed by a rapid breakdown.\* the visual result, especially for those vortex rings with little wake, is a dyed region of fluid at the bottom of the tube where the ring formed, a dyed region at the top of the tube where the ring collapsed, and clear water in between. The smallest vortex rings with very high Reynolds numbers, however, had sufficient energy to propel them completely out of the tube.

TRANSITIONAL VORTEX RINGS. Between the three groups of vortex rings which were labeled above as coming from the smallest, intermediate, and largest orifices, are "transitional" vortex rings.

---

\*The increase in radius is understood by considering the image vortex ring on the opposite side of the free surface. For beautiful photographs of the breakdown of a vortex ring at a surface, see Magarvey and MacLatchy (33).

These rings are characterized by two major features. First, one observes in these vortex rings characteristics from both the higher Reynolds number and lower Reynolds number rings they separate. Secondly, these transitional vortex rings generally show more signs of large amplitude instability than do the others. For example, the transitional vortex rings between the high Reynolds number/small orifice and the intermediate Reynolds number/intermediate orifice vortex rings ( $d/D \sim 0.15, 0.25$ ) show signs of generally larger scale turbulent motions, but visually the development of turbulence appears to be somewhat intermittent. Relative to the rings at the highest Reynolds numbers, they generally exhibit larger amplitude oscillations as well. One such transitional ring exhibited a "rocking" type of instability (see Section 4-4.3), and another a large amplitude bending mode of oscillation. The transitional vortex rings between the intermediate and the largest size orifices ( $d/D \sim 0.48$ ), on the other hand, show signs of large amplitude instability in the sense that a greater number of these rings would rather abruptly move towards, and interact with the tube wall. At these Reynolds numbers other researchers have observed the development and growth of large amplitude fairly long wavelength waves along the core centerline (Section 2-4.2).

INTERACTION WITH THE TUBE WALL. The interaction of a vortex ring with the tube wall is an interesting phenomenon. Except for the vortex rings produced with an orifice which was intentionally made very irregular (Section 4-4.3), the location where the ring collides with the wall appears to be random. As a vortex ring makes contact, one side tends to remain fixed, or "stick" to the wall while the other rotates around.\* From the hydrogen bubble visualizations one observes

---

\*Again this can be understood by visualizing the image system with the 2-D analog of Fig. 3-8.

that when the core of the vortex ring touches the wall, vortex stretching manifests itself as a rapid twisting of the vortex core before the ring collapses into a generally turbulent mass of water. Subsequently, this turbulent, vortical region is observed to rotate away from the tube wall, apparently the result of the cancellation of some vorticity by viscous forces at the wall, resulting in a net vortical motion away from the wall.

### 4-3 QUANTITATIVE RESULTS

#### 4-3.1 Data Acquisition

Data was reduced for 26 sequences or "runs" using both the dye and hydrogen bubble visualization techniques. The runs are numbered from 1 to 26 in the sequence indicated in Table 4-1. The values for  $Re_T$  given in this table are rough and should be used only as a guide. The calculated values of  $Re_T$ , more accurate values of  $d/D$ ,  $Re_j$ , and other information associated with each run are given in Table A-1 of Appendix A. The first step in the acquisition of data was to project each run onto a large sheet of graph paper and, by advancing the projector frame at a time, carefully outlining the vortex ring with as much detail as possible at many locations in its evolution. With the 4-stage timer, the film speed was accurately determined for each run. Thus, knowing the number of frames between each outline, we were able to determine the time history of the vortex rings. Because of the care (and time) which was taken in this initial process of "freezing" the vortex evolution onto a large sheet of paper, the outlines have proved invaluable in later interpretations of the data.

At an average of 35 points per run the following data was recorded for each vortex ring (refer to Fig. 2-5):

Run Number	$\frac{d}{D}$	Rough $Re_T$	Visualization
1	0.10	5000	dye
2	0.10	4000	dye
3	0.10	3000	dye
4	0.15	5000	dye
5	0.15	5000	H <sub>2</sub>
6	0.15	4000	dye
7	0.15	4000	H <sub>2</sub>
8	0.15	4000	H <sub>2</sub>
9	0.15	3000	dye
10	0.15	3000	H <sub>2</sub>
11	0.25	5000	dye
12	0.25	5000	H <sub>2</sub>
13	0.25	3000	dye
14	0.32	5000	dye
15	0.32	4000	dye
16	0.32	3000	dye
17	0.42	5000	dye
18	0.42	5000	H <sub>2</sub>
19	0.42	4000	dye
20	0.48	5000	dye
21	0.48	5000	H <sub>2</sub>
22	0.48	4000	dye
23	0.48	3000	dye
24	0.64	5000	dye
25	0.64	4000	dye
26	Irregular orifice		dye

TABLE 4-1

General identification for experimental vortex ring runs

- $x(t)$  The distance from the orifice; i.e., the trajectory.
- $R(t)$  The radius to the core centerline. This was obtained accurately for the vortex rings visualized with hydrogen bubbles, and for three rings visualized with dye. The others were estimated.
- $R'(t)$  The radius of the vortex ring to the outermost streamline. From the dyed rings, this is taken to be the edge of the dyed region.
- $T(t)$  The thickness of the vortex ring. Also obtained from the dye visualizations, this measurement was generally less accurate than that for  $R'$  due to the presence of a wake.

Initially the data was reduced completely by hand [4], but when the PDP-11/45 computer was made available for my use all the data was stored on peripheral disk back storage and subsequent data reduction handled via algol programs.

CORRECTIONS. For vortex rings formed with the smaller orifices it is often the case that the piston stops ejecting water while the vortex ring is traveling up the tube. The trajectories for these rings were therefore corrected by subtracting the piston trajectory from the vortex ring trajectory. That is:

$$x(t) \rightarrow \begin{cases} x(t) - x_p(t) & t < \tau_p \\ x(t) - X_p & t > \tau_p \end{cases} \quad (4-4)$$

where  $\tau_p$  and  $X_p$  are the piston travel time and stroke length respectively. In addition it was necessary to correct the radial values for the effect of refraction. This was made difficult by the presence of three substances with different refractive indices: a cylindrical column of water, a 1 cm. thick plexiglass tube, and the surrounding air. Defining  $\rho_A$  as the apparent radius as seen from outside the tube and  $\rho$  as the real radius, a short algorithm was developed to calculate  $\rho/\rho_0$  as a function of  $\rho_A/\rho_0$ . The result is

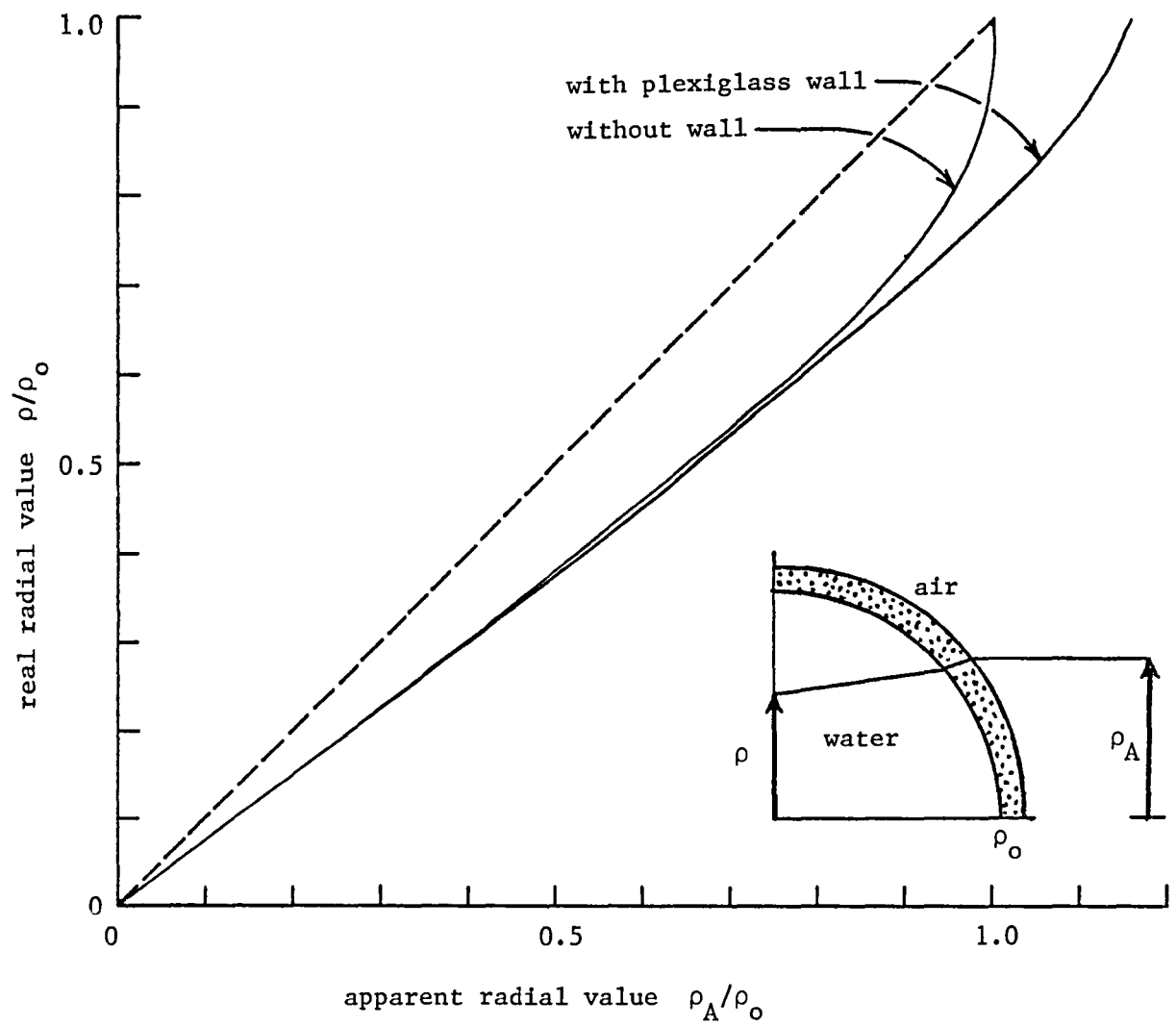


FIGURE 4-5

Refraction corrections: apparent vs. real radius.

plotted in Fig. 4-5. All values of  $R$  and  $R'$  were corrected for refraction with this algorithm.

#### 4-3.2 Vortex Ring Velocity

The trajectory of each of the 26 runs was plotted using linear, semi-log, and log-log scales. It was discovered that for many runs one, two, or three linear periods, or "regimes," can be readily identified on one of the three trajectory plots. In each regime the properly plotted trajectory can be fit with a straight line, the slope of the straight line changing from one regime to the next over a relatively short period of time.

DATA ANALYSIS. Having made the initial discovery that for some vortex rings the time dependent form of the ring trajectory (and thus velocity) can be identified within regimes, an extremely careful analysis was undertaken to objectively search for and identify such regimes in all the runs, and to accurately determine the slopes and intercepts of each linear regime.

One approach used was to compute and plot, using each of the three scales, the velocity distribution for each run. Between each two data points the slope, or "velocity" was computed. The velocity range was then divided into bins and the number of slopes in each bin determined and plotted. Ideally, a trajectory with three linear regimes, for example, would have three peaks in the velocity distribution, and as the number of bins is increased, each of these peaks should split into two or more due to oscillations about the mean. Of course, the noise level should go up as well. An example is shown in Fig. 4-6 for Run 9. Using a linear scale, three regimes can be clearly identified, resulting in three broad peaks in the velocity distribution with 10 bins. Increasing the number of bins to 15, the three peaks are better defined and begin to split. With 30 bins each major peak has split into two smaller peaks. In general, however,

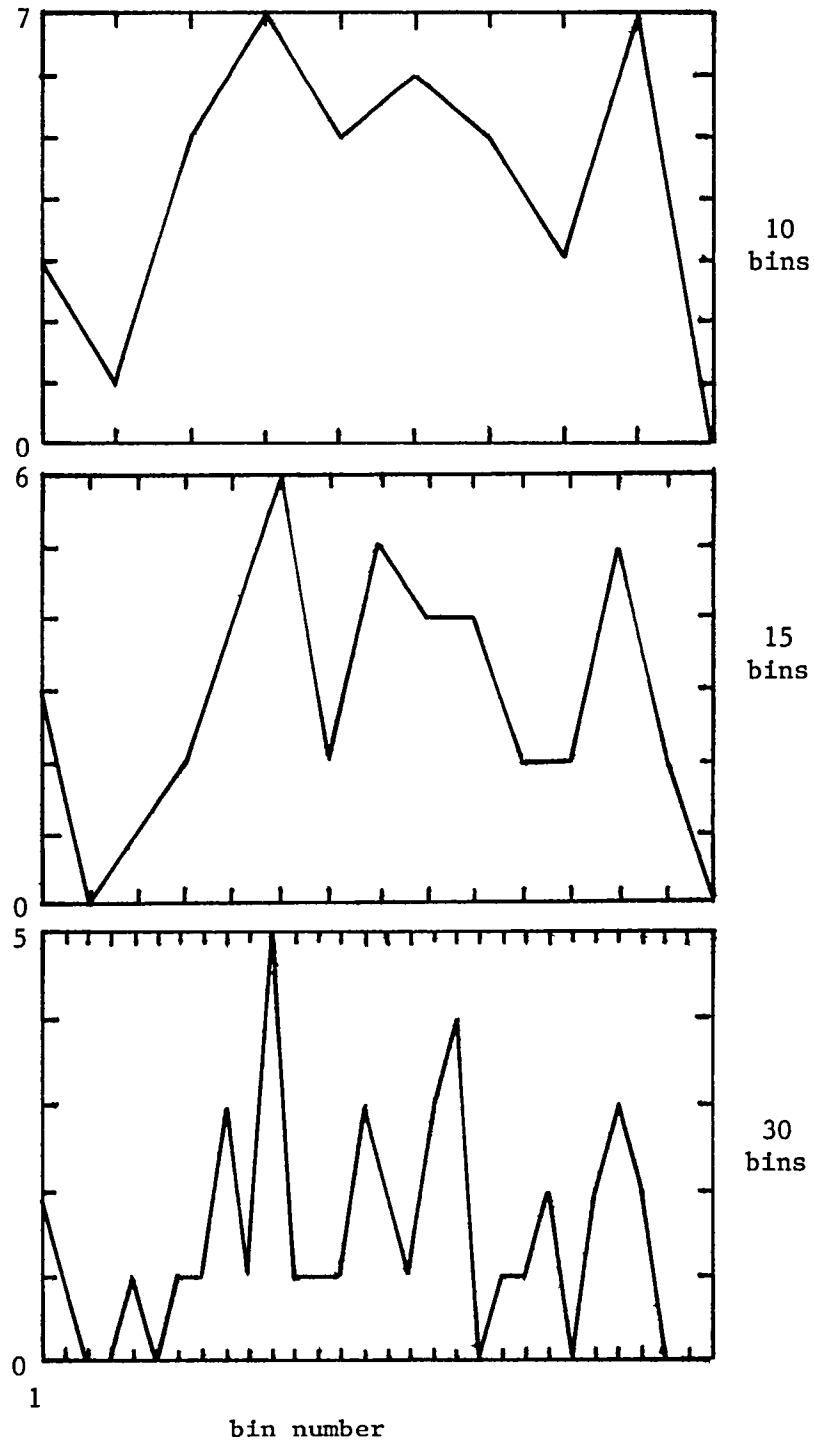


FIGURE 4-6  
The velocity distribution for Run 9.

this method did not work well. Due to the low number of points in each bin to begin with, the noise level is usually too high to obtain the quantitative information desired.

A more fruitful approach to objectively identify these linear regimes is to choose a point near the beginning of a regime, and compute the slope from that data point to each successive point. Numbering the data points 1, 2, 3, ... , and plotting the slope from the first point to each successive point vs. the point number, we would expect that if a linear region exists, the plot would oscillate at first, but soon settle down around the mean slope of that regime. The end of the regime would be identified as the location where the plot begins to move away from the mean slope. Having identified the end of a regime, one can then choose a fixed point near this end, and repeat the procedure in the opposite direction in order to identify the beginning of the regime.

This technique worked quite well, with two modifications. First, rather than compute the direct slope to successive points, the least squares fit to a straight line was computed. The resulting plot can be expected to dampen more rapidly to the mean value desired. In addition, the mean value for the slope of a regime is now obtained with a least squares fit over all the data points within that regime. The second modification was to compute the average residuals along with the least squares fit, and plot them also against point number. When the end of a regime is encountered, the value of the residual increases sharply. The result is an excellent indication of the beginning or end of a regime.

Using Run 9 again as an example, a plot of least squares fit slopes and residuals from point 9 (the beginning of the first regime) to succeeding points is shown in Fig. 4-7. The end of the first regime is clearly identified from the plot of the residuals as point 20, and the slope is seen to oscillate but soon settle down around the value 83.7.

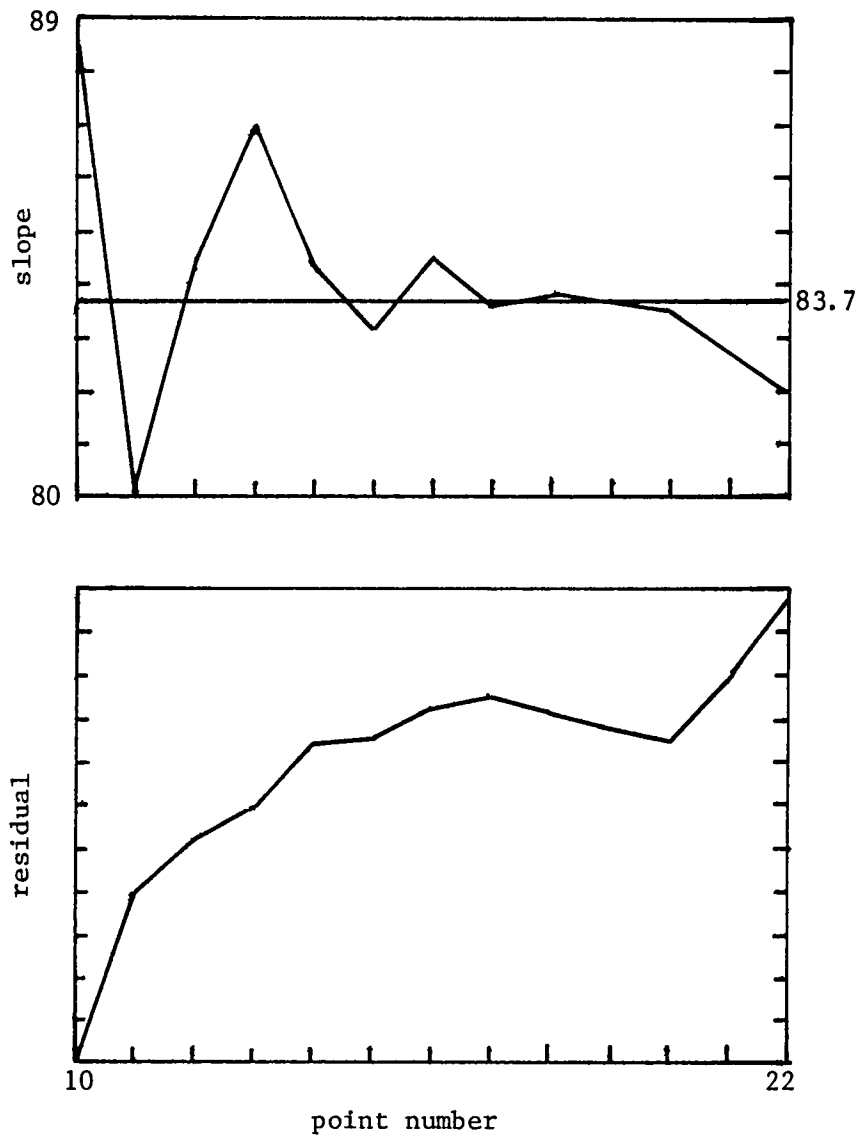


FIGURE 4-7

The least squares fit slopes and residuals vs. point number for Run 9.

RESULTS. The result of this analysis is that one, two, or three linear regimes can be identified for all our experimentally produced vortex rings (except for Run 8; see Section 4-4.3). We find that based on the scale used, the vortex rings can be divided into three groups which parallel the three classifications discussed qualitatively in the last section. These groups are:

1. Smallest orifices/Highest values of jet and ring Reynolds number:  

$$x(t) \propto \ln t \quad (\text{semi-log scale}).$$
2. Intermediate orifices/Intermediate values of jet and ring Reynolds number:  

$$x(t) \propto t \quad (\text{linear scale})$$
3. Largest Orifices/Lowest values of jet and ring Reynolds number:  

$$\ln x(t) \propto \ln t \quad (\text{log-log scale}).$$

The slopes for each regime for the 26 runs are given in Table A-2 of Appendix A.

The observation that regimes can be identified in the trajectory has significance with respect to the velocity of the vortex ring. What we have found is that at all Reynolds numbers vortex rings propagate through regimes where the time dependent form of the ring velocity can be identified, two regimes being separated by a sudden change in the velocity of the vortex ring. In addition, we find that the form of time dependence can be grouped by Reynolds number as follows:

1. High Reynolds number, turbulent vortex rings:

$$U = \frac{A_n}{t} \quad \text{where } A_n > A_{n-1} \quad (4-5a)$$

2. Intermediate Reynolds number, laminar vortex rings:

$$U = B_n \quad \text{where } B_n < B_{n-1} \quad (4-5b)$$

3. Low Reynolds number, viscous vortex rings:

$$U = \text{constant} \times t^{-\alpha_n} \quad \text{where } \alpha_n > \alpha_{n-1} \quad (4-5c)$$

The subscript  $n$  indicates a regime; the values  $A_n$ ,  $B_n$ , and  $\alpha_n$  are constants within a regime but different from one to the next. For example, a vortex ring of "intermediate" Reynolds number travels with a constant mean velocity for a period of time, goes through a rapid change involving a decrease in speed, and continues into the next regime again with a constant velocity, but slower.

Consistent with the description of "transitional" vortex rings given in the last section, we find that the transition in the time dependent form of ring velocity as you move from one group to the next does not happen abruptly. For example, the first two regimes of Run 4 are best represented with a semi-log scale but the third regime with a linear scale, indicating a transition from the turbulent to the laminar group. Between the intermediate and low Reynolds numbers is Run 22, where a linear scale is best in the first regime, but a log-log scale in the second.

One additional note should be made with respect to repeatability of these results. After reducing the data for Runs 9 (dye) and 10 (hydrogen bubble) it was discovered that the values for  $\tau_p$ ,  $X_p$  and therefore  $Re_T$  and  $Re_j$  were nearly the same. One would hope therefore, that the trajectories of the two vortex rings would be close to one another. Indeed, as is shown in Fig. 4-8, when plotted one on top of the other there is very little difference between the two. This observation gives us confidence in the stability of our experimental procedure.

### 4-3.3 Vortex Ring Radius and Thickness

Along with the trajectory, the radii  $R$  and  $R'$  and the thickness  $T$  of the vortex rings were measured. Radial values were corrected for refraction from the calculations presented in Fig. 4-5. Values of  $R'$  and  $T$  were obtained from the vortex rings visualized with dye, and  $R$  from those visualized with hydrogen bubbles. Accurate values of  $R$  were also obtained from dye visualization measurements in Runs 13 and

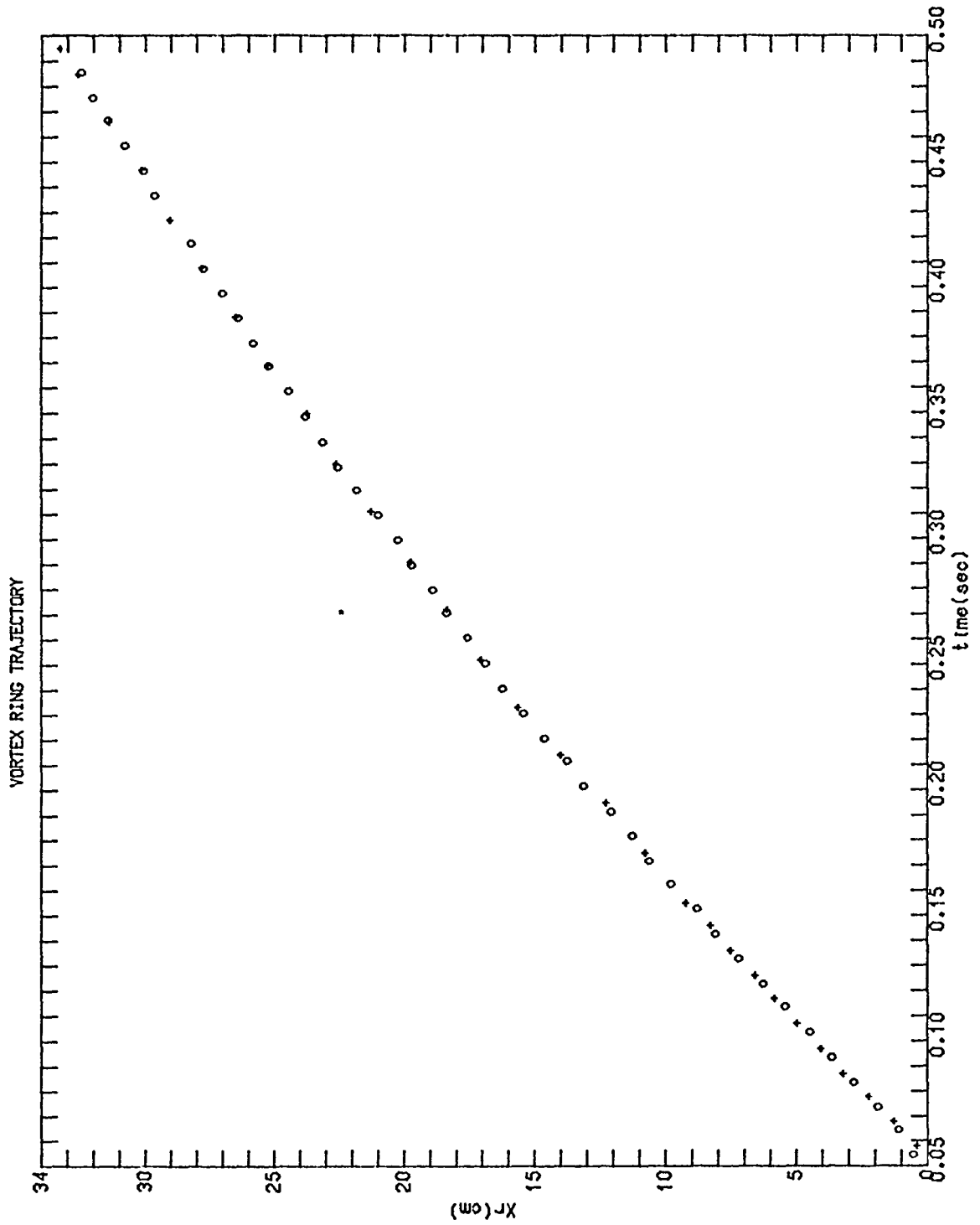


FIGURE 4-8

Repeatability: comparison in trajectory  
between Runs 9 and 10

circle: run 9  
cross: run 10

15, and fairly accurate values in Run 14. With these runs clear water, which was entrained upon formation of the vortex ring, marked the center of the core.

The volume of the vortex ring was computed from  $T$  and  $R'$  using the formula for an ellipsoid,

$$V = \frac{4}{3} \pi R'^2 T \quad (4-6)$$

in order to compare with the volume of fluid ejected from the orifice  $V_{ej}$ .

The ratios  $R'/\rho_0$ ,  $R/\rho_0$ ,  $T/\rho_0$ ,  $V/V_{ej}$ , and  $T/R'$  were computed and plotted as a function of time for each run. These plots are given also in Appendix A, Figs. A-1 through A-26. The mean of  $R'/\rho_0$  and  $T/R'$  are approximated with straight lines calculated by a least squares fit.

Using these plots together with the traced images of the vortex rings, a formation time is determined for each run. The vortex ring is estimated to have completed its initial formation process and to be independent of the ejection at this time. A list of these initial times  $t_0$  and the resulting initial ring Reynolds numbers for each run is given in Table B-1 of Appendix B.

#### 4-4 DISCUSSION

##### 4-4.1 Reynolds Number Dependence

It was found that the three classes of vortex rings which are identified by the time dependent form of velocity can be grouped by Reynolds number. In Section 2-3.2 we pointed out that the velocity of a vortex ring is directly proportional to the strength and inversely proportional to the radius of the vortex ring. That is,

$$\Gamma \sim UR \quad (4-7)$$

A change in velocity, therefore, is an indication of changes in the total circulation of the vortex ring which result from diffusion of vorticity from the core and convection into the wake.

HIGH REYNOLDS NUMBERS. The vortex rings at very high Reynolds numbers are found to be dominated by small scale turbulent motions. Qualitative observations of these rings suggest that vorticity is constantly being ejected from the vortex ring into a rather heavy wake, apparently a result of turbulent diffusion from the core (see photograph in Fig. 3-4 and drawing in Fig. 2-7b). This being the case, one would expect from Eq. (4-7) a decrease in velocity consistent with a rapid loss of strength from turbulent diffusion and convection of vorticity.

From the trajectory plots we find that for  $Re_R \sim 20000 - 30000$  and above the decrease in vortex ring velocity goes inversely with time. From Eq. (4-5a),  $U = A_n/t$ .  $A_n$  increases from one regime to the next, suggesting a possible increase in velocity; however, the slope analysis indicates that the velocity at best remains constant during this short transitional period, and might decrease slightly.

Both Maxworthy [34] and Krutzsch [28] have reported a  $1/t$  velocity dependence for vortex rings at high Reynolds numbers, as well as a transitional period where the velocity rapidly changes. Their data, however, indicates a decrease in the slope  $A_n$  rather than an increase. The reason for the discrepancy is unclear.

LOW REYNOLDS NUMBERS. At the opposite extreme are the vortex rings at very low Reynolds numbers which are dominated by viscosity. The observance of a laminar wake suggests a loss of vorticity from the vortex ring resulting from viscous diffusion of vorticity from the core and convection into the wake. We would expect, therefore, a decrease in total circulation and velocity consistent with the much slower process of molecular diffusion.

Our experimental results indicate that for  $Re_R \sim 1000 - 2000$  and

below, a much less rapid decrease in velocity is observed. From Eq. (4-5c):

$$U \sim \frac{1}{t^{\alpha_n}} \quad (4-5c)$$

where  $\alpha_n$  increases from one regime to the next and has values  $\sim 0.13$  to  $0.27$ . This result is consistent with the models for viscous vortex rings discussed in Section 2-4.2. For the extreme of a thin, viscous core of vorticity the velocity decreases more slowly than (4-5c), like  $-\ln t$ . On the other hand, in the asymptotic limit of large times, when the core has the maximum thickness possible, the velocity decrease is more rapid than (4-5c), like  $t^{-3/2}$ . The measured rate of velocity decrease is consistent with these models since the size of the core for experimentally produced vortex rings is generally somewhere between these two mathematical extremes. It is interesting that both the asymptotic and the measured velocities have a power law form. The observation that  $\alpha_n$  increases from one regime to the next might suggest that for large times  $\alpha_n \rightarrow 3/2$ .

INTERMEDIATE REYNOLDS NUMBERS. We have found that for a very wide range of Reynolds numbers  $Re_R \sim 2000$  to  $20000$ , the vortex rings propagate through regimes of constant velocity. That is,

$$U = B_n$$

where  $B_n$  decreases from one regime to the next. These vortex rings tend to be well formed with little or no apparent wake, indicating little loss of vorticity from the ring, and therefore little change in ring strength; an example is shown in the photograph just before the abstract. Whereas the vortex rings at high Reynolds numbers are very turbulent in character, and those at low Reynolds numbers are viscous, the vortex rings in the intermediate Reynolds number range exhibit a basically inviscid character. It appears that the Reynolds number is high enough for these rings that viscosity is not important, yet low

enough that turbulence has not developed.

#### 4-4.2 Periods of Rapid Change: Instabilities

Between each regime is a short period of rapid change in velocity, suggesting sudden changes in the structure of the vortex ring. It is natural to suspect that these sudden changes in velocity are related in some way to the development of instabilities along the vortex core. There is some evidence to support this view.

Waves along the vortex core result in oscillations in the measured vortex ring radius about a mean (see figures in Appendix A). It is reasonable to suppose that a breakdown in the structure of the core, say by the breaking of unstable waves [36], would manifest itself as unusually large oscillations, or a sudden change in the ring radius. As the core reorganizes from such a breakdown, finite amounts, or chunks, of vortical fluid might be ripped from the core, convected to the outermost region of the vortex ring, and finally deposited into a wake. Such a sudden loss of a finite amount of vorticity would result in a sudden loss of circulation, and therefore a rapid decrease in ring velocity. We might also expect that as a vortical chunk is convected around the core it would eventually show up as a bulge in the outermost dyed streamline, moving around the vortex ring into the wake--at some time later than the occurrence of the decrease in velocity.

Bulges following the pattern just described have been observed in several of our vortex rings, resulting in an increase in  $R'$  as the bulge moves around the ring into the wake (see, for example, Fig. A-14b, Appendix A). Likewise, one can observe in the data large oscillations and sudden increases in  $R$  and  $R'$  at times which appear to be correlated with the periods of rapid velocity change. From the hydrogen bubble visualizations one observes as well periods where the vortex core suddenly contorts into an S shape.

In order to test for a possible correlation, all of these

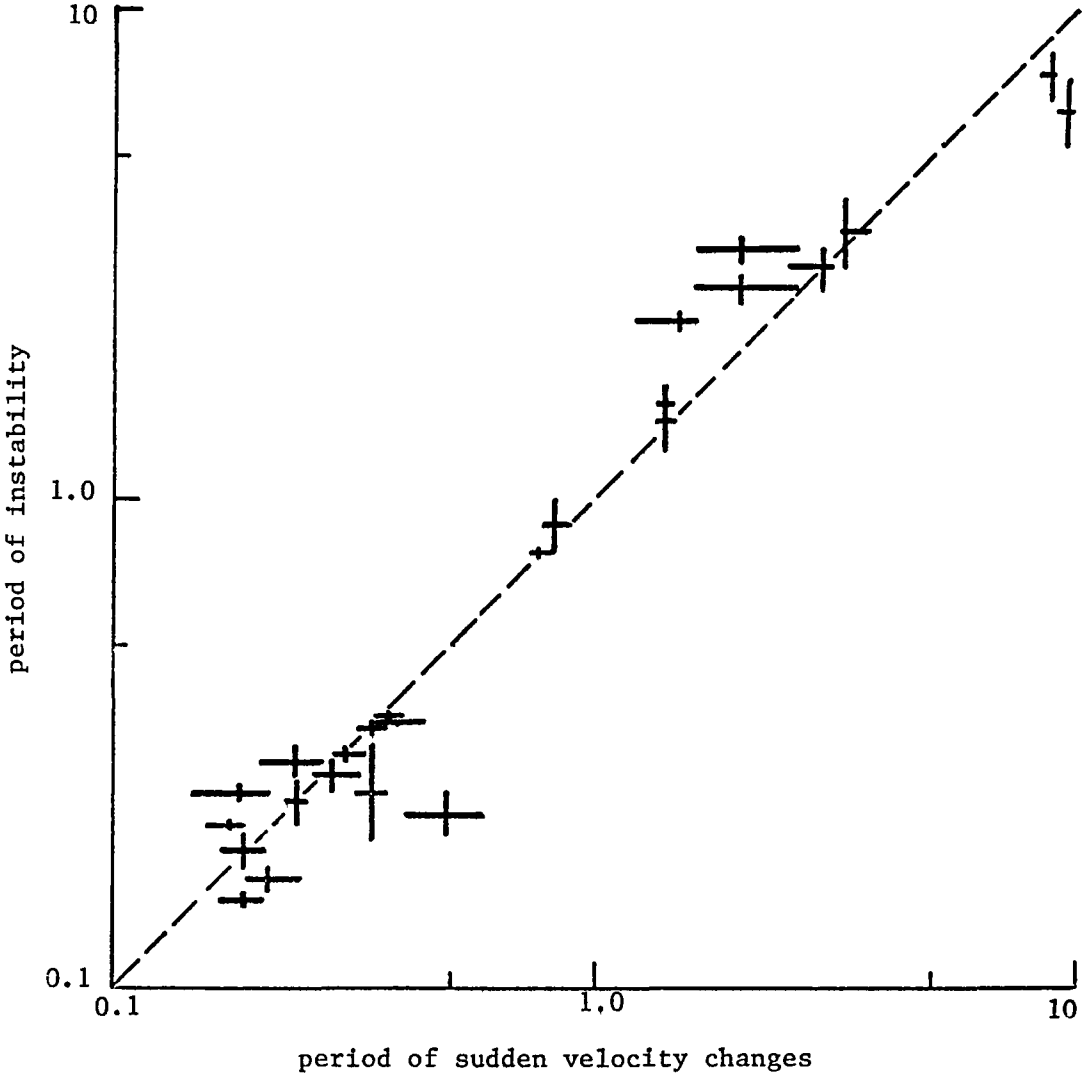


FIGURE 4-9  
Correlation of sudden velocity changes  
with instabilities.

periods of apparent instability were recorded and plotted against the nearest period of sudden change in vortex ring velocity. This plot is shown in Fig. 4-9. Many of the regions of instability correlate well with the regions of sudden velocity change. There is certainly a suggestion that the sudden changes in the velocity of the vortex ring are related in some way to the development of instabilities along the vortex core.

#### 4-4.3 Additional Observations

In several runs other observations were made which should be noted.

ROCKING INSTABILITY. We discussed in Section 4-2 the transitional Reynolds numbers which appear to be characterized in part by the occurrence of unusually large-amplitude oscillations. An example is the vortex ring of Run 5, representing a transition between the high Reynolds number, turbulent vortex rings, and the intermediate Reynolds number, inviscid vortex rings. This vortex ring was basically turbulent in character, but exhibited an interesting oscillation. From hydrogen bubble visualizations, we observe that early in its life the vortex core suddenly became contorted, marking the initiation of a two cycle oscillation, or rocking motion, as indicated schematically in Fig. 4-10. Although the vortex ring traveled straight up the tube it oscillated through two changes in orientation. Accompanying these changes, the radius of the vortex ring was observed to increase and then decrease (see Fig. A-5b). Since  $U \sim D/R$  we observe as well an increase and decrease in the mean velocity of the vortex ring around the general  $1/t$  decrease characteristic of turbulent rings. This large amplitude oscillation in the mean velocity is shown in Fig. 4-11. The points represent the velocity computed directly between data values, and the solid curve is the  $1/t$  dependence about which the data points oscillate. The

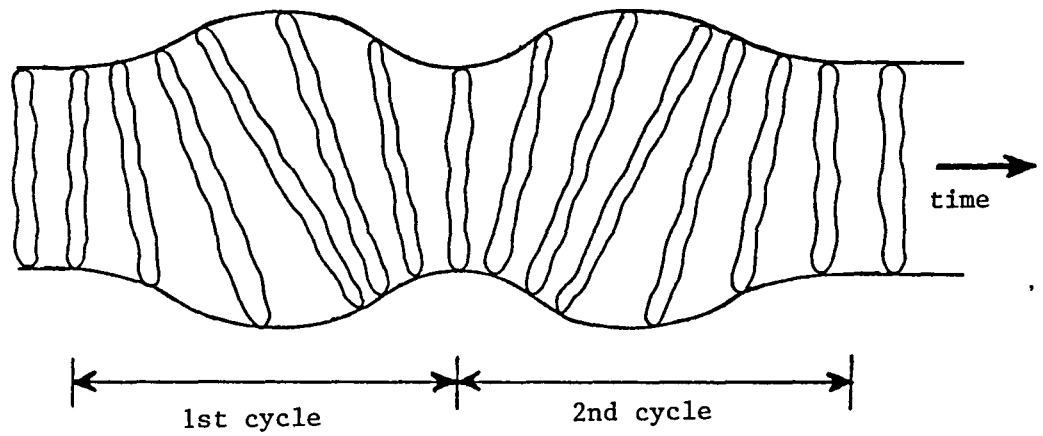


FIGURE 4-10

The rocking oscillation observed in Run 5.  
The change in radius has been exaggerated for  
clarity.

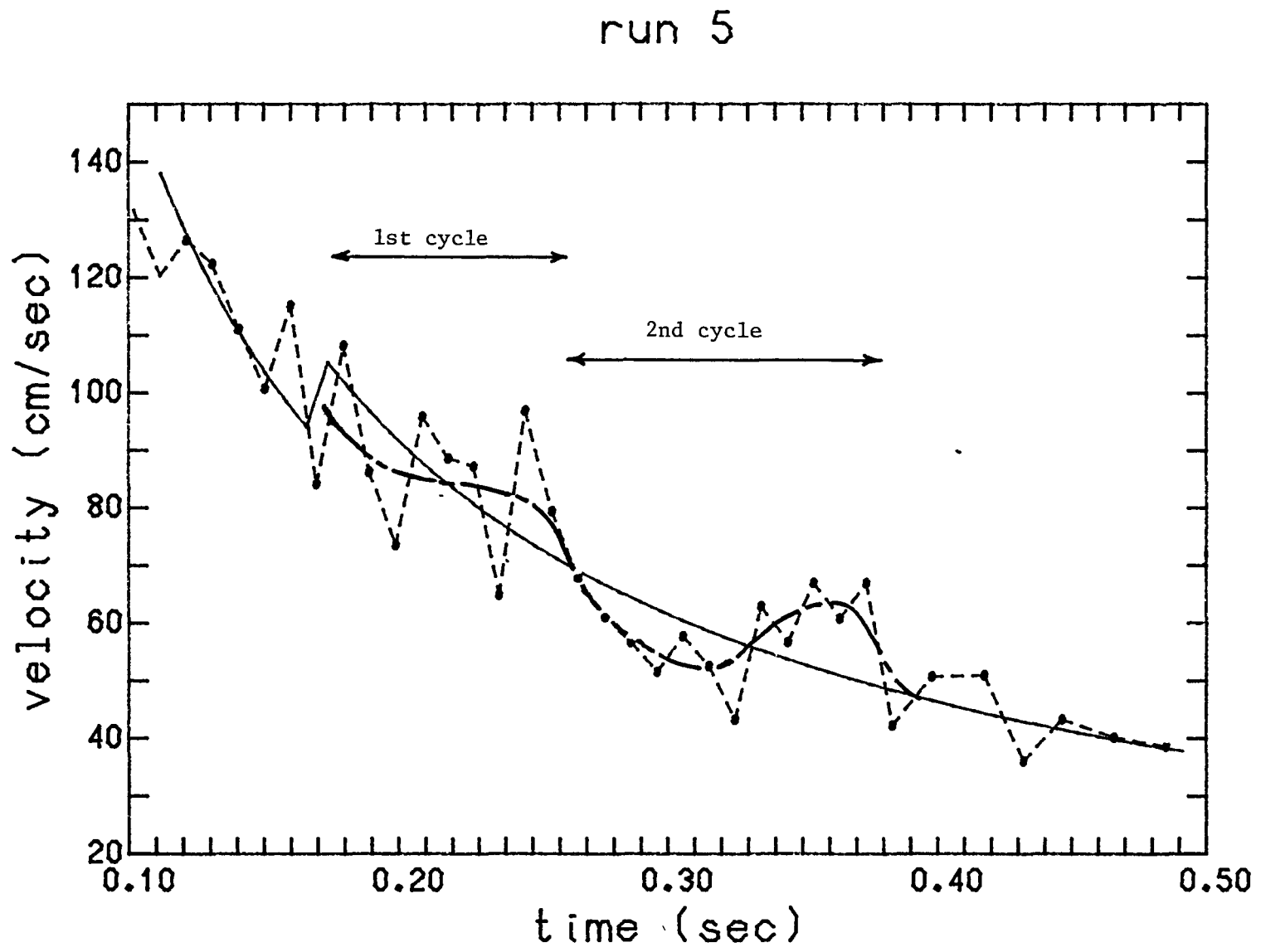


FIGURE 4-11

Rocking Oscillation: velocity plot for Run 5

two-cycle oscillation in velocity shows up as smooth, large-amplitude deviations from the mean trajectory curve of Fig. A-5a.

TURBULENCE IN THE AMBIENT FLUID. In general, the 26 runs for which data was reduced were chosen from sequences where motions in the ambient fluid were minimal. Run 8, however, was chosen because the turbulence level in the water through which the ring would propagate was obviously quite high. Since Run number 7 has nearly the same initial conditions as Run 8, the two trajectories are compared in Fig. A-8. Initially the trajectories coincide, but as the vortex ring of Run 8 enters the turbulent region, it abruptly slows down. The sudden increase in the turbulence level (or in the turbulent viscosity) apparently results in a very rapid increase in turbulent diffusion, and in the loss of vorticity from the vortex ring. The subsequent decrease in strength and impulse, then, appears as a rapid decrease in the velocity of the vortex ring.

VISCOUS INTERACTION WITH THE TUBE WALL. In Section 4-2 we discussed the interaction of vortex rings with the tube wall for cases where the ring Reynolds number is high enough that upon contact with the tube wall, the vortex ring rapidly breaks down into a turbulent mass of fluid. When the Reynolds number is very low, however, changes in ring structure can come about only through molecular motions.

Such was the case with Run 24. After formation the vortex ring is observed to move towards the tube wall. Upon contact, the core of the vortex ring nearest the tube wall is observed to grow very large in size, apparently a result of viscous production of vorticity at the tube wall which is of opposite sign to that in the core. In this run, however, the vortex ring did not completely break down at the tube wall, but reformed and proceeded to move towards the opposite side of the tube.

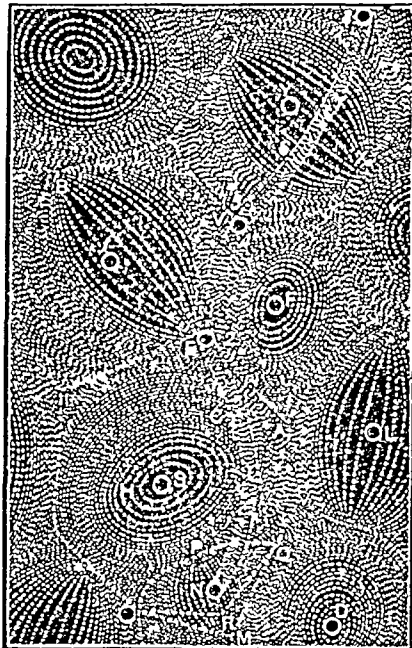
Especially significant is that in both the period before the vortex ring made contact with the wall, and after it reformed and

moved towards the opposite wall, the velocity exhibited a power law time dependence (see Fig. A-24). This observation lends support to the supposition that a power law is characteristic of the velocity of vortex rings at very low Reynolds numbers, and therefore characteristic of the rate of loss of circulation due to viscous diffusion. In addition, since this vortex ring clearly went through a breakdown and reformation process as it interacted with the tube wall, we might conclude that the rapid changes in vortex ring velocity observed in general between regimes are also due to a breakdown and reformation of the structure of the vortex ring.

IRREGULAR OCCLUSION. Along similar lines are the results for a turbulent vortex ring formed from a very irregular orifice (Run 26). With application to arterial stenoses (see Section 5-4), clay was applied to the tube wall around an orifice, creating an extremely irregular occlusion. The jet Reynolds number was  $\sim 44900$ ; a turbulent, incoherent vortex ring was observed to travel up the tube and collide with the tube wall always at the same location. As shown in Fig. A-26, even for this very irregular vortex ring a  $1/t$  dependence in velocity is observed with a sudden change in speed at one, and possible two points in its evolution. This lends support to a  $1/t$  dependence in velocity as characteristic of vortex rings which are dominated by turbulent diffusion.

# 5

## Combination of Theory with Experiment



*Descartes' Vortex System*

### 5-1 TOTAL CIRCULATION AS A FUNCTION OF TIME

In Chapter 3 we developed the mathematics to kinematically relate the total circulation of a vortex ring in a tube to its speed, size, and shape. In this chapter we use these kinematic relationships to compute the total circulation as a function of time for our experimentally produced vortex rings. The concepts behind this calculation are discussed at length in Section 2-5.

COMPUTATION. The basic kinematic relationships were derived in Section 3-4.1, where we related the following non-dimensional parameters:

$$\hat{U} = \frac{U}{\Gamma/4\pi R}, \quad \varepsilon = \frac{R}{\rho_0}, \quad \text{and} \quad \frac{R'}{R} \quad \text{or} \quad \frac{T}{R} \quad (5-1)$$

$\hat{U}$  is further divided into  $\hat{U}_0 - \hat{U}_1$ , the velocity of the vortex ring if it were in an unbounded flow less the velocity induced by the presence of the tube.  $\hat{U}_1$ , a function only of  $\varepsilon$ , is given by Eq. (3-32).  $\hat{U}_0$  is parameterized using the core parameter  $a/R$  as defined by the modified Kelvin/Lamb formula\*:

$$\hat{U}_0 = \ln \frac{8R}{a} - \frac{1}{3} \quad (5-2)$$

\*For a detailed description of the use of  $a/R$  see Section 3-4.1.

Since the relationships among the parameters in (5-1) were computed totally from kinematic considerations, they apply at any instant in time where the shape of a vortex ring is well represented by concentrating its total circulation along a circular filament. As we discussed in Section 2-5, such a representation involves two approximations. The first, concerning the effect of a finite core on the shape of a vortex ring, was addressed in Section 3-4.2, and the second, which concerns the effect of a wake, will be discussed in Section 5-2.1.

Because when using dye visualizations, measurements of  $R'$  are generally more accurate than measurements of  $R$ , we recast the relationships involving  $R$  into more useful relationships involving  $R'$ . In Figs. 3-11 and 3-12 are shown the calculations for  $T/R$  and  $R'/R$  as a function of  $a/R$  for different values of  $\epsilon$ . Combining these calculations we compute  $T/R'$  as a function of  $R'/\rho_0$  for different values of  $a/R$ , as shown in Fig. 5-1.  $R'/\rho_0 = 0$  corresponds to the unbounded vortex ring. As we noted earlier, we see that the thickness (and volume) of a vortex ring increases with increasing  $a/R$ , or decreasing velocity; for  $R'/\rho_0 \lesssim 0.4$  there is relatively little influence from the tube wall on the shape of the vortex ring.

The calculations represented by Figs. 5-1 and 3-12 are in a form suitable for calculating the total circulation from flow visualization measurements. At any instant in time, we compute  $\Gamma$  as follows:

1. A flow visualization measurement of  $T/R'$  and  $R'/\rho_0$  defines a point on Fig. 5-1.  $a/R$  is determined by interpolating between the constant  $a/R$  curves.
2. Knowing  $a/R$  and  $R'/\rho_0$ ,  $\epsilon$  is determined from the calculations which led to Fig. 3-12.
3. Knowing  $a/R$  and  $\epsilon$ ,  $\hat{U}_0$  is calculated from Eq. (5-2) and  $\hat{U}_1$  from Eq. (3-32). Subtracting the two we find  $\hat{U}$ .
4. Having computed  $\hat{U}$  and  $R (= \epsilon \rho_0)$ , we see from Eq. (5-1) that a flow visualization measurement of  $U$  yields the total circulation,  $\Gamma$ .

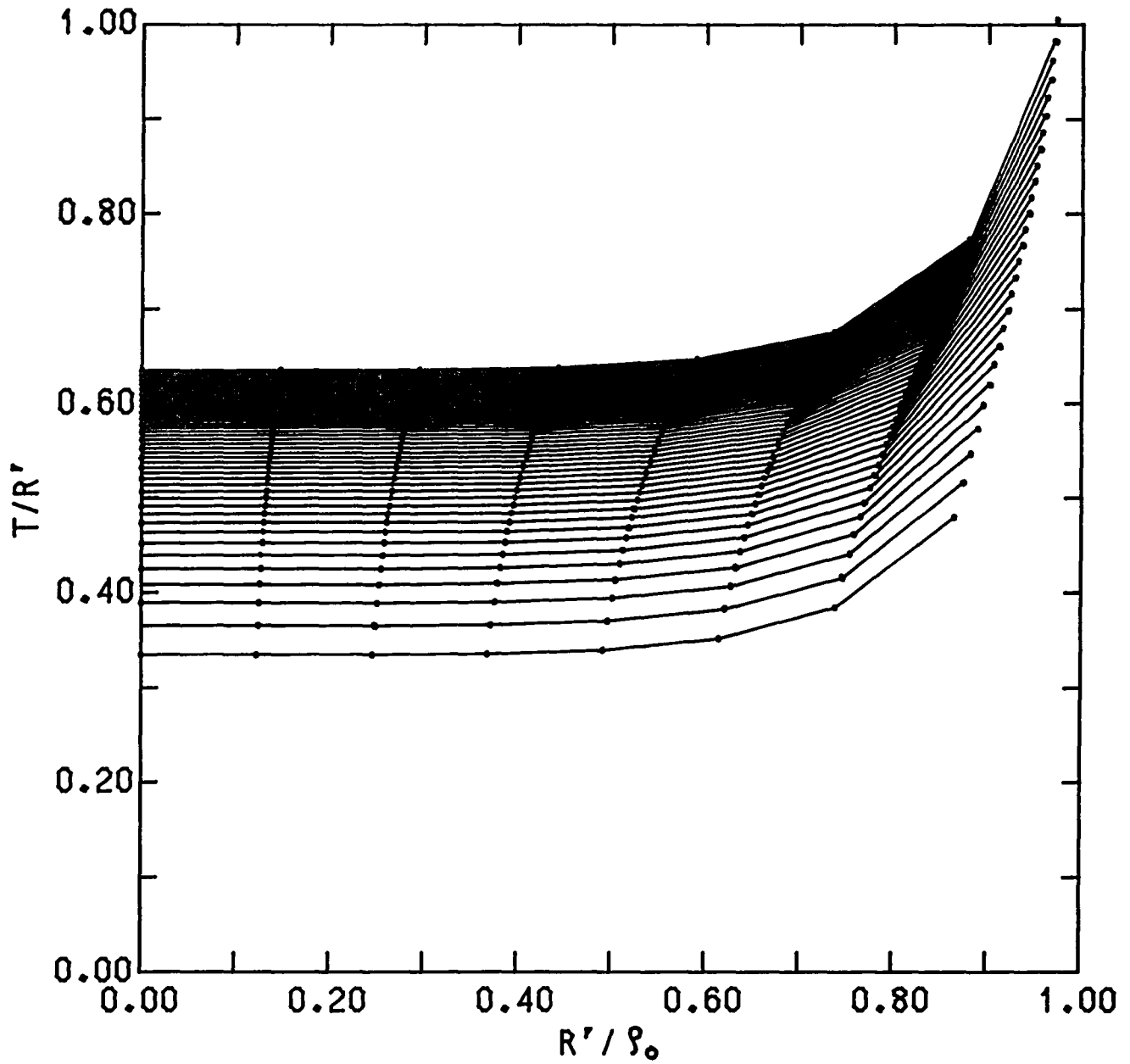


FIGURE 5-1

The variation of  $T/R'$  with  $R'/\rho_0$  for different values of  $\hat{U}_0$ .

Beginning with the lowest curve,  $a/R = 0.04, 0.05, \dots, 0.50$

We have calculated not only the strength of the vortex ring, but also its radius,  $R$  from measurements of  $R'$ ,  $T$ , and  $U$ . This algorithm is used with our flow visualization measurements to compute the change in total circulation as the vortex rings travel up the tube.

As discussed in the last chapter, the trajectory, radius, and thickness of our experimentally produced vortex rings are well represented by a mean motion plus oscillations about the mean which result from instabilities and waves along the vortex core. Since it is the mean motion with which we are interested, smooth curves are passed through the data to compute  $\Gamma$ .

The analysis of the mean trajectory was discussed in the last chapter. We discovered the existence of regimes for all our vortex rings, where the time dependent form of the velocity is given by Eqs. (4-5). The vortex ring strength is computed using the values within each regime as given in Table A-2. A discontinuity in  $\Gamma$  will therefore occur at the (artificial) points of discontinuity in velocity between regimes.

A least squares fit to straight line segments is used as well to approximate the mean values of  $R'/\rho_0$  and  $T/R'$ . As shown in Appendix A by the dashed curves, in most cases a straight line is a reasonable fit to the data. As a result, however, small discontinuities are necessarily inserted into the calculation for  $\Gamma$ .

**RESULTS.** The total circulation is calculated as a function of time for 17 runs in which the initial ring Reynolds number  $Re_R$  ranged from 690 to 50'00. These results, plotted along with the velocity of the vortex ring for comparison, are presented in Appendix B, Figs. B-1 through B-17. The velocity is indicated with dashed curves, the circulation with solid curves. In order to compare the velocity and strength in a reasonable way, the scales are adjusted so that each tick mark represents roughly 10% of the mean value.

It should be remembered that the mean values of the vortex ring data have been fitted with piecewise smooth functions, so that

discontinuities result in the plots of velocity and strength. In reality, of course, these changes occur smoothly, although over a short period of time. Using the least squares analysis as a guide, approximate transitions over these short periods have been indicated with smooth, dotted curves.

FORMATION. As we expect from Eq. (4-7) and as discussed in Section 4-4.1, in most cases the strength of a vortex ring as it propagates up the tube follows the velocity of the vortex ring. However, some differences are apparent. In many cases, even though the velocity is constant or decreasing at the beginning of a run, the strength is increasing. Careful examination of the plots in Appendix A and the original outlines made from the movies indicates that the vortex ring is forming during this period and vorticity is still being concentrated in the core. Thus, the strength of the ring increases during this formation process as suggested by the plots.

UNCERTAINTY. The uncertainty in these plots is very difficult to assess. In order to get a feel for the extent of the oscillations about the mean, the velocity and strength were computed and plotted point by point. This involves the calculation of derivatives by taking differences between data points, resulting in deviations from the mean which are very large and unrealistic. Indeed, this is perhaps the primary reason for fitting the vortex ring trajectory with a smooth curve before taking derivatives to compute the ring velocity. Calculating the velocity and strength between every two data points, however, provides a check for the calculations in which mean values of the vortex ring parameters are used.

An example calculation is shown in Fig. 5-2 for Run 1. The points and dashed lines represent the values computed directly from the data, and the solid curve represents the mean computed by fitting the data with piecewise smooth curves. We see from Fig. 5-2 that the transition region, which appears as a discontinuity when the mean

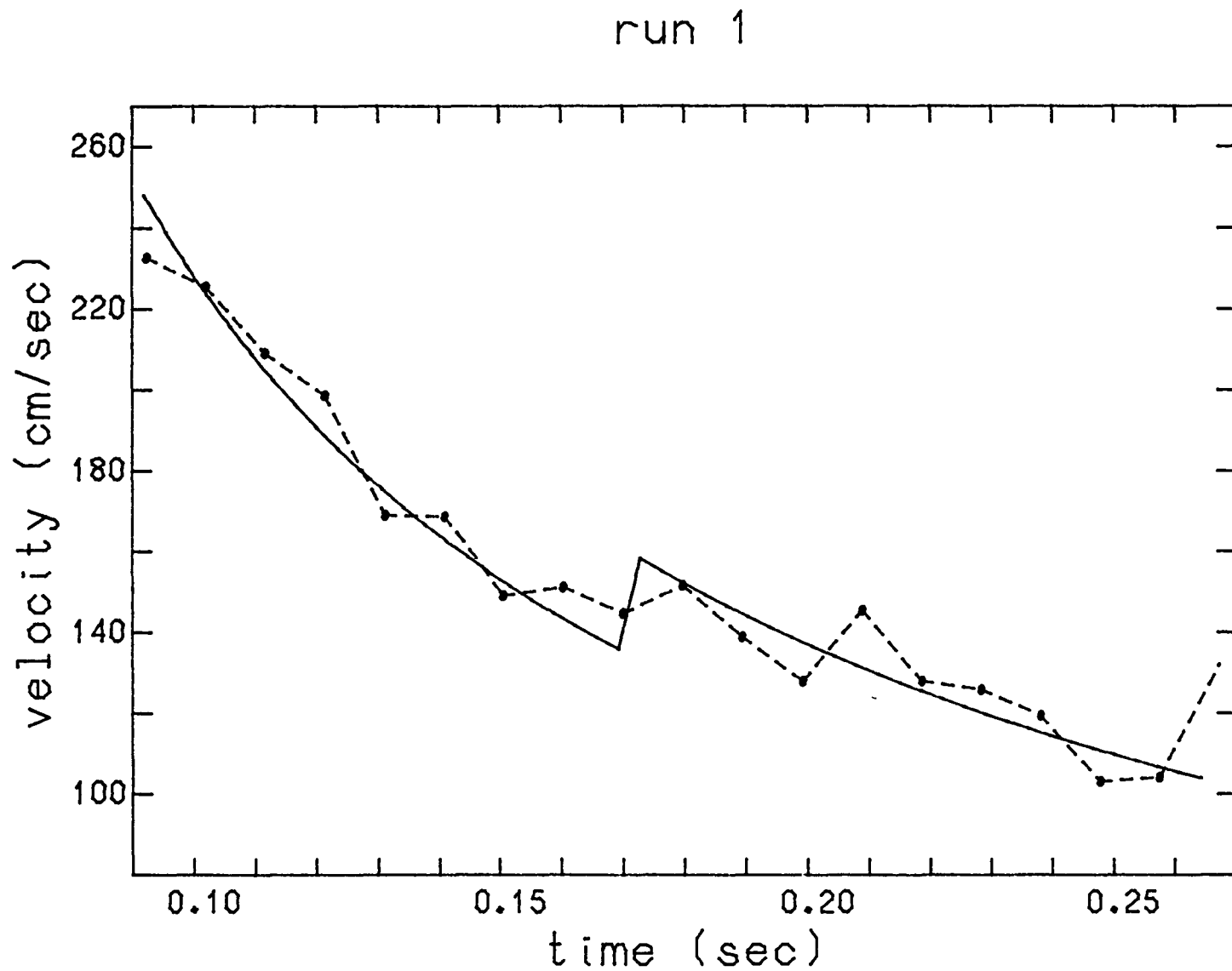


FIGURE 5-2

Comparison of mean velocity and strength with point by point calculations for Run 1. (a) velocity

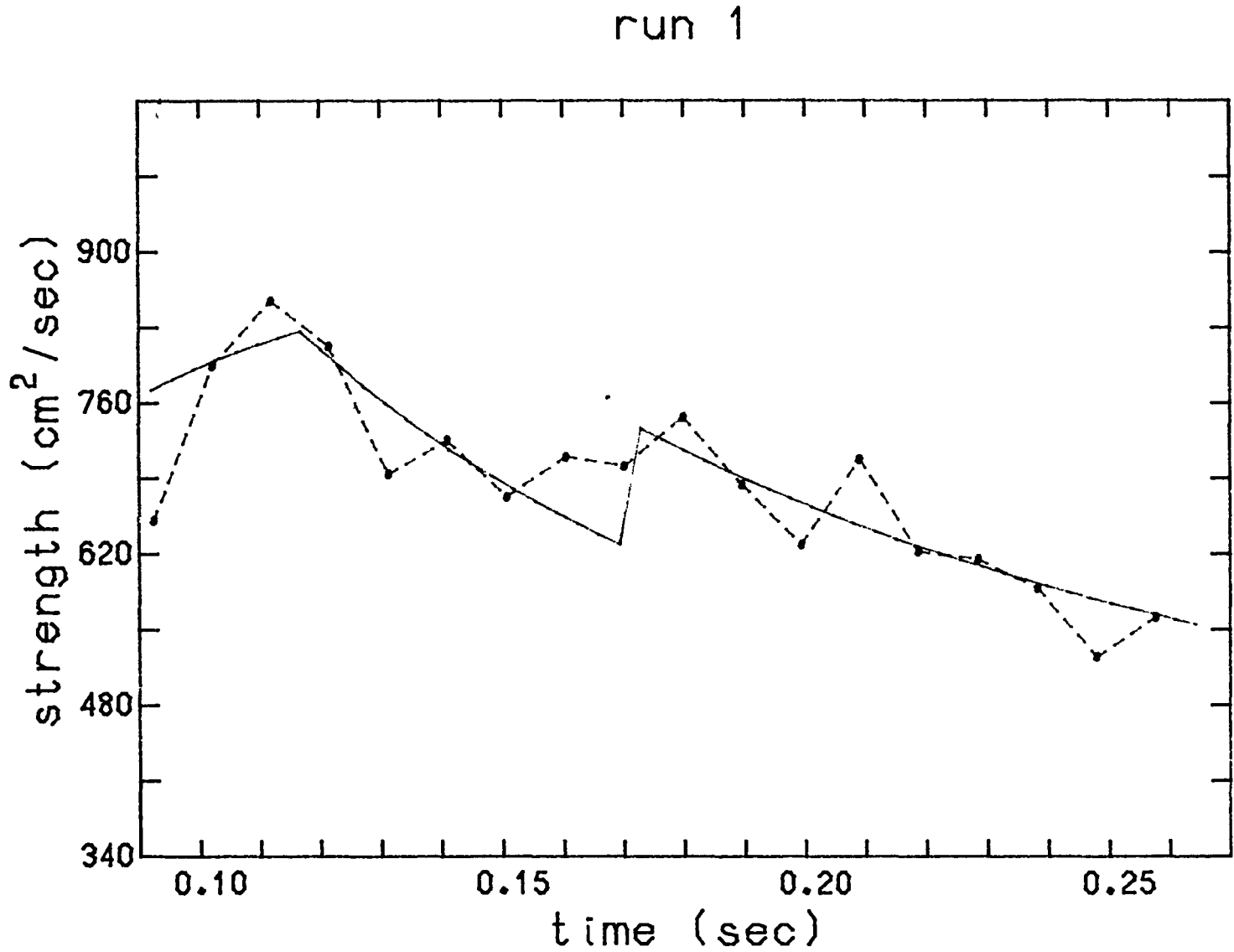


FIGURE 5-2

Comparison of mean velocity and strength with point by point calculations for Run 1. (b) strength

curves are used, is shown as a smooth but rapid change when the velocity and strength are computed point by point.

## 5-2 ACCURACY OF THE COMPUTATION METHOD

### 5-2.1 The Effect of Wake Vorticity on Ring Shape

The kinematic model which is used to compute the circulation is based on two approximations (Section 2-5). The effect of a finite core on the shape of a vortex ring was assessed in Section 3-4.2 and found to be of little consequence. We have yet to assess the importance of vorticity in the wake on the shape of a vortex ring.

Clearly any such effect will be most important for the rings with the heaviest wakes, so we consider the experimentally produced vortex rings which have the highest (Run 1) and lowest (Run 25) Reynolds numbers. Taking the difference of the initial and final strengths from Figs. B-1 and B-17, and dividing by the distance the vortex ring has traveled, we find that for Run 1 the average strength per unit length is  $\sim 12.3 \text{ cm}^2/\text{sec}/\text{cm}$  and for Run 25  $\sim 0.15 \text{ cm}^2/\text{sec}/\text{cm}$ . If we now divide by the average total circulation of each vortex ring we find that, on the average:

$$\frac{\text{strength in 1 cm. of wake}}{\text{strength of vortex ring}} = \begin{cases} 0.018 & \text{Run 1} \\ 0.013 & \text{Run 25} \end{cases}$$

That is, for the highest Reynolds number ring there is about 1.8% of the total circulation in 1 cm. of wake and about 1.3% for the vortex ring at the lowest Reynolds number. We therefore use Run 1, the worst case, to test the influence of a wake on vortex ring shape.

We consider the same parameters which were used to test the effect of a finite core:  $\epsilon = 0.40$  and  $a/R = 0.25$ . From the movies we observe that trailing vorticity tends to be distributed in a region

about half the radius of the vortex ring. In order to model the wake, then, we distribute the vorticity within this region behind the vortex ring over two rows of circular vortex filaments. The strength of each filament is weighted as estimated for Run 1. Using the linearity of the Biot-Savart law, the streamline field is computed by summing the individual fields of the vortex elements.

The streamlines for the vortex ring with and without a wake are given in Fig. 5-3. The vortex elements which model the wake are indicated with dots. The effect of the wake is to distort the streamlines behind the vortex ring and to cause a slight asymmetry about the  $z = 0$  plane in the shape of the vortex ring. As is shown in Fig. 5-3c, the rear end of the ring is drawn out slightly resulting in a slightly thicker vortex ring.

The difference in thickness due to the presence of the wake, as compared with a wakeless vortex ring, is about 3%. This is well within the precision of the experimental measurements. Furthermore we have chosen a vortex ring with a heavy wake so that for other rings the effect is probably not even as great. We therefore conclude that the effect of the wake is negligible for typical vortex rings, and the size and shape can be accurately predicted by concentrating the total circulation of a vortex ring along a circle.

### 5-2.2 Comparisons with Measured and Estimated Values

We would like to test the accuracy of this method with other methods for computing the total circulation of a vortex ring. To do this it is necessary to have both flow visualization measurements of  $T$ ,  $R'$ , and  $U$  as well as an independent calculation for  $\Gamma$ .

MEASUREMENT. Sullivan *et al.* [60] have measured  $\Gamma$ ,  $U$ ,  $R$ , and  $a/R$  using a laser doppler velocimeter (LDV) for two vortex rings produced in air at different Reynolds numbers. They include a photograph for one vortex ring, that with the lower value of Reynolds

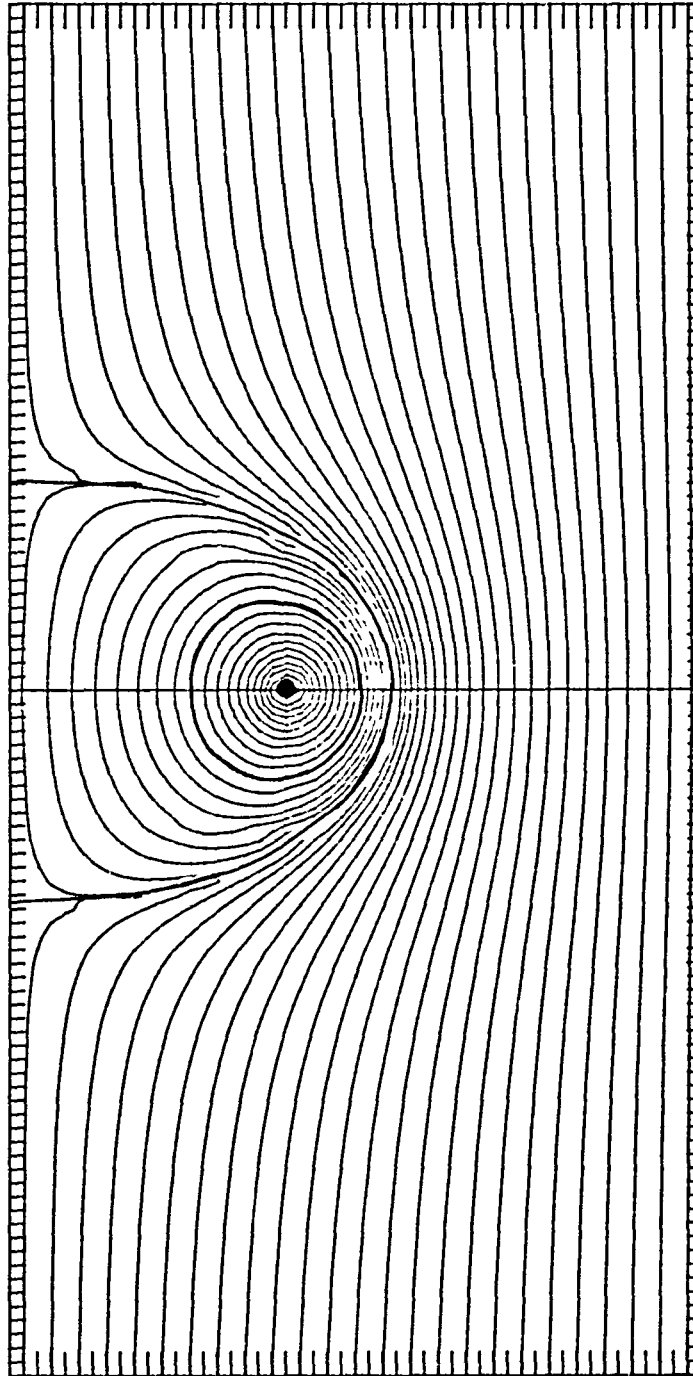


FIGURE 5-3

The streamlines for a vortex ring with a wake compared with a wakeless vortex ring.

a) The wakeless vortex ring.

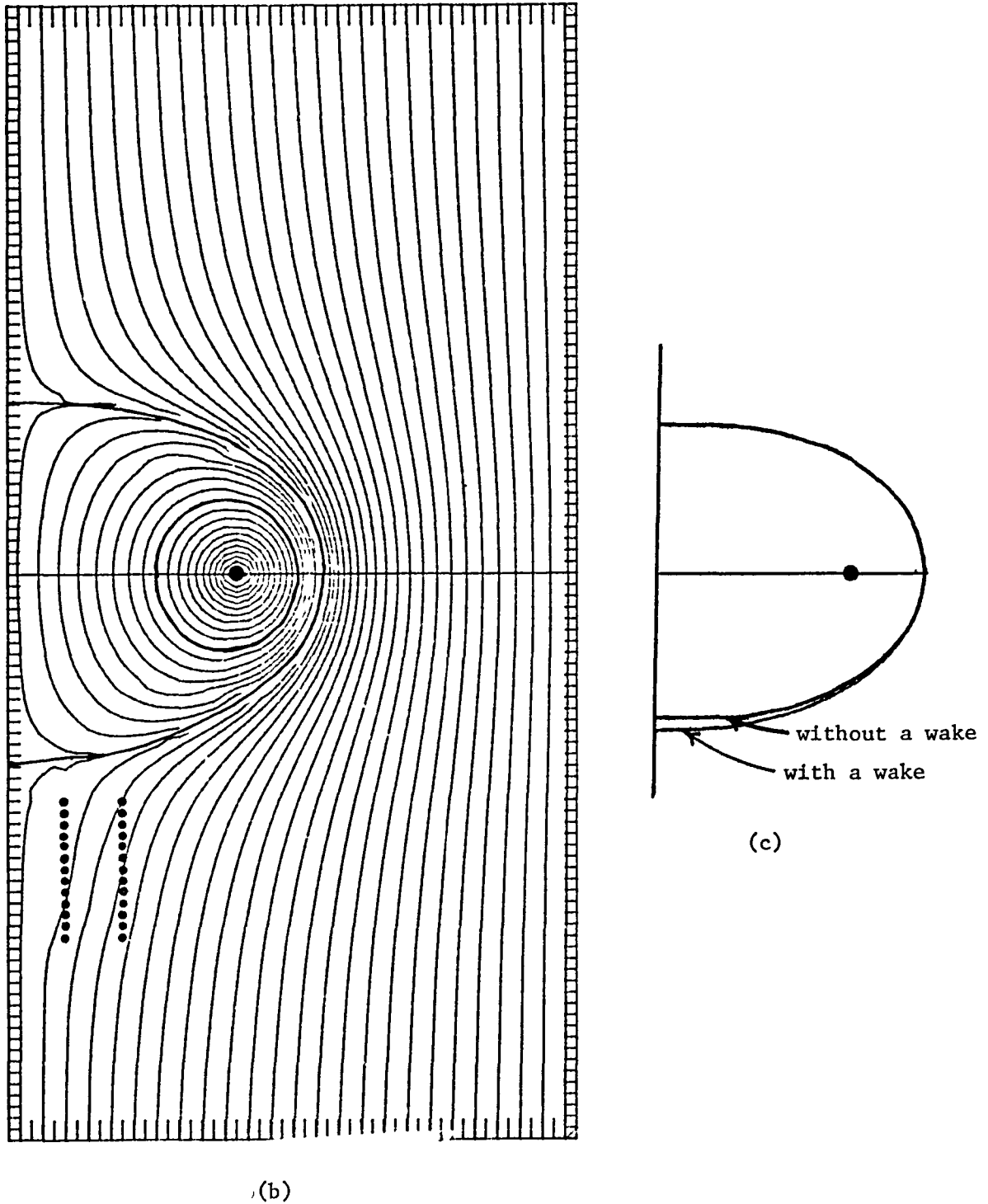


FIGURE 5-3

The streamlines for a vortex ring with a wake compared with a wakeless vortex ring.

b) The vortex ring with a wake.

c) Comparison of outermost closed streamlines.

number ( $Re_R = 3040$ ,  $Re_\Gamma = 7780$ ), thus allowing comparison with our method. Measurements with the LDV require the repeatable production of vortex rings, so the photograph is only one of many rings measured. By integrating the measured velocities around the core, they calculated a total circulation of  $1124 \text{ cm}^2/\text{sec}$ . Using the photograph to measure  $T$  and  $R'$  and their measurement for  $U$  we calculate with our method a total circulation of  $1135 \pm 60 \text{ cm}^2/\text{sec}$ .

ESTIMATES. The initial strength of our experimentally produced vortex rings can be approximated by relating the total circulation of the fluid ejected by the piston to the jet velocity and orifice size. If you consider a slug of fluid of length  $L$  ejected from the orifice with velocity  $u_j(z)$  the total circulation content of the ejected fluid is given by\*:

$$\Gamma_{ej} = \int_0^L u_j dz \quad (5-3)$$

The total circulation of a newly formed vortex ring is therefore approximately given by

$$\Gamma(t_0) = \frac{V(t_0)}{V_{ej}} \Gamma_{ej} \quad (5-4)$$

where  $V(t_0)$  is the initial volume of the vortex ring and  $V_{ej}$  is the volume of fluid ejected from the orifice. Using these expressions, the initial strengths of our vortex rings were estimated and compared with our calculated values.

In Fig. 5-4 are shown the comparisons between the values of total circulation calculated using the kinematic theory, and the values measured by Sullivan et al. and estimated from Eq. (5-4). The comparison is felt to be excellent.

---

\*This expression, which is straightforward to derive, agrees with that used by Saffman (55) to estimate the initial circulation of vortex rings. Maxworthy (36), however, includes a factor of  $1/2$  for reasons which are unclear.

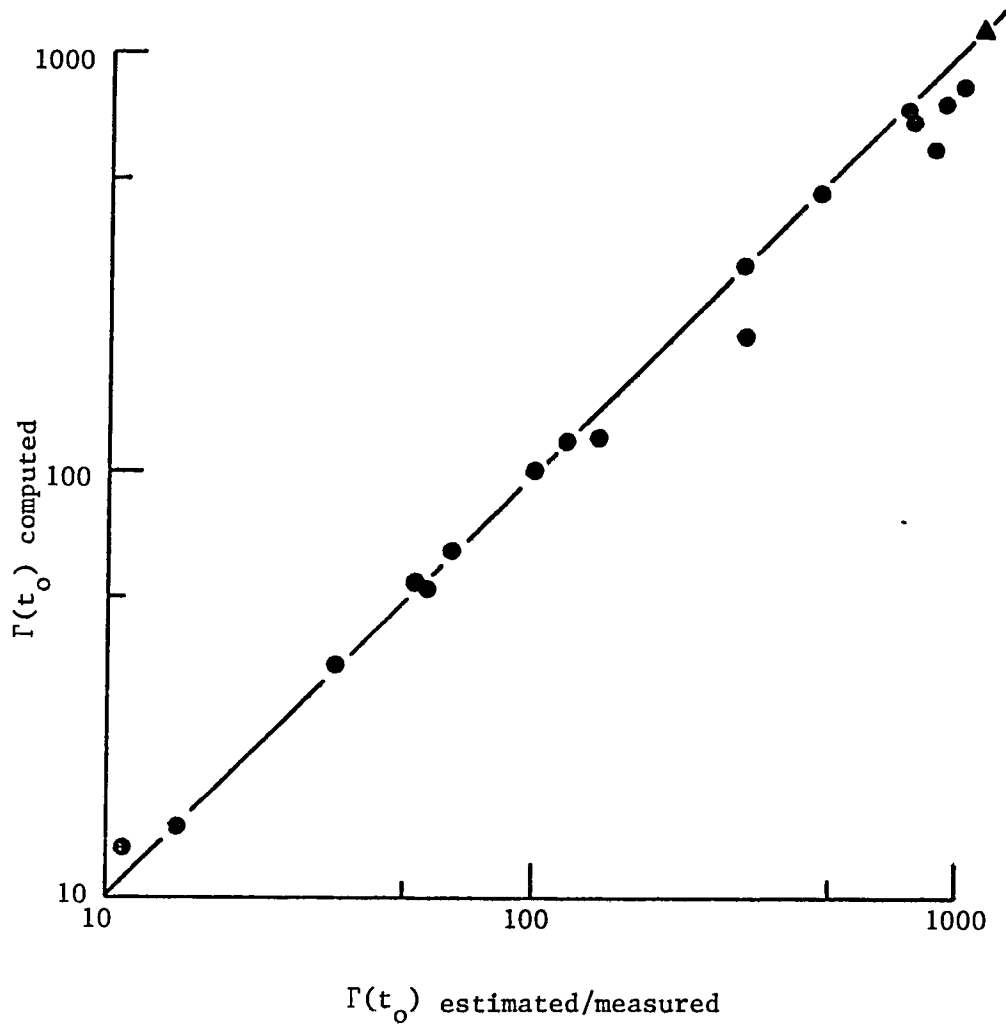


FIGURE 5-4

Comparison of vortex ring strengths computed using the kinematic theory with estimates and one measurement.

● estimated from Eq. (5-4)

▲ measured by Sullivan et al.

VORTEX RING RADIUS. Earlier we pointed out that in the process of computing the strength of vortex rings from measurements of  $T$ ,  $R'$ , and  $U$  we compute the radius  $R$  as well. For most of our dye visualizations the estimates of  $R$  are not accurate enough to warrant comparisons with the computed values of  $R$ . For Runs 13 and 15, however, we were able to obtain accurate measurements of both  $R'$  and  $R$  due to the presence of clear water along the core centerline. We were also able to provide a good estimate for  $R$  in Run 14, although not as accurate as for the other two runs. It would be of interest, therefore, to compare the data for these runs with the mean values of  $R$  computed using the kinematic theory. These comparisons are shown by solid curves in Figs. A-13b, A-14b, and A-15b of Appendix A. The comparisons for Runs 13 and 15 are excellent and for Run 14 quite good. It is interesting that in both Runs 13 and 14 the predicted value for  $R$  initially decreases as does the data. We also made the comparison between the computed values of  $R$  from the dye visualization of Run 9 with the hydrogen bubble measurements for  $R$  in Run 10. These two runs were found from the trajectory and experimental parameters to be very close to one another. The solid line through the data in Fig. A-10b shows the comparison and once again is quite good.

One additional note can be made with regard to the accuracy of the Kelvin/ Lamb formula, Eq. (2-15). Sullivan's measurements suggest that the Kelvin/ Lamb formula overestimates the velocity of vortex rings by as much as 30 to 40%. Thus, even if it were possible to measure  $a/R$  using flow visualization, the expression cannot be expected to accurately predict the strength of a vortex ring.

### 5-3 VORTEX RINGS AND THE REYNOLDS NUMBER

REYNOLDS NUMBER RELATIONSHIPS. As discussed in Section 2-4.2, two definitions for the Reynolds number have been commonly used to

characterize vortex rings:

$$\text{Re}_R = \frac{2UR}{\nu} \qquad \text{Re}_\Gamma = \frac{\Gamma}{\nu} \qquad (5-5)$$

As we found from Eqs. (2-16) and (2-22b)  $\Gamma \sim UR$  so we expect  $\text{Re}_R$  and  $\text{Re}_\Gamma$  to be closely related. Having computed  $\Gamma$  for our experimentally produced vortex rings, it would be of interest to compare these two definitions. In Fig. 5-5 we have plotted  $\text{Re}_R$  against  $\text{Re}_\Gamma$  for our newly formed vortex rings. This plot suggests that at the initial time of formation,  $t_0$ :

$$\text{Re}_\Gamma \sim 2\text{Re}_R \quad (\text{at } t = t_0) \qquad (5-6)$$

Inserting the definitions in (5-5) results in:

$$\Gamma \approx 4UR \quad (\text{at } t = t_0) \qquad (5-7)$$

The Kelvin/Lamb formula, Eq. (2-17) suggests that the proportionality factor between  $\Gamma$  and  $UR$  is a function of the core size,  $a/R$ :

$$\Gamma = 4\pi UR \left[ \ln \frac{8R}{a} - \frac{1}{3} \right]^{-1} \qquad (5-8)$$

Using this formula together with Eq. (5-7) to estimate the core parameter of the newly formed vortex rings we find that

$$a/R \sim 0.25 \qquad (\text{at } t = t_0) \qquad (5-9)$$

It was for this reason that  $a/R = 0.25$  was chosen in our assessment of the effect of a finite core (Section 3-4.2) and wake (Section 5-2.1) on the shape of a vortex ring.

It would also be of interest to study relationships between the Reynolds number of vortex rings and a Reynolds number based on the ejection of fluid from the orifice. We have observed qualitatively that as the jet Reynolds number increases, so does the ring Reynolds number. In Fig. 5-6 we have plotted  $\text{Re}_R$  and  $\text{Re}_\Gamma$  against  $\text{Re}_j$  on a log-log scale. We note that at  $\text{Re}_j \sim 25000$  there is an abrupt change

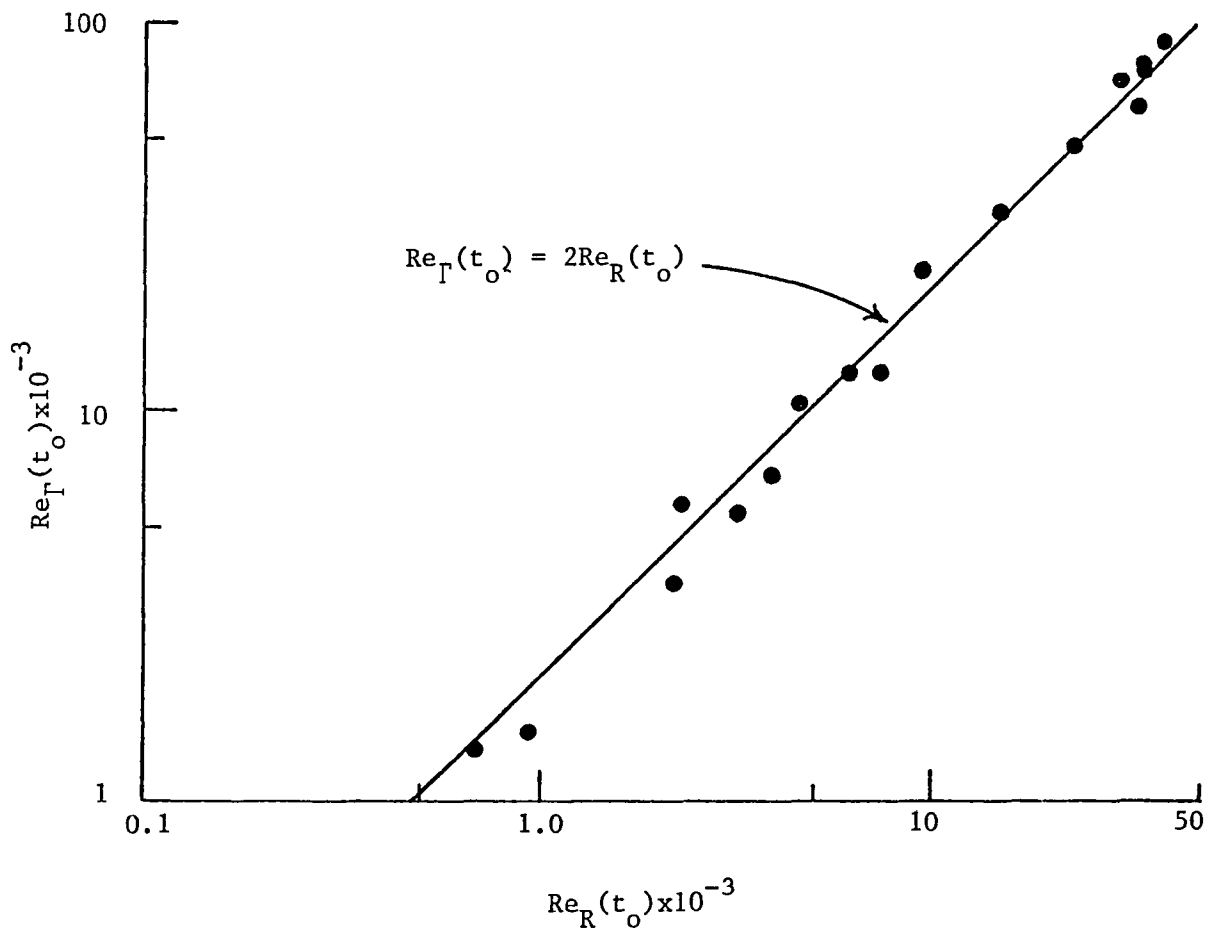


FIGURE 5-5

Relationship between  $Re_R$  and  $Re_\Gamma$  for newly formed vortex rings.

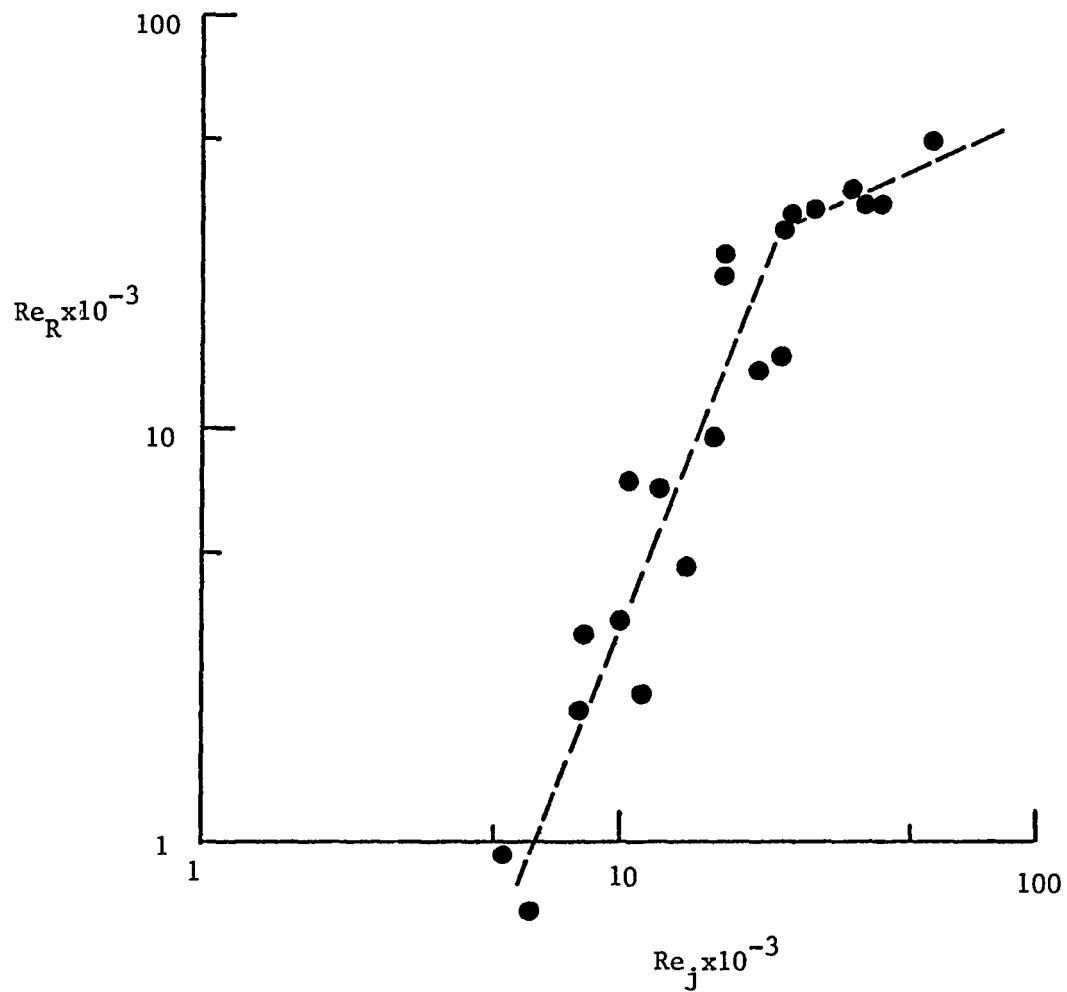


FIGURE 5-6  
Relationships between  $Re_R$  or  $Re_\Gamma$  and  $Re_j$   
for newly formed vortex rings.

a)  $Re_R$

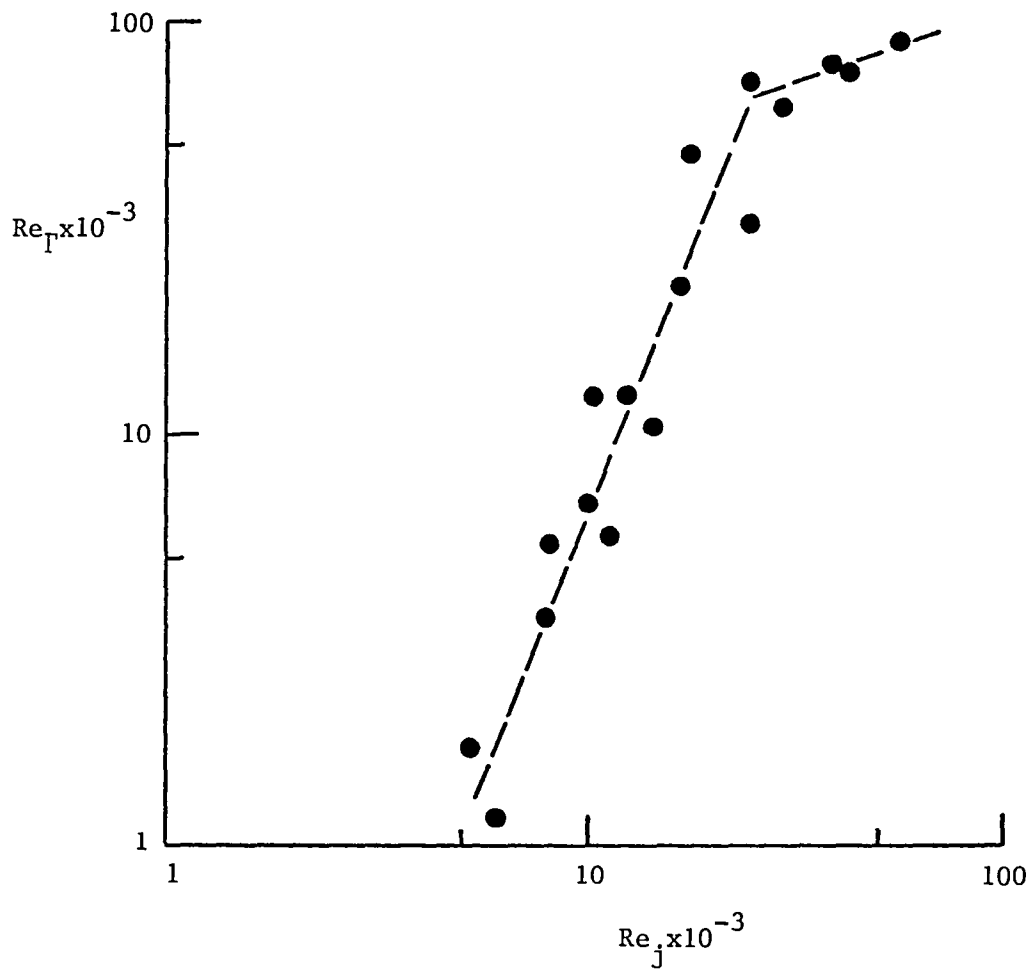


FIGURE 5-6  
Relationships between  $Re_R$  or  $Re_\Gamma$  and  $Re_j$   
for newly formed vortex rings.  
b)  $Re_\Gamma$

in the trend. This suggests transition to turbulence in the Reynolds number ranges:

$$\begin{array}{ll} \text{Re}_j & 20000 - 30000 \\ \text{Re}_R & 25000 - 35000 \\ \text{Re}_\Gamma & 50000 - 70000 \end{array}$$

REYNOLDS NUMBER GROUPS. In Section 4-4 we discussed correlations between the three Reynolds number groups of vortex rings, and the rate at which vorticity diffuses from the core and is convected into the wake. These ideas are supported by our computations of the time rate of change in strength, shown in Appendix B. The rate of decrease in total circulation from high Reynolds number, turbulent vortex rings is observed to be much greater than the rate for low Reynolds number, viscous vortex rings, an indication of a more rapid rate of diffusion due to turbulent motions as compared with molecular motions. Most interesting, perhaps, is the very wide range of intermediate Reynolds numbers in which the strength of the vortex ring changes very little (in a regime), consistent with the absence of an observable wake. These vortex rings appear to have a basically inviscid character.

In order to characterize these groups in a concise way consider the coefficient of drag for a vortex ring defined in the usual way as

$$C_D = \frac{D}{\frac{1}{2}\rho_m U^2 S} \quad (5-10)$$

$D$  is the drag force on the vortex ring,  $U$  its speed, and  $S$  the frontal surface area.  $D$  and  $S$  are given by:

$$D = (\rho_m V) \frac{dU}{dt} \quad S = \pi R^2 \quad V = \frac{4}{3}\pi R^2 T$$

Inserting these values into (5-10) yields

$$C_D = \frac{8}{3} \frac{T}{U^2} \frac{dU}{dt} \quad (5-11)$$

In the case of a solid sphere drag is a result of shear forces along the sphere's surface and flow separation behind the sphere. The drag force of a vortex ring, however, results from the loss of vorticity, strength, and impulse from within the volume of fluid comprising the vortex ring. Within a regime, the high and low Reynolds number vortex rings will therefore have a value of  $C_D$  consistent with the rate at which they lose vorticity, whereas vortex rings at intermediate Reynolds numbers exhibit no drag, and thus have a zero coefficient of drag.

Since it is the motion within regimes which characterizes the three groups of vortex rings, we choose points in the middle of each regime to compute  $C_D$ . These values are shown plotted against  $Re_\Gamma$  in Fig. 5-7. This figure nicely illustrates the three groups of vortex rings. The high Reynolds number, turbulent vortex rings have the highest values of  $C_D$ ; the low Reynolds number, viscous rings have generally lower values of  $C_D$ ; and those vortex rings in the intermediate Reynolds number, "inviscid" group have zero coefficient of drag.

The transition region between these groups is expected to depend in general not only on the Reynolds number, but also on such factors as geometry and roughness of the orifice, piston speed characteristics, the state of the ambient fluid into which the vortex ring propagates, etc.

#### 5-4 ARTERIAL STENOSES AND THE WALL PRESSURE

A motivation for the study of vortex rings propagating up a tube is its application to arterial stenoses. An arterial stenosis is a constriction in an artery which results from the buildup of cholesterol along the arterial wall, or from a diseased heart valve which will not open completely. As blood is forced through these

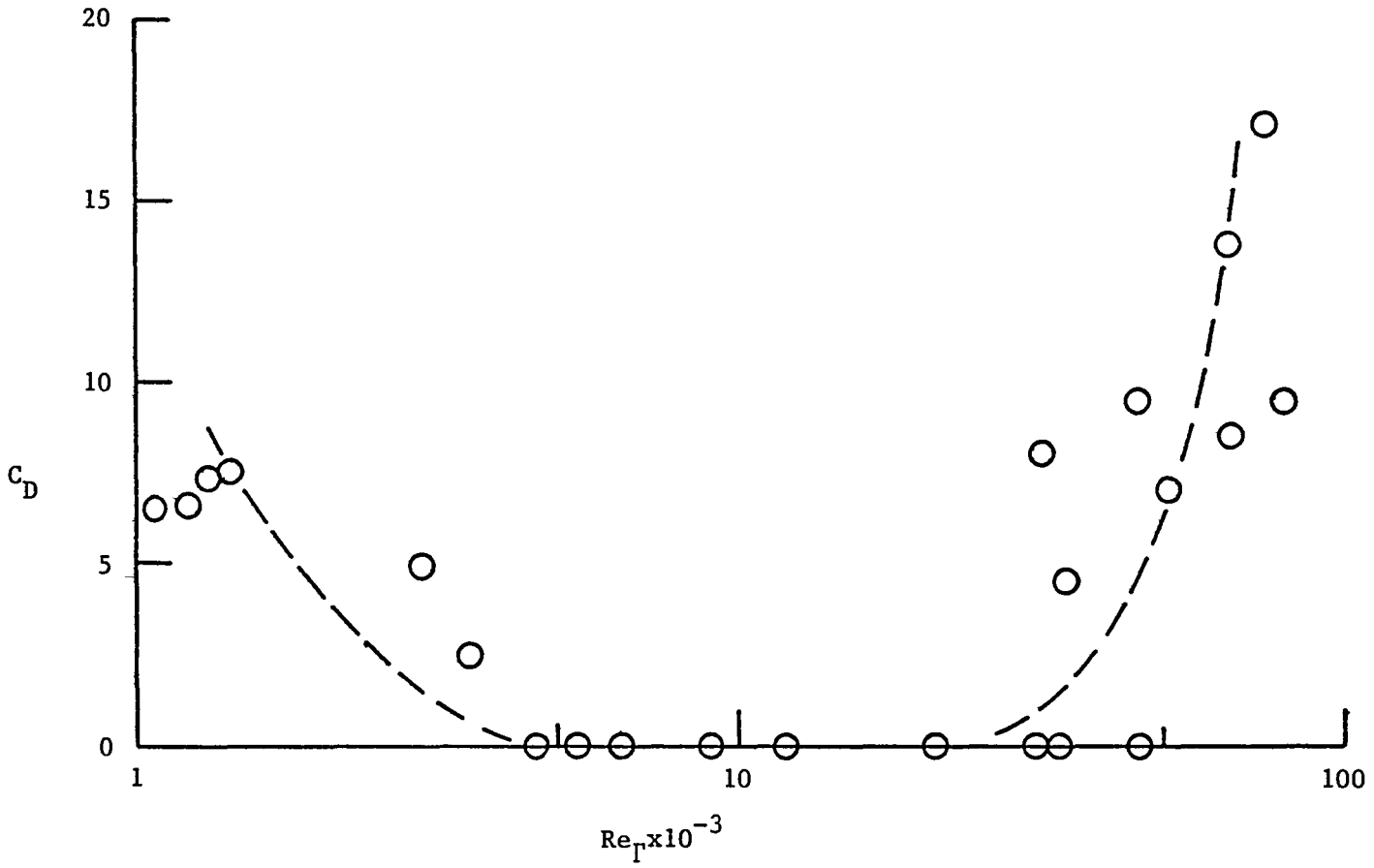


FIGURE 5-7  
The drag coefficient of vortex rings  
plotted against Reynolds Number

constrictions, sounds called murmurs are produced. Murmurs can be heard with a stethoscope, and have been used in a qualitative way for years to assess the severity of a stenosis. To determine with precision the degree and location of a stenosis, however, usually requires investigative surgery or the use of radioactive tracers.

In recent years interest has developed in the possibility of using murmurs in a more quantitative way in order to predict with more accuracy the severity and location of a stenosis. Understanding the source of murmurs, however, requires an understanding of the formation, development, and structure of the turbulent flowfield which is produced as blood is forced through the constriction.

Based on the suggestion that the flow of blood through a stenosis reaches a quasi-steady state at peak systole, studies in the past have concentrated mainly on steady flow models [65]. As is shown in Fig. 5-8, however, the acceleration of blood into the aorta is extremely rapid ( $\sim 4650 \text{ cm/sec}^2$ ), so that, at least for a valvular stenosis, the flow is dominated by pulsatile effects. Farther from the heart a steady component is superposed over the ejection pulse, but pulsatile effects, especially for highly occluded vessels, are still expected to play an important role in the development of the post-stenotic flowfield.

As is indicated in Fig. 5-8 our experiment was designed using parameters relating to the arterial stenosis. Because the peak Reynolds number of blood ejected from the aorta is about 5000 we chose tube Reynolds numbers of roughly 5000, 4000, and 3000, and a piston travel time of roughly 0.170 seconds to correspond to a single ejection of blood from the heart. With regard to arterial stenoses we are most interested in the smallest orifices which correspond to the highest degree of occlusion. These orifices are associated with the production of turbulent vortex rings followed by the production of a turbulent jet. Entirely a result of the pulsatile nature of the flow, the vortex ring travels up the vessel and collides with the vessel wall, causing large pressure fluctuations.

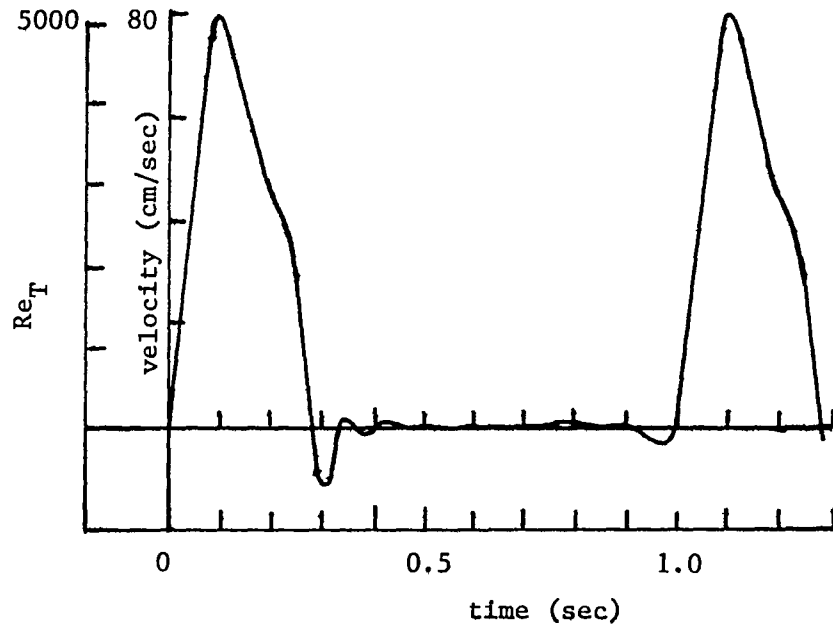


FIGURE 5-8  
Speed and Reynolds number of blood ejected from  
the human heart into the aorta.

IRREGULAR OCCLUSION. In order to visualize the development of vortex rings with a more physiologically realistic occlusion, an orifice was made very irregular by applying clay to the tube interior to an area reduction of roughly 92%. It was found that highly turbulent, rather incoherent vortex rings could still be readily identified and observed to travel up the tube, colliding with the tube wall always at the same location.

WALL PRESSURE. Since the fluctuations of the arterial wall are heard at the surface of the body as noise we would like to analyse the pressure at the tube wall due to the passage of a vortex ring, and compare this with an estimate of the magnitude of pressure fluctuations which might result from a collision with the arterial wall. The pressure at the tube wall can be calculated from the unsteady Bernoulli equation:

$$\rho_m \frac{\partial \phi}{\partial t} + \frac{1}{2} \rho_m u^2 + p = \text{constant} \quad (5-12)$$

$u$  is the velocity at the tube wall and  $\phi$  is the unsteady potential function. Since

$$\phi = \phi(\rho_0, z - \int_0^t U(\zeta) d\zeta)$$

we find that the pressure at the tube wall relative to the pressure at infinity is given by:

$$P - P_\infty = -\frac{1}{2} \rho_m (u^2 - 2uU) \quad (5-13)$$

where  $U$  is the velocity of the vortex ring. We write  $u$  in the non-dimensional form:

$$u(\rho_0, z) = \frac{\Gamma}{4\pi R} \hat{u}(\rho_0, z) \quad (5-14)$$

Computations for  $\hat{u}$ , obtained by taking the  $z$  derivative of  $\phi$  in Eqs.

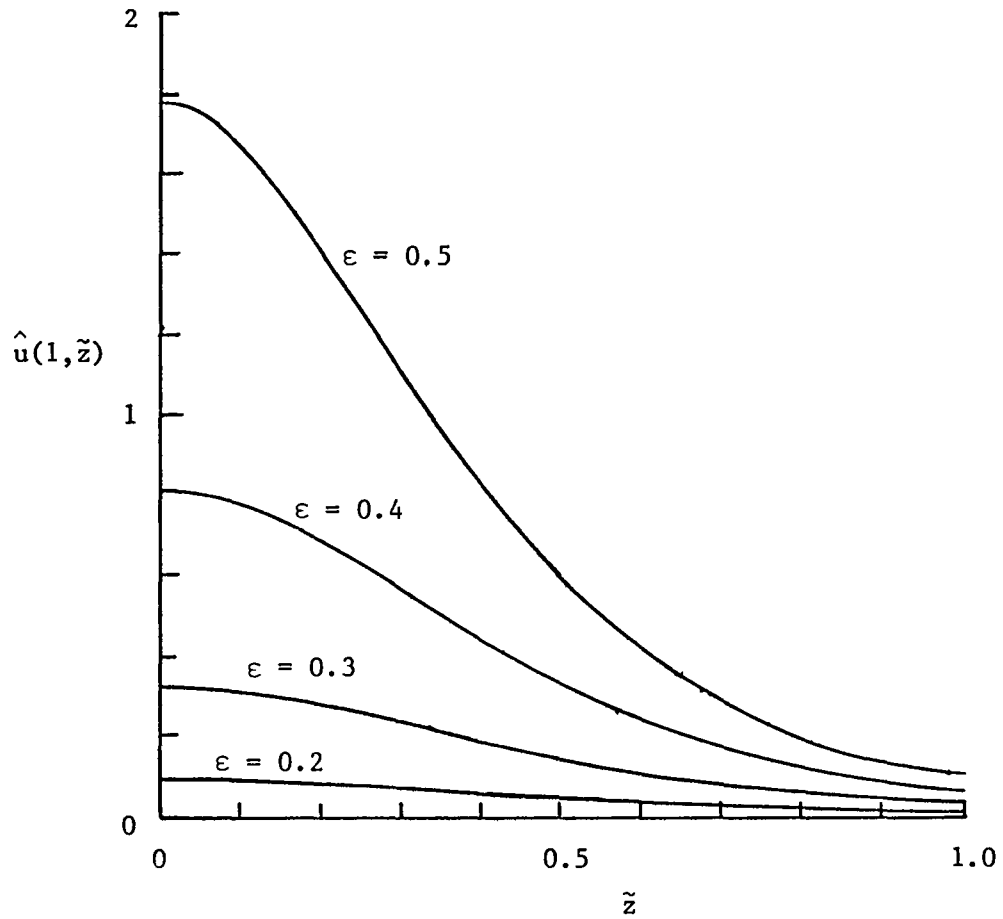


FIGURE 5-9

The non-dimensional wall velocity as a function of  $z/\rho_0$  for different values of  $\epsilon$ .

(3-19), (3-23) and (3-27) are given in Fig. 5-9 for different values of  $\epsilon$ .

In order to compute the pressure at the tube wall as a vortex ring passes by we need to know  $\Gamma$ ,  $U$ , and  $R$  as a function of time.  $U$  and  $R$  are obtained from experimental measurements, and we now have computations for  $\Gamma$ . Since we are concerned most with the smallest occlusions which produce the most energetic vortex rings, we compute the pressure as a function of time at 1.5 tube diameters from the orifice for Runs 1 and 3. The results are given in Figs. 5-10 and 5-11. Time is measured from the formation of the vortex ring and the vertical line indicates the time at which the vortex ring passes the point where the pressure is computed. We note that the peak pressure drop does not necessarily coincide with the time when the vortex ring is 1.5 diameters downstream, and that the pressure profile is asymmetric. This is because the vortex ring is both losing strength and increasing in size as it travels up the tube.

The peak pressure change at the tube wall due to the passage of these turbulent vortex rings is apparently on the order of  $1/3 - 1$  mbar. It is interesting to note that this is the same order of magnitude as the peak rms wall pressure measured in steady flow models of arterial stenoses [65].

The pressure resulting from a collision with the vessel wall, however, can be expected to be much higher. Using Eq. (2-14) to estimate the impulse of the vortex ring, one can obtain an order of magnitude estimate for the pressure imparted to the tube wall due to a collision by a vortex ring. Based on values for the smallest orifices one estimates pressures at least one order of magnitude larger than what is shown in Figs. 5-10 and 5-11. This would suggest that the production of vortex rings behind arterial stenoses might be important with respect to flow-induced vibrations at the vessel wall. Indeed, the repetition in collisions of vortex rings with the vessel wall behind an arterial stenosis might account for the commonly observed phenomenon of post-stenotic dilatation--the weakening of the arterial wall behind an arterial stenosis.

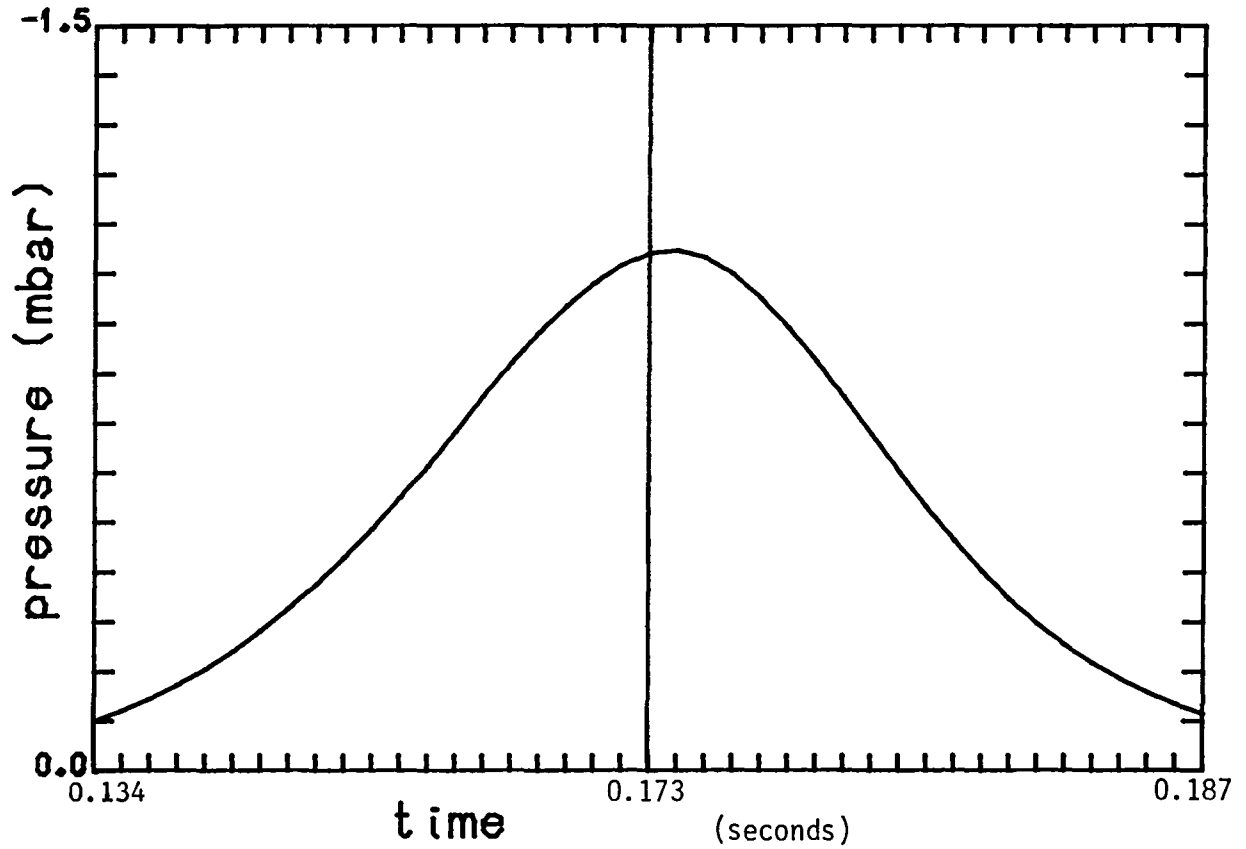


FIGURE 5-10

The pressure at the tube wall 1.5 diameters from the orifice for Run 1.

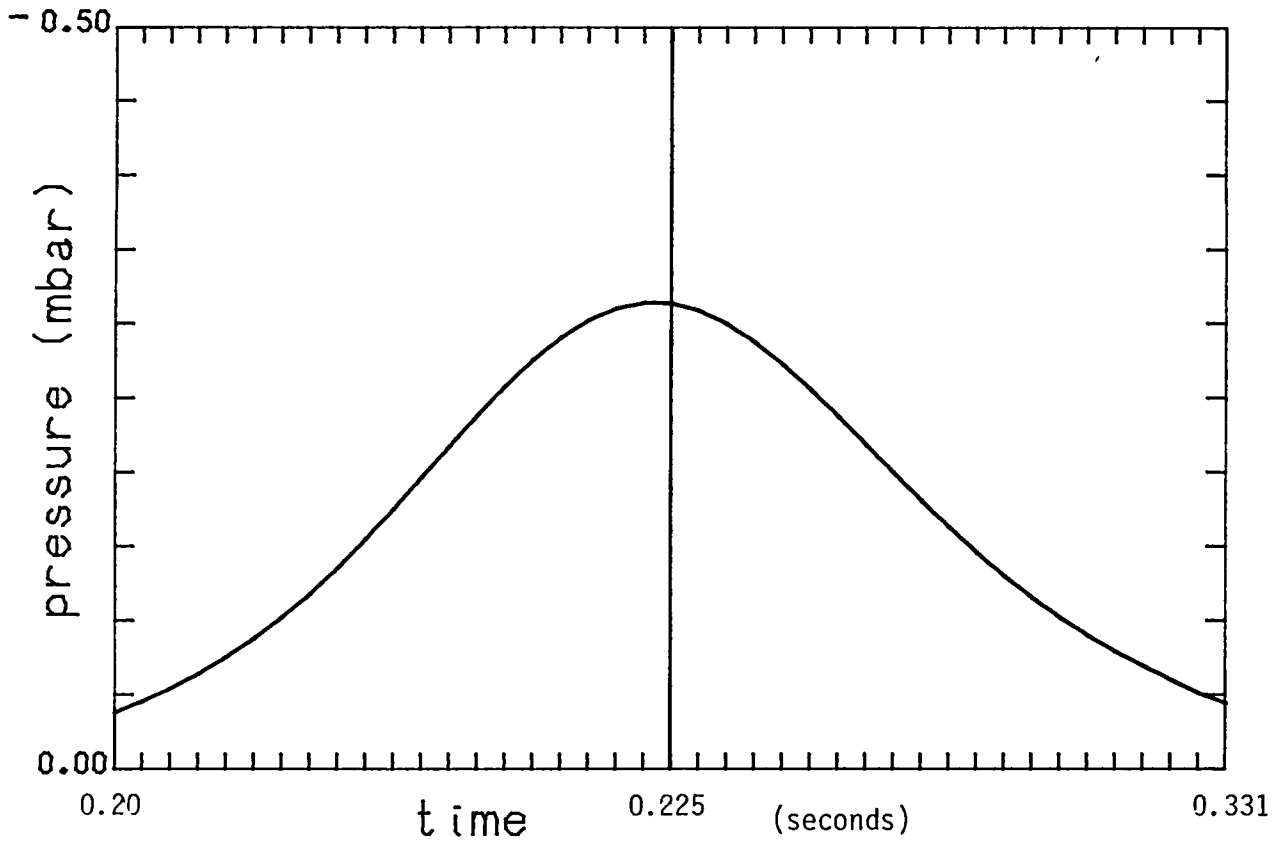


FIGURE 5-11

The pressure at the tube wall 1.5  
tube diameters from the orifice for Run 3.

# 6

## Summary

*(The) world tube represents an infinitely complex process of . . . movement and development which is centered in a region indicated by the boundaries of the tube. However, even outside the tube, each 'particle' has a field that extends through space and merges with the fields of other particles. A more vivid image of the sort of thing that is meant is afforded by considering wave forms as vortex structures in a flowing stream . . . The flow patterns merge and unite, in one whole movement of the flowing stream. There is no sharp division between them, nor are they to be regarded as separately or independently existent entities.*

*-from D. Bohm, "Fragmentation and Wholeness"*

As is indicated by the title of this report, kinematic and dynamic aspects of vortex ring propagation in a tube have been discussed. The kinematics is embodied in the mathematics which was developed in Chapter 3, and the dynamics enters via the flow visualization measurements discussed in Chapter 4. Using the purely kinematic theory together with the data, we computed the change in vortex ring strength as a function of time, a dynamic result. We should now like to summarize what we have learned.

**KINEMATICS.** We exploit two important properties of the Biot-Savart Law. First, since only conservation of mass for an incompressible flow is used in its derivation, it is a purely kinematic expression. Whether the flow is viscous in character or is dominated by turbulent fluctuations, if the vorticity field is known or can be adequately modeled at a given instant in time, then the velocity field can in principle be computed at that time from the Biot-Savart Law. We provide such a model for a vortex ring in a tube in order to compute the kinematic relationships among the vortex ring velocity, radius, thickness, and strength. To the extent to which our model is accurate in computing these relationships, it applies for all vortex rings be they viscous in nature, or highly turbulent.

Another important aspect of the Biot-Savart Law is the linearity of the vorticity field with respect to the velocity field. Making use

of this property we split the vorticity field in two parts: the vortex ring itself, and the wake. We found that effects of the wake on the shape of the vortex ring are at most about 3% and can be neglected.

In addition, we show that the effect of a finite core on the vortex ring shape is slight, so that we can accurately model the vortex ring by concentrating its total circulation along a circular vortex filament placed axisymmetrically in a tube. In a frame of reference fixed with respect to the tube we find that the outer flowfield of a bounded vortex ring, like the unbounded vortex ring, has a dipole character, but with more of an axial flow due to the confining nature of the tube [Fig. 3-4]. The wall-induced flow on the vortex ring is in a direction opposite to its motion [Fig. 3-5] so that the tube acts to slow the vortex ring down. The extent to which the speed of the vortex ring is decreased (as compared with the same ring in an unbounded flow) depends on the relative radius of the vortex ring to that of the tube [Eq. (3-32), Fig. 3-7].

In a frame of reference moving with the vortex ring, the extent of the vortex ring, that is, the volume of fluid moving with the core is defined. The speed with which the vortex ring travels depends on dynamic considerations such as the change in size of the core, the distribution of vorticity, etc.; however, general kinematic relationships among the ring velocity, strength, size, and shape must be met at all times. We compute these relationships [Figs. 3-11 and 3-12], and find that, for a vortex ring with specified strength and size (i.e., radius), the thickness and volume of the vortex ring increases with decreasing speed. In addition, we find that the effect of the tube is to increase its volume further. Thus, from kinematics, we conclude that the effect of a tube on a vortex ring is, in general, to decrease its velocity and increase its volume as compared with the same vortex ring in an unbounded flow.

DYNAMICS. Once the total circulation, radius, and velocity of a vortex ring have been established from the dynamic processes of vortex formation, convection, and diffusion, the shape of the vortex ring is specified by the kinematic relationships just described. We therefore work backwards, and from measurements of the velocity, radius, and thickness of a vortex ring traveling up a tube, determine its total circulation as a function of time-- a dynamic calculation. It should be kept in mind, however, that the dynamics enters through the experimental measurements of the time rates of change in ring velocity, thickness, and radius--the role of kinematics is to relate these quantities at any instant in time to the total circulation of the vortex ring.

With experimental measurements of vortex rings from very low to very high Reynolds numbers we find that the vortex rings can be divided into three groups which are characterized by the rate at which total circulation is lost from the ring into a wake [Fig. 5-7]. At very high ring Reynolds numbers ( $Re_R \sim 20000 - 30000$  and above), turbulent diffusion of vorticity and its subsequent convection out of the vortex ring results in a roughly  $1/t$  decrease in ring velocity and strength. On the other hand, at very low Reynolds numbers ( $\sim 1000 - 2000$  and below) the much slower process of molecular diffusion results in a less rapid decrease in vortex ring velocity and strength, like  $1/t^\alpha$  where  $\alpha \sim 0.13$  to  $0.27$  for our experimentally measured vortex rings. There is a very wide range of intermediate Reynolds numbers ( $\sim 2000 - 20000$ ), however, where the vortex ring has basically an inviscid character. Viscous diffusion proceeds at such a slow rate that very little vorticity is lost from the vortex ring, and the total circulation of the vortex ring remains essentially constant.

We also discovered, however, that for all our experimentally produced vortex rings, periods of rapid change in ring velocity and strength would periodically occur. That is, the time dependent forms of ring velocity and strength just described are identified in regimes, two regimes being separated by a rapid change in ring

velocity and strength. These periods of rapid change are postulated to result in some way from the growth of unstable waves along the core of the vortex ring which, as they break, might result in a periodic reorganization of the core.

Relating to pulsatile effects in arterial stenoses, the pressure at the tube wall 1.5 diameters from the orifice was calculated for our smallest occlusion. It was found that the maximum drop in pressure as these vortex rings travel up the tube is on the order of 1/2 mbar, the same order of magnitude as the peak rms pressure measured in steady flow models. Collisions of vortex rings with the vessel wall, however, might result in significantly higher pressure fluctuations, accounting perhaps for the observation that behind an arterial stenosis the vessel wall is often found to be weakened.

SIGNIFICANCE AND FUTURE STUDY. We have found from our experimental measurements that vortex rings behave in a viscous, turbulent, or inviscid manner, depending in large part on the Reynolds number. Although other researchers have observed the viscous and turbulent regions, the existence of a group of vortex rings with an inviscid character had not been previously established. Likewise, although other researchers have observed single periods of breakdown and rapid change in velocity for turbulent vortex rings, it is significant that transition periods have now been observed for vortex rings at all Reynolds numbers, and in many cases more than one.

Such observations have relevance not only with respect to the evolution of single vortex rings, but with more complicated flows involving concentrated regions of vorticity. The different rates at which circulation is lost from the core might have implications with respect to the evolution of more general vortex flows. The rapid changes in vortex strength and the possible instability mechanisms associated with them might play a role in the production of smaller scales of turbulence from larger scales, especially for shear flows.

If found to be the case in more general turbulent flows, sudden

losses of vorticity as vortex tubes become unstable, break, and reform, when averaged over long periods of time might produce large contributions to a turbulent viscosity. In addition, since the sound field in turbulent jets arises from non-steady oscillations in the potential function, sudden changes in vortex ring strength (and therefore in the potential field) might be expected to result in the production of noise. It would be of considerable practical interest, therefore, to examine these periods of rapid change in vortex ring strength in more detail, to determine what mechanisms are involved, and to search for such mechanisms in the development of more general turbulent flows.

Using the kinematic nature of vorticity we have developed a method to calculate the total circulation of vortex rings from flow visualization measurements. This technique is considerably simpler to apply than previous methods which require knowledge of the velocity field within the vortex ring, and we now have the ability to compute the time rate of change in strength for single vortex rings as they propagate. With respect to the evolution of vortex rings, then, it would be of interest to apply this technique to more extended studies. For example, by varying systematically the piston characteristics, volume of fluid ejected, type of orifice used, etc. additional relationships between the initial conditions and the loss of circulation from the vortex ring as it evolves can be established.

We might note in closing that the technique we have developed to calculate the total circulation of vortex rings from flow visualization measurements can be applied just as well to the study of vortex pairs, with application, for example, to studies of trailing vortices behind airfoils with finite span.

## APPENDIX A

### VORTEX RING TRAJECTORY, SIZE, AND SHAPE PLOTS for Runs 1 - 26

#### definitions:

$x_r$	Distance from the orifice. [cm].
$t$	Time. [sec.]
$R$	Radius of vortex ring to core centerline.
$R'$	Radius of vortex ring to outermost dyed region.
$T$	Thickness of vortex ring to outermost dyed region.
$V$	Volume of vortex ring, $4/3 \pi R'^2 T$
$V_{ej}$	Volume of fluid ejected through the orifice.

Table A-1: Summary of experimental values for each run.

Table A-2: Summary of regime slopes for each run.

Figures A-1 to A-26:

- a) Vortex ring trajectory plots
- b) Vortex ring size and shape plots

Run		$\frac{d}{D}$	$Re_T$	(sec.) $\tau_p$	(in.) $x_p$	(cm/sec) $u_p$	$Re_j$	$u_j$	(cm) $d$
1	dye	.1000	5598	.169	.300	4.509	55978	450.9	1.188
2	dye	.1000	4254	.172	.232	3.426	42540	345.6	1.188
3	dye	.1000	2471	.208	.163	1.990	24712	199.0	1.188
4	dye	.1497	5840	.162	.300	4.704	38931	209.05	1.778
5	H <sub>2</sub>	.1497	5468	.173	.300	4.405	36456	195.8	1.778
6	dye	.1497	4426	.166	.233	3.565	29508	158.4	1.778
7	H <sub>2</sub>	.1497	3858	.188	.230	3.107	25719	138.1	1.778
8	H <sub>2</sub>	.1497	3719	.195	.230	2.996	24796	133.2	1.778
9	dye	.1497	2650	.194	.163	2.134	17664	94.8	1.778
10	H <sub>2</sub>	.1497	2675	.191	.162	2.154	17831	95.75	1.778
11	dye	.2525	6224	.152	.300	5.013	24649	78.63	3.000
12	H <sub>2</sub>	.2525	5419	.174	.299	4.365	21461	68.38	3.000
13	dye	.2524	2623	.196	.163	2.112	10388	33.13	3.000
14	dye	.3207	5406	.175	.300	4.354	16857	42.33	3.810
15	dye	.3207	4025	.178	.230	3.282	12550	31.91	3.810
16	dye	.3207	2647	.193	.162	2.132	8254	20.73	3.810
17	dye	.4209	6143	.154	.300	4.948	14596	27.94	5.000
18	H <sub>2</sub>	.4209	5409	.172	.295	4.356	12852	24.62	5.000
19	dye	.4209	4266	.170	.230	3.436	10136	19.40	5.000
20	dye	.4811	5468	.174	.300	4.405	11366	19.04	5.715
21	H <sub>2</sub>	.4811	5715	.165	.299	4.603	11881	19.88	5.715
22	dye	.4811	3871	.189	.232	3.118	8048	13.48	5.715
23	dye	.4811	2554	.200	.162	2.057	5310	8.891	5.715
24	dye	.6414	5005	.189	.300	4.032	7803	9.800	7.620
25	dye	.6414	3899	.186	.230	3.141	6079	7.635	7.620
26	dye	~.3	~13470	~.070	.299	10.85	~44900	~120	$A_d/A_D$ ~.92

TABLE A-1

Summary of experimental values for each run

Run	A <sub>1</sub>	A <sub>2</sub>	A <sub>3</sub>	B <sub>1</sub>	B <sub>2</sub>	B <sub>3</sub>	γ <sub>1</sub>	γ <sub>2</sub>	γ <sub>3</sub>	C <sub>1</sub>	C <sub>2</sub>	C <sub>3</sub>
1	23.244	27.636										
2	22.803	28.364										
3	24.236	26.948				(70.128)						
4	17.253	23.240	(28.725)									85.741
5	15.997	18.721	(rocking oscillation)									
6				110.20	88.346							
7				101.52	86.500							
8	turbulence											
9				83.686	70.421	63.520						
10				83.836	70.435	62.410						
11				41.363	37.861							
12				35.807	32.448	28.995						
13				19.249	17.016							
14				18.145	16.676	14.358						
15				14.532	13.715	13.056						
16				7.175	6.518	6.017						
17				9.813	8.866	8.550						
18				8.417	7.816							
19				6.694	5.944							
20					4.819	4.396						
21				6.252								
22				3.853	(3.170)			.8280			1.568	
23				(1.562)			.8239	.7650		2.529	2.875	
24							.8664	.7313		2.202	2.989	
25							.8623	.7681		2.093	2.589	
26	3.913	5.974	10.873	(irregular occlusion)								

} repeatability

TABLE A-2

Summary of regime slopes for each run

group 1:  $x = A_n \ln t + \text{const.}$      $U = \frac{A_n}{t}$   
group 2:  $x = B_n t + \text{const.}$      $U = B_n$   
group 3:  $\ln x = \gamma_n \ln t + \ln C_n$      $U = \gamma_n C_n t^{\gamma_n - 1}$   
(x) = cm    (U) = cm/sec.    n = regime

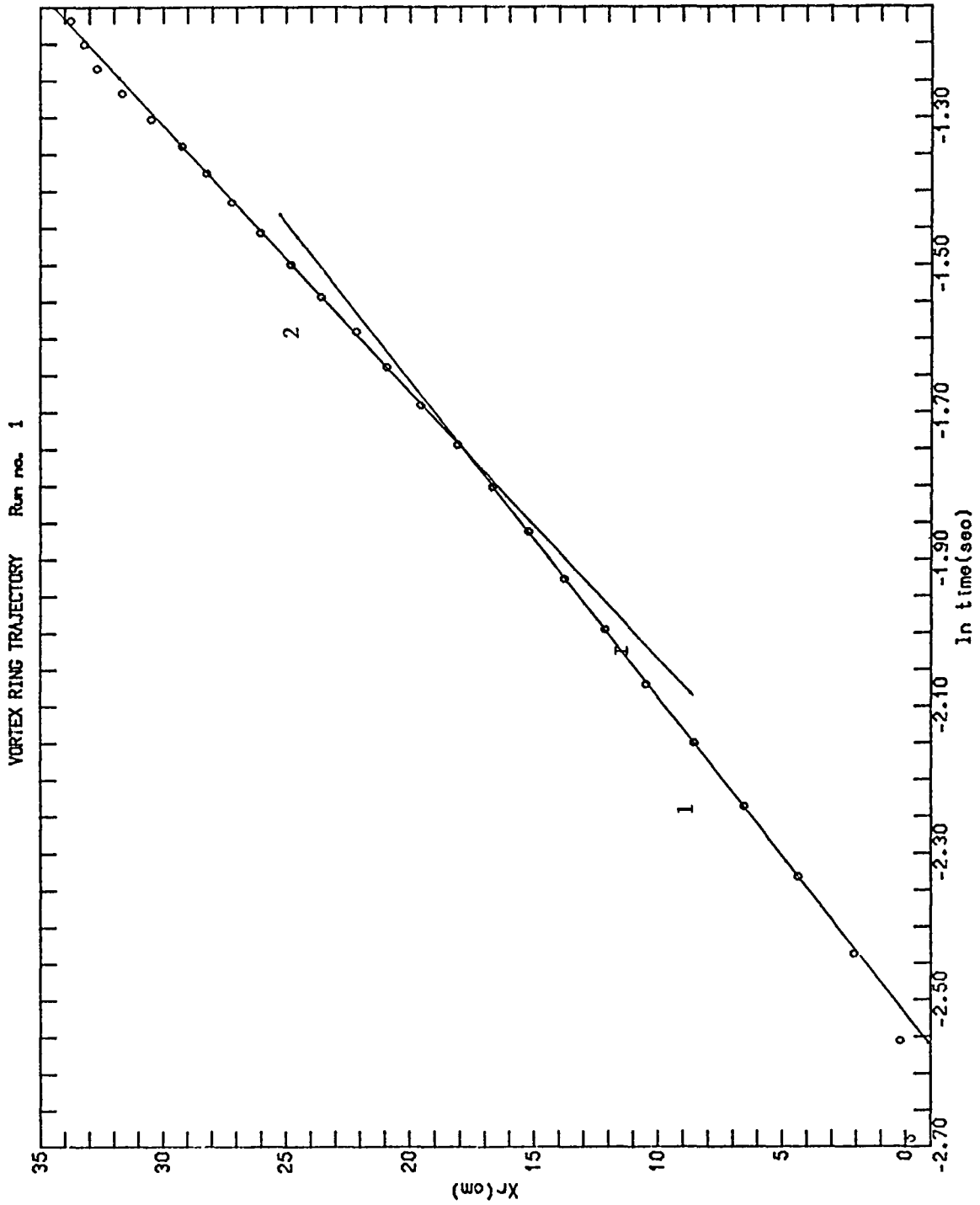


FIGURE A-1a  
 Run 1  $d/D = 0.10$   $Re_j = 55978$   
 Dye

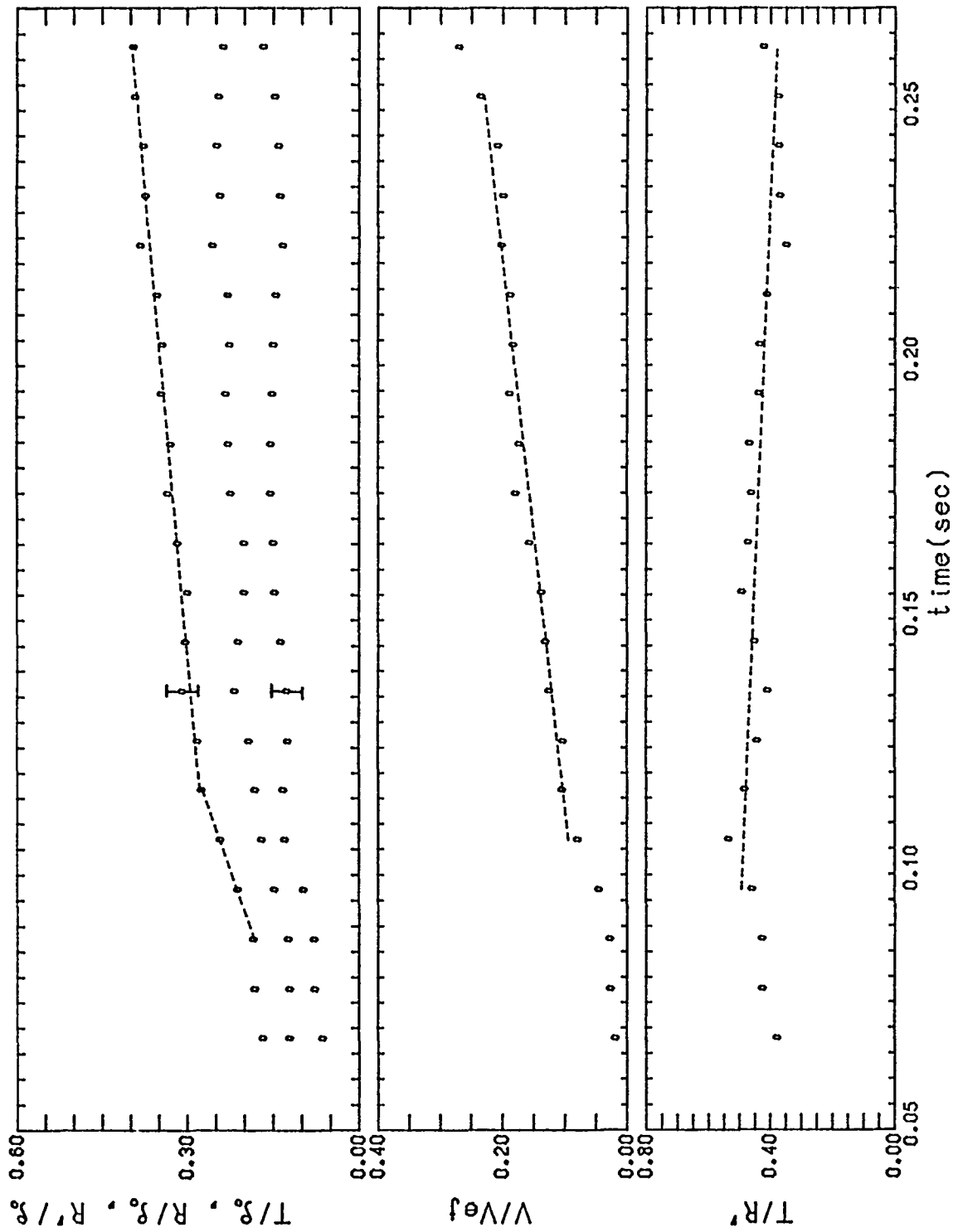


FIGURE A-1b  
 Run 1  $d/D = 0.10$   $Re_j = 55978$   
 Dye

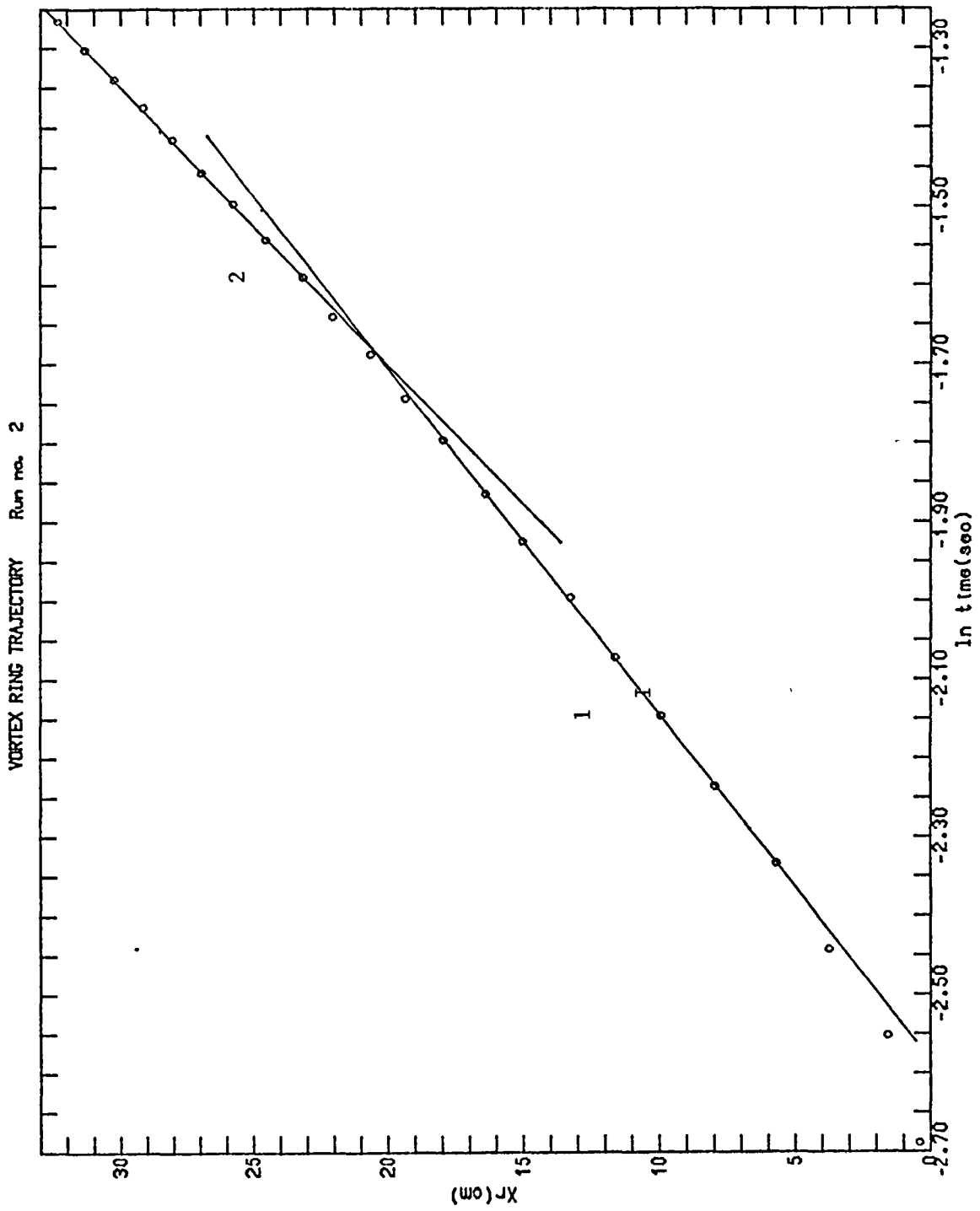


FIGURE A-2a  
 Run 2  $d/D = 0.10$   $Re_j = 42540$   
 Dye

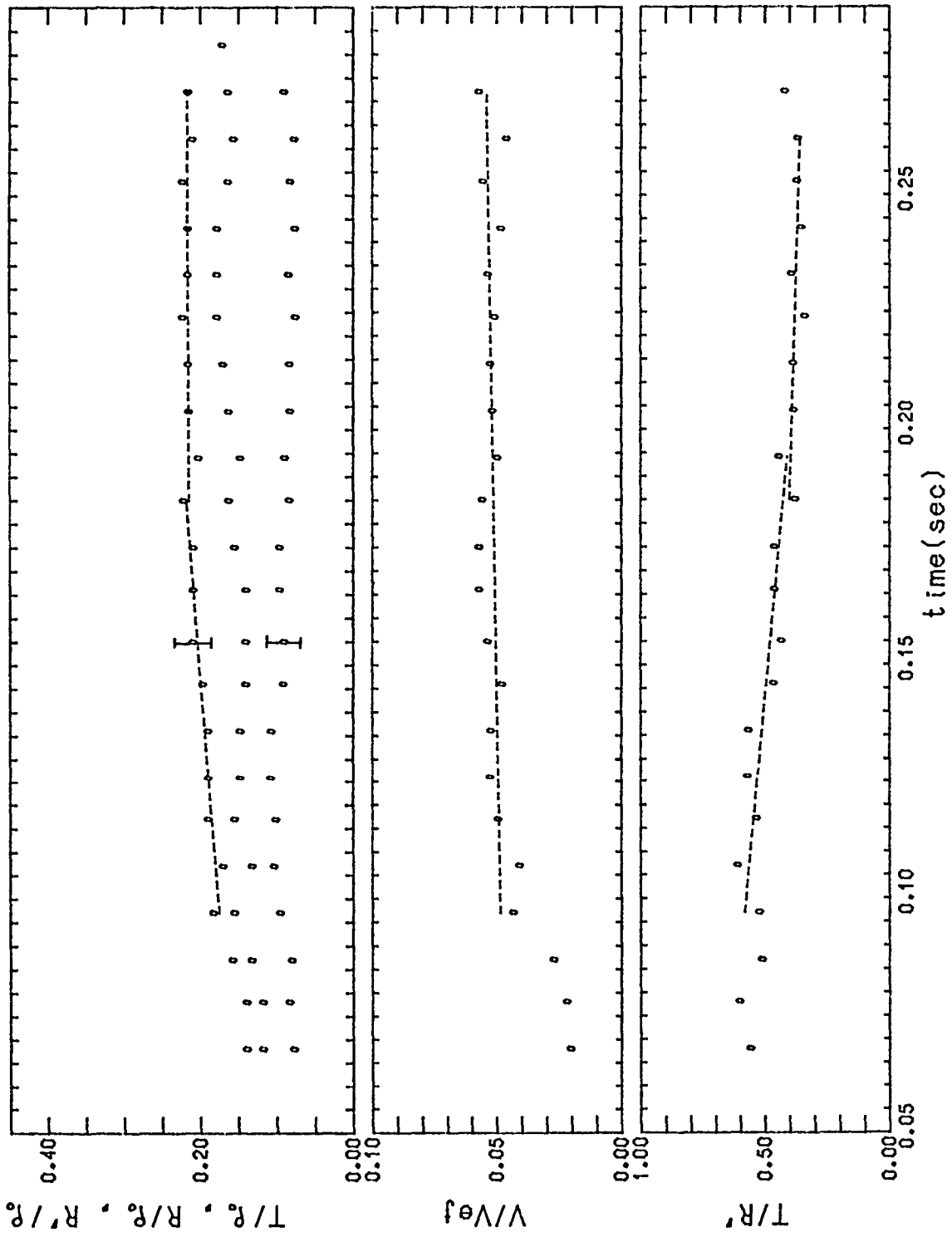


FIGURE A-2b  
 Run 2  $d/D = 0.10$   $Re_j = 42540$   
 Dye

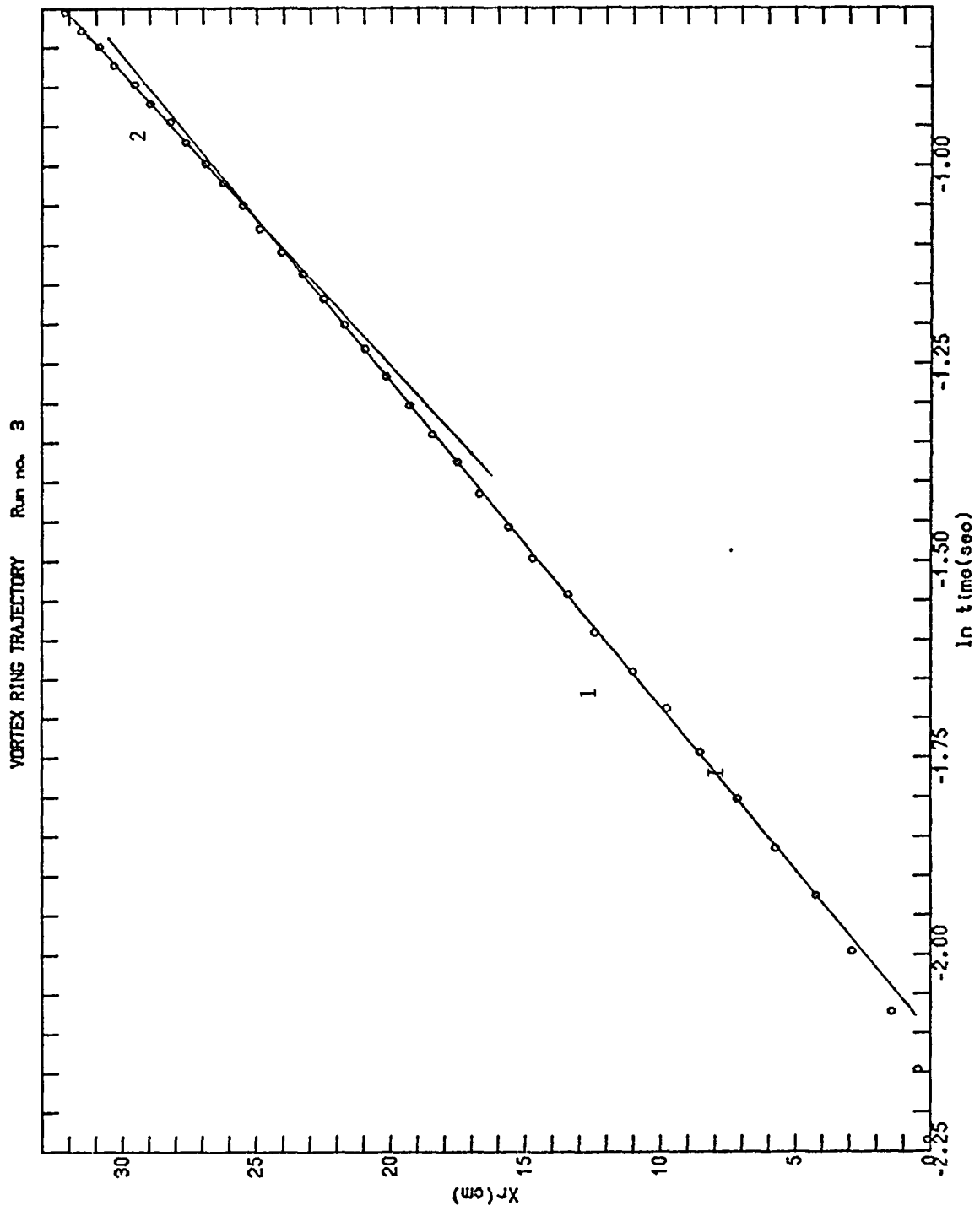


FIGURE A-3a  
 Run 3  $d/D = 0.10$   $Re_j = 24712$   
 Dye

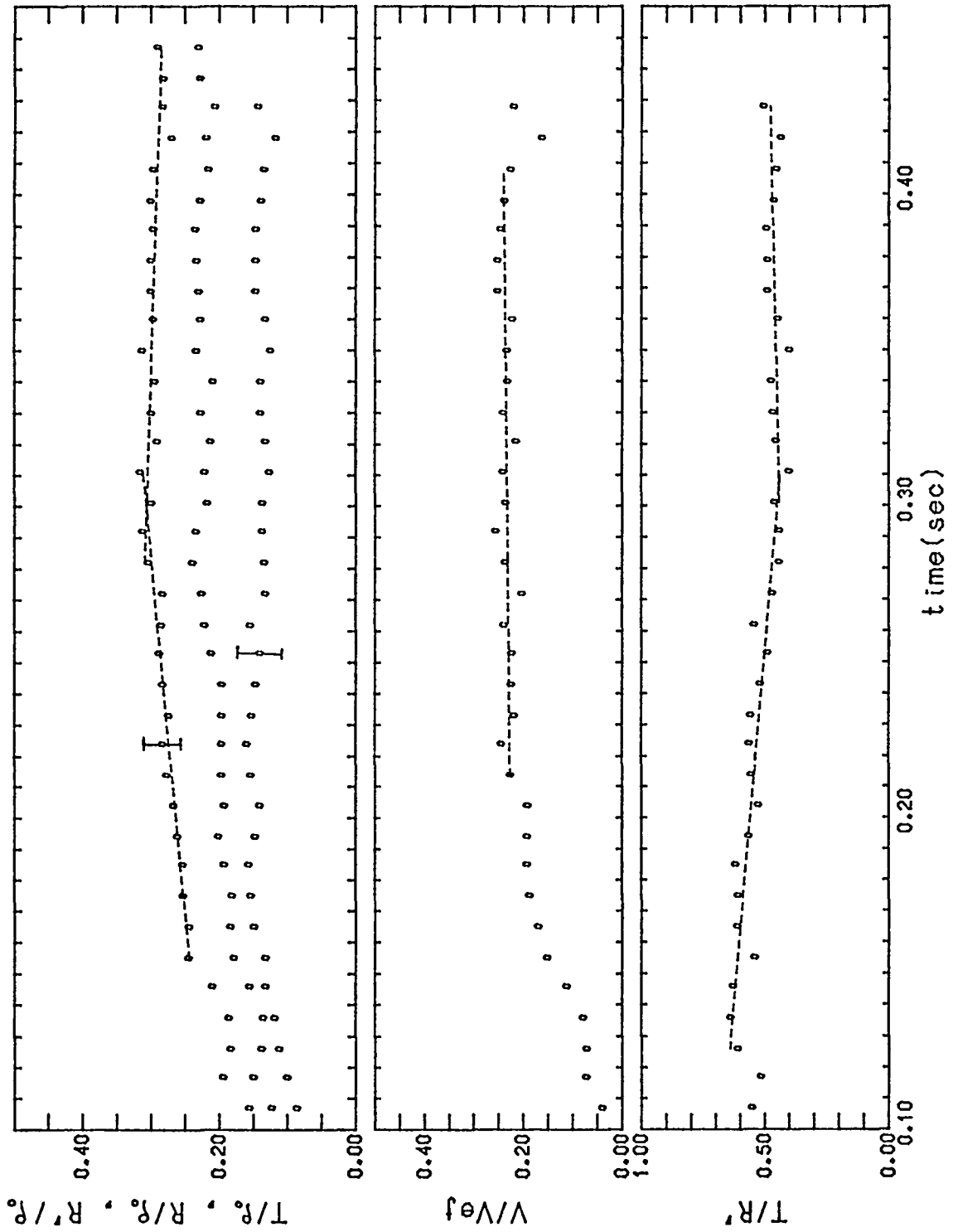


FIGURE A-3b  
 Run 3  $d/D = 0.10$   $Re_j = 24712$   
 Dye

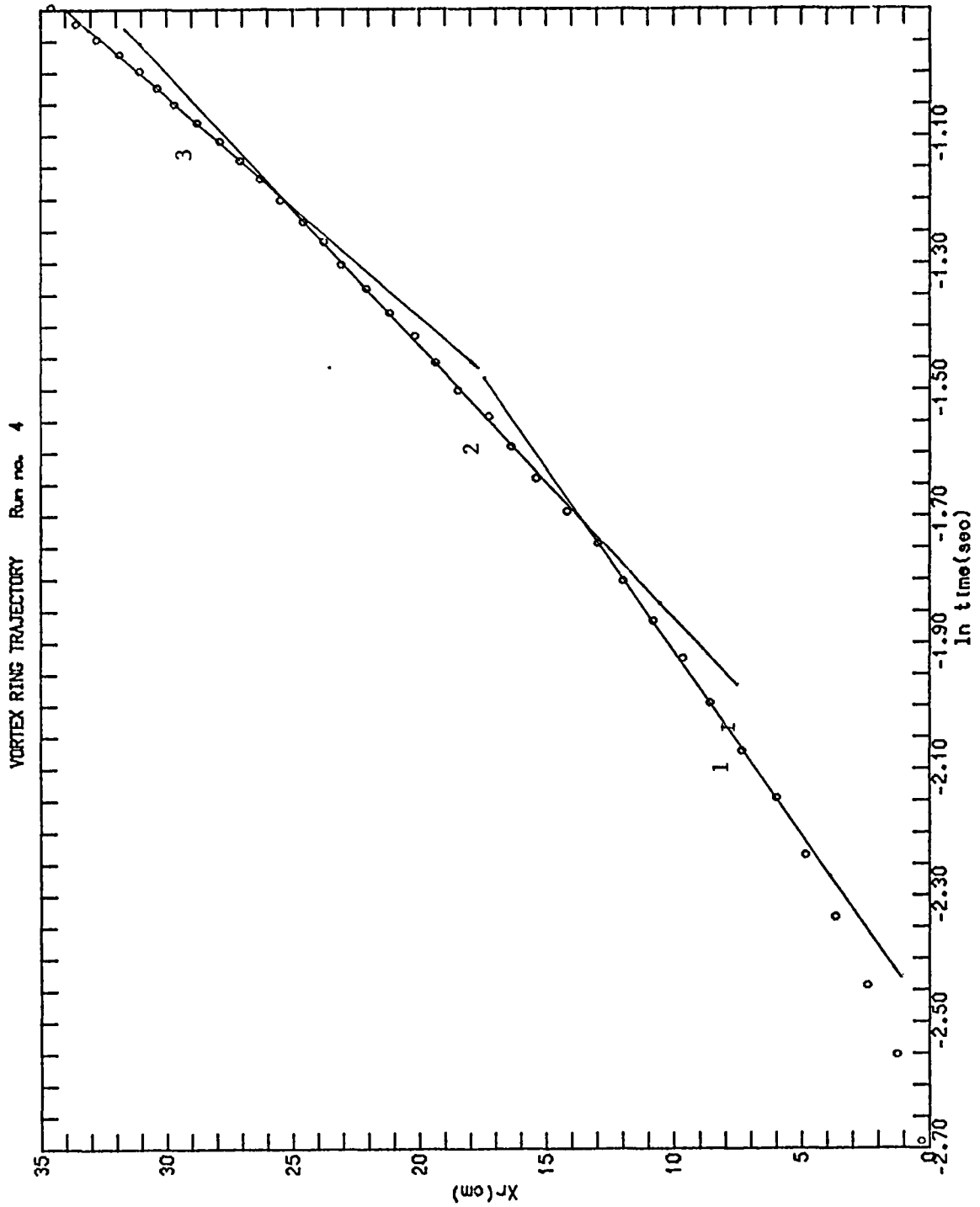


FIGURE A-4a  
Run 4  $d/D = 0.15$   $Re_j = 38931$   
Dye

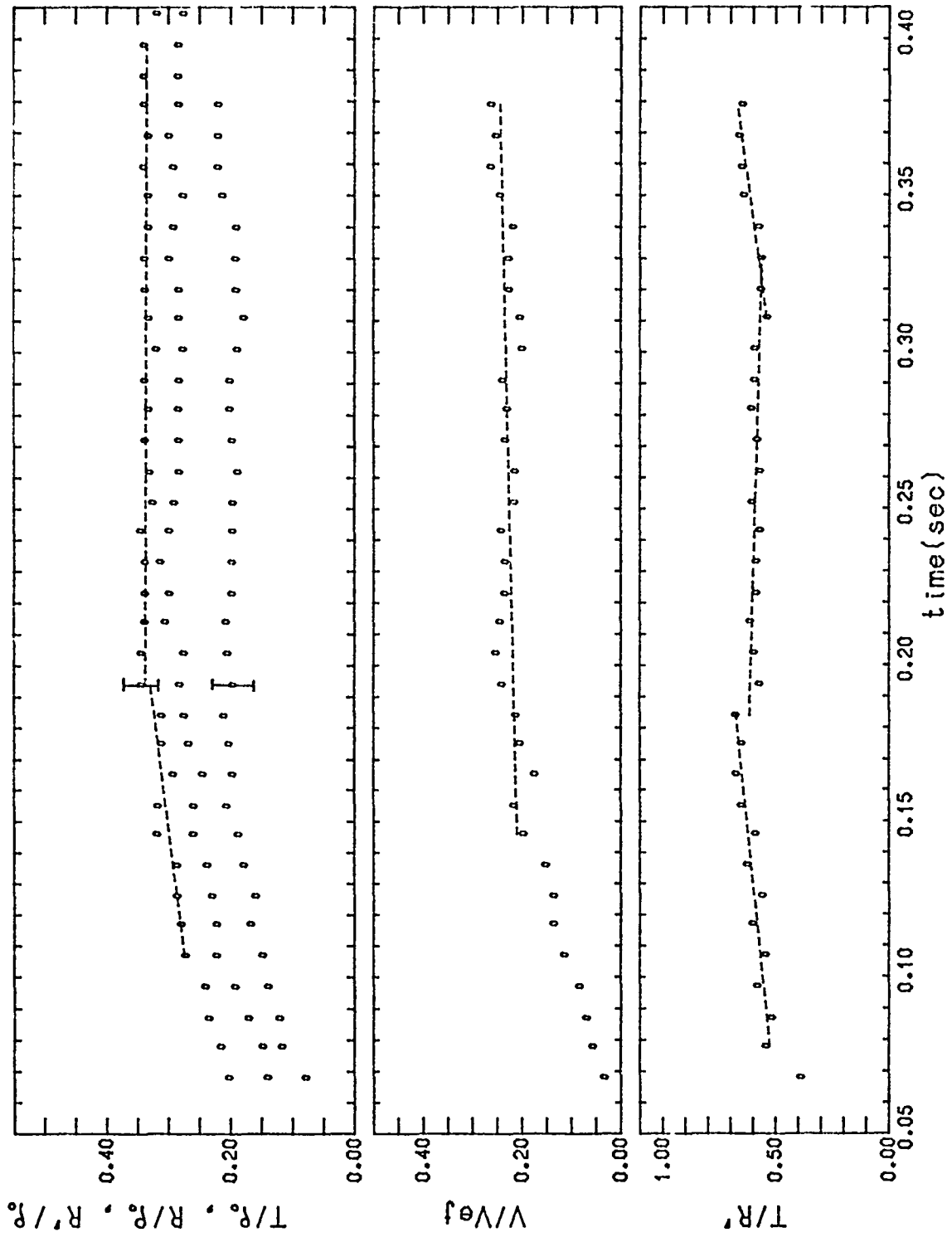


FIGURE A-4b  
 Run 4  $d/D = 0.15$   $Re_j = 38931$   
 Dye

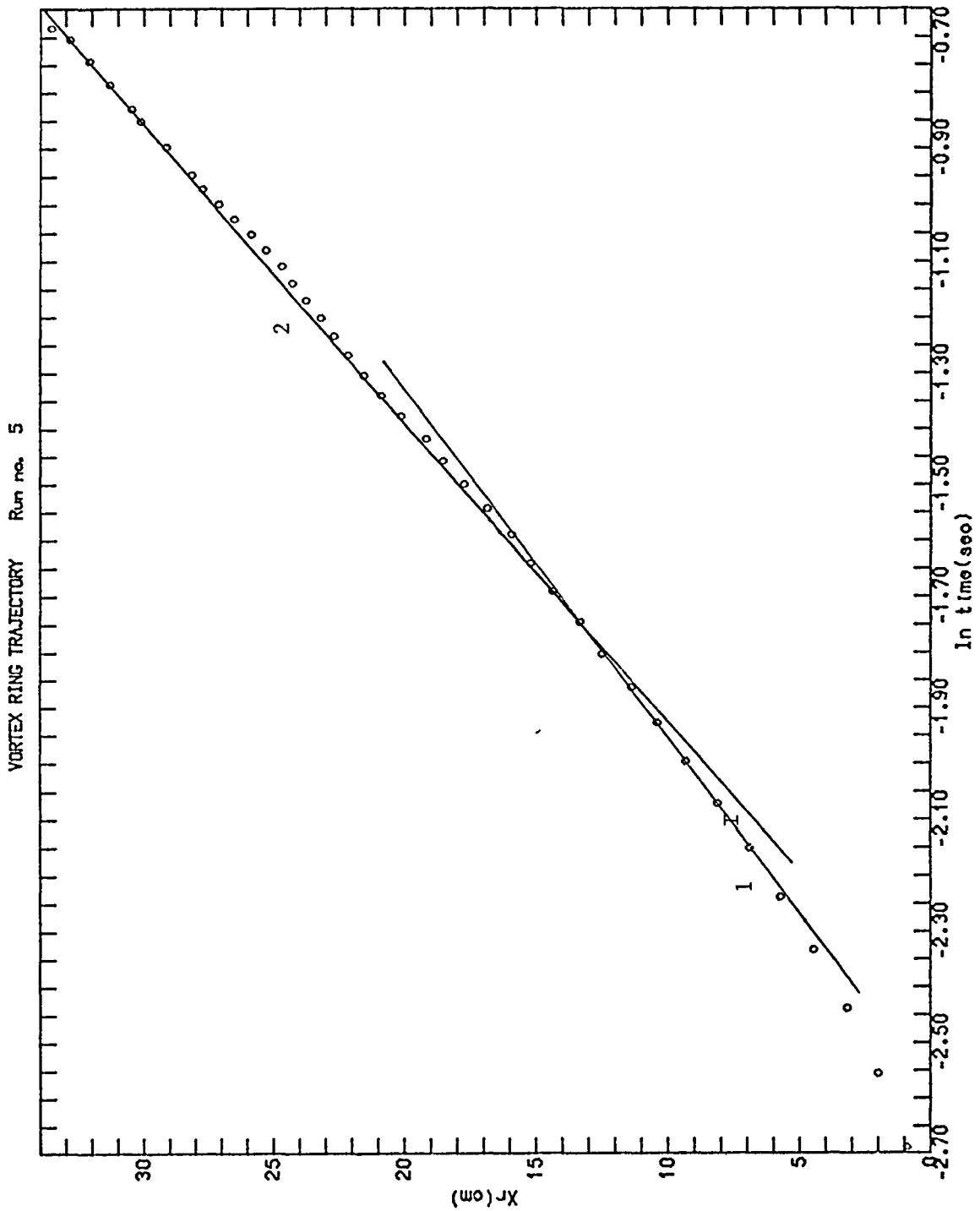


FIGURE A-5a  
 Run 5  $d/D = 0.15$   $Re_j = 36456$   
 Rocking oscillation. (Section 4-4.3)  
 $H_2$

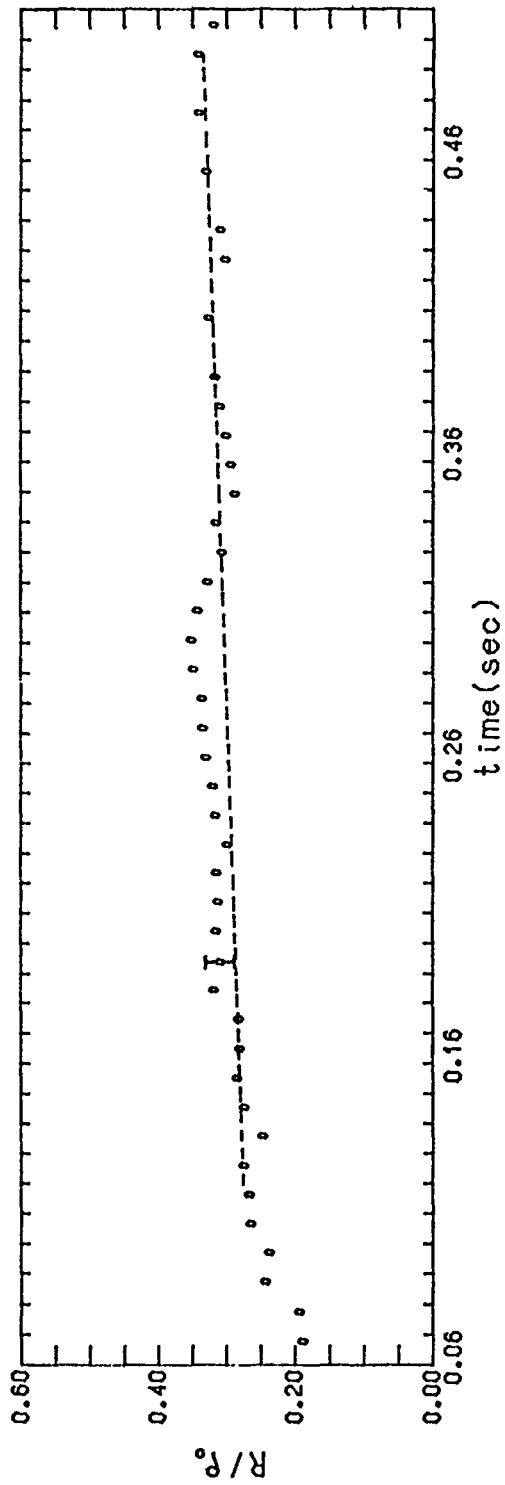


FIGURE A-5b  
Run 5  $d/D = 0.15$   $Re_j = 36456$   
Rocking oscillation.  
 $H_2$

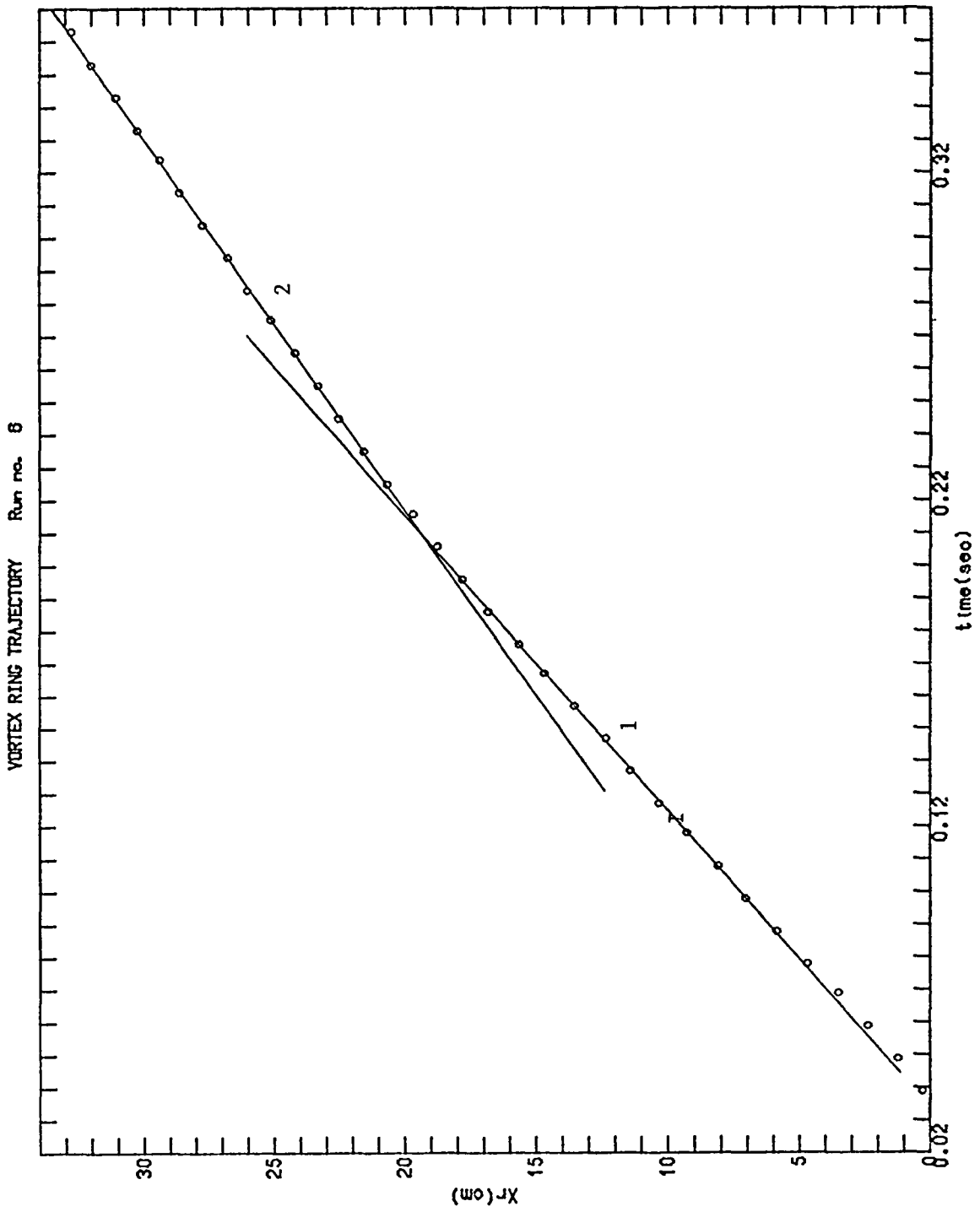


FIGURE A-6a  
 Run 6  $d/D = 0.15$   $Re_j = 29508$   
 Dye

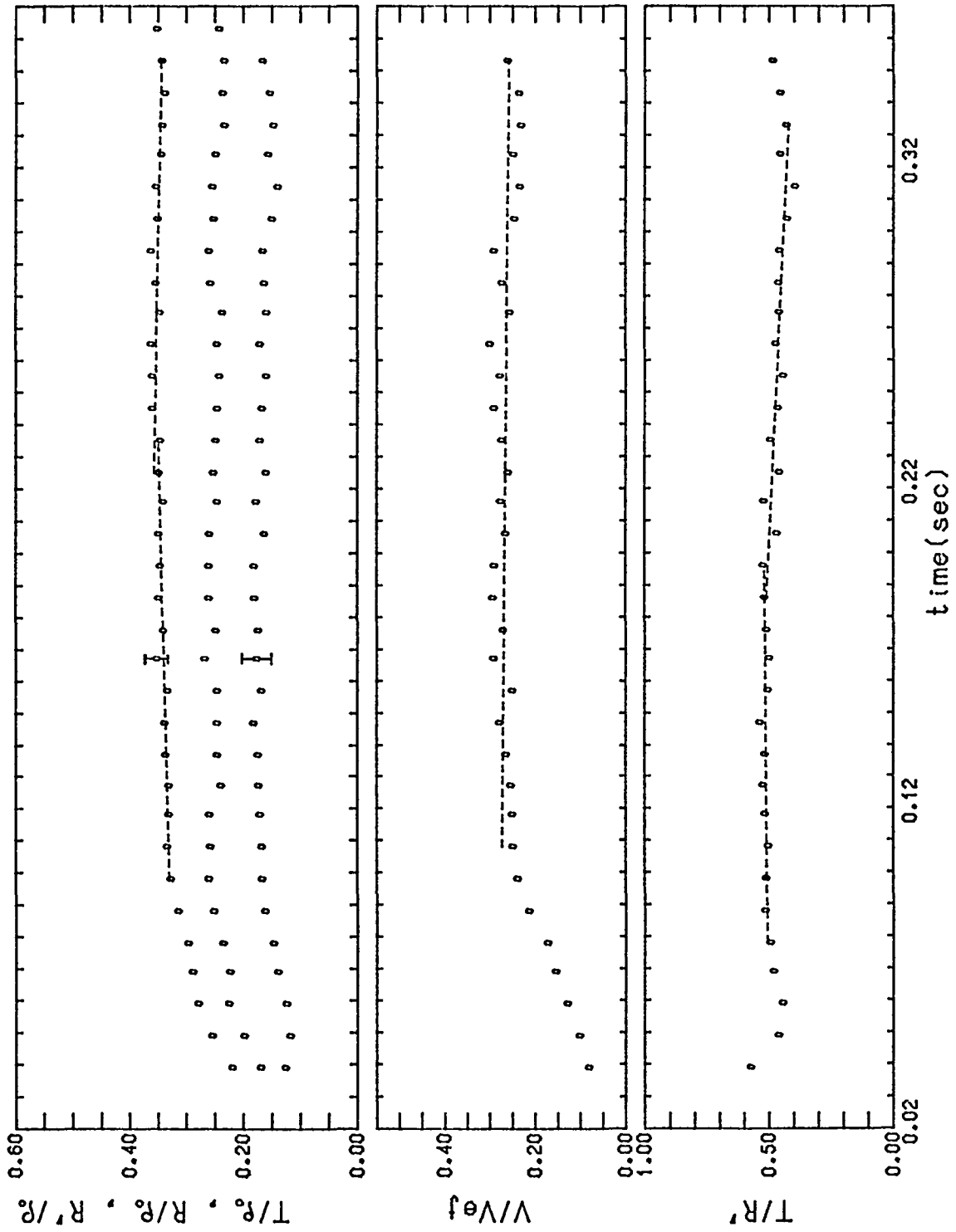


FIGURE A-6b  
 Run 6  $d/D = 0.15$   $Re_j = 29508$   
 Dye

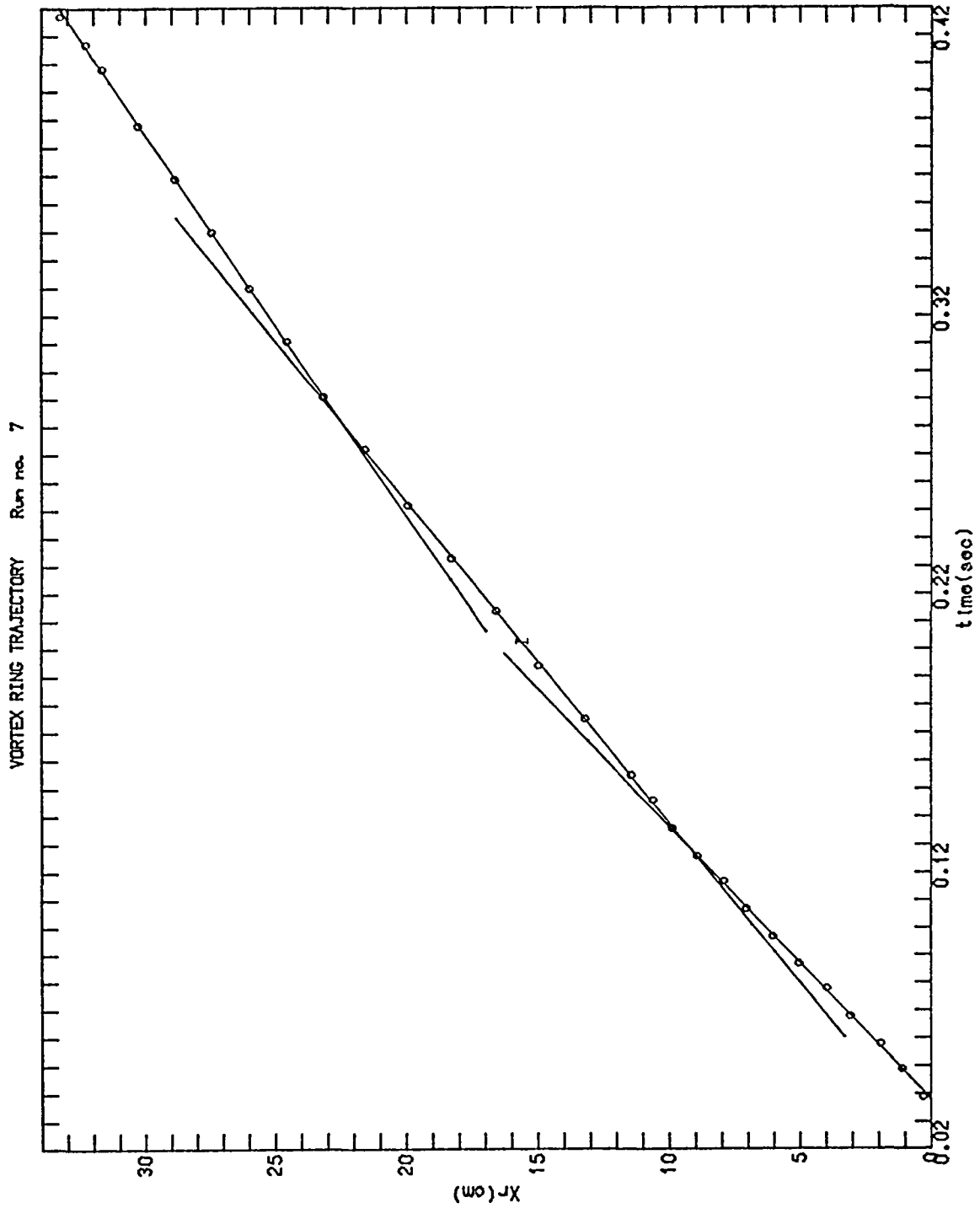


FIGURE A-7a  
 Run 7     $d/D = 0.15$      $Re_j = 25719$   
 $H_2$

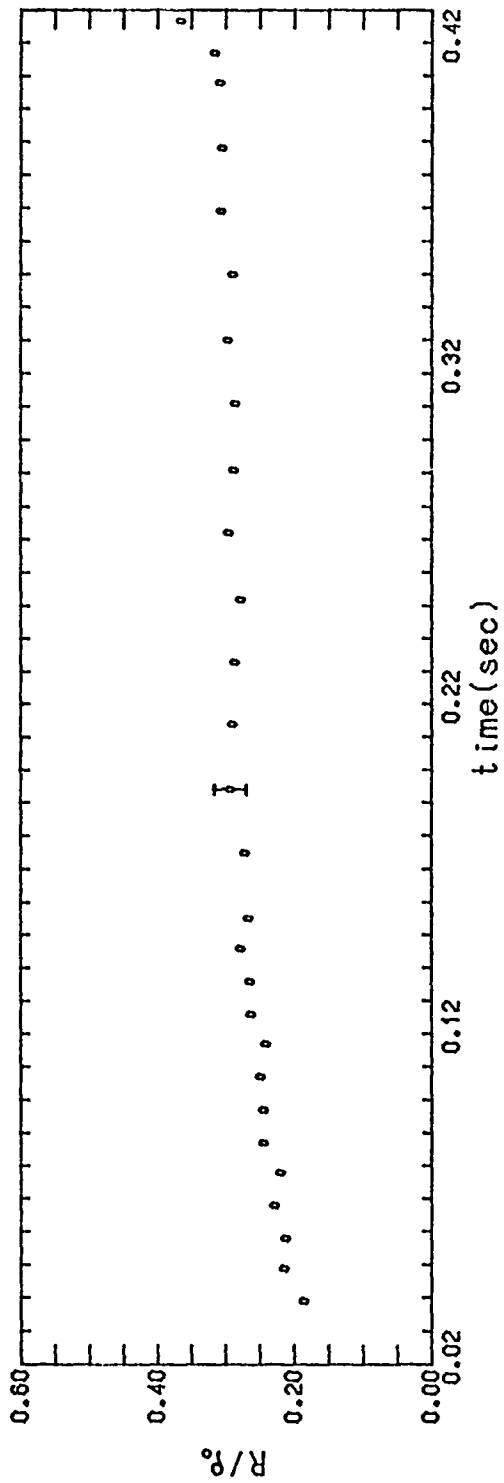


FIGURE A-7b  
 Run 7  $d/D = 0.15$   $Re_j = 25719$   
 $H_2$

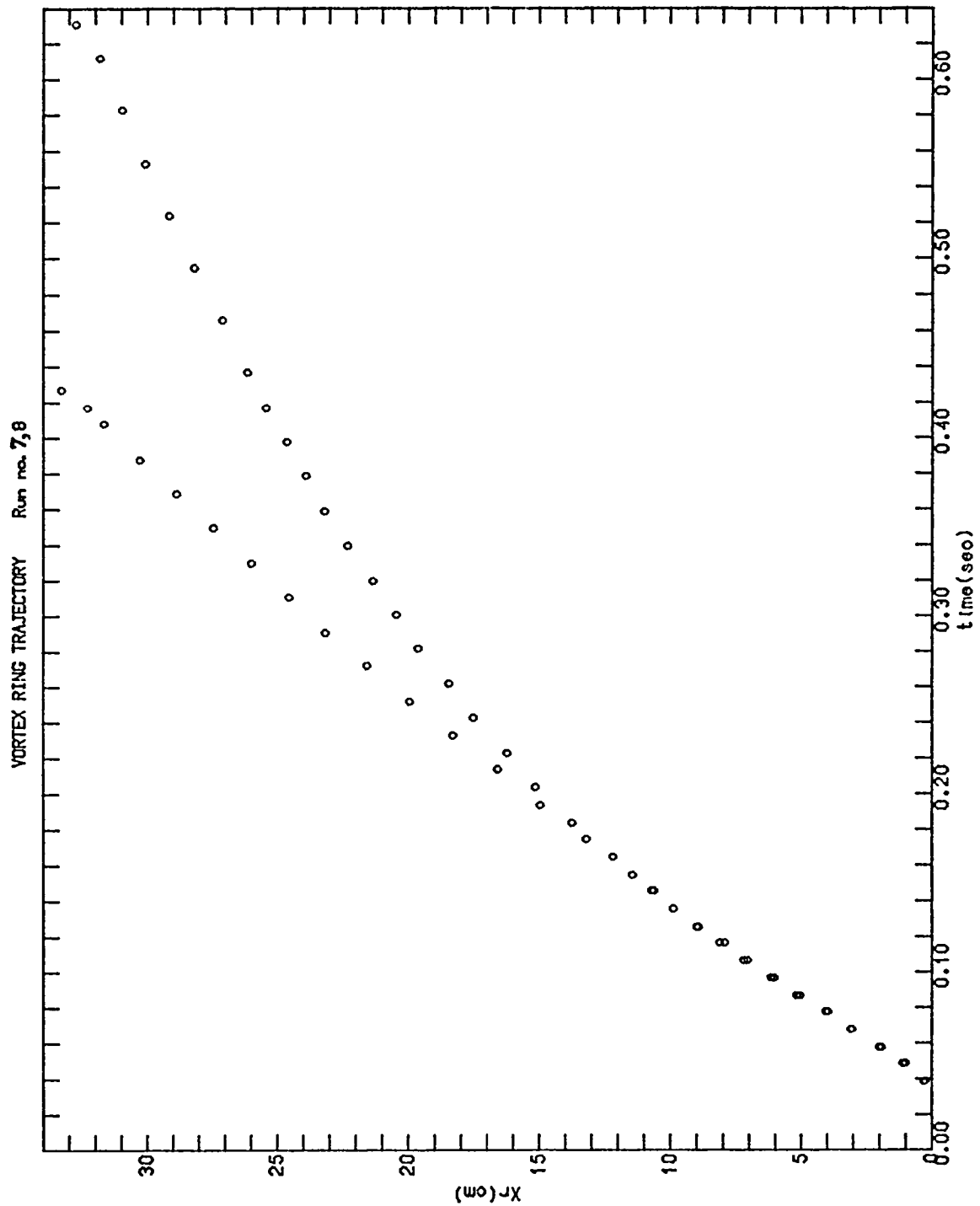


FIGURE A-8

Run 8  $d/D = 0.15$   $Re_j = 24796$  $H_2$ 

The effect of turbulence in the ambient fluid.

Upper points: Run 7

Lower points: Run 8

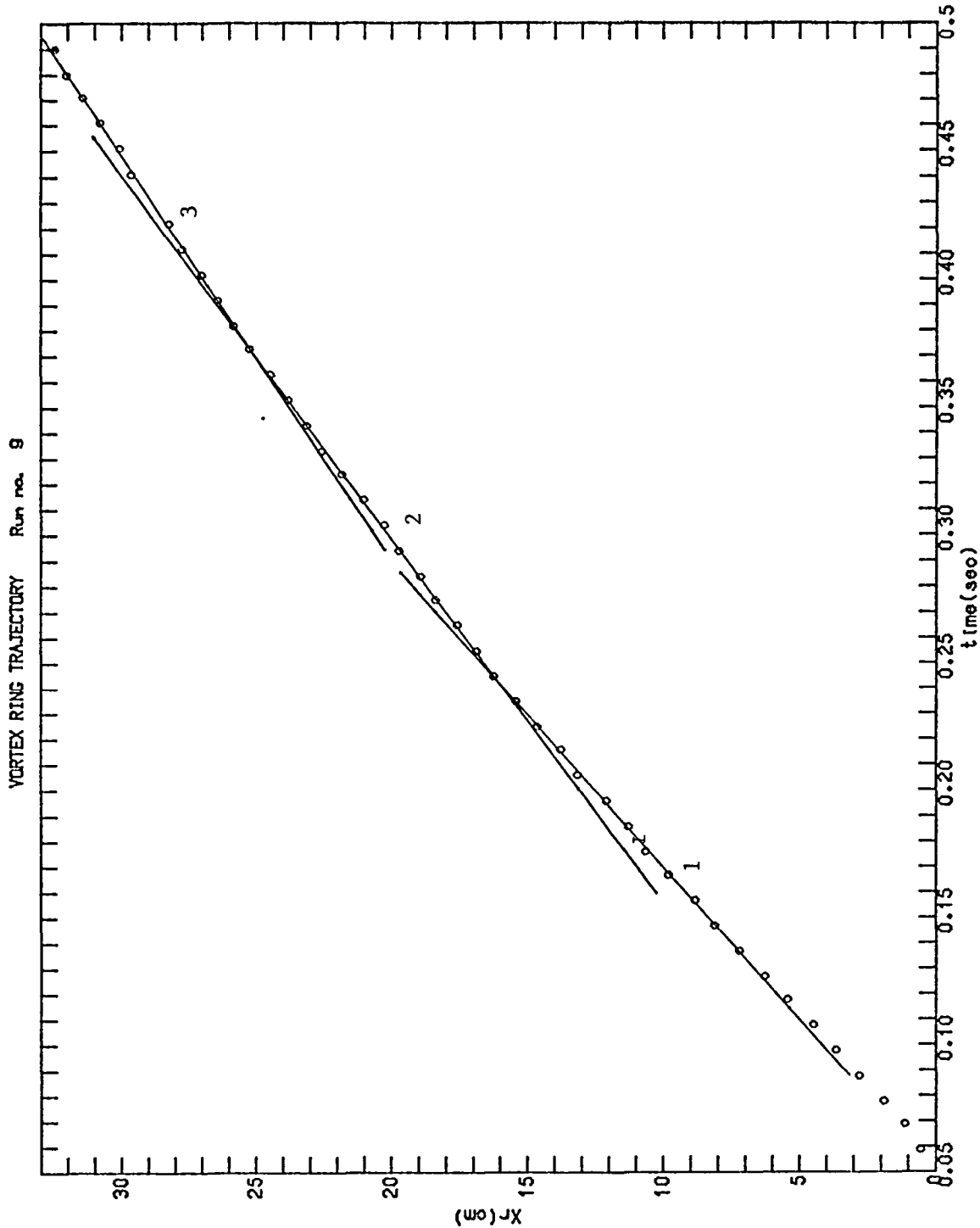
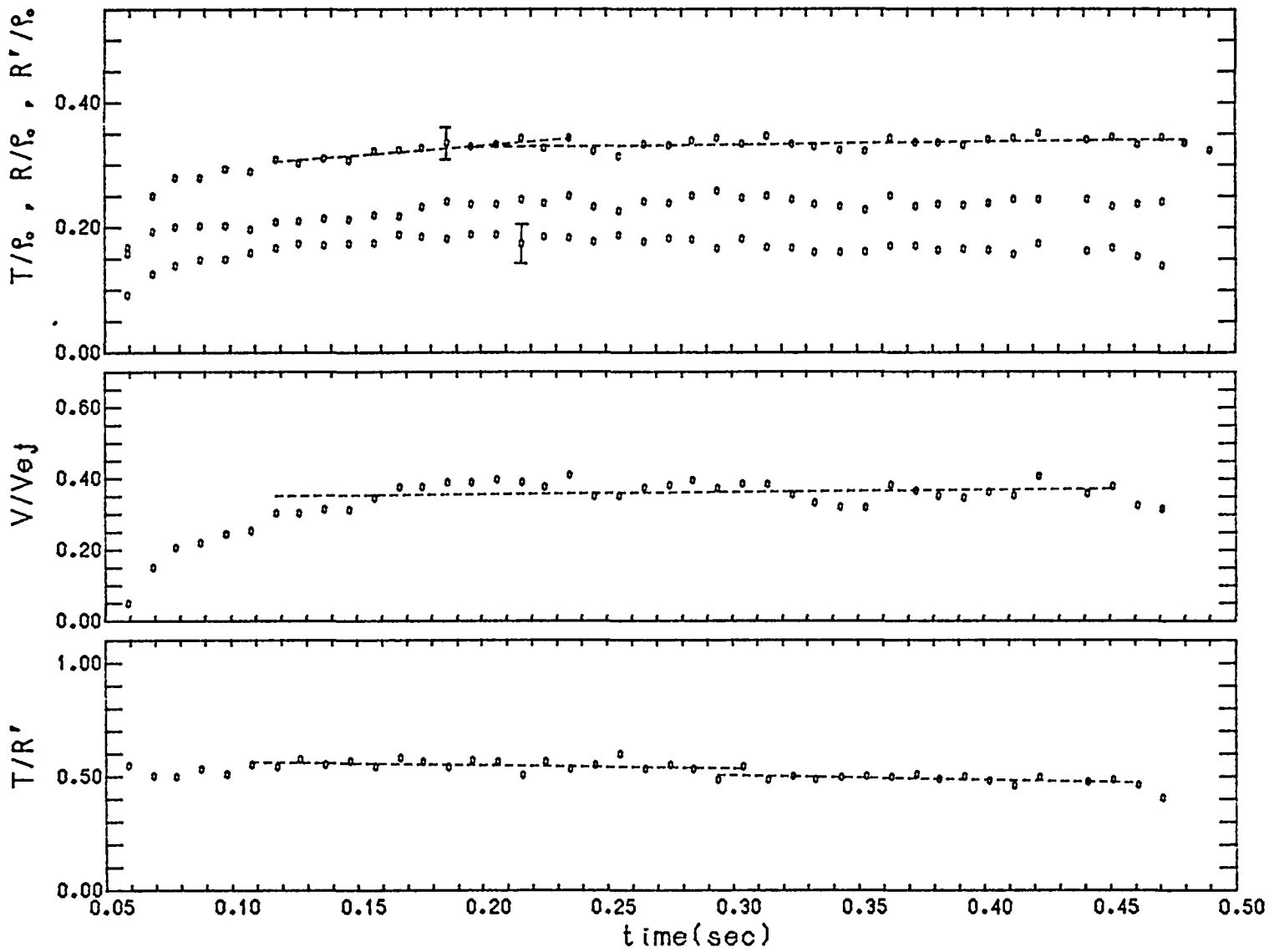


FIGURE A-9a  
Run 9  $d/D = 0.15$   $Re_j = 17664$   
Dye  
Repeatability: see Fig. 4-8

FIGURE A-9b  
Run 9  $d/D = 0.15$   $Re_j = 17664$   
Dye



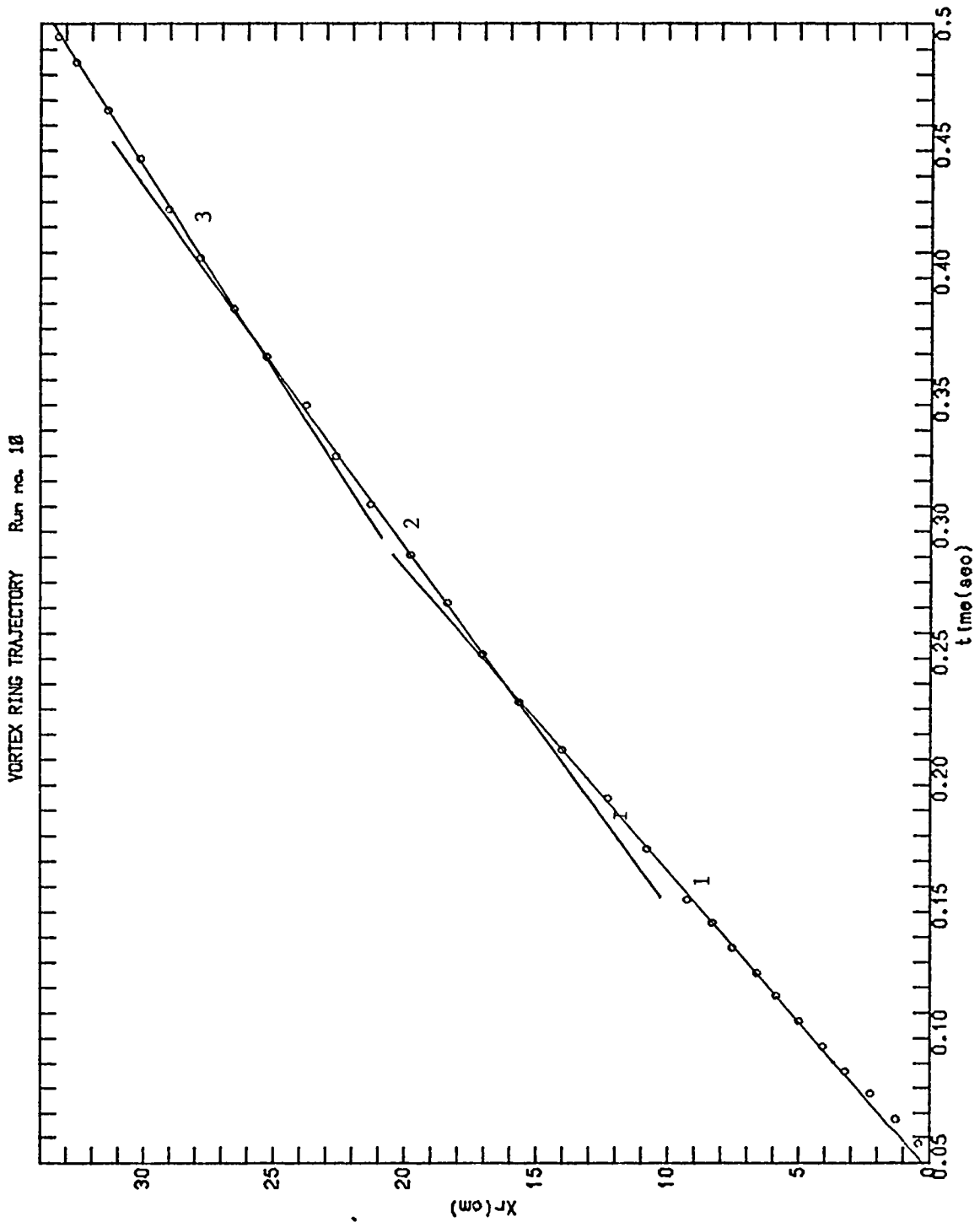


FIGURE A-10a  
 Run 10  $d/D = 0.15$   $Re_j = 17831$   
 $H_2$

Repeatability: see Fig. 4-8

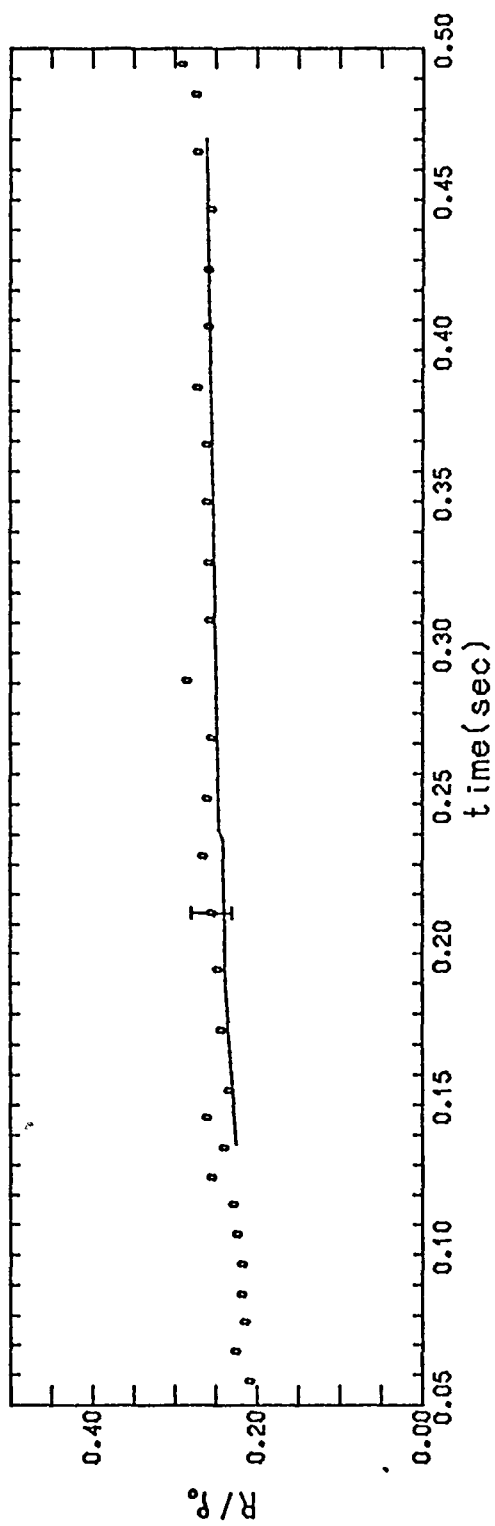


FIGURE A-10b  
 Run 10  $d/D = 0.15$   $Re_j = 17831$   
 $H_2$

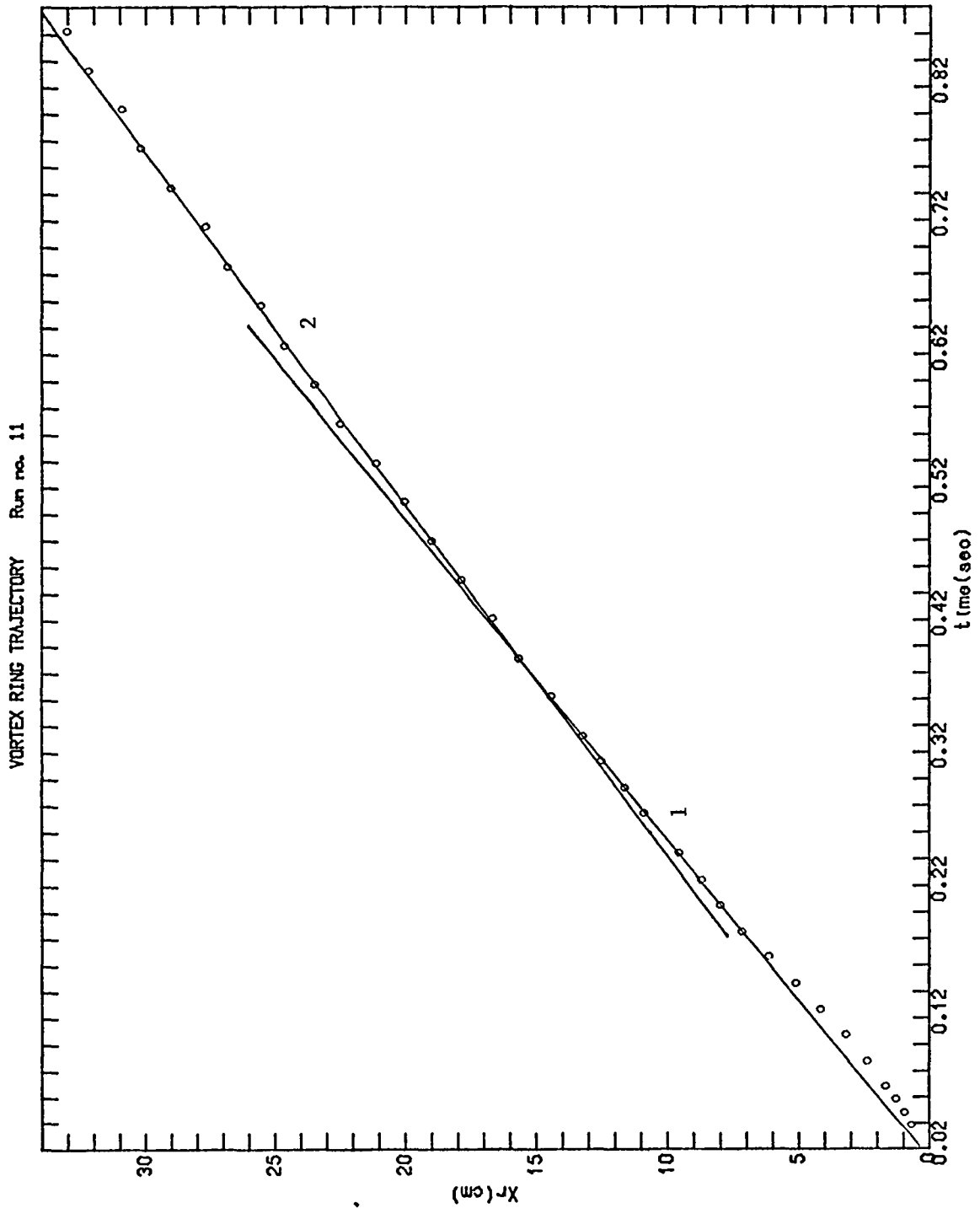


FIGURE A-11a  
 Run 11  $d/D = 0.25$   $Re_j = 24649$   
 Dye

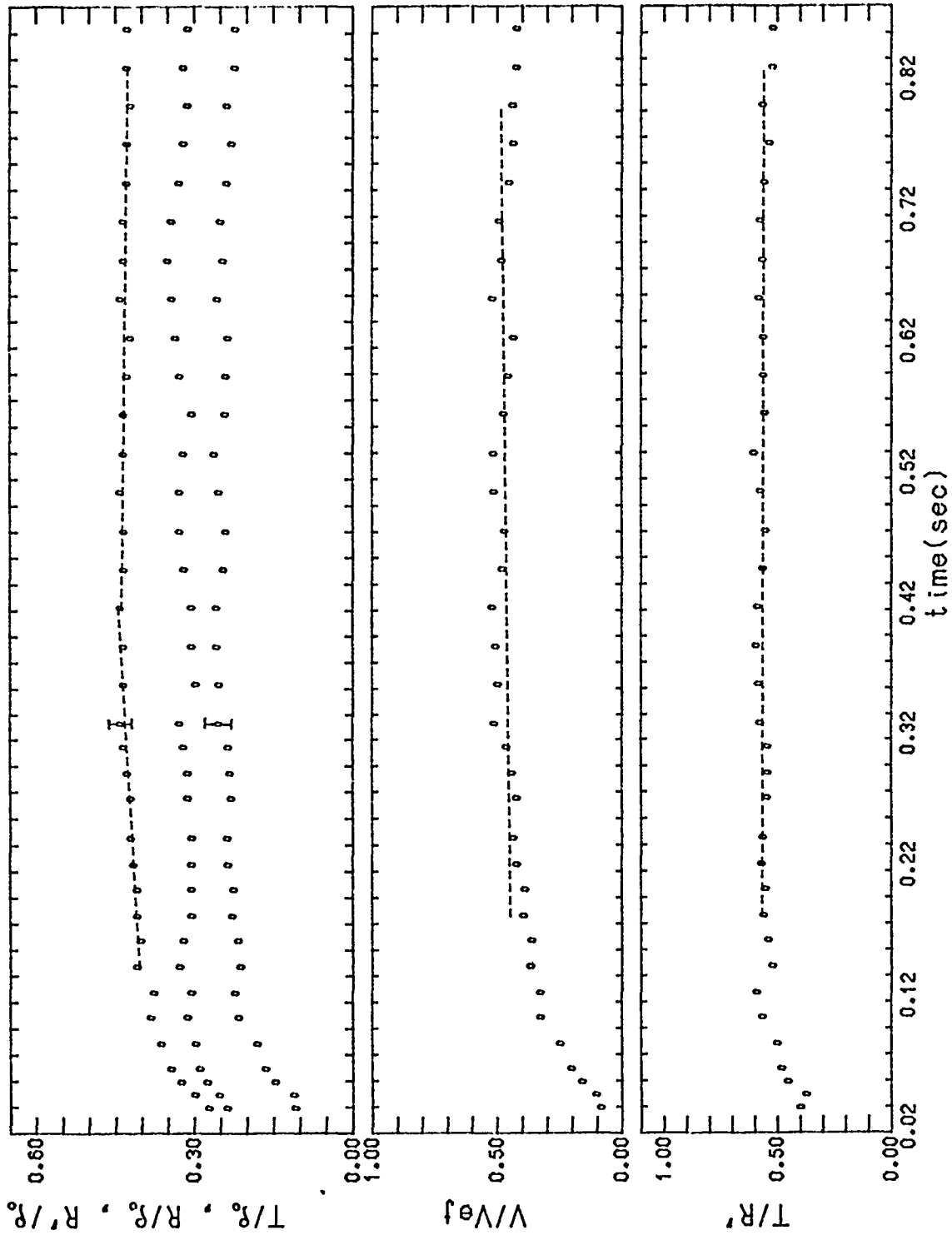


FIGURE A-11b  
 Run 11  $d/D = 0.25$   $Re_j = 24649$   
 Dye

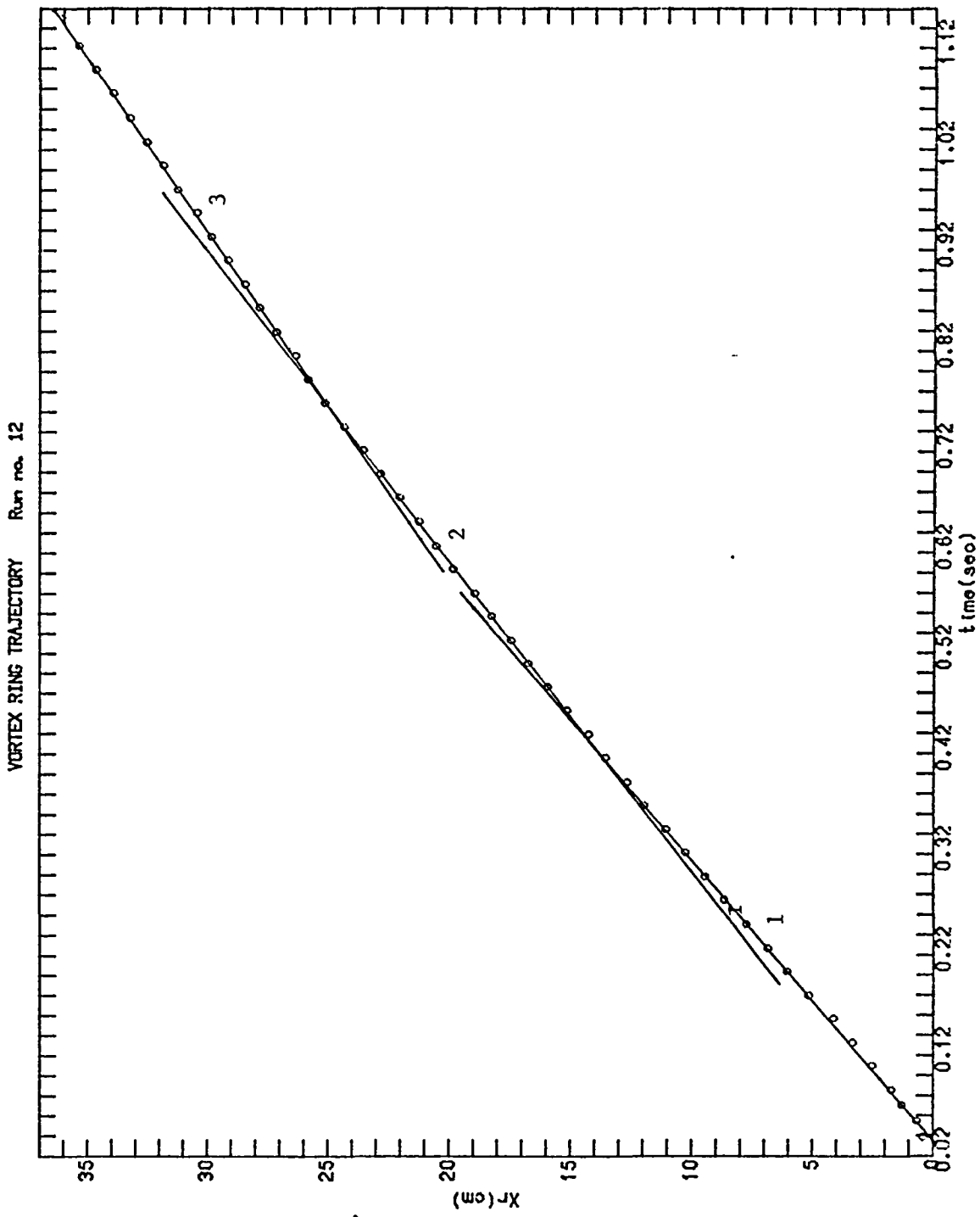


FIGURE A-12a  
 Run 12     $d/D = 0.25$      $Re_j = 21461$   
 $H_2$

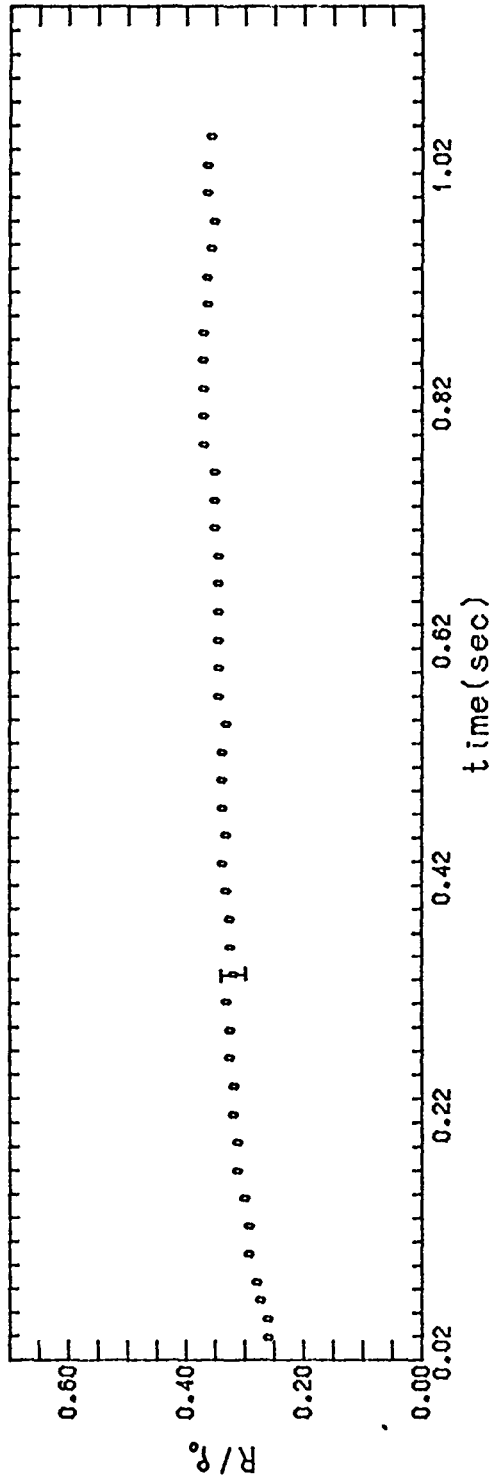


FIGURE A-12b  
Run 12     $d/D = 0.25$      $Re_j = 21461$   
 $H_2$

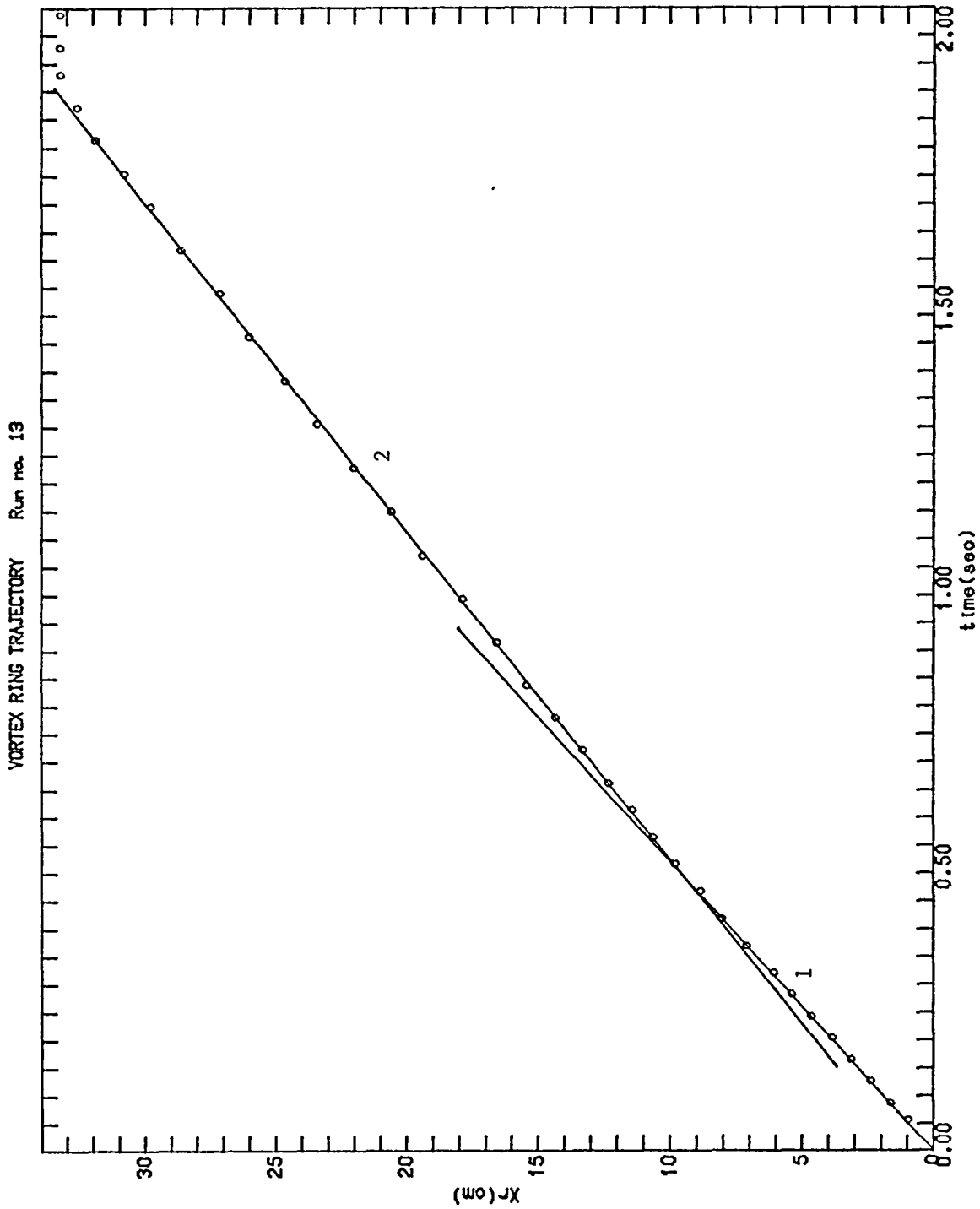


FIGURE A-13a  
Run 13  $d/D = 0.25$   $Re_j = 10388$   
Dye

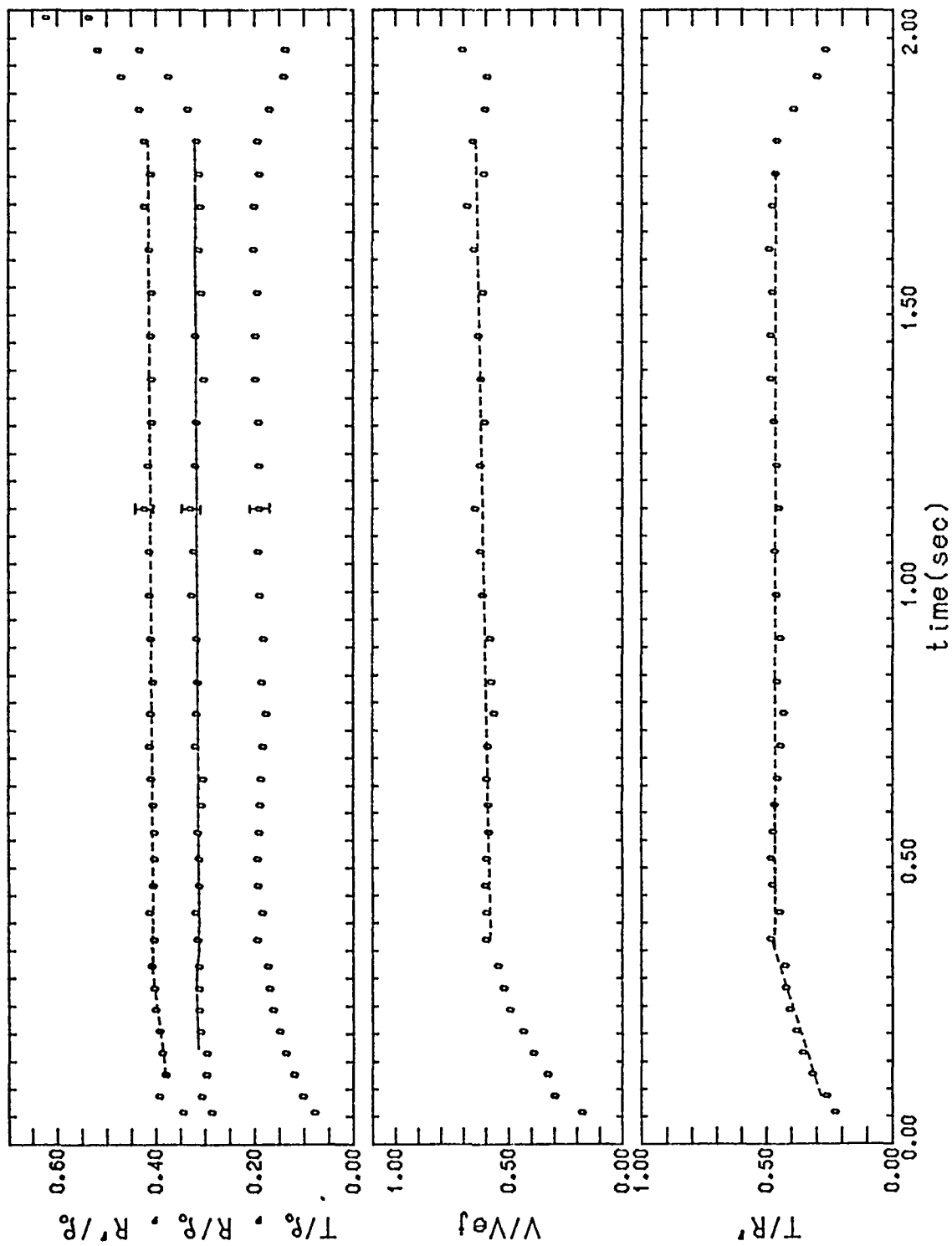


FIGURE A-13b  
 Run 13  $d/D = 0.25$   $Re_j = 10388$   
 Dye

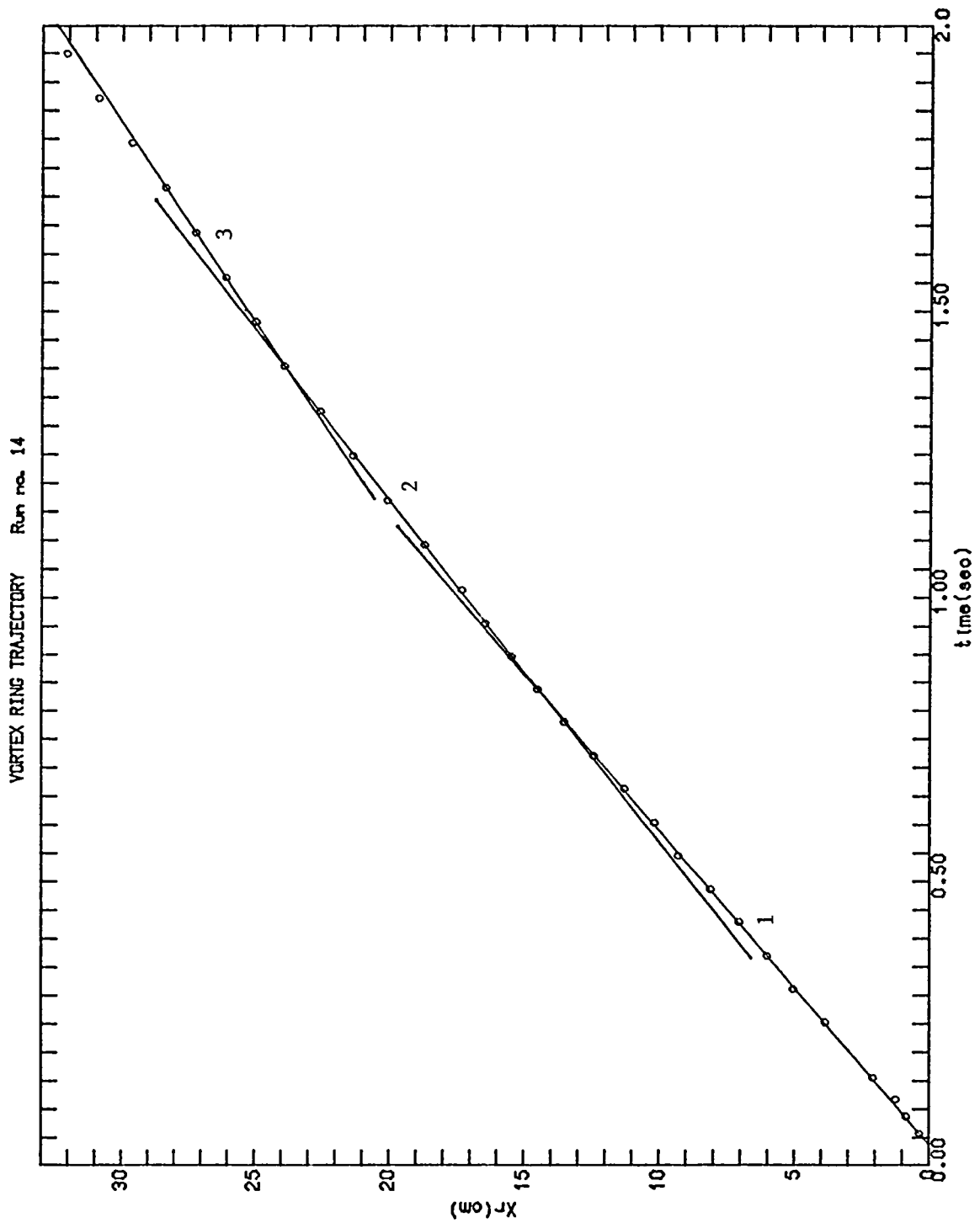


FIGURE A-14a  
 Run 14  $d/D = 0.32$   $Re_j = 16857$   
 Dye

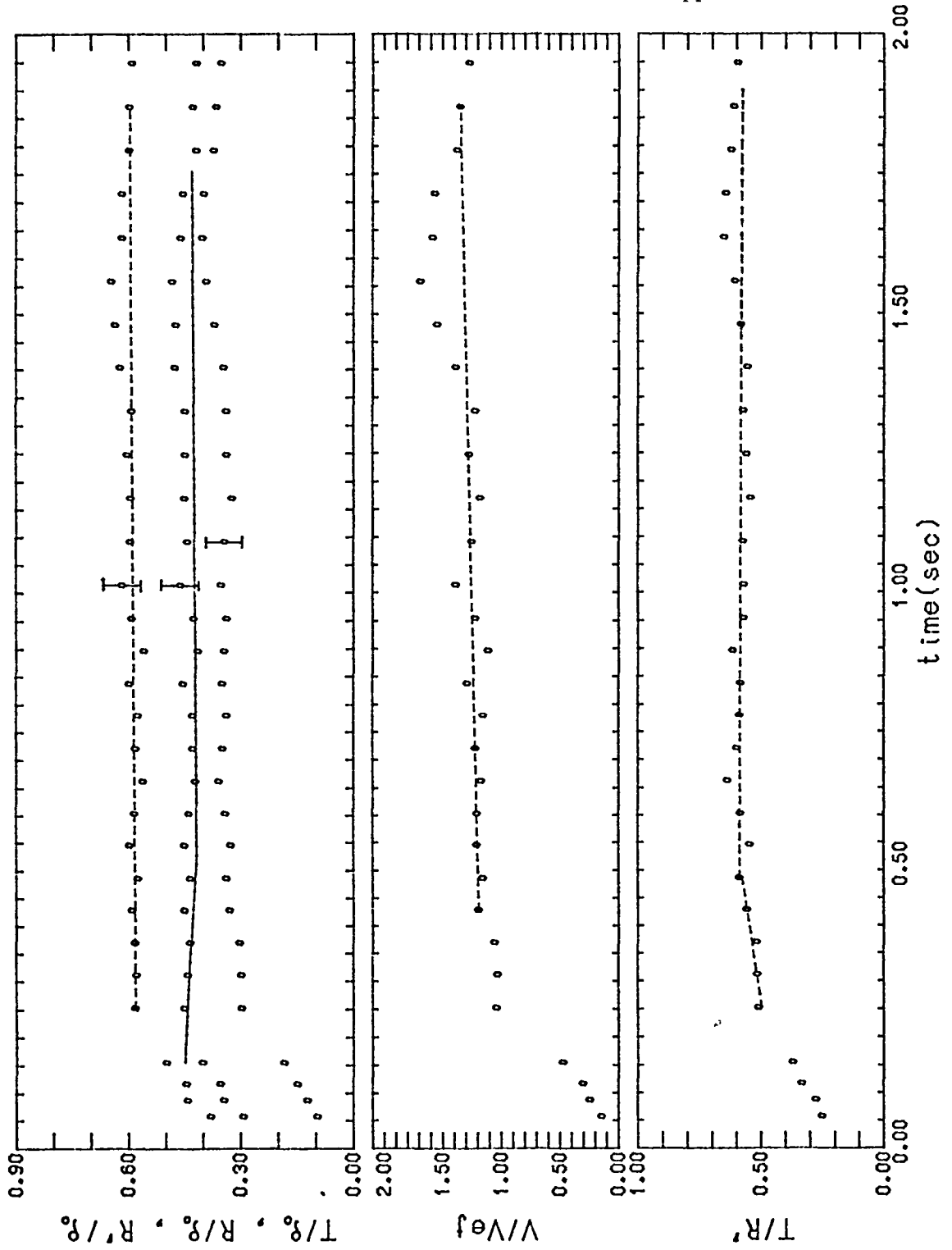


FIGURE A-14b  
 Run 14  $d/D = 0.32$   $Re_j = 16857$   
 Dye

Increase in  $R'$  due to a "bulge" in outer region (Section 4-4.2).

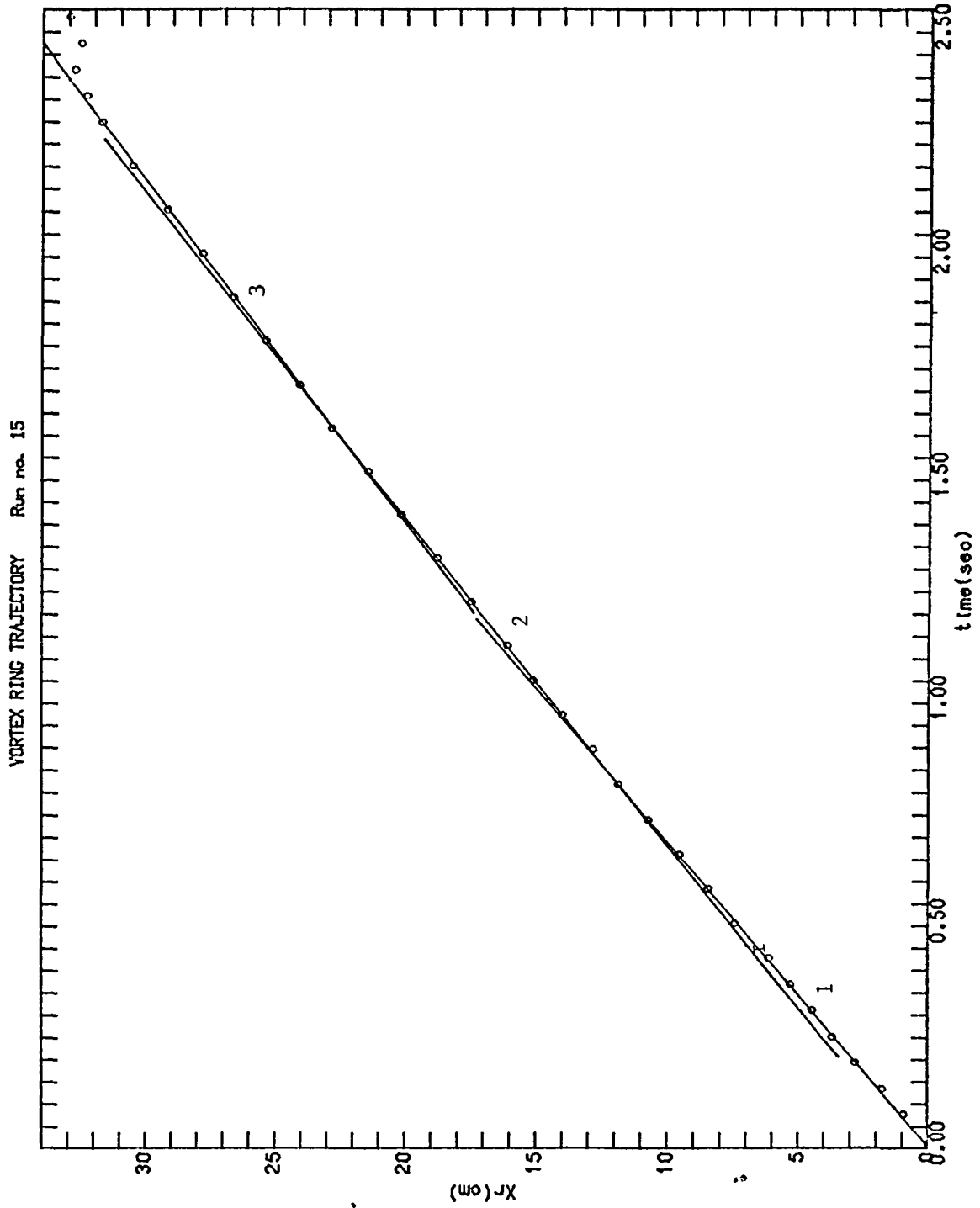


FIGURE A-15a  
 Run 15  $d/D = 0.32$   $Re_j = 12550$   
 Dye

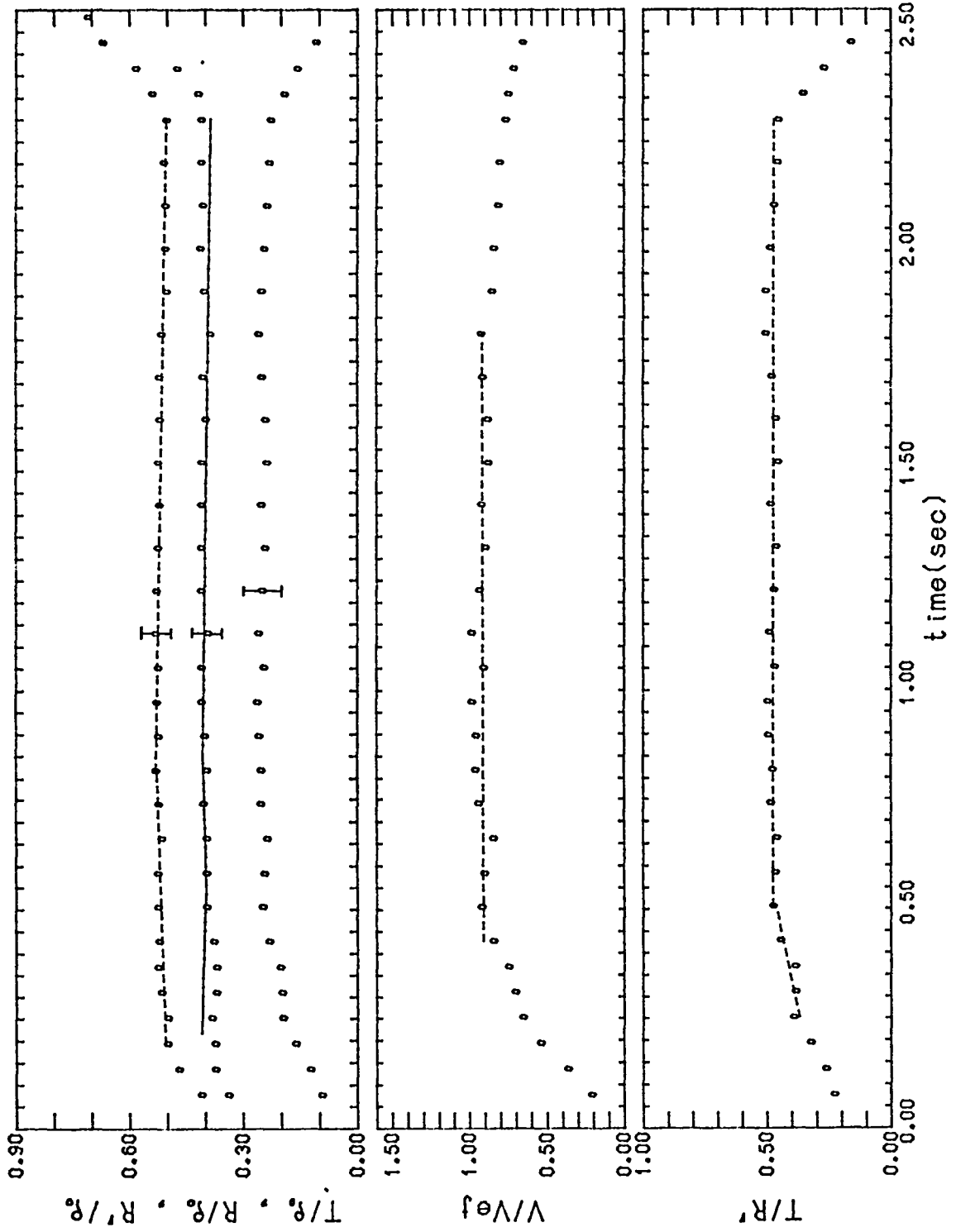


FIGURE A-15b  
 Run 15  $d/D = 0.32$   $Re_j = 12550$   
 Dye

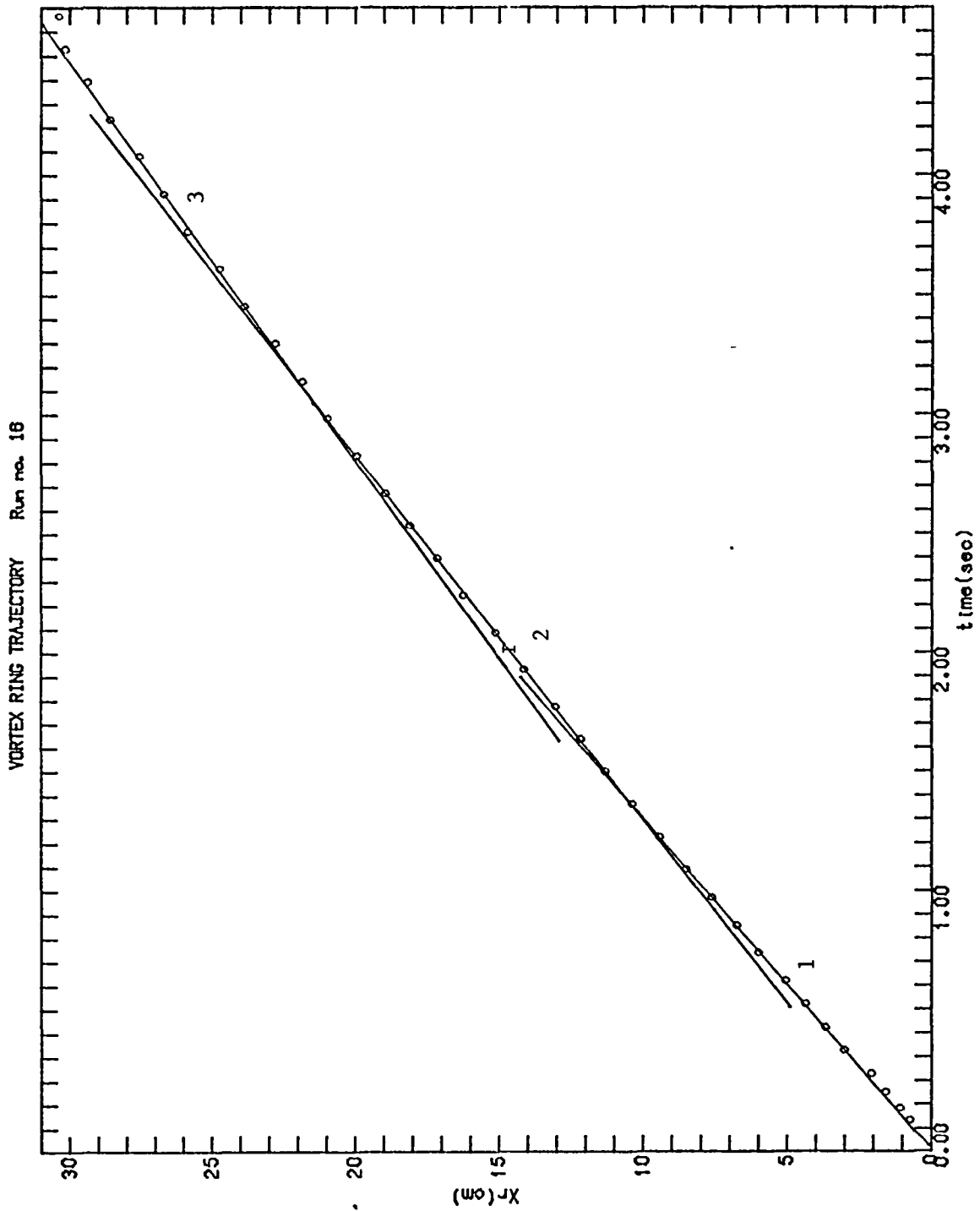


FIGURE A-16a  
 Run 16  $d/D = 0.32$   $Re_j = 8254$   
 Dye

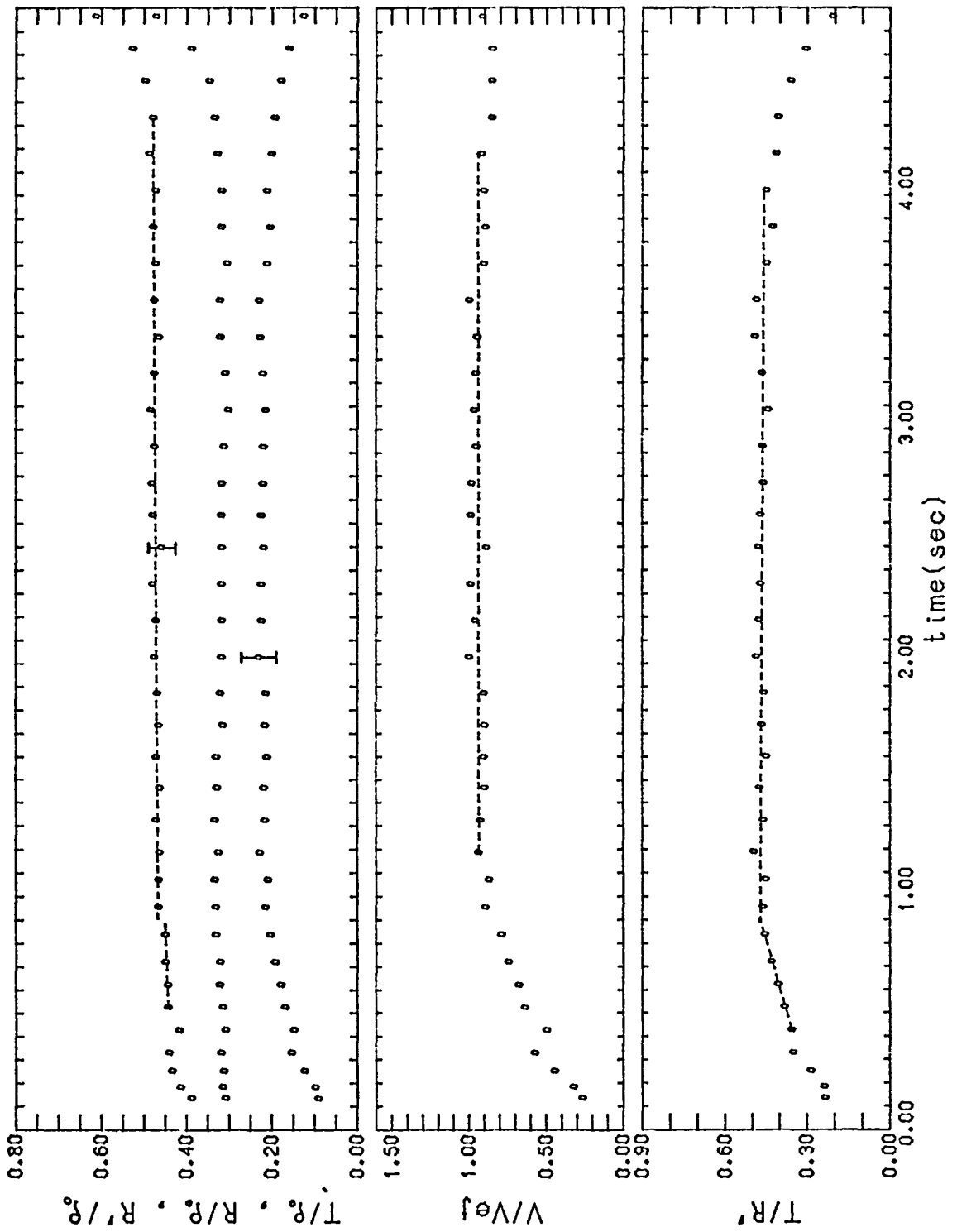


FIGURE A-16b  
 Run 16  $d/D = 0.32$   $Re_j = 8254$   
 Dye

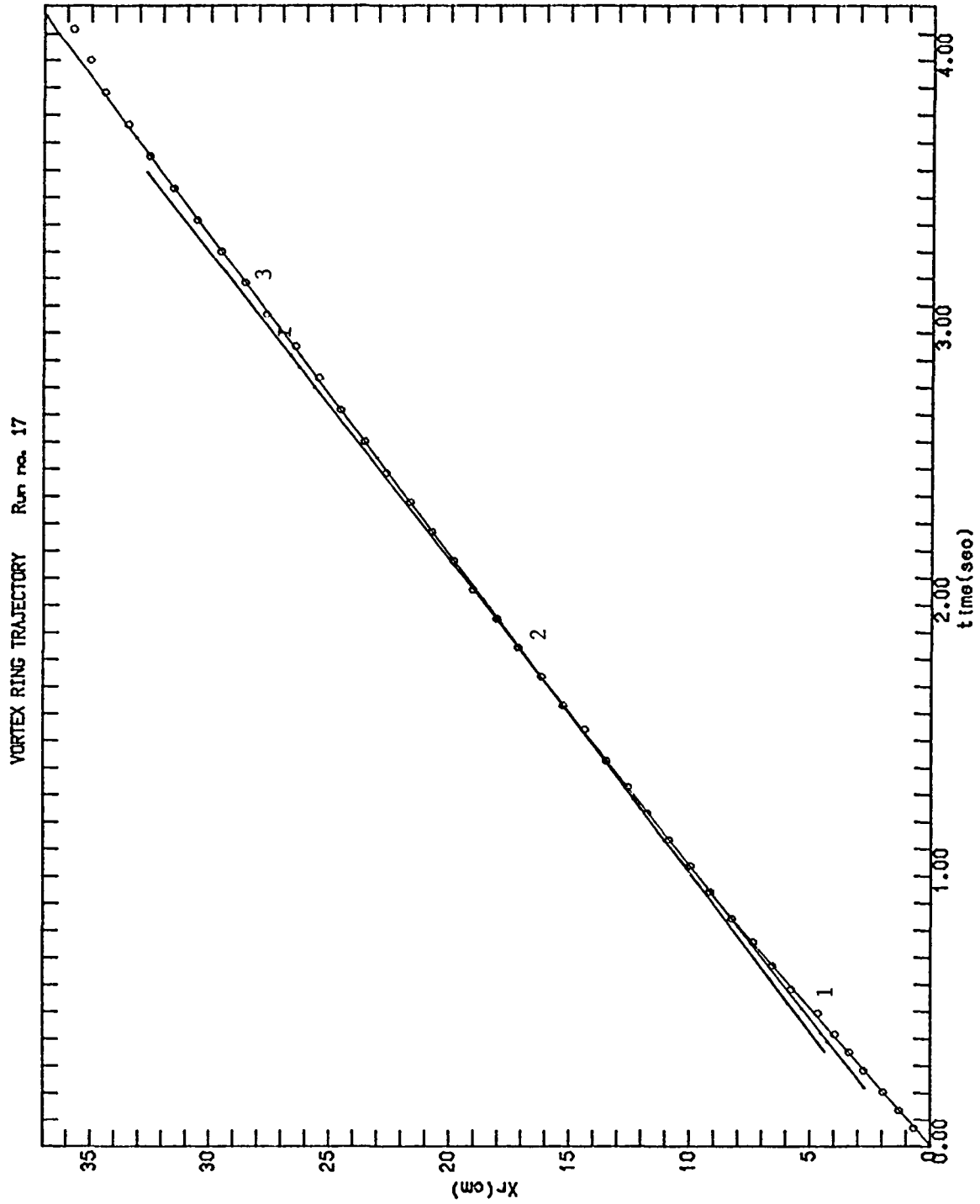


FIGURE A-17a  
Run 17  $d/D = 0.42$   $Re_j = 14596$   
Dye

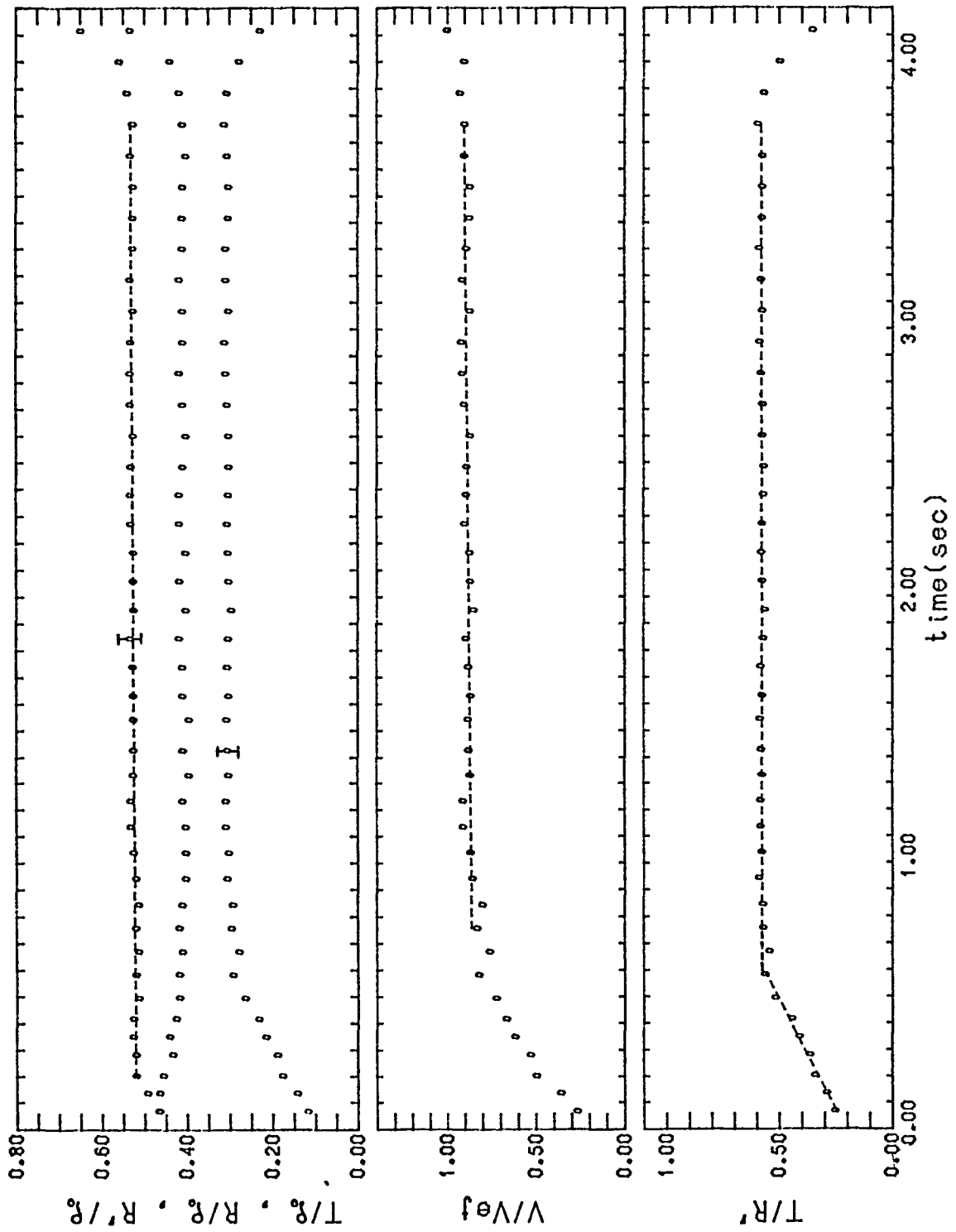


FIGURE A-17b  
 Run 17  $d/D = 0.42$   $Re_j = 14596$   
 Dye

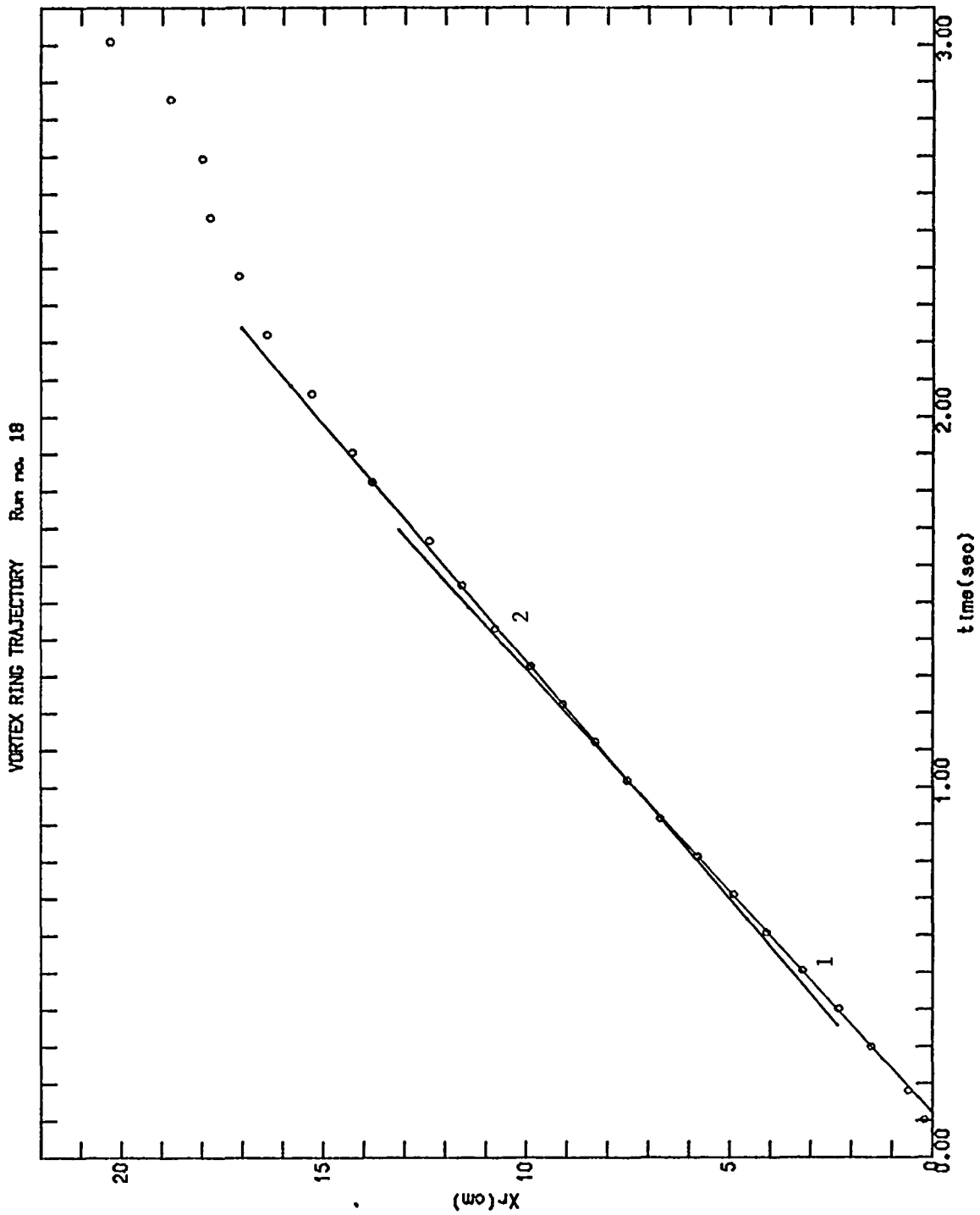


FIGURE A-18a  
Run 18  $d/D = 0.42$   $Re_j = 12852$   
 $H_2$

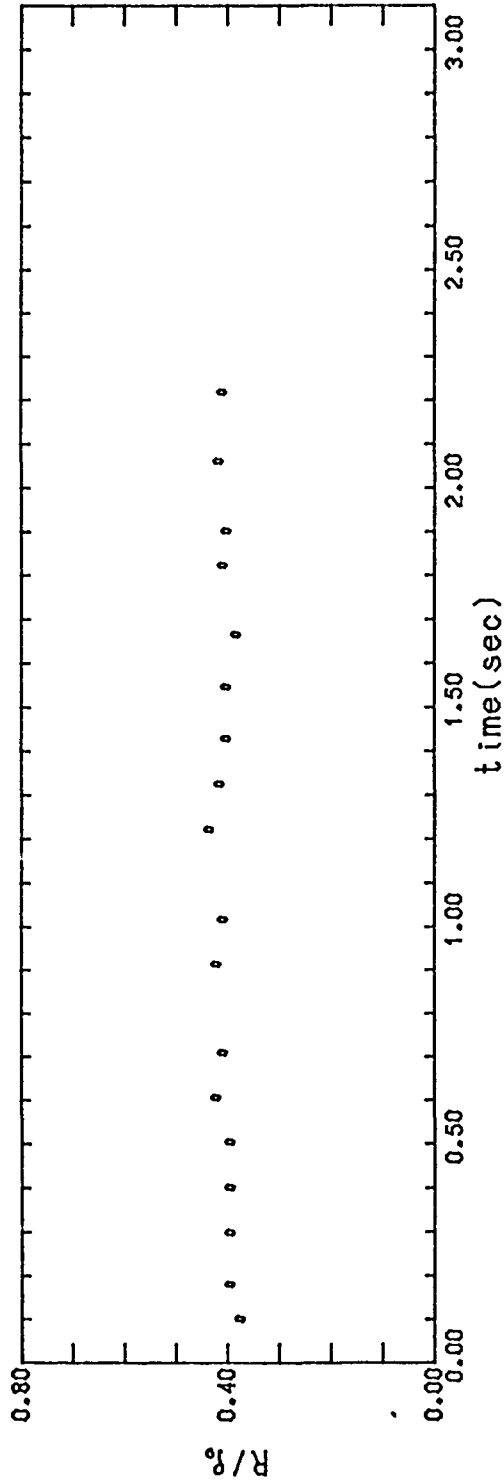


FIGURE A-18b  
 Run 18  $d/D = 0.42$   $Re_j = 12852$   
 $H_2$

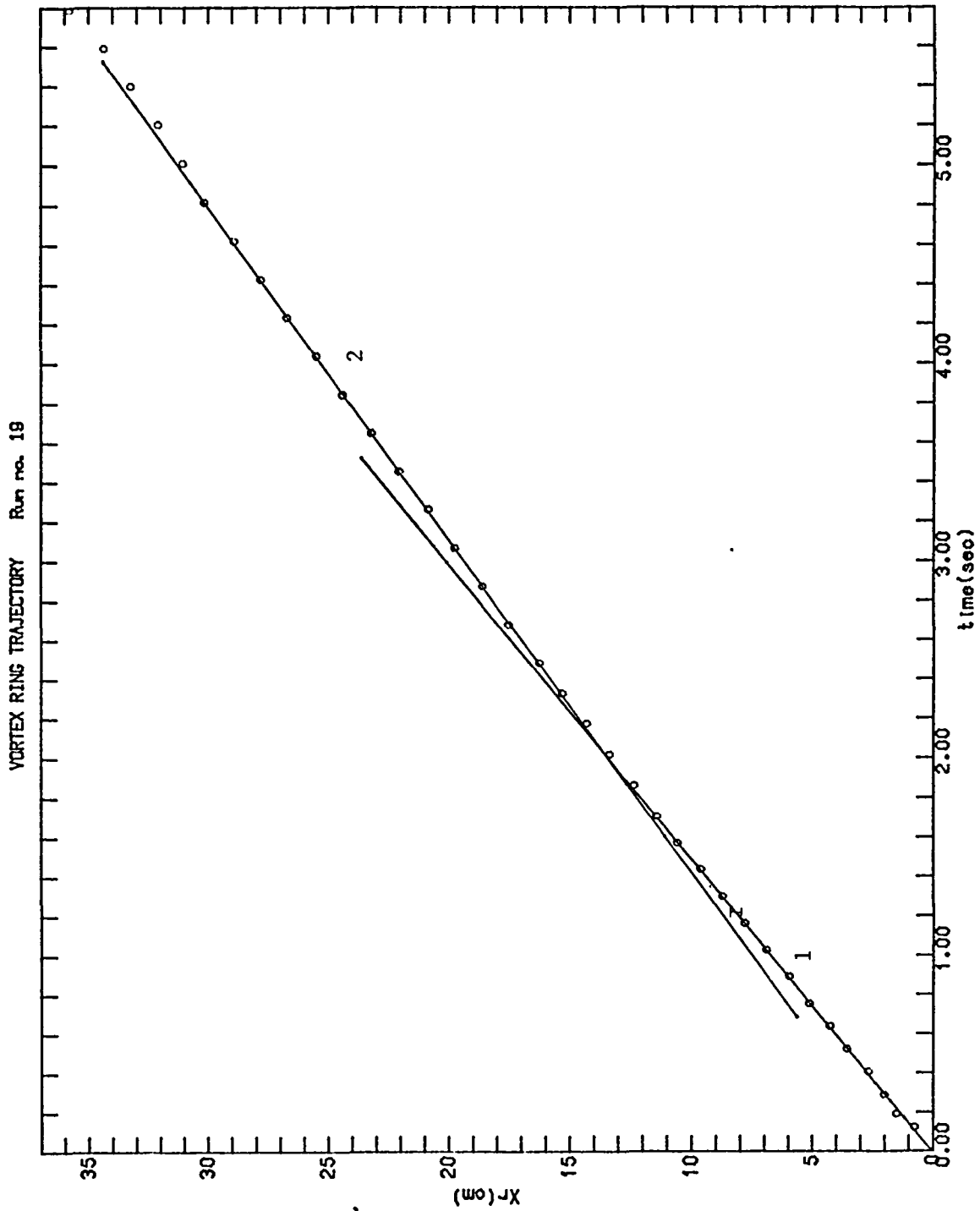


FIGURE A-19a  
 Run 19  $d/D = 0.42$   $Re_j = 10136$   
 Dye

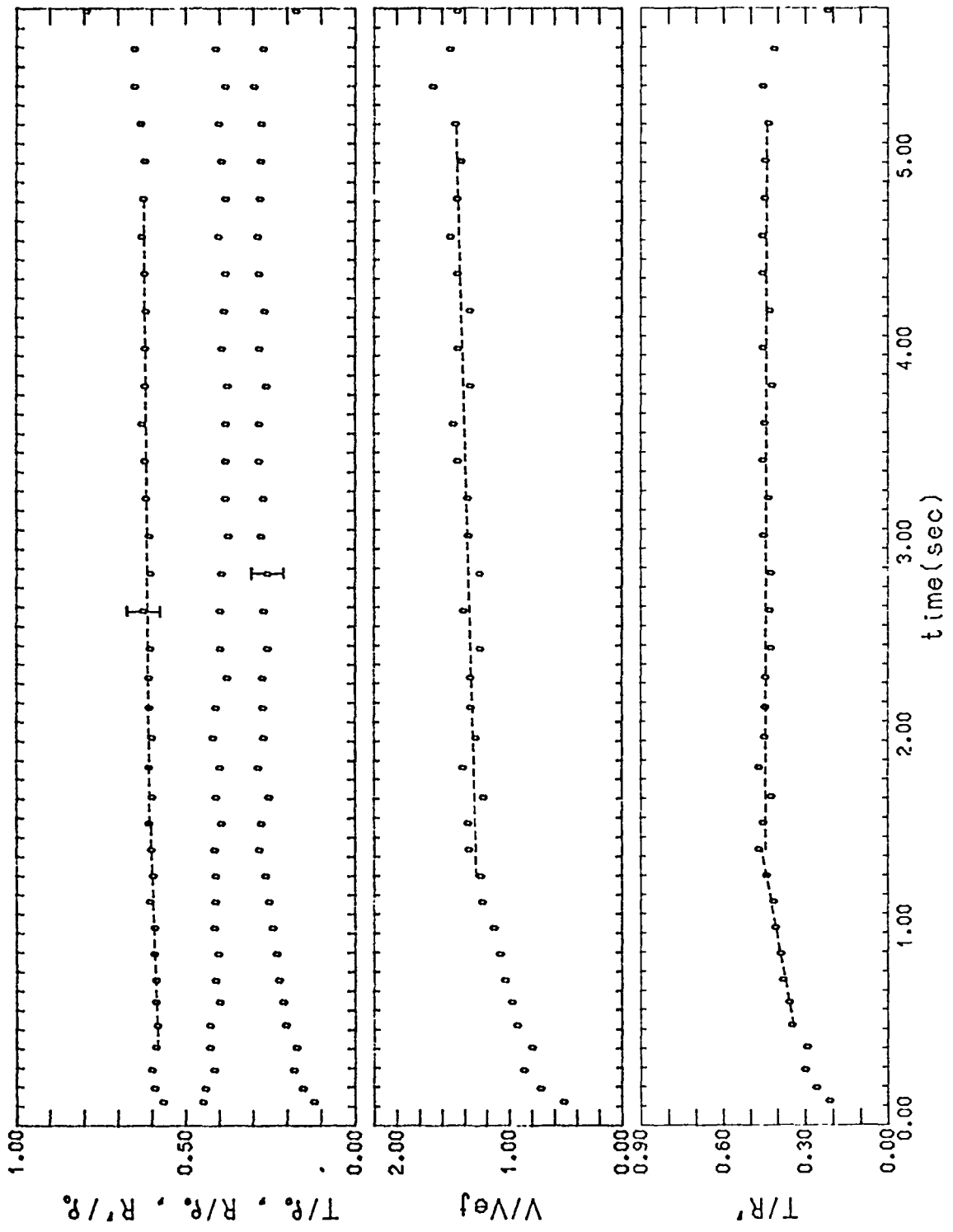


FIGURE A-19b  
 Run 19  $d/D = 0.42$   $Re_j = 10136$   
 Dye

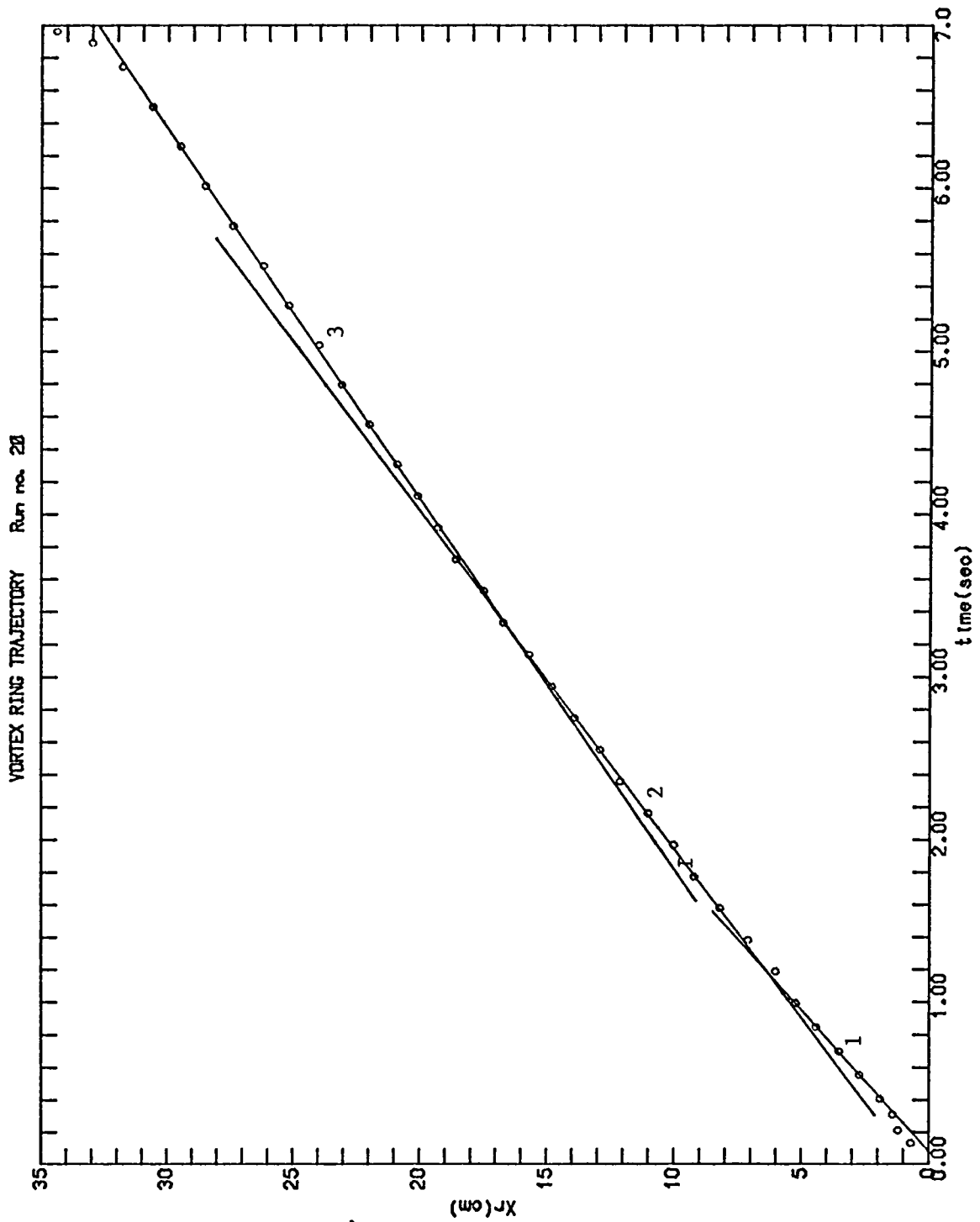


FIGURE A-20a  
 Run 20  $d/D = 0.48$   $Re_j = 11366$   
 Dye

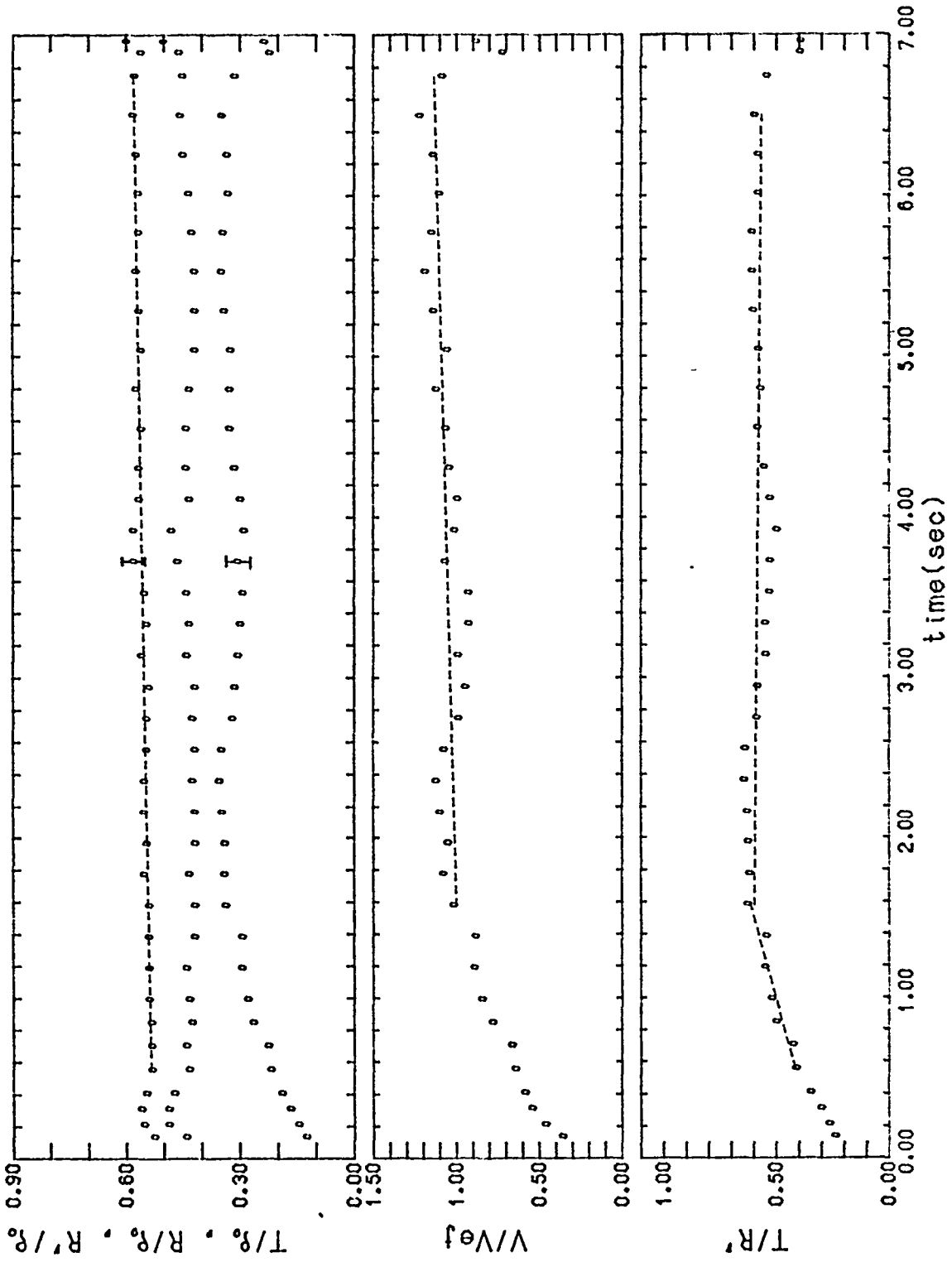


FIGURE A-20b  
 Run 20  $d/D = 0.48$   $Re_j = 11366$   
 Dye

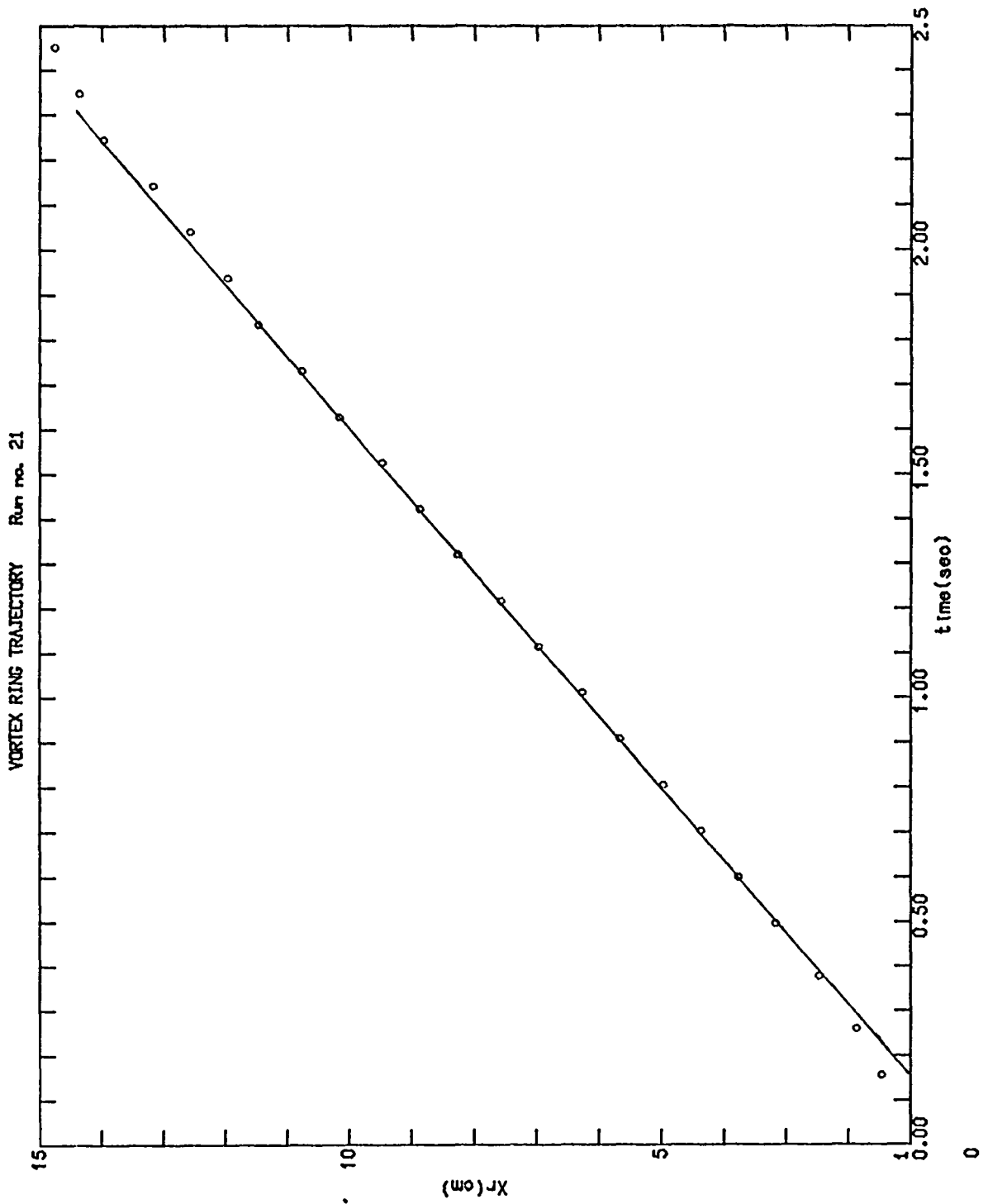


FIGURE A-21  
Run 21  $d/D = 0.48$   $Re_j = 11881$   
 $H_2$

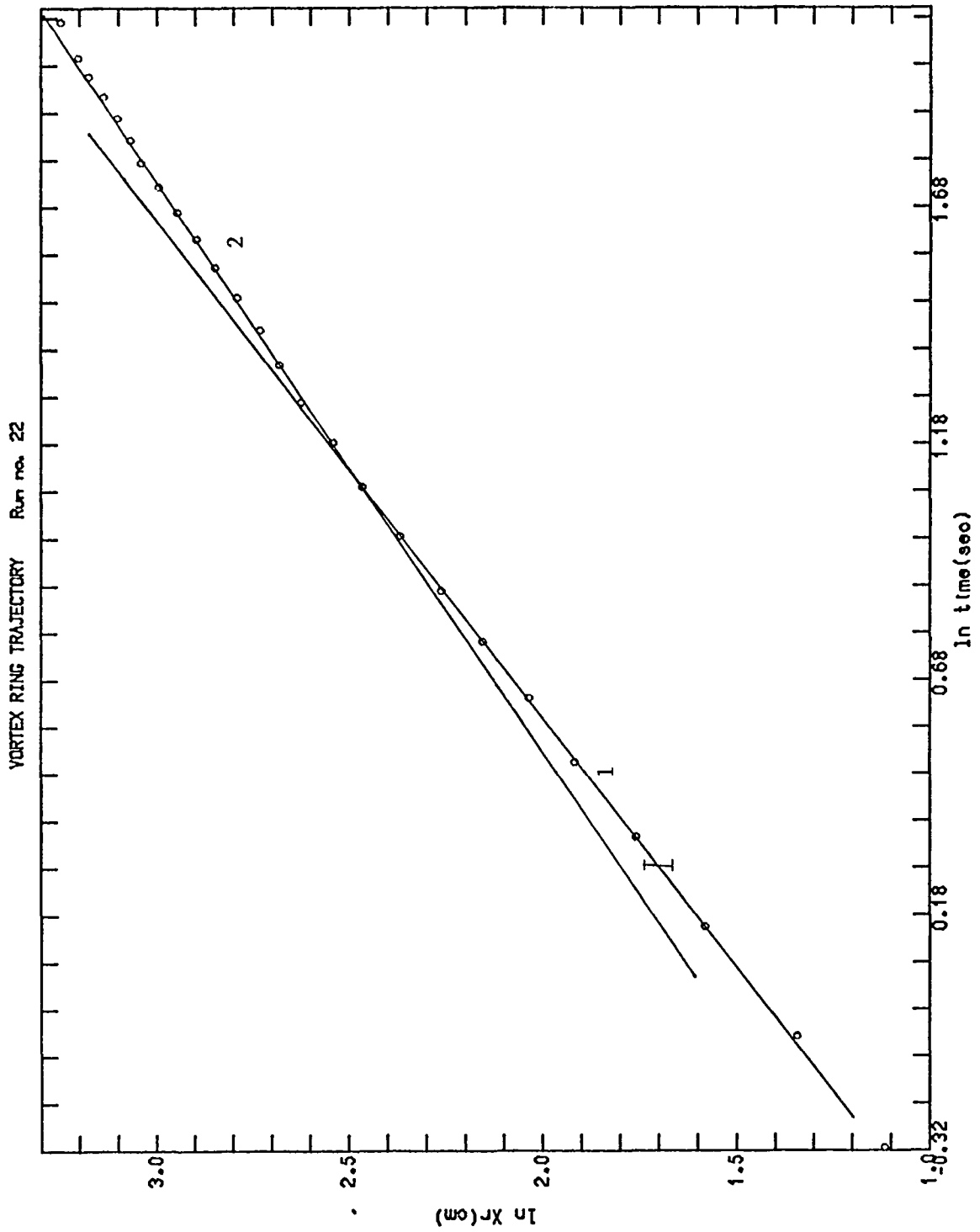


FIGURE A-22a  
 Run 22  $d/D = 0.48$   $Re_j = 8048$   
 Dye

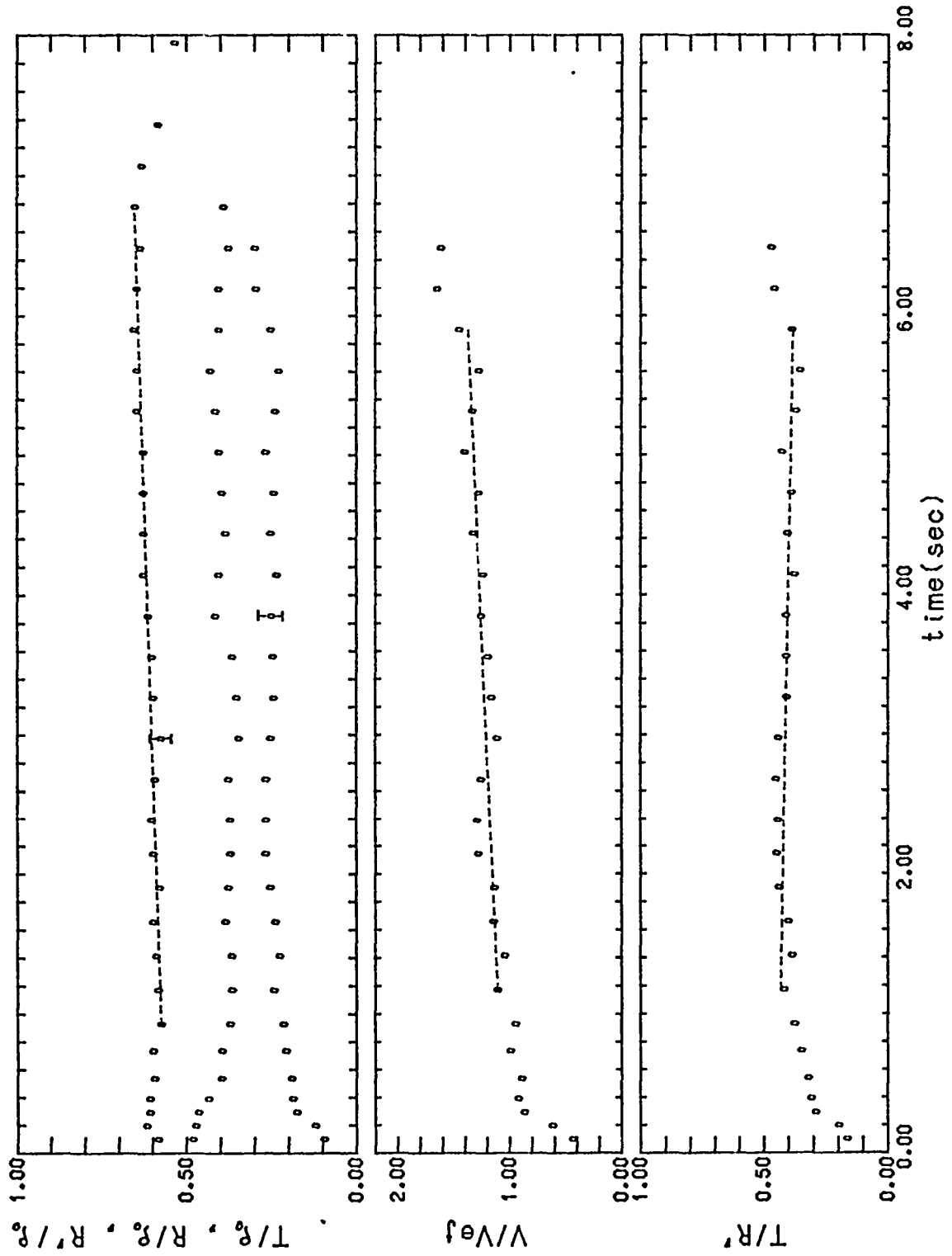


FIGURE A-22b  
 Run 22  $d/D = 0.48$   $Re_j = 8048$   
 Dye

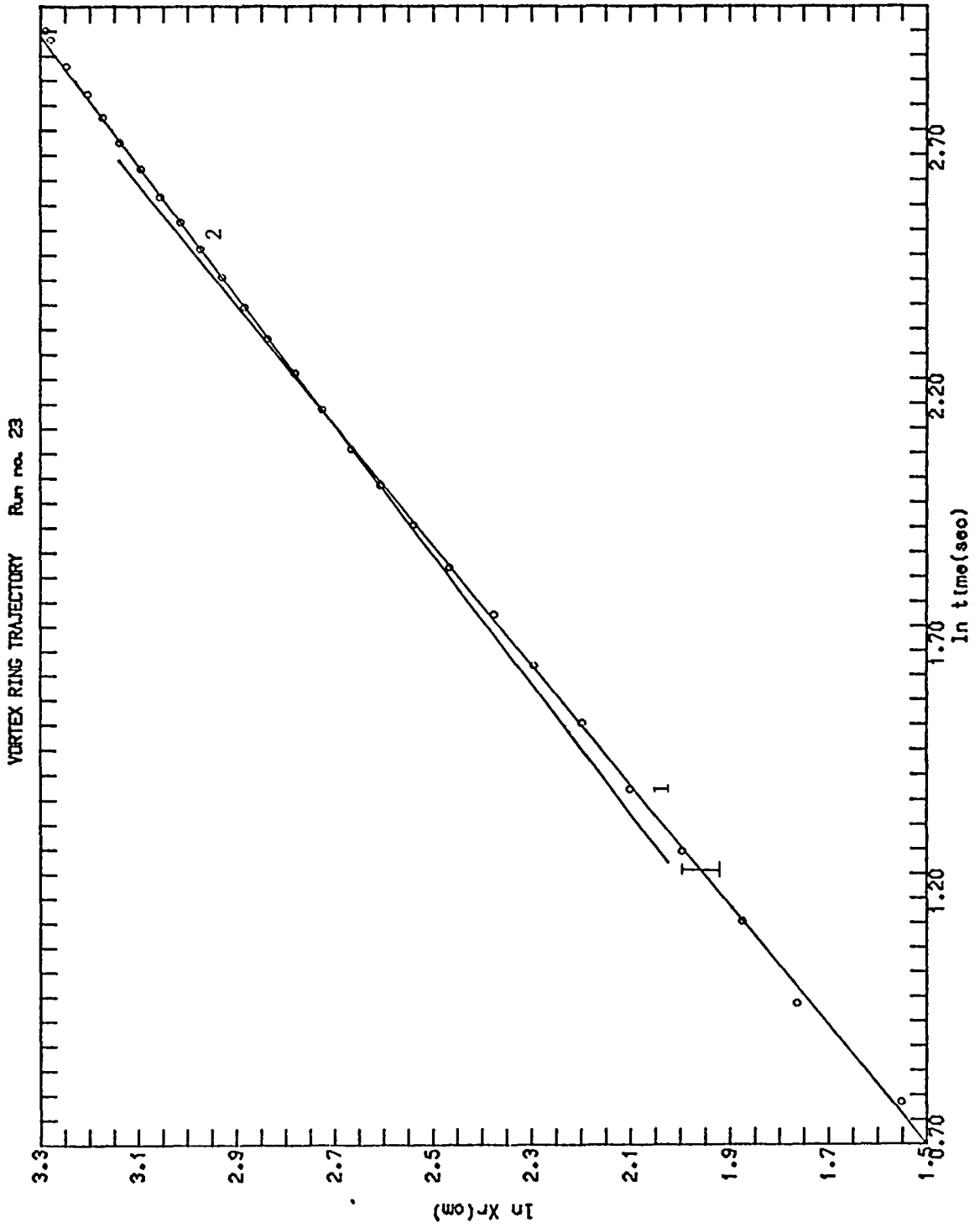


FIGURE A-23a  
 Run 23  $d/D = 0.48$   $Re_j = 5310$   
 Dye

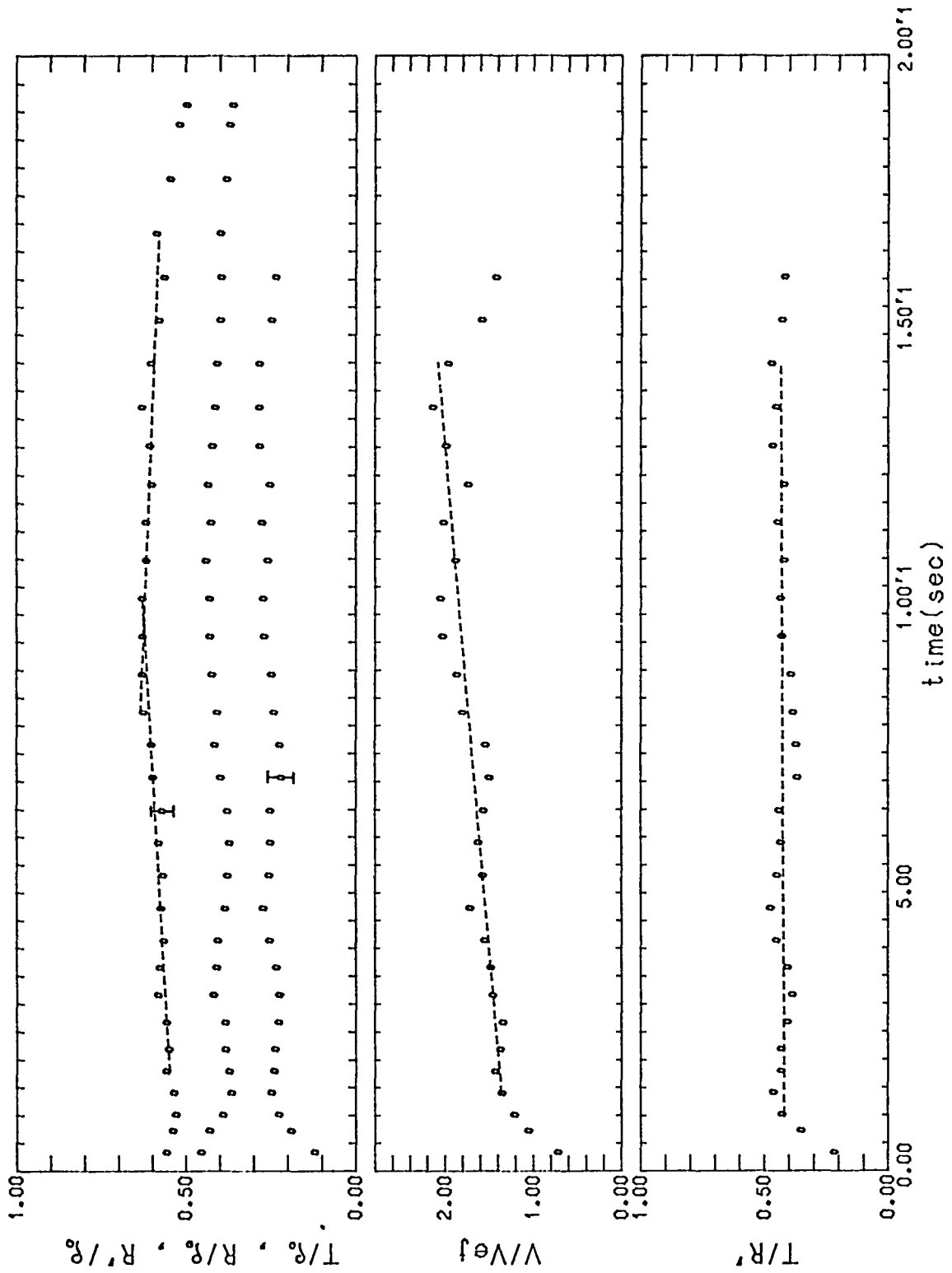


FIGURE A-23b  
 Run 23  $d/D = 0.48$   $Re_j = 5310$   
 Dye

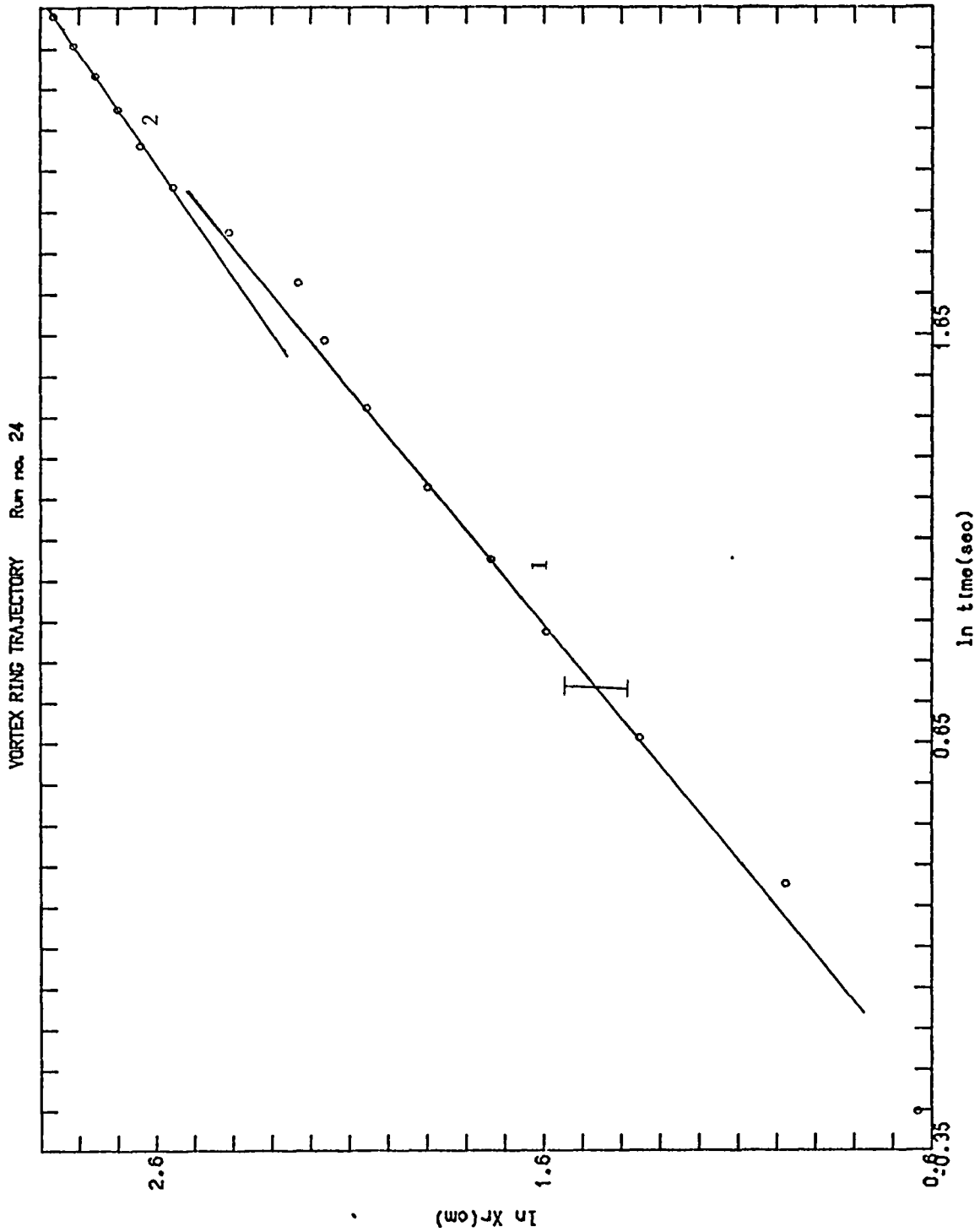


FIGURE A-24a  
 Run 24  $d/D = 0.64$   $Re_j = 7803$   
 Dye

Viscous interaction with the tube wall, and reformation (Section 4-4.3).

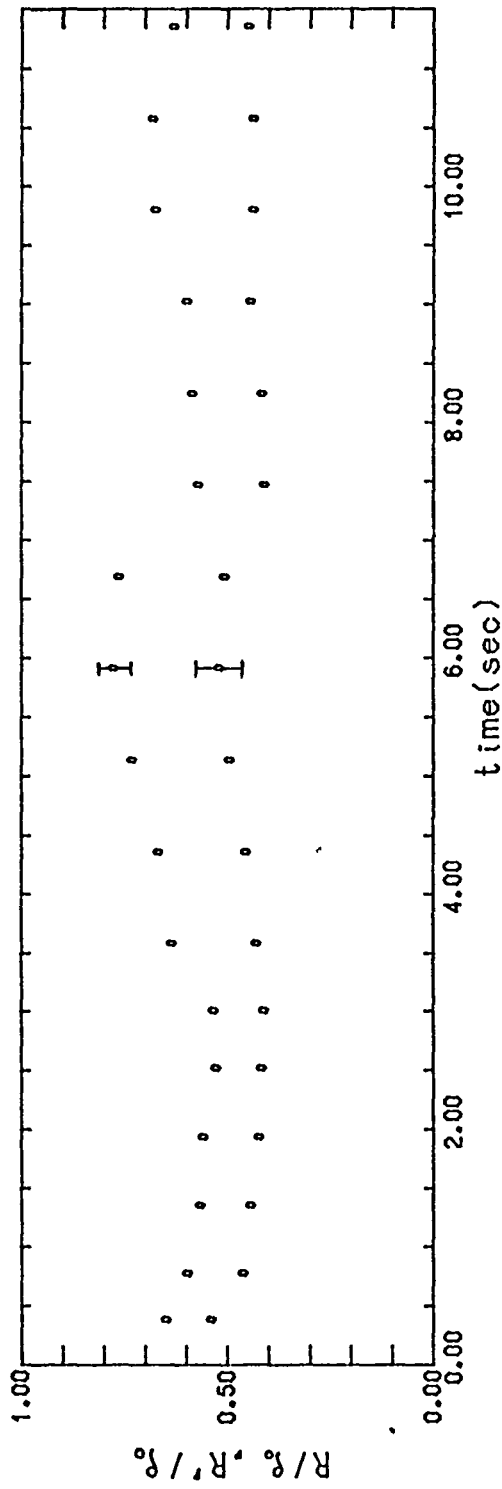


FIGURE A-24b  
 Run 24  $d/D = 0.64$   $Re_j = 7803$   
 Dye

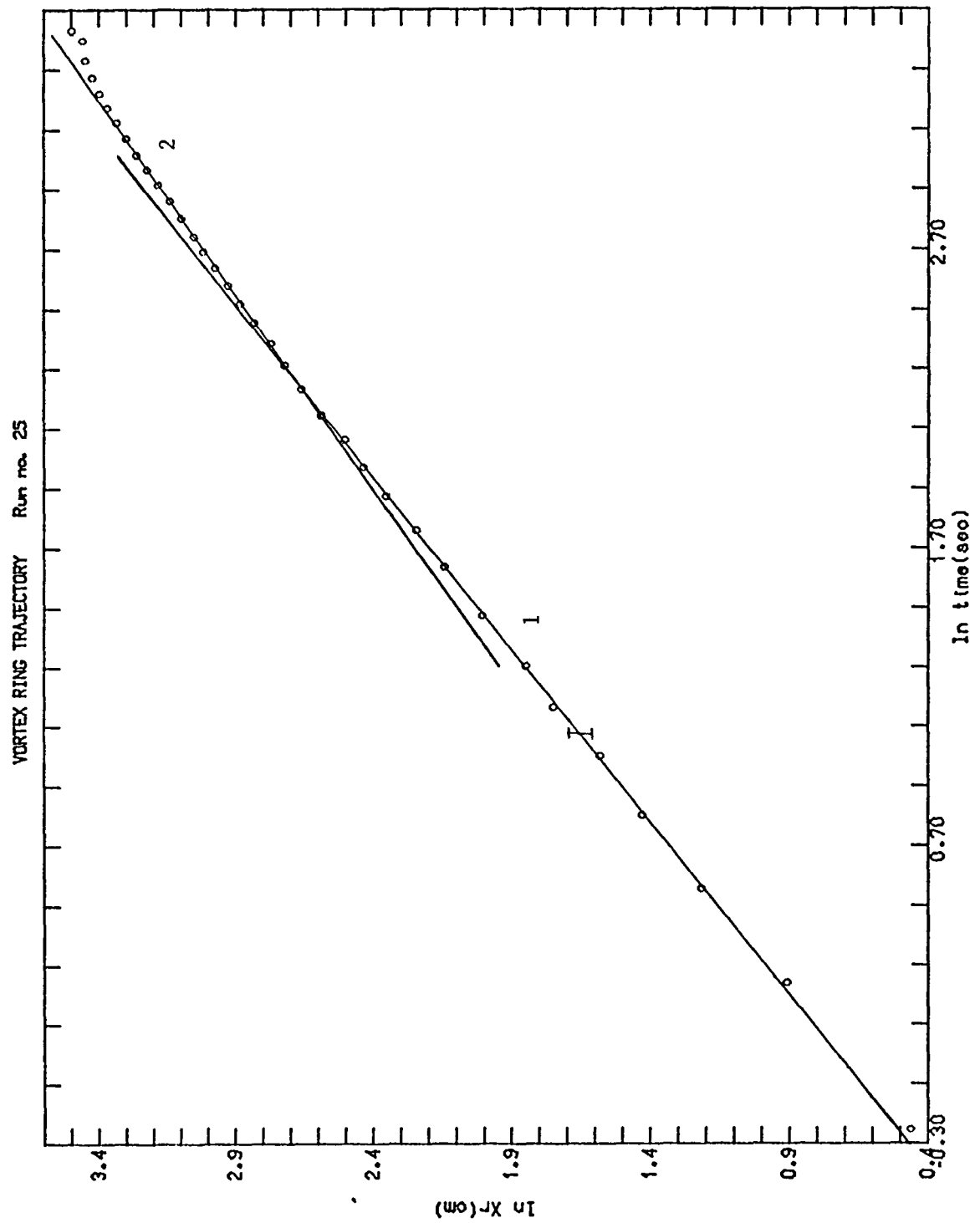


FIGURE A-25a  
 Run 25  $d/D = 0.64$   $Re_j = 3899$   
 Dye

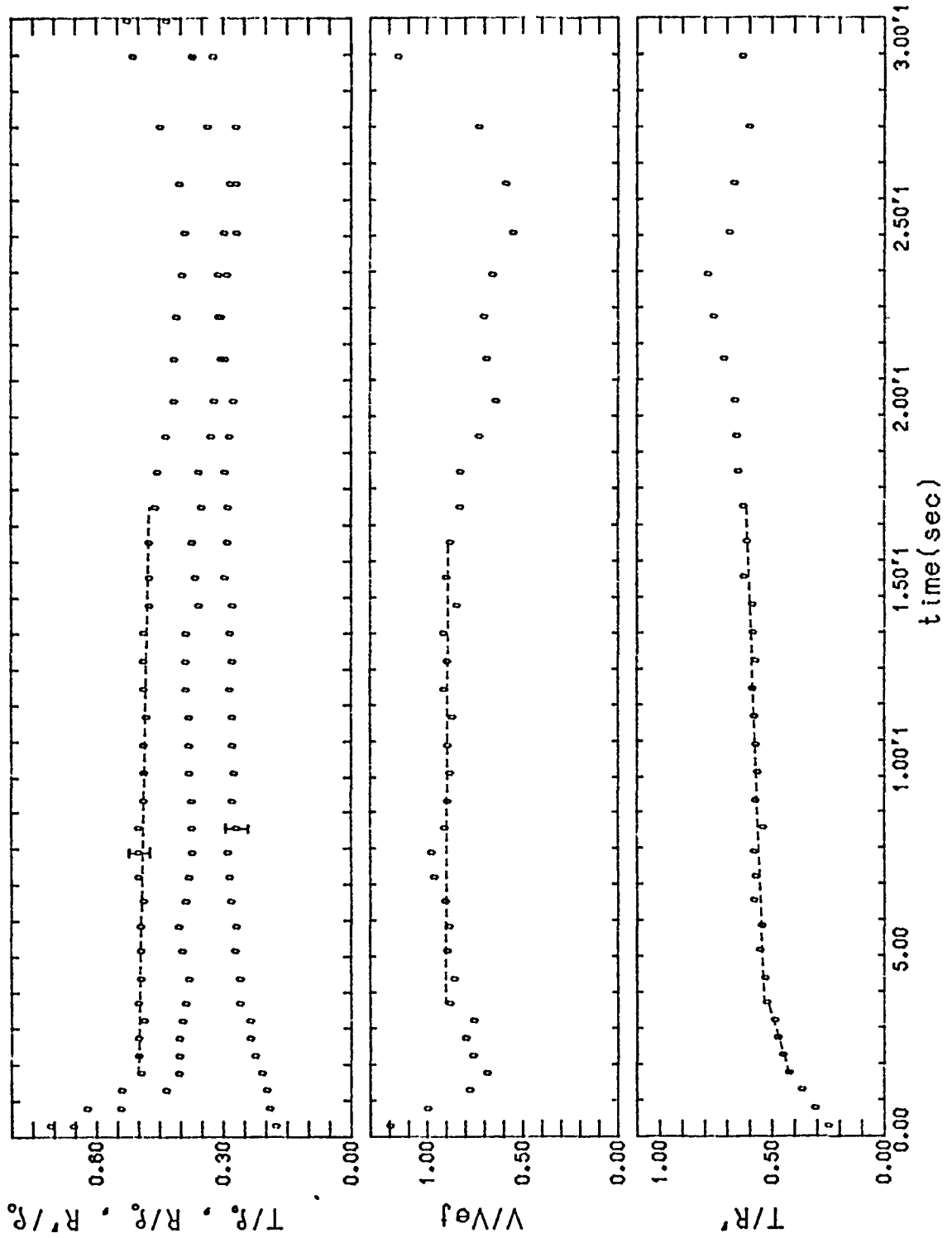


FIGURE A-25b  
 Run 25  $d/D = 0.64$   $Re_j = 3899$   
 Dye

The "apparent" decrease in  $R'$  and  $R$  is due to the bending back of the vortex ring (Section 4-2).

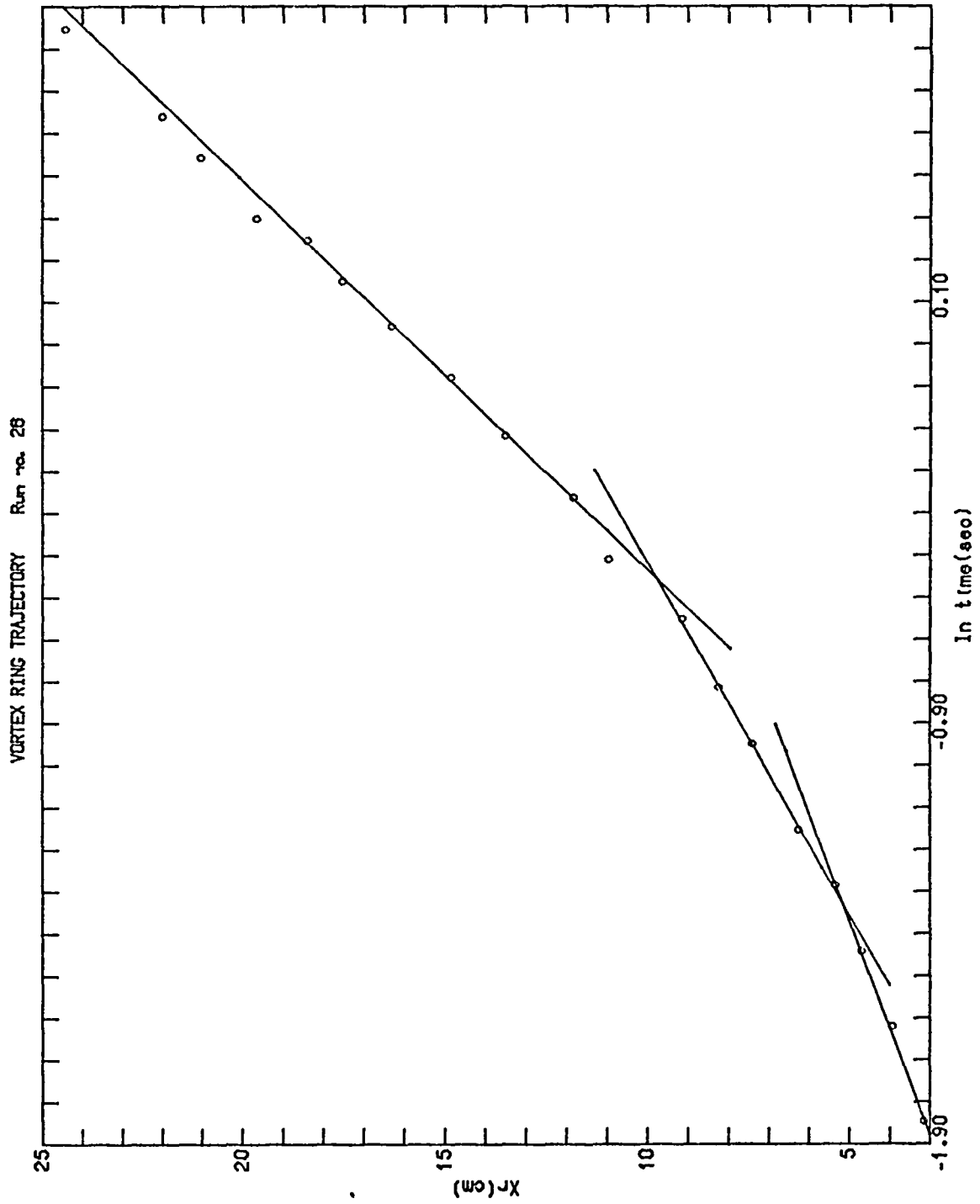


FIGURE A-26  
 Run 26  $A_d/A_D \sim 0.92$   $Re_j \sim 44900$   
 Dye

Irregular occlusion (Section 4-4.3 and 5-4).

## APPENDIX B

### VORTEX RING STRENGTH AND VELOCITY PLOTS

Table B-1: Initial vortex ring parameters for each run

Figures B-1 to B-17: Computed values of total circulation as a function of time plotted with the vortex ring velocity.

Total circulation, or strength: solid curves  
Vortex ring velocity: dashed curves

Run	(sec.) $t_o$	$\epsilon$	( $\text{cm}^2/\text{sec.}$ ) $\Gamma_o$	$Re_R$	$Re_\Gamma$
1	.112	.19	827	50144	89560
2	.102	.13	731	35091	76393
3	.170	.18	684	31050	71481
4	.122	.20	756	35233	79005
5	.145	.28		38045	
6	.100	.25	584	33858	61030
7	.126	.26		33101	
8					
9	.126	.23	460	23421	48072
10	.136	.25		26459	
11	.186	.30	311	15181	32501
12	.180	.31		13845	
13	.370	.31	118	7455	12331
14	.450	.42	220	9530	22991
15	.500	.40	120	7217	12540
16	.960	.36	52.2	3197	5455
17	.583	.38	100	4641	10450
18					
19	1.327	.47	64.6	3894	6751
20	1.489	.38	54.2	2291	5664
21					
22	1.170	.45	34.5	2205	3605
23	3.00	.44	14.5	937	1515
24					
25	3.693	.37	13.0	688	1359
26					

TABLE B-1

Initial vortex ring parameters for each run

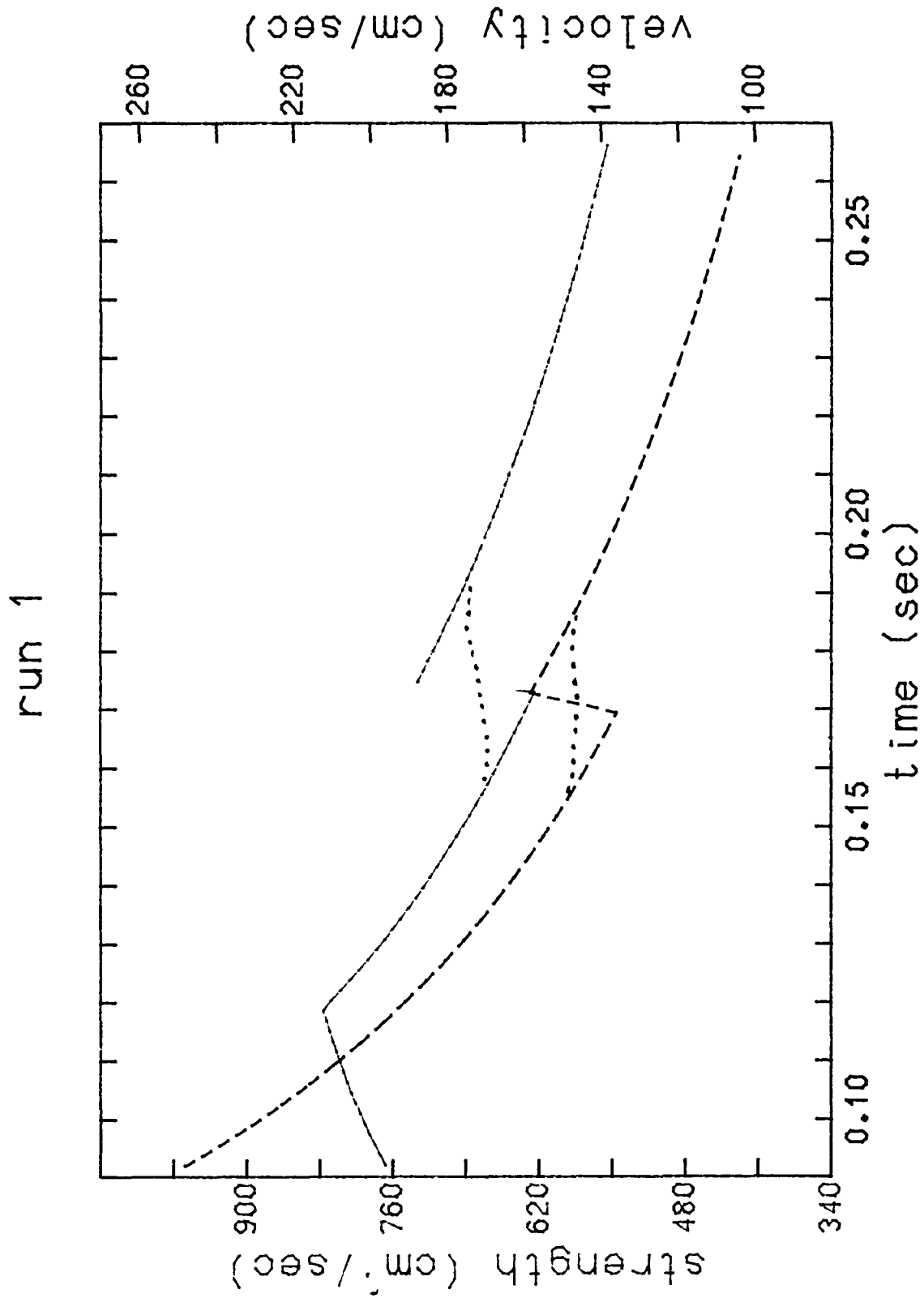


FIGURE B-1  
Run 1

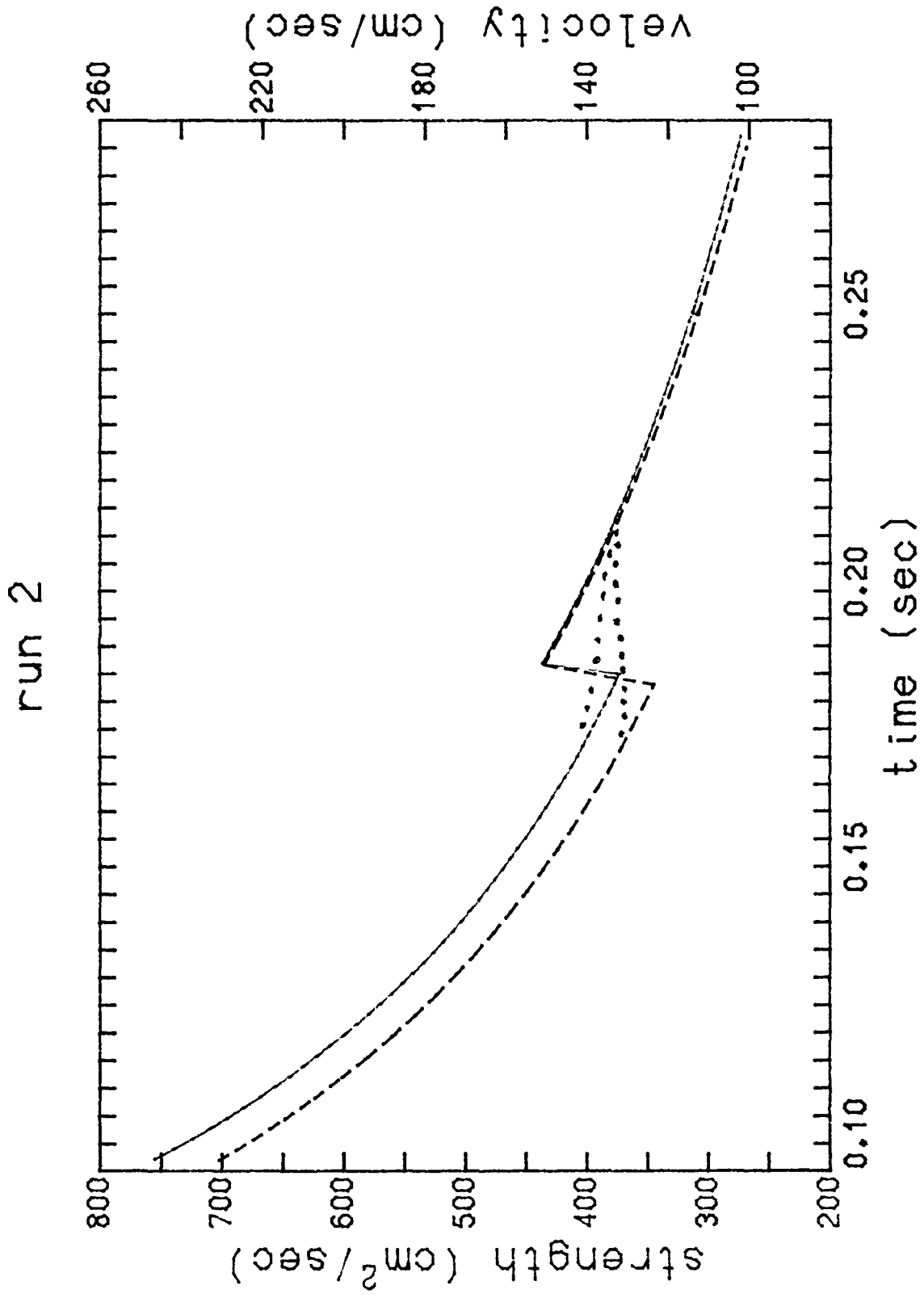


FIGURE B-2  
Run 2

run 3

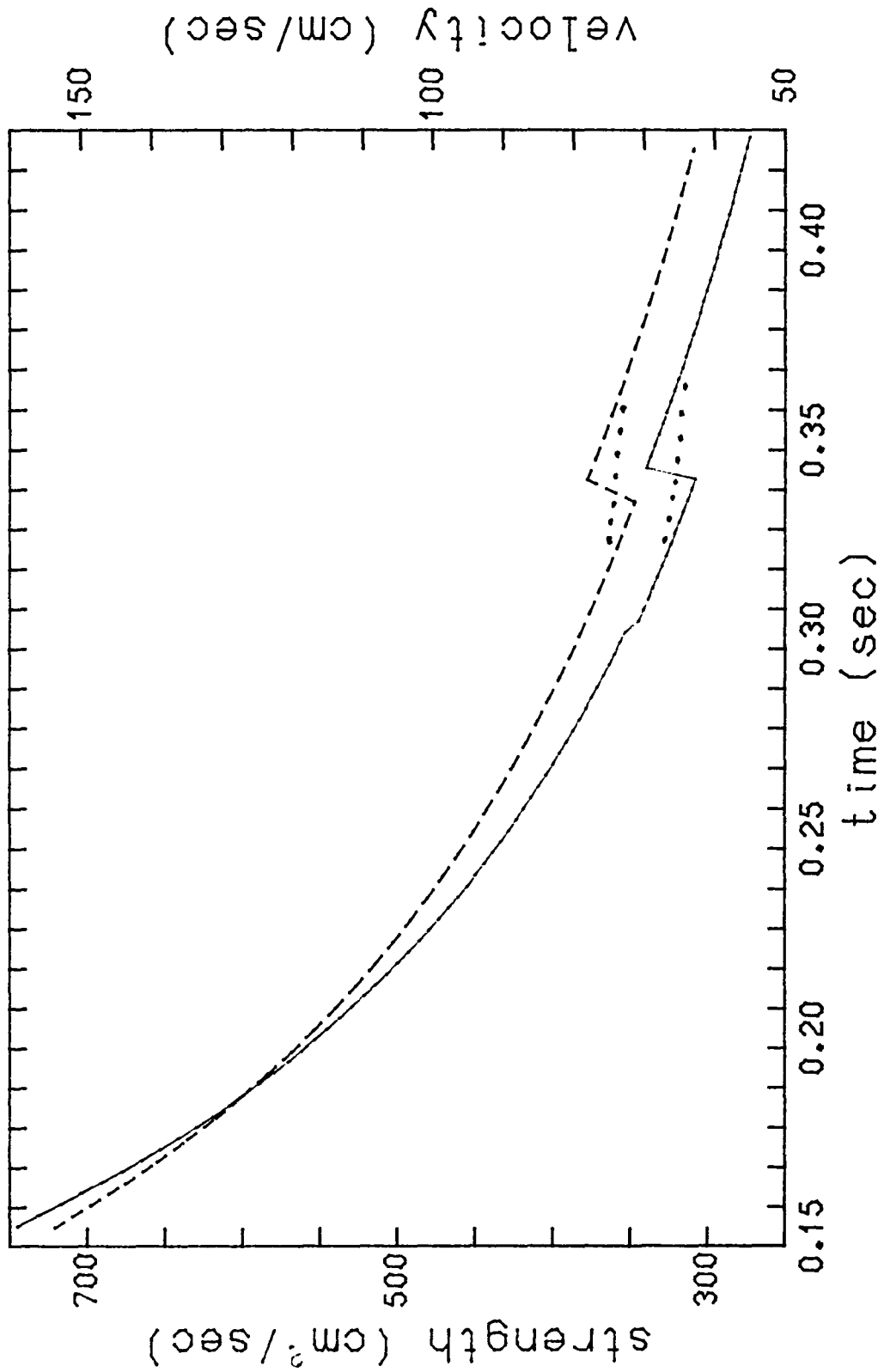


FIGURE B-3  
Run 3

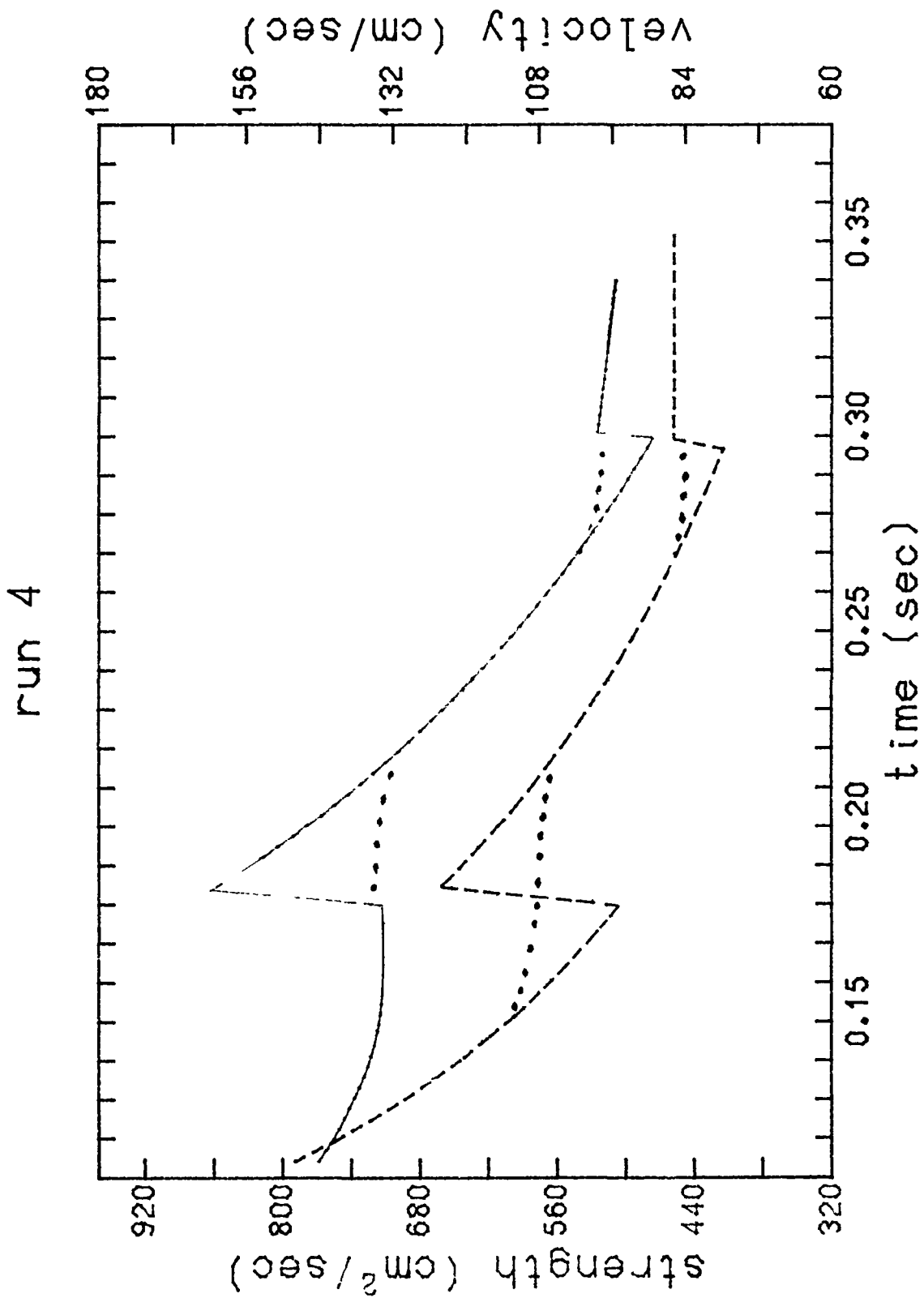


FIGURE B-4  
Run 4

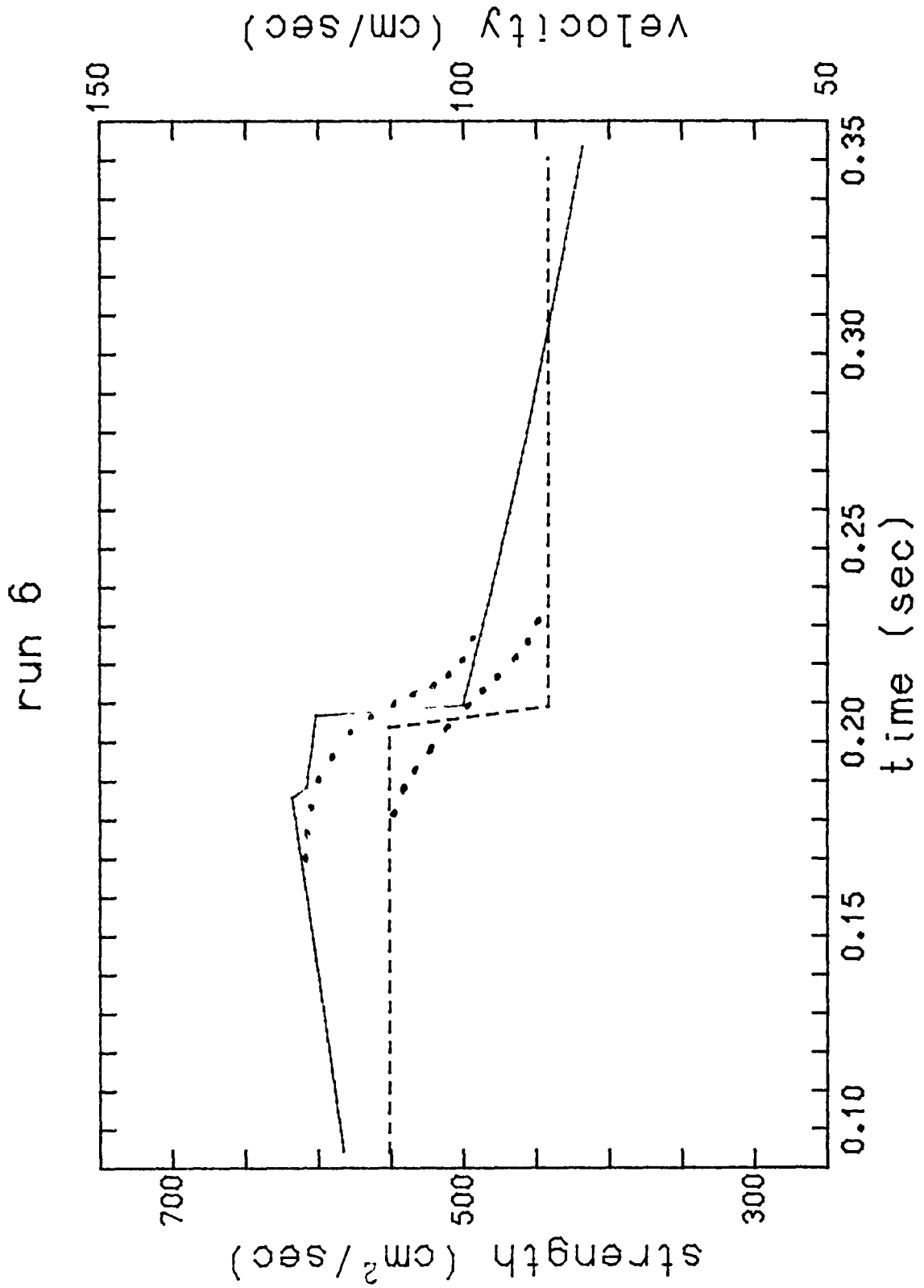


FIGURE B-5  
Run 6

run 9

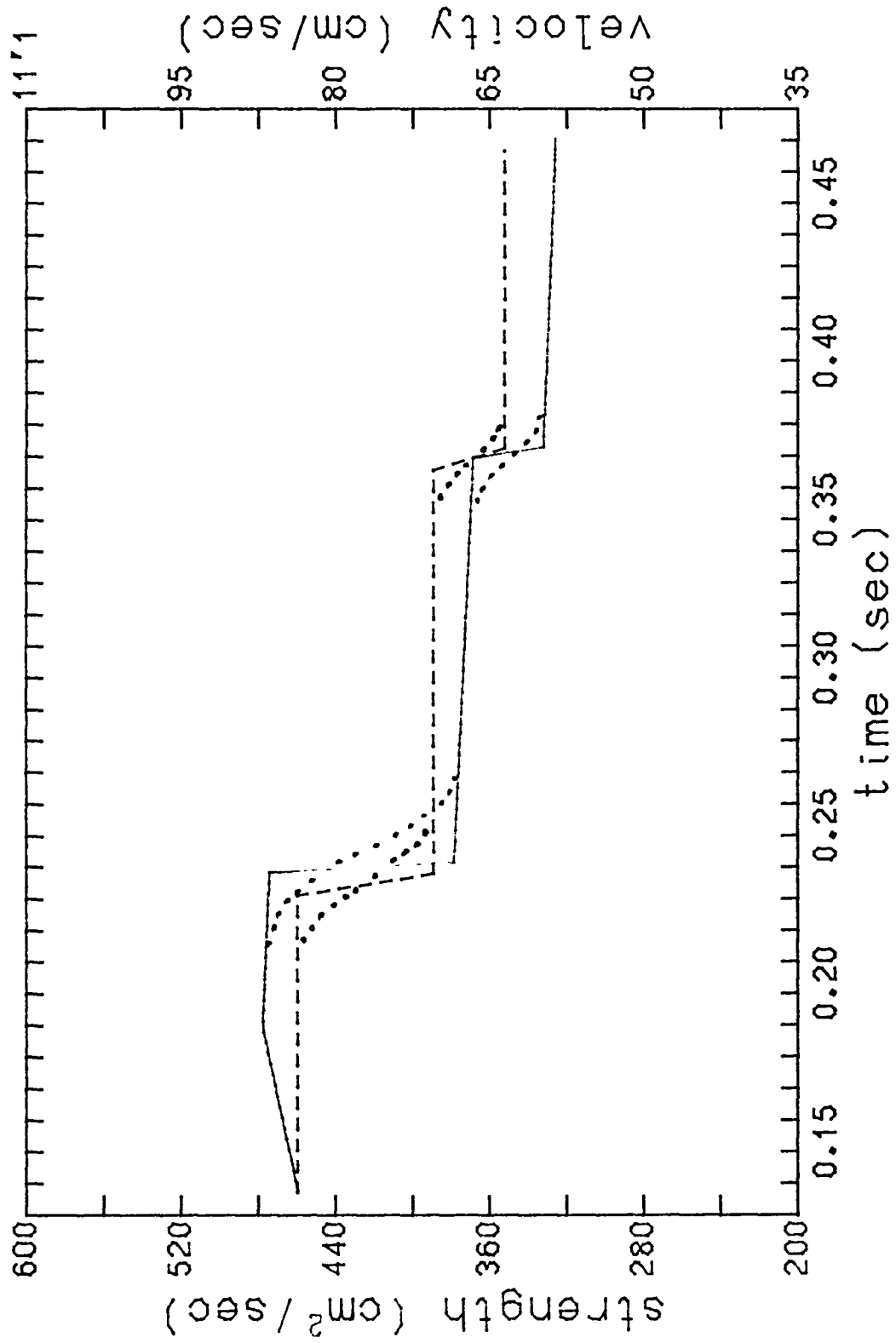


FIGURE B-6  
Run 9

run 11

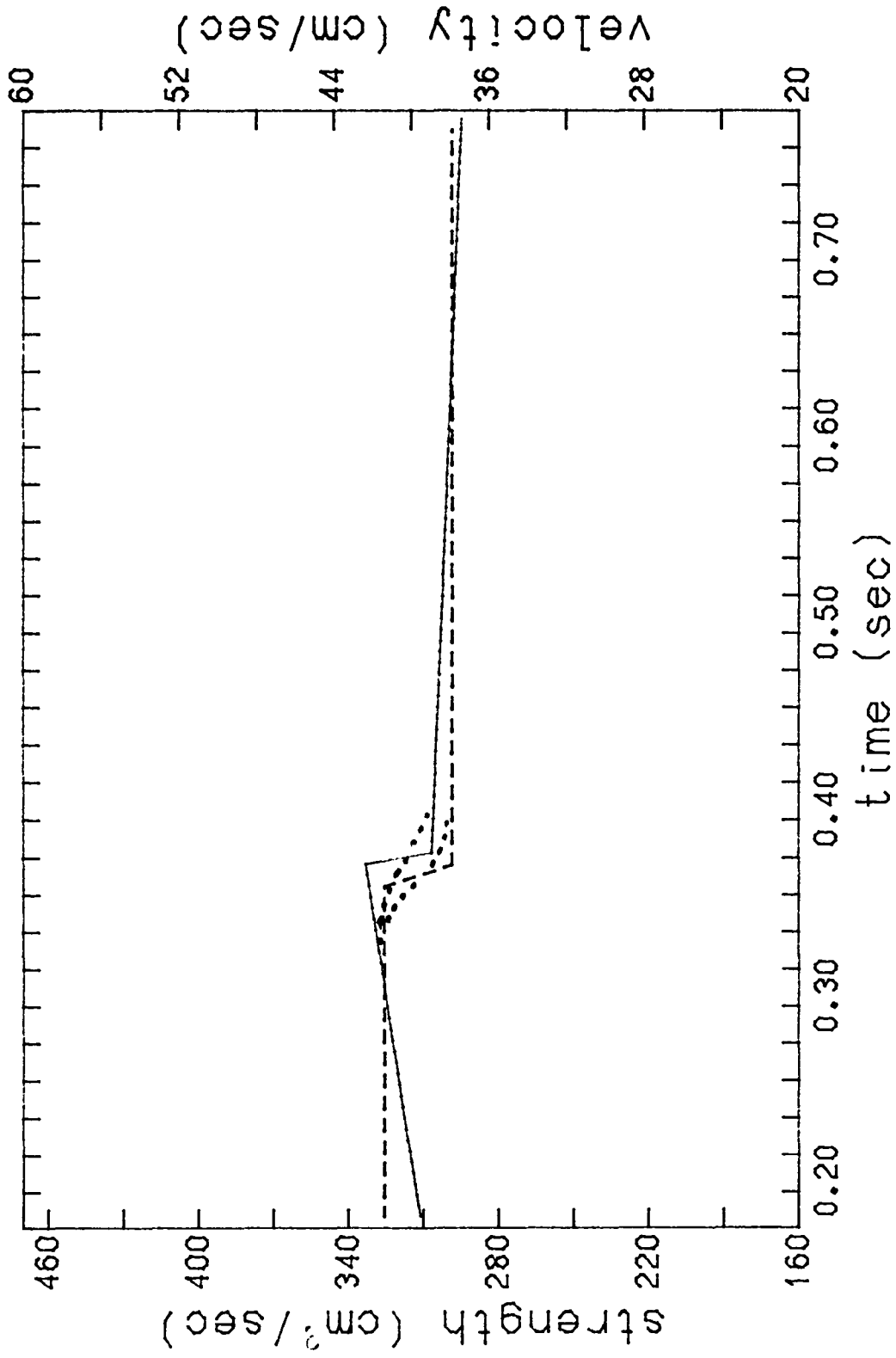


FIGURE B-7  
Run 11

run 13

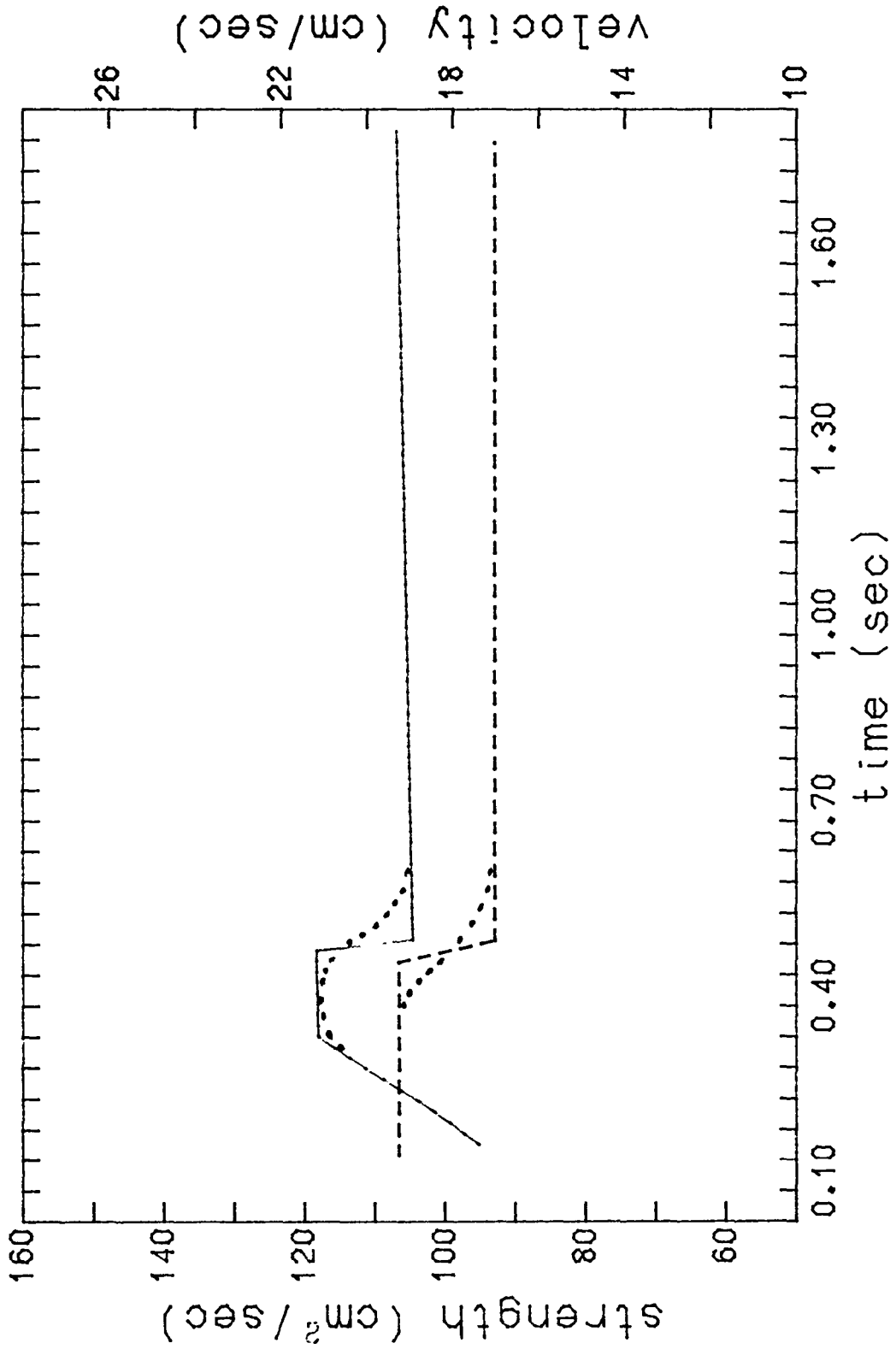


FIGURE B-8  
Run 13

run 14

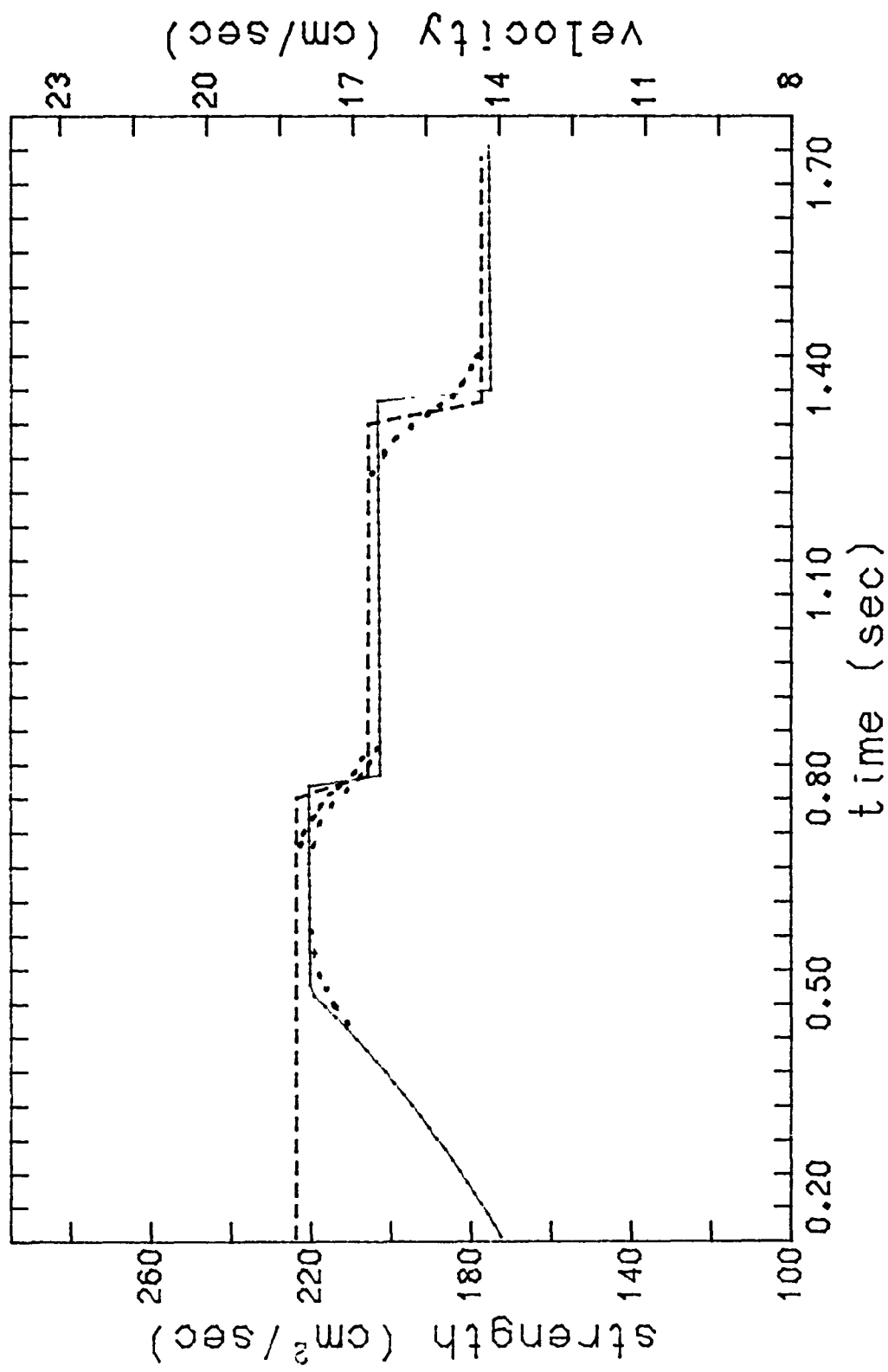


FIGURE B-9  
Run 14

run 15

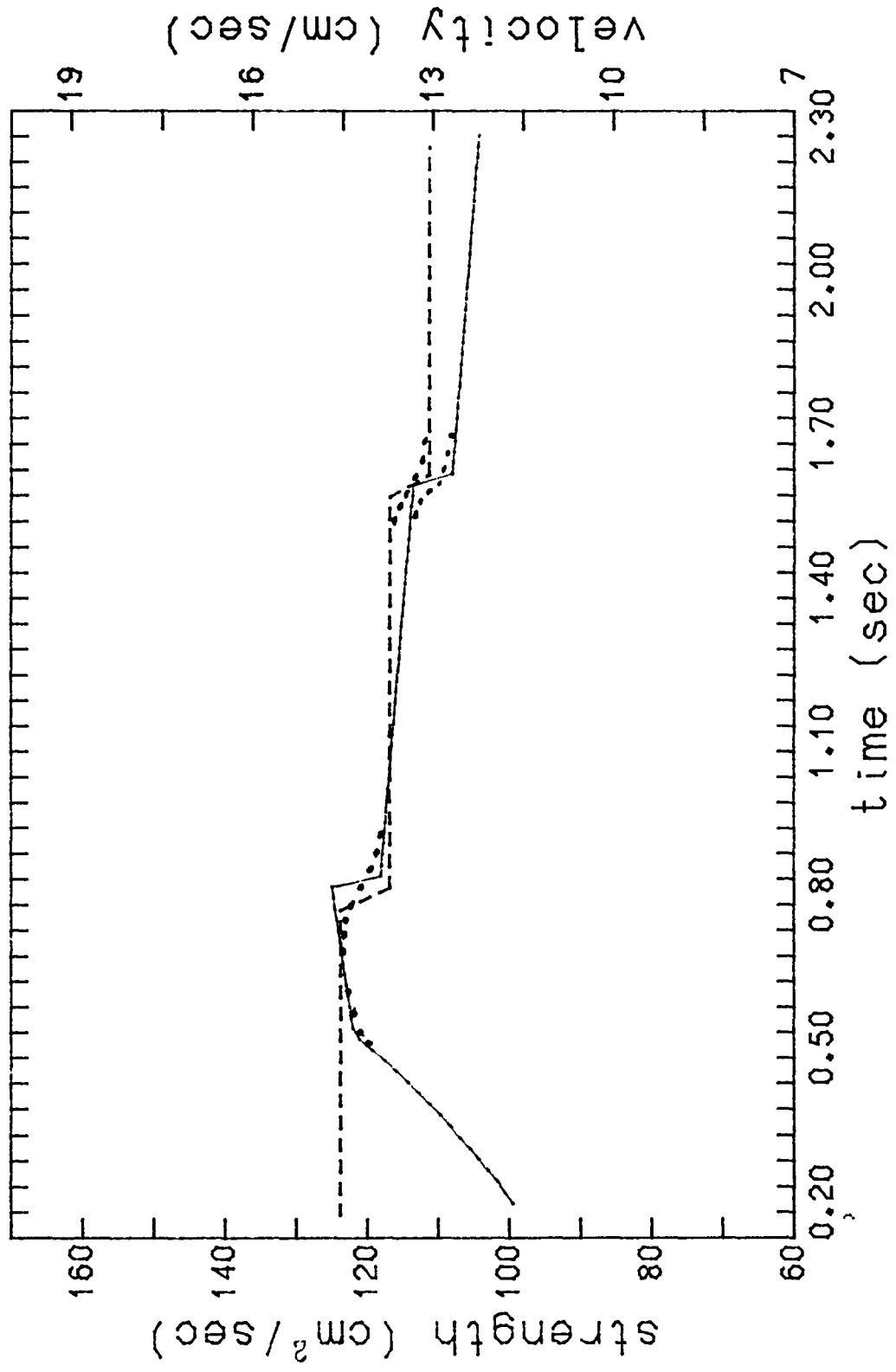


FIGURE B-10  
Run 15

run 16

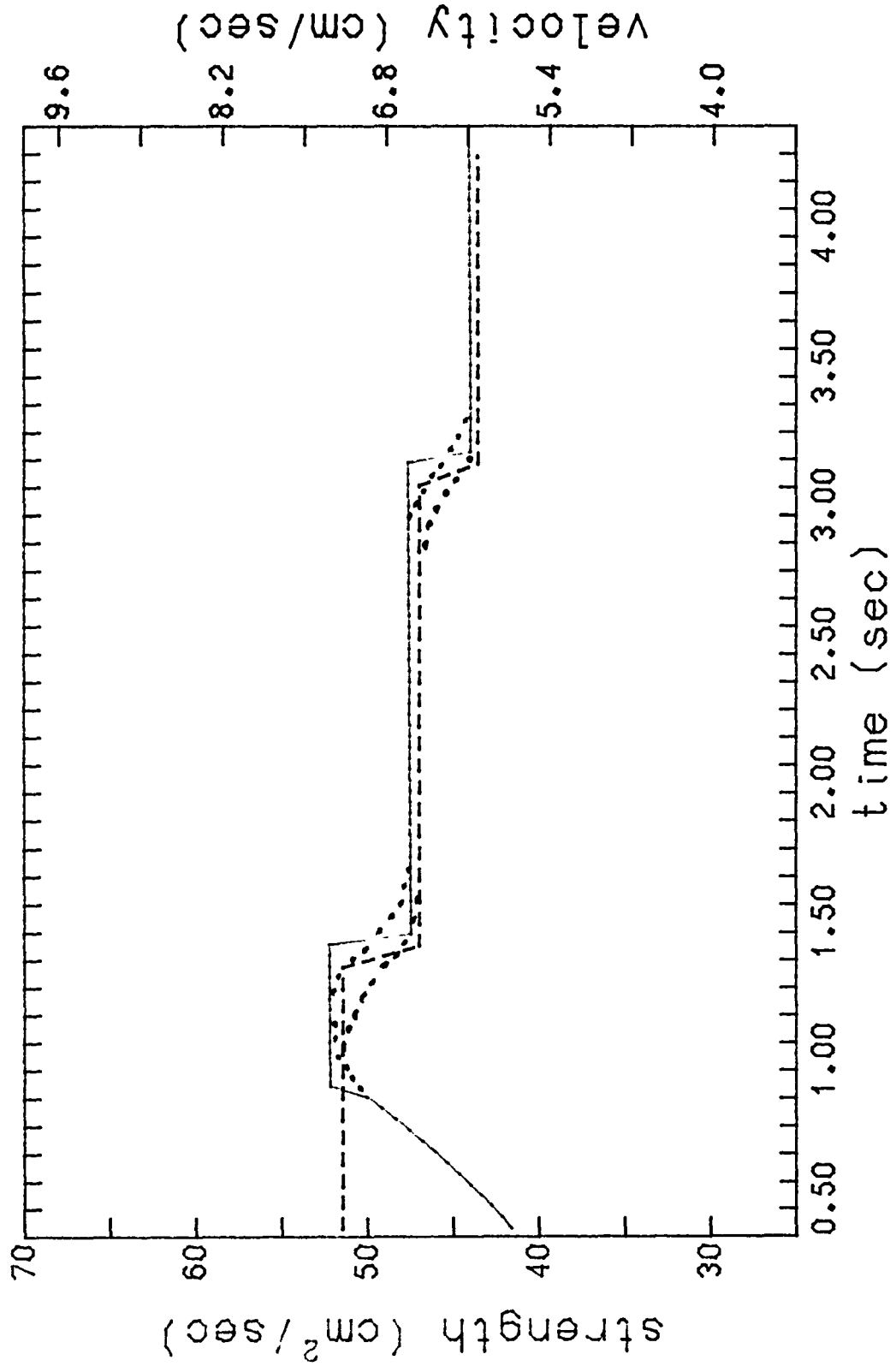


FIGURE B-11  
Run 16

run 17

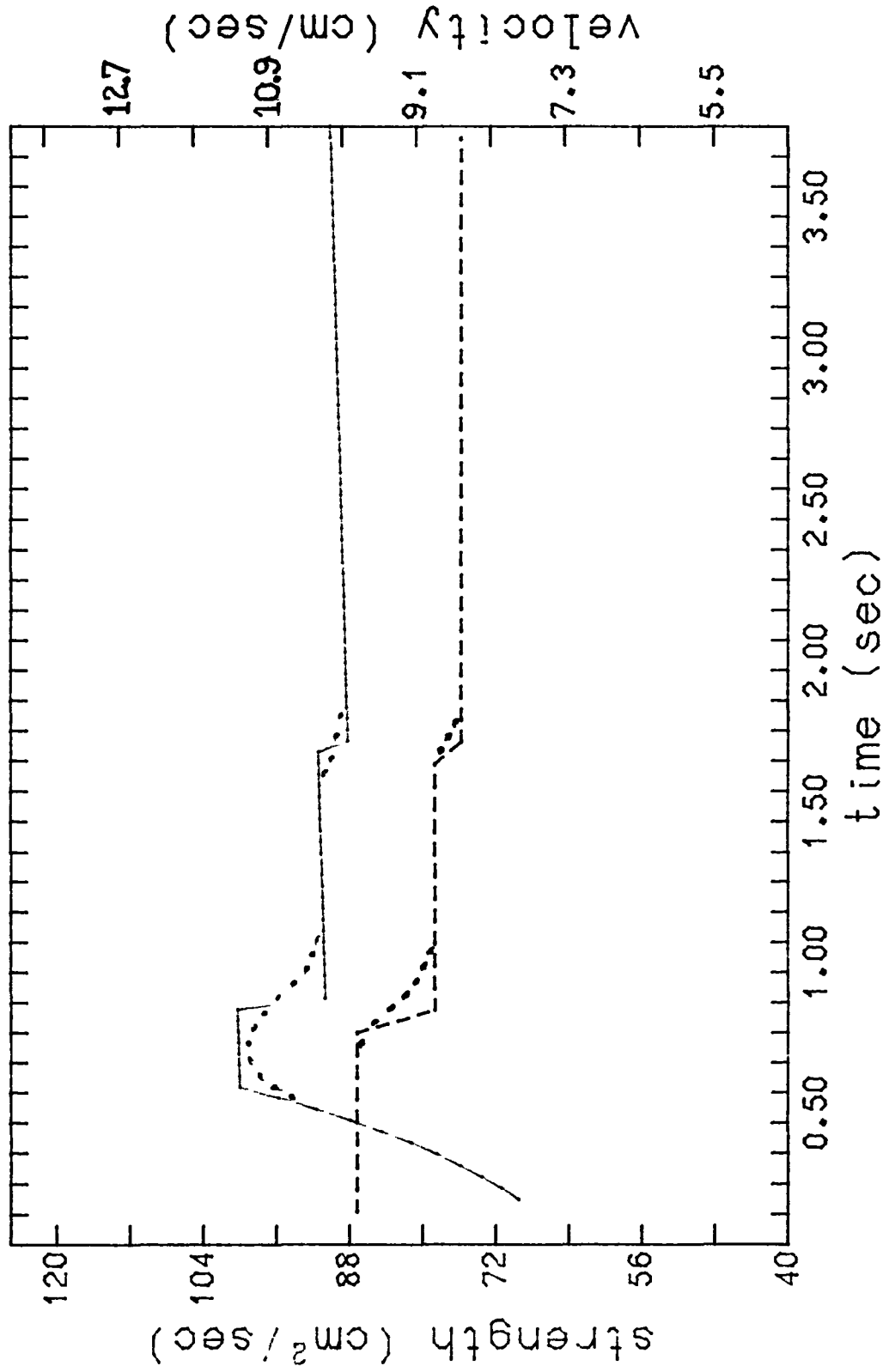


FIGURE B-12  
Run 17

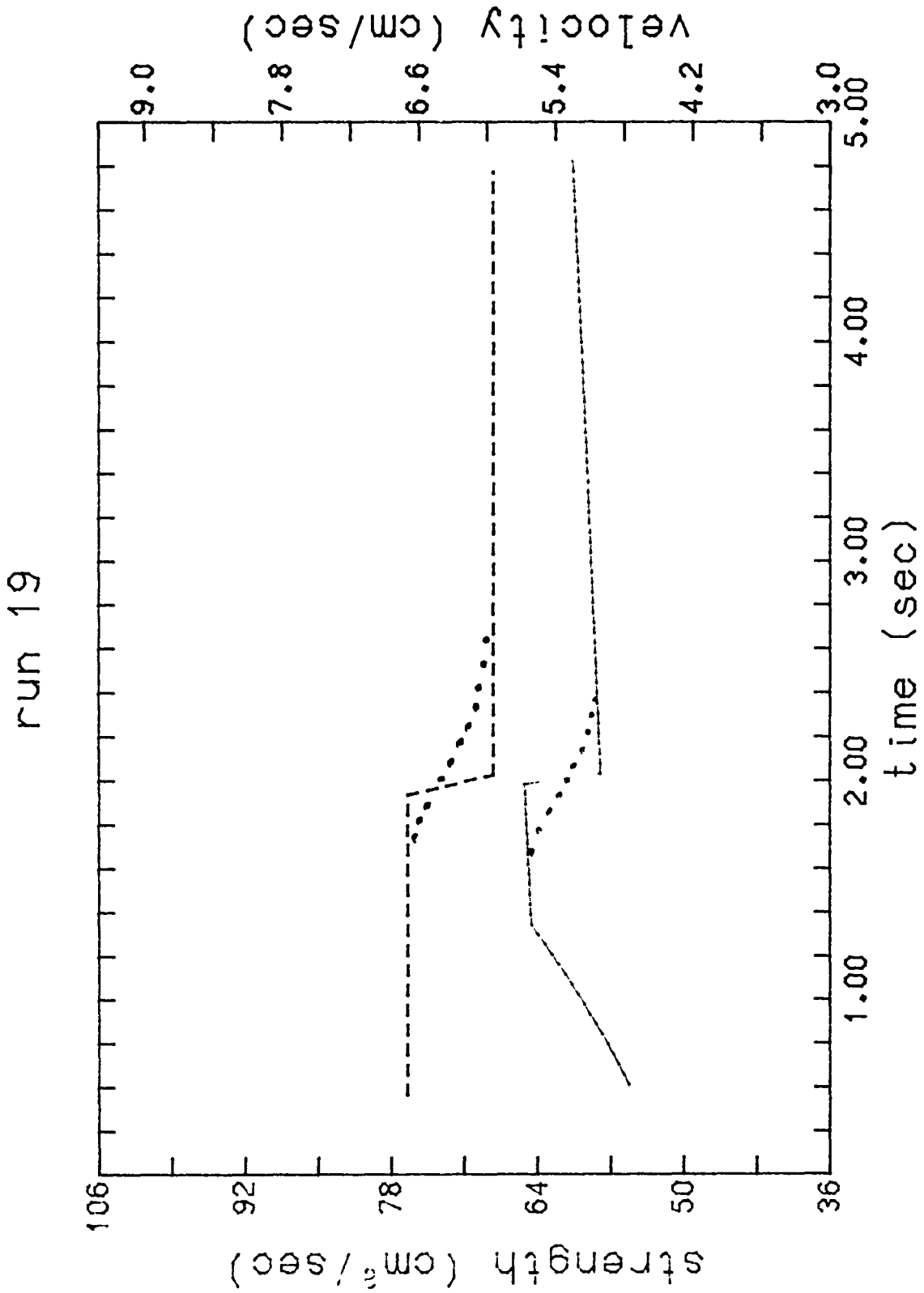


FIGURE B-13  
Run 19

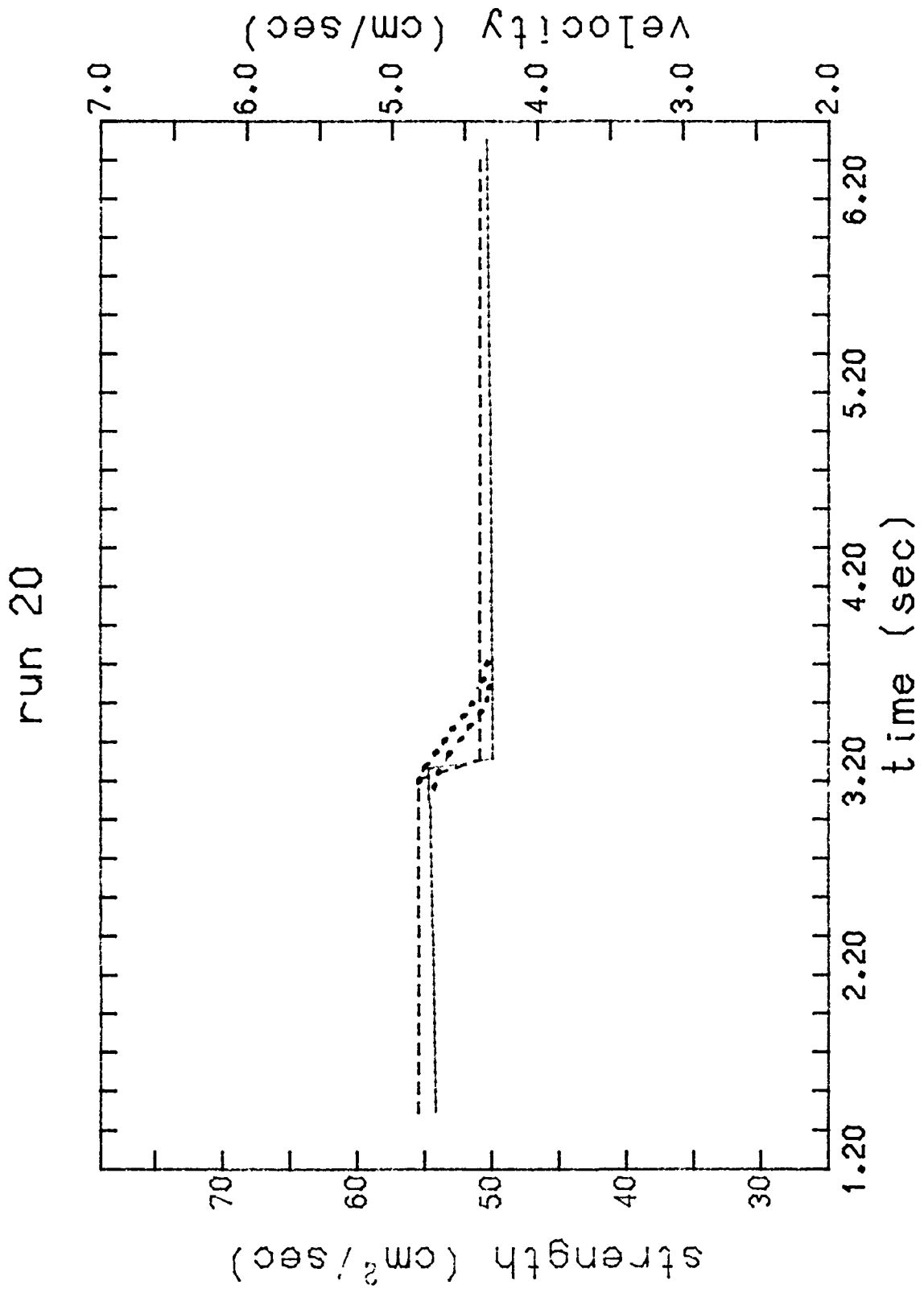


FIGURE B-14  
Run 20

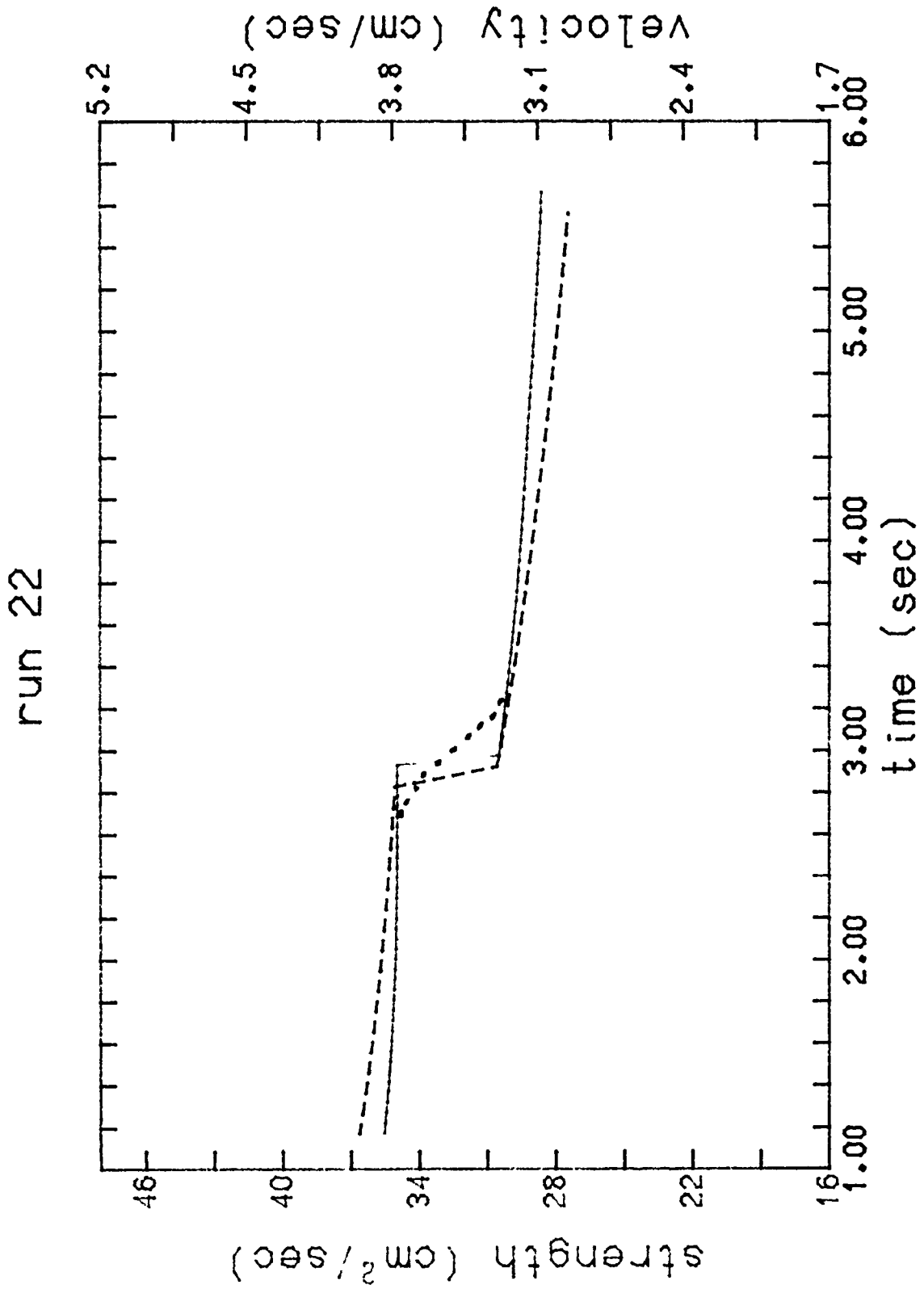


FIGURE B-15  
Run 22

run 23

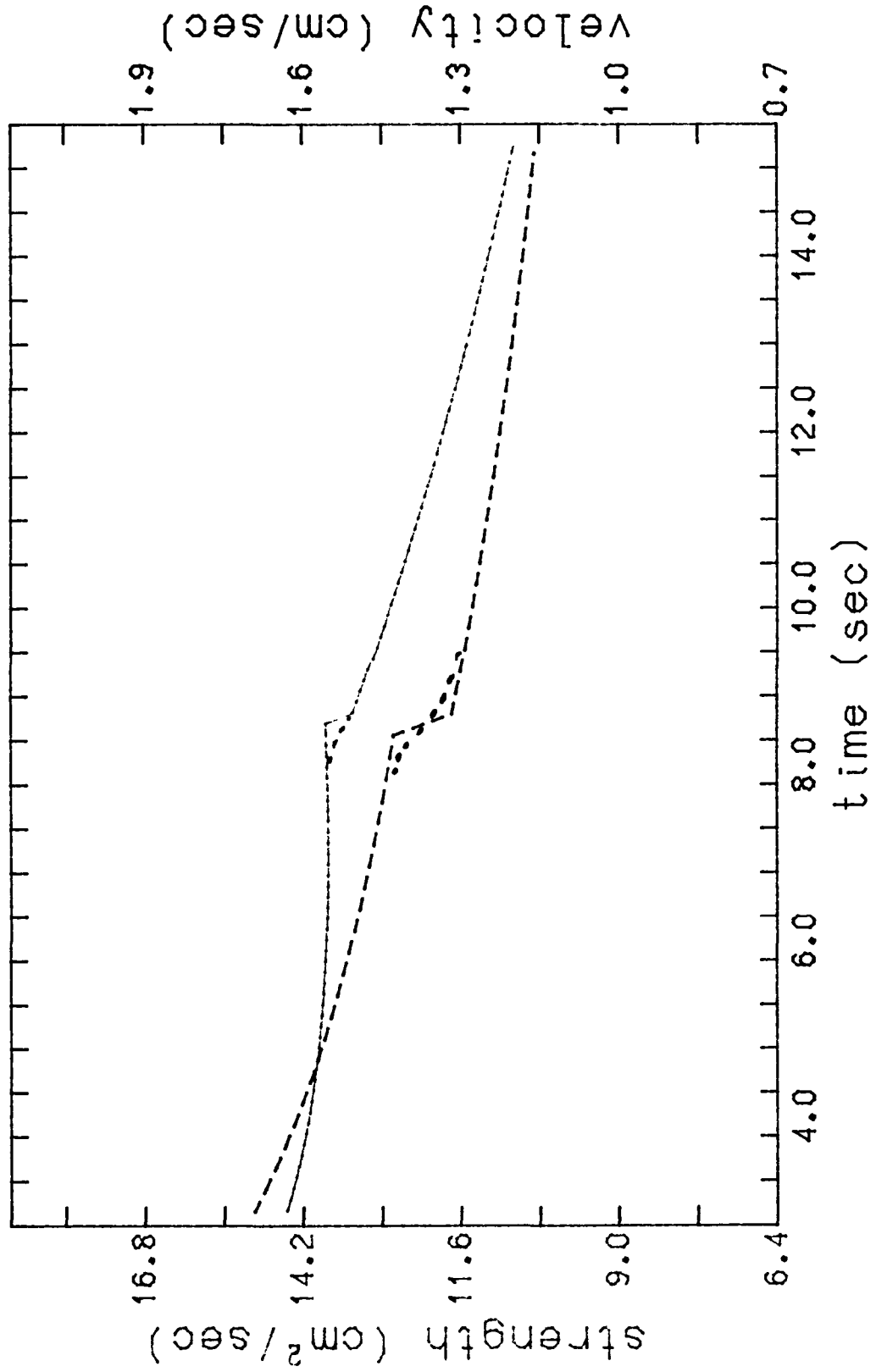


FIGURE B-16  
Run 23

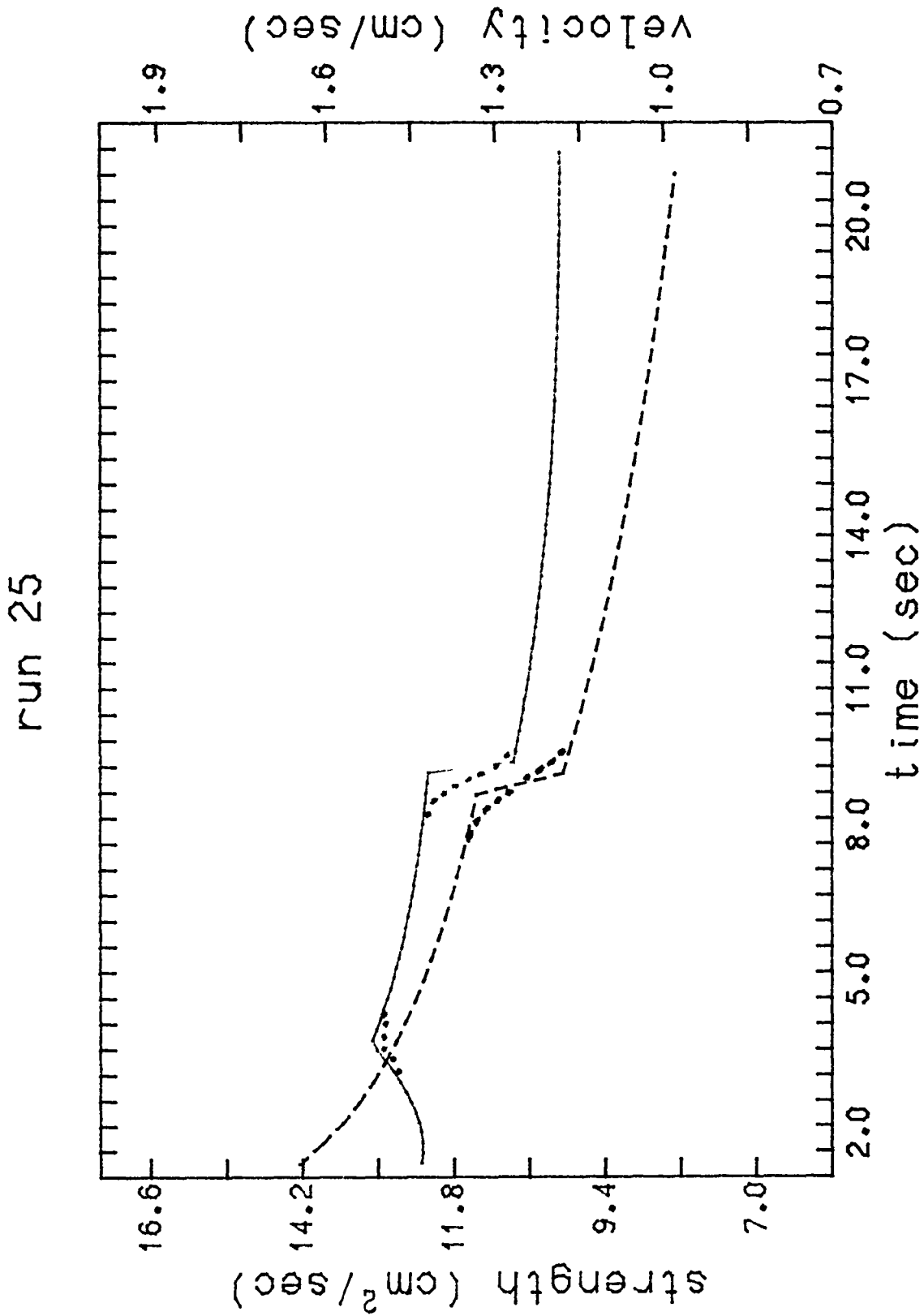


FIGURE B-17

Run 25

# Bibliography

1. Arms, R.J., Hama, F.R. (1965), "Localized-Induction Concept on a Curved Vortex and Motion of an Elliptic Vortex Ring," Phys. Fluids , 8 , 553.
2. Batchelor, G.K. (1967), An Introduction to Fluid Dynamics , Cambridge University Press.
3. Brasseur, J.G., Chang, I-D. (1979), "Flow Visualization of the Post-Stenotic Flowfield in Pulsatile Flow," Proc. 1979 Biomech. Symp. , 157.
4. Brasseur, J.G., Koutsoyannis, S.P., Chang, I-D. (1976), "Formation and Propagation of Vortex Rings in Axisymmetric, Bounded, Pulsed Flow," SUDAAR Report No. 502, Stanford University.
5. Cassanova, R. (1975), "An Experimental Investigation of Steady and Pulsatile Flow Through Partial Occlusions in a Rigid Tube," Ph.D. Dissertation, Georgia Inst. of Technology.
6. Chang, I.C., Chang I-D. (1968), "Potential of a Charged Sphere Inside a Grounded Cylindrical Tube," J. Math. and Physics , 47 , 366.
7. Chen, C.-J., Chang, L.-M. (1972), "Flow Patterns of a Circular Vortex Ring with Density Difference Under Gravity," J. Appl. Mechanics , December, 869.
8. Cone Jr., C.D. (1962), "The Soaring Flight of Birds," Scientific American , April, 659.
9. Davies, P.O.A.L., Yule, A.J. (1975), "Coherent Structures in Turbulence," J. Fluid Mech. , 69 , 513.
10. Dyson, F.W. (1893), "The Potential of an Anchor Ring," Trans. Roy. Soc. London , A184 , 1041.
11. Feynman, R.P. (1957), "Application of Quantum Mechanics," Progress in Low Temperature Physics , Vol. 1, Ed.: C.J. Gortner, North-Holland Pub. Co., Amsterdam, p.17.
12. Fineman, J.C., Chase, C.E. (1963), "Energy of a Vortex Ring in a

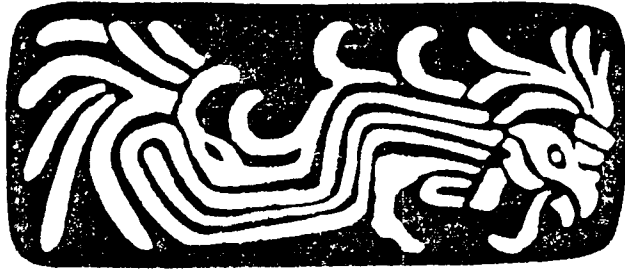
- Tube and Critical Velocities in Liquid Helium II," Phys. Rev. ,  
129 , 1.
13. Fohl, T. (1967), "Turbulent Effects in the Formation of Buoyant Vortex Rings," J. Appl. Physics , 38 , 4097.
  14. Fohl, T. Turner, J.S. (1975), "Colliding Vortex Rings," Phys. Fluids , 18 , 433.
  15. Fraenkel, L.E. (1970), "On Steady Vortex Rings of Small Cross-Section in an Ideal Fluid," Proc. Roy. Soc. London , A316 , 29.
  16. Fraenkel, L.E. (1972), "Examples of Steady Vortex Rings of Small Cross-Section in an Ideal Fluid," J. Fluid Mech. , 51 , 119.
  17. Frydenlund, O. (1974), "An Experimental Investigation of Heavy Vortex Rings Rising Against Gravity," Physica Norvegica , 7 , 113.
  18. Gopal, E.S.R. (1963), "Motion and Stability of Vortices in a Finite Channel: Application to Liquid Helium II," Ann. Phys. , 25 , 196.
  19. Hecht, A.M., Bilanin, A.J., Hirsh, J.E., Snedeker, R.S. (1979), "Turbulent Vortices in Stratified Fluids," AIAA Paper #79-0151.
  20. Helmholtz, H. (1867), "On Integrals of the Hydrodynamical Equations which Express Vortex Motion," Phil. Mag. , 33 , 485.
  21. Hicks, W.M. (1884), "On the Steady Motion and Small Vibrations of a Hollow Vortex," Phil. Trans. Roy. Soc. London , A175 , 161.
  22. Hicks, W.M. (1885), "Researches on the Theory of Vortex Rings," Phil. Trans. Roy. Soc. London , A176 , 725.
  23. Hicks, W.M. (1922), "On the Mutual Threading of Vortex Rings," Proc. Roy. Soc. London , A102 , 111.
  24. Hill, M.J.M. (1894), "On a Spherical Vortex," Phil. Trans. Roy. Soc. London , A185 , 213.
  25. Johnson, G.M. (1971), "An Empirical Model of the Motion of Turbulent Vortex Rings," AIAA Journal , 9 , 763.
  26. Kambe, T., Takao, T. (1971), "Motion of Distorted Vortex Rings," J. Phys. Soc. Japan , 31 , 591.
  27. Kambe, T., Oshima, Y. (1975), "Generation and Decay of Viscous

- Vortex Rings," J. Phys. Soc. Japan , 38 , 271.
28. Kruttsch, C.-H. (1939), "Über eine experimentell beobachtete Erscheinung an Wirbelringen bei ihrer translatorischen Bewegung in wirklichen Flüssigkeiten," Ann. Phys. , 35 , 497.
  29. Lamb, H. (1932), Hydrodynamics , Dover.
  30. Leiss, C., Didden, N. (1976), "Experimente zum Einfluss der Anfangsbedingungen auf die Instabilität von Ringwirbeln," Z. angew. Math. Mech. , 56 , T206.
  31. Linden, P.F. (1973), "The Interaction of a Vortex Ring with a Sharp Density Interface: a Model for Turbulent Entrainment," J. Fluid Mech. , 60 , 467.
  32. Magarvey, R.H., MacLatchy, C.S. (1964), "The Formation and Structure of Vortex Rings," Can. J. Phys. , 42 , 678.
  33. Magarvey, R.H., MacLatchy, C.S. (1964), "The Disintegration of Vortex Rings," Can. J. Phys. , 42 , 684.
  34. Maxworthy, T. (1972), "The Structure and Stability of Vortex Rings," J. Fluid Mech. , 51 , 15.
  35. Maxworthy, T. (1974), "Turbulent Vortex Rings," J. Fluid Mech. , 64 , 227.
  36. Maxworthy, T. (1977), "Some Experimental Studies of Vortex Rings," J. Fluid Mech. , 81 , 465.
  37. Meng, J.C.S. (1978), "The Physics of Vortex Ring Evolution in a Stratified and Shearing Environment," J. Fluid Mech. , 84 , 455.
  38. Miloh, T., Schlein, D.J. (1977), "Passage of a Vortex Ring Through a Circular Aperture in an Infinite Plane," Phys. Fluids , 20 , 1219.
  39. Moring, W. (1978), "On Vortex Sound at Low Mach Number," J. Fluid Mech. , 85 , 685.
  40. Moore, D.W. Saffman, P.G. (1974), "A Note on the Stability of a Vortex Ring of Small Cross Section," Proc. Roy. Soc. London , A338 , 535.
  41. Morton, B.R. (1960), "Weak Thermal Vortex Rings," J. Fluid Mech. , 9 , 107.

42. Norbury, J. (1972), "A Steady Vortex Ring Close to Hill's Spherical Vortex," Proc. Camb. Phil. Soc. , 72 , 253.
43. Norbury, J. (1973), "A Family of Steady Vortex Rings," J. Fluid Mech. , 57 , 417.
44. O'Brien, V. (1961), "Steady Spheroidal Vortices--More Exact Solutions to the Navier-Stokes Equations," Quart. Appl. Math. , 19 , 163.
45. Oka, S. (1936), "On the Instability and Breaking Up of a Ring of Liquid into Small Drops," Physico-Math. Soc. Japan , 18 , 525.
46. Okabe, J., Inoue, S. (1961), "The Generation of Vortex Rings," Rep. Res. Inst. Appl. Mech. , Kyushu University, 8 , 91.
47. Okabe, J., Inoue, S. (1961), "The Generation of Vortex Rings II," Rep. Res. Inst. Appl. Mech. , Kyushu University, 9 , 147.
48. Oshima, Y. (1972), "Motion of Vortex Rings in Water," J. Phys. Soc. Japan , 32 , 1125.
49. Oshima, Y., Kambe, T., Asaka, S. (1975), "Interaction of Two Vortex Rings Moving Along a Common Axis of Symmetry," J. Phys. Soc. Japan , 38 , 1159.
50. Phillips, O.M. (1956), "The Final Period of Decay of Non-homogeneous Turbulence," Proc. Camb. Phil. Soc. , 52 , 135.
51. Pullin, D.I. (1979), "Vortex Ring Formation at Tube and Orifice Openings," Phys. Fluids , 22 , 401.
52. Rayner, J.M.V. (1979), "A Vortex Theory of Animal Flight, Part 1 and Part 2," J. Fluid Mech. , 91 , 697 and 731.
53. Riley, N. (1974), "Flows with Concentrated Vorticity: A Report on EUROMECH 41," J. Fluid Mech. , 62 , 33.
54. Saffman, P.G. (1970), "The Velocity of Viscous Vortex Rings," Stud. Appl. Math. , 49 , 371.
55. Saffman, P.G. (1975), "On the Formation of Vortex Rings," Stud. Appl. Math. , /ul 54 , 261.
56. Saffman, P.G. (1978), "The Number of Waves on Unstable Vortex Rings," J. Fluid Mech. , 84 , 625.
57. Sallet, D.W., Widmayer, R.S. (1974), "An Experimental Investigation of Laminar and Turbulent Vortex Rings in Air," Z. Flugwiss , 22 , 207.

58. Sallet, D.W. (1975), "Impulsive Motion of a Circular Disk Which Causes a Vortex Ring," Phys. Fluids , 18 , 109.
59. Shlien, D.J., Thompson, D.W. (1975), "Some Experiments on the Motion of an Isolated Laminar Thermal," J. Fluid Mech. , 72 , 35.
60. Sullivan, J.P., Widnall, S.E., Ezekiel, S. (1973), " Study of Vortex Rings using a Laser Doppler Velocimeter," AIAA Journal , 11 , 1384.
61. Taylor, G.I. (1953), "Formation of a Vortex Ring by Giving an Impulse to a Circular Disk and Then Dissolving it Away," J. Appl. Phys. , 24 , 104.
62. Thomson, J.J. (1883), A Treatise on the Motion of Vortex Rings , MacMillan and Co., London.
63. Thomson, J.J. (1885), "On the Formation of Vortex Rings by Drops Falling into Liquids and some Allied Phenomenon," Proc. Roy.Soc. London , 39 , 417.
64. Thomson, W. or Lord Kelvin (1910), Mathematical and Physical Papers , Vol. IV, Articles No. 1, 2, 3, 10, Cambridge University Press.
65. Tobin, R., Chang, I-D. (1976), "Wall Pressure Spectra Scaling Downstream of Stenoses in Steady Tube Flow," J. Biomech. , 9 , 633.
66. Tsai, C-Y., Widnall, S.E. (1976), "The Instability of Short Waves on a Straight Vortex Filament in a Weak Externally Imposed Strain Field," J. Fluid Mech. , 73 , 721.
67. Tung, C., Ting, L. (1967), "Motion and Decay of a Vortex Ring," Phys. Fluids , 10 , 901.
68. Turner, J.S. (1957), "Buoyant Vortex Rings," Proc. Roy. Soc. London , A239 , 61.
69. Turner, J.S. (1960), "A Comparison Between Buoyant Vortex Rings and Vortex Pairs," J. Fluid Mech. , 7 , 419.
70. Turner, J.S. (1964), "The Flow into an Expanding Spherical Vortex," J. Fluid Mech. , 18 , 195.
71. Van Dyke, M. (1974), "Analysis and Improvement of Perturbation Series," Q.J. Mech. Appl. Math. , 27 , 423.

72. Walraven, A. (1970), "Energy and Motion of Vortex Rings in Liquid Helium II in the Presence of Various Plane Obstacles," Phys. Rev. , 1 , 145.
73. Wells, D.R. (1962), "Observation of Plasma Vortex Rings," Phys. Fluids , 5 , 1016.
74. Widnall, S.E., Sullivan, J.P. (1973), "On the Stability of Vortex Rings," Proc. Roy. Soc. London , A332 , 335.
75. Widnall, S.E., Bliss, D.B., Tsai, C.-Y. (1974), "The Instability of Short Waves on a Vortex Ring," J. Fluid Mech. , 66 , 35.
76. Widnall, S.E. (1975), "The Structure and Dynamics of Vortex Filaments," Ann. Rev. Fl. Mech. , 7 , 141.
77. Widnall, S.E., Tsai, C.-Y. (1977), "The Instability of the Thin Vortex Ring of Constant Vorticity," Phil. Trans. Roy. Soc. London , 287 , No. 1344.
78. Winant, C.D., Browand, F.K. (1974), "Vortex Pairing: The Mechanism of Turbulent Mixing-layer Growth at Moderate Reynolds Number," J. Fluid Mech. , 63 , 237.
79. Yamada, H., Matsu, T. (1978), "Preliminary Study of Mutual Slip-Through of a Pair of Vortices," Phys. Fluids , 21 , 292.



The true artist is a *tlacuilo*  
he paints with red-and-black ink  
with black water  
the true artist is wise  
god is in his heart he paints god  
into things  
he knows all colors  
he makes shapes he draws feet  
and faces  
he paints shadows  
he is a Toltec  
he has a dialogue with his own heart

-poems from ancient Mexico  
retold from Nahuatl texts

*To Agnes*

**End of Document**